2014

Nonlinear optical response and transport properties in graphene

Yee Sin Ang
University of Wollongong

School of Physics

Nonlinear optical response and transport properties in graphene

Yee Sin Ang

Supervisor

Prof. Chao Zhang

This thesis is presented as required for the

Award of the Degree of

Doctor of Philosophy

of the

University of Wollongong

Aug 2014

Declaration

I, Yee Sin Ang, declare that this thesis, submitted in fulfilment of the requirements for the award of Doctor of Philosophy, of the School of Physics, University of Wollongong, is wholly my own work unless otherwise referenced or acknowledged. The document has not been submitted for qualifications at any other academic institution.

Yee Sin Ang, August 13, 2014

Acknowledgments

I would like to express my deepest gratitude to my thesis supervisor Prof. Chao Zhang for his tremendous support of my PhD study and research. Throughout these four years, he has continuously encouraged and inspired me in exploring the beautiful world of physics. I appreciate his vast knowledge and skills in many areas of physics. His insightful comments has greatly shaped my PhD research. It is certainly impossible to complete my dissertation without his patient guidance.

I acknowledge Prof. Zhongshui Ma from the Peking University for his collaboration and I sincerely appreciate his willingness to share many interesting research ideas. I thank Dr. David Martin for taking time out of his busy schedule to proof read my articles. I would also like to thank the UOW physics academics, especially Prof. Roger Lewis, A. Prof. Josip Horvat, A. Prof. Michael Lerch, Dr. George Tackas and Duncan Fisher for their supports throughout my PhD years.

I thank the UOW Physics Society students: Lachlan Marnham, Tom O'Brien, Matthew Sanderson and Matt Westlake for inviting me to many of the interesting Society activities which have greatly brightened up my PhD life. I thank my fellow PhD student Qin-Jun Chen for the thought-provoking discussions on the numerical techniques; Kai Yang Li and Bo Zhang for many many cups of afternoon coffee. These coffees had efficiently fueled up the writing of this thesis.

I must acknowledge my best friends for their accompaniments throughout my PhD years. I thank Ben Kok Hau Lee, Dr. Ivan Seng, Hovis Ho and Shaun Lin for all the fun gatherings and trips we had. I would also like to thank my best friends in Singapore, Chun Yun Kee and Hung Seng Yew. Their supports have been the most important motivation whenever I was overwhelmed by the stress of research. I would also like to thank Ru Er Chang for her supports and cares during the finalization of this thesis.

Last but not least, I would like to thank my parents for the love and supports they provided me throughout my life.

Abstract

We study the nonlinear optical response of single layer layer graphene (SLG) and several of its sister-structures, and the transport properties of bilayer graphene (BLG) and two-dimensional electron gas with Rashba spin-orbit interaction (R2DEG) in this Thesis.

We found that SLG exhibits a strong intraband nonlinear optical response, requiring a moderate field strength in the order of 10^4 V/cm. In the presence of a strong electric field strength, the third-order nonlinear current density increases at elevated temperature. The situation becomes more complicated in the case of gapped graphene. We found that the nonlinear optical response of gapped graphene is sensitively influenced by the temperature and the magnitude of the bandgap.

For the interband nonlinear optical response, the presence of the k-parabolic term in the Hamiltonian of these structures not only preserve their nonlinear interband optical response, but also induces a temperature robustness. These systems exhibit enhanced optical nonlinearity at higher temperature. In gapped graphene, the three-photon interband nonlinear optical absorption generates a sub-gap nonlinear response peak. Together with the linear response peak, gapped graphene exhibits two-color response at terahertz frequency regime. In graphene superlattice, the Dirac cone is elliptically deformed and it is found that this elliptical deformation of the band structure enhances both of the linear and nonlinear optical responses.

In the transport study of bilayer graphene/superconductor (BLG/S) heterojunction we obtained two main results. First, *retro* reflection of electron can occur at the interface. This retro-type reflection is the most unusual and it represents the last missing pieces of the quantum transport phenomena at a superconductor heterojunction where specular electron reflection, retro and specular Andreev reflections have all been demonstrated. Second, due to the unique spinor structure of the BLG low energy quasiparticle wavefunction, electron transmitting into the superconductor is strictly forbidden and this results in the total absence of the Andreev reflection in a BLG/S heterojunction.

The consequences of band topology on the electron transport properties of R2DEG are studied. Because of the band turning and the band crossing of the two spin-plit branches, the electron transport exhibits hybrid behaviors of massless and massive

chiral fermions. Furthermore, we found that the tunneling at the vicinity of the band crossing point produces a spin-polarizing effect.

Finally, we calculate the energy loss rate of a fast charged particle scattering off graphene. We found that the absence of backscattering is not only an intrinsic property between two massless Dirac quasiparticles, but it also occurs between an external charged particle and a massless Dirac quasiparticles. Graphene becomes completely transparent to a charged particle of kinetic energy lower than approximately 3 eV.

List of Publications

Journal Article

- Ang, Y. S., Sultan, S. and Zhang, C., Nonlinear optical spectrum of bilayer graphene in the terahertz regime, *Appl. Phys. Lett.* **97**, 243110 (2010).
- Ang, Y. S. and Zhang, C., Subgap optical conductivity in semihydrogenated graphene, *Appl. Phys. Lett.* **98**, 042107 (2011).
- Ang, Y. S., Zhang, C. and Kee, C. Y., Energy-loss rate of a fast particle in graphene, *Appl. Phys. Lett.* **99**, 053111 (2011).
- Sultan, S., Ang, Y. S. and Zhang, C., Room-temperature strong terahertz photon mixing in graphene, *J. Opt. Soc. Am. B* **29**, 3, 274-279 (2012).
- Ang, Y. S., Sultan, S., Tawfiq, A., Cao, J. and Zhang, C., Terahertz photon mixing effect in gapped graphene, *J. Infrared, Millimeter and Terahertz Waves* **33**, 8, 816-824 (2012).
- Ang, Y. S. and Zhang, C., Enhanced optical conductance in graphene superlattice due to anisotropic band dispersion, *J. Phys. D: Appl. Phys.* **45**, 395303 (2012).
- Chen, Q., Ang, Y. S., Lewis, R. A., Wang, X. and Zhang, C., Photomixing in topological insulator HgTe/CdTe quantum wells in terahertz regime, *Appl. Phys. Lett.* **101**, 211109 (2012).
- Ang, Y. S., Ma, Z. and Zhang, C., Retro reflection of electrons at the interface of bilayer graphene and superconductor, *Sci. Rep.* **2**, 1013 (2012).
- Chen, Q., Ang, Y. S., Lewis, R. A., Wang, X. and Zhang, C., Energy loss rate of a charged particle in HgTe/(HgTe, CdTe) quantum wells, *Appl. Phys. Lett.* **103**, 192107 (2013).
- Sanderson, M., Ang, Y. S. and Zhang, C., Klein paradox and cone transport in AA-stacked bilayer graphene, *Phys. Rev. B* **88**, 245404 (2013).

- Ang, Y. S., Ma, Z. and Zhang, C., Chiral-like tunneling in two-dimensional electron gas with Rashba spin-orbit interaction, *Sci. Rep.* **4**, 3780 (2013).

- Ang, Y. S., Cao, J. C. and Zhang, C., Nonlinear terahertz optical response of two-dimensional electronic system with Rashba spin-orbit interaction, *Eur. Phys. J. B* **87**, 2, 1 - 7 (2014).

- Cao, W. H. and Ang, Y. S., Effect of asymmetry on nonlinear optical response in graphene, Eur. Phys. Lett. 107, 37007 (2014).

- Ang, Y. S. and Zhang, C., (manuscript in preparation) Quantum ratchet effect in two-dimensional electron gas with Rashba spin-orbit interaction (2014).

Conference Paper

- Ang, Y. S., Sultan, S., Vickers, R. E. M. and Zhang, C., Nonlinear optical properties of bilayer graphene in terahertz regime, *36th Conference on Infrared, Millimeter and Terahertz Waves (IRMMW-THz 2011)*, Houston, USA.

- Ang, Y. S. and Zhang, C., Two-color nonlinear optical response of graphene with broken AB-symmetry, *36th Conference on Infrared, Millimeter and Terahertz Waves (IRMMW-THz 2011)*, Houston, USA.

- Ang, Y. and Zhang, C., Strong nonlinear optical response of bilayer graphene in the terahertz regime, *Key Engineering Materials*, **500**, 62-65 (2012).

- Ang, Y. S., Chen, Q., Wang, X., Lewis, R. A. and Zhang, C., Terahertz photon mixing effect in graphene and topological insulator, *37th Conference on Infrared, Millimeter and Terahertz Waves (IRMMW-THz 2012)*, Wollongong, Australia.

- Ang, Y. S. and Zhang, C., Intraband nonlinear terahertz waves absorption of gapped graphene, *37th Conference on Infrared, Millimeter and Terahertz Waves (IRMMW-THz 2012)*, Wollongong, Australia.

- Ang, Y. S. and Zhang, C., Nonlinear optical response of graphene superlattice in Terahertz frequency regime, *International Photonics and Opto-electronics Meetings (POEM2012)*, Wuhan, China.

- Zhang, C. and Ang, Y. S., Nonlinear transmittance of bilayer graphene in terahertz regime, *International Photonics and Opto-electronics Meetings (POEM2012)*, Wuhan, China.

- Ang, Y. S., Chen, Q. and Zhang, C., Nonlinear optical spectrum of two-dimensional electron gas with Rashba spin-orbit interaction in THz frequency regime, *38th Conference on Infrared, Millimeter and Terahertz Waves (IRMMW-THz 2013)*, Mainz, Germany.

Contents

List of Figures **x**

1 Introduction **1**
1.1 Electronic properties of graphene 5
1.1.1 Single layer graphene 5
1.1.2 AB-stacked bilayer graphene 8
1.1.3 AA-stacked bilayer graphene 10
1.2 Nonlinear optical properties of graphene 12
1.2.1 Semiclassical electron transport theory 14
1.2.2 n-photon electron coupling wavefunction 15
1.3 Klein transport in graphene: band crossing, touching and turning . . 16
1.4 Overview of this Thesis 20

2 Nonlinear optical response in graphene **21**
2.1 Introduction 21
2.2 Optical response of graphene in a weak electric field 22
2.2.1 Linear optical response 25
2.2.2 Nonlinear optical response 26
2.2.3 Critical electric field and photon-mixing effect 30
2.3 Optical response of graphene in a strong electric field 32
2.3.1 Population redistribution due to a strong electric field 32
2.3.2 Nonlinear optical response of strong field driven massless Dirac Fermion 35
2.3.3 Critical electric field in the strong-field regime 38
2.4 Optical response of gapped graphene in a strong electric field 40
2.5 Discussion 45

3 Nonlinear optical response in bilayer graphene and 2D electron gas with Rashba spin-orbit coupling **48**
3.1 Nonlinear optical response of bilayer graphene 48
3.1.1 Recursion equations for n-photon-electron coupling 49

3.1.2 Optical current operator and density . . . 52
3.1.3 Linear optical response: derivation . . . 54
3.1.4 Nonlinear optical response . . . 58
3.1.5 Discussion . . . 61
3.2 Nonlinear optical response in 2D semiconductor with Rashba spin-orbit interaction . . . 62
3.2.1 Recursion equations of R2DEG in an external electric field . . . 62
3.2.2 Linear optical conductivity . . . 65
3.2.3 Third-order nonlinear optical conductivity . . . 66
3.2.4 Effects of v_R and m^* on R2DG Nonlinear Optical Response . . . 69
3.2.5 Discussion . . . 72

4 Nonlinear optical response in graphene: bandgap opening and band anisotropy 74
4.1 Subgap nonlinear conductivity in semihydrogenated graphene . . . 75
4.1.1 Recursion equations and linear optical current density . . . 75
4.1.2 Linear optical response . . . 78
4.1.3 Nonlinear optical response of semihydrogenated graphene . . . 81
4.2 Optical spectrum of graphene superlattice . . . 86
4.2.1 Recursion equations of anisotropic massless Dirac fermion . . . 87
4.2.2 Linear optical response . . . 91
4.2.3 Discussion . . . 95

5 Retro reflection of electrons at the interface of bilayer graphene and superconductor 97
5.1 Specular reflection and retro reflection . . . 97
5.2 Retro electron reflection in bilayer graphene . . . 102
5.3 Absence of Andreev reflection in a BLG/S junction . . . 105
5.4 BLG/S junction as a valley-selective Veselago electron-mirror . . . 111
5.5 Discussion . . . 115

6 Chiral-like tunneling in 2D semiconductors with Rashba spin-orbit coupling 116
6.1 Real spin chiral-like tunneling of electrons in R2DEG . . . 116
6.2 Transmission and reflection probabilities . . . 120
6.3 π Berry phase electron backscattering . . . 125
6.4 Spin-polarized transmission through a *n-p* junction . . . 127
6.5 Discussion . . . 130

7 Energy loss rate of a fast charged particle in graphene 131
7.1 Introduction 131
7.2 Absence of backscattering of an external charged particle scattering . 132
7.3 Energy loss rate, mean scattering time and diffusion constant 134
7.4 Discussion 137

8 Conclusion and outlooks 139

Bibliography 143

Appendices

A Derivation of $\sigma(\omega)$ and $\sigma(3\omega)$ of bilayer graphene 153
A.1 $n = 2$ and $n = 3$ spinor components 153
A.2 Derivation of $\sigma_3(\omega)$ 154
A.3 Derivation of $\sigma_3(3\omega)$ 159

List of Figures

1.1 Graphene, an atomically thin layer of carbon atoms arranged in honeycomb structure. 2
1.2 Crystal structure of single layer graphene. Blue and red circle denotes sublattices $\mathcal{A}$ and $\mathcal{B}$ respectively. 6
1.3 (a) Crystal structure of single layer graphene. Blue and red circle denotes sublattices $\mathcal{A}$ and $\mathcal{B}$ respectively. (b) The linear energy spectrum at K and K' point. The valence band touches the conduction band at the Dirac point. 7
1.4 (a) Crystal structure of AB-stacked bilayer graphene. (b) Trigonal warping effect of the low energy band structure. 9
1.5 Crystal structure of AA-stacked bilayer graphene. 11
1.6 Klein transport of (a) single layer graphene; and (b) bilayer graphene. At normal incidence, the branches of opposite pseudospins are decoupled (represented by solid and dashed curve). (c) The band structure in the graphene side of a graphene/superconductor heterojunction. The green (red) arrow denotes the Andreev process involving a conduction (valence) hole. (d) Specular (red) and retro (green) Andreev reflection. 17
1.7 Hybrid transport when the decoupled branches both turn and cross: (a) R2DEG; and (b) bilayer graphene with trigonal warping effect. . . 18

2.1 Temperature dependence of third order nonlinear current density for $\mu < 0$ at $f = 1$ THz. 27
2.2 Temperature dependence of third order nonlinear current density for $\mu > 0$ at $f = 1$ THz. 28
2.3 Temperature dependence of β at $f = 1$ THz. β exhibits contrasting behavior at low and high temperature regimes. 31

2.4 (a) Temperature dependence of the strong-field critical fields $E_c^{(S)}$at $f = 1$ THz for $\mu = 0.06$ eV (dotted), $\mu = 0.08$ eV (dashed) and $\mu = 0.1$ eV (solid). The Weak-field critical field E_c for $\mu = 0.1$ eV is also shown (dash-dotted). (b) Temperature dependence of the strong field $\beta^{(S)}$ at $f = 1$ THz for $\mu = 0.06$ eV (dotted), $\mu = 0.08$ eV (dashed) and $\mu = 0.1$ eV (solid). 39
2.5 Temperature dependence of strong-field third order nonlinear current density at $f = 1$ THz. Note that $T = T_{lattice}$ if non-equilibrium heating is ignored and $T = T_{hot}$ if non-equilibrium heating is considered. Since $T_{hot} > T_{lattice}$, the nonlinear optical response is significantly stronger if carrier heating is considered. 40
2.6 Δ and temperature dependence of the third-order nonlinear current density at $f = 1.5$ THz and $\mu = 0.1$eV. 45

3.1 Frequency dependence of the linear optical conductivity at different interlayer coupling strength. Dotted curve: 0.1α, dashed curve: 0.5α, solid curve: α, dash-dotted curve: 1.5α, where $\alpha = 1/2m^*$ and $m^* = 0.33m_e$ [70]. The low frequency conductivity always approach $6\sigma_0$ regardless the strength of the interlayer coupling. 57
3.2 Frequency dependence of the third-order nonlinear optical conductivities at zero and room temperatures. The electric field strength is 1000 V/cm. 58
3.3 Linear and nonlinaer conductances vs. temperature for frequency of 1 THz. The electric field is 600 V/cm 59
3.4 Frequency dependent critical fields at zero and room temperatures. . 60
3.5 Temperature dependent critical fields for frequency of 1 THz. 61
3.6 (a) Band structure of R2DG. The Fermi energy is at $\varepsilon_F = 0$. The red (dashed) arrow denote forbidden interband transition. The blue (solid) arrow denote permissible interband transition; (b) Linear conductivity. Rashba energy of $E_R = 2.1$ meV is used. The conductivity is normalized by $\sigma_R = e^2/8\hbar$. 65
3.7 Third order nonlinear optical conductivities $\sigma(\omega)$ (solid curve) and $\sigma(3\omega)$ (dashed curve) at $E = 1000$ V/cm. (a) $T = 0$ K, the sharp edges marks the cut-off of 1-photon edge (I), 2-photon edge (II) and 3-photon edge (III); (b) $T = 300K$. 67

3.8 Temperature dependence of critical electric field strength $E_c(\omega)$ (solid curve) and $E_c(3\omega)$ (dashed curve) at various frequency: (a) 1 THz, (b) 2 THz, (c) 5 THz, and (d) 7 THz. The low temperature nonlinear conductivities are mainly contributed by 1-photon edge. At higher temperature, the smearing of 2-photon and 3-photon edges enhances the NOR, resulting in gradually decreasing critical field strength. . . 68

3.9 v_R-dependence of the nonlinear conductivities, $\sigma_3(\omega)$ (solid curve) and $\sigma_3(3\omega)$ (dashed curve), at: (a) $T = 0$ K; (b) $T = 300$ K with $E = 1000$ V/cm. v_R-dependence of the critical electric fields, $E_c(\omega)$ (solid curve) and $E_c(3\omega)$ (dashed curve), at: (c) $T = 0$ K; and (d) $T = 300$ K. The frequency is set to 1 THz and effective mass $m^* = 0.05m_e$. The shaded region in the (a) and (c) denotes the regime when the Rashba splitting is too small to accommodate the optical transition of electrons. 70

3.10 m^* dependence of the critical electric field strengths, $E_c(\omega)$ (solid curve) and $E_c(3\omega)$ (dashed curve), of the frequency tripling term at 1 THz: (a) $T = 4$ K and (b) $T = 15$ K ($v_R = 5 \times 10^4$ m/s). (c) Temperature dependence of $E_c(3\omega)$ at various values of m^*. At low temperature, $E_c(3\omega)$ is a complicated function of m^* but is, in general, smaller for larger m^* (except $m^* = 0.05m_e$) due to the photon-edges. At high temperature regime, $E_c(3\omega)$ is smaller for small m^*. The parabolic term H_0 is therefore an important component in achieving strong optical nonlinearity at elevated temperature. 71

3.11 (Color online) Comparison between $E_c(3\omega)$ of graphene [89] and R2DG in BiTeI layered semiconductor and Bi/Ag(111) surface alloys: (a) 1 THz; (b) 2 THz; (c) 5 THz; and (d) 7 THz. Although at low temperature regime single layer graphene (SLG) has stronger optical nonlinearity (lower E_c), this optical nonlinearity does not survive at higher temperature. In contrast, R2DG shows stronger optical nonlinearity at elevated temperature. 72

4.1 The frequency dependent optical conductance in the low frequency regime for two temperatures. The electric field is 3600 V/cm. The absorption edge for the frequency tripled response is shifted to $\Delta/3$. The inset is a schematic showing different optical processes. 82

4.2 The frequency dependence of the critical field $E(3\omega)$ for SHG and pure (gapless) graphene. The inset shows the reduction of the critical field in SHG. Note that there exists a cut-off frequency $f_c = \Delta/3h \approx 2.4$ THz since $\sigma_3(3\omega) = 0$ at frequency smaller than f_c. 84

4.3 The temperature dependence of the critical field at two different frequencies of 2.4 and 5 THz. 85
4.4 Band structure of graphene superlattice (inset). In the p_x-p_y plan, the Dirac cone is elongated elliptically in the y-direction. L, w and U are the superlattice periodicity, potential width and potential height, respectively, of the Kronig-Penney type graphene superlattice. 88
4.5 The frequency dependence of $\sigma_3(3\omega)$ at $E = 1000$ V/cm and 300 K. . 94
4.6 Anisotropic gapped graphene frequency-tripling conductivity at 300 K and $E = 3400$ V/cm and $\Delta = 0.03$ eV. 95

5.1 (a) Since electron group velocity component v_y is locked to the momentum component k_y, conservation of k_y allows only specular electron reflection (SER) to occur; (b) retro electron reflection (RER) requires v_y to be 'unlocked' from k_y such that reversal of v_y can still occur while conserving k_y; (c) constant energy slice of a parabolic (or linear) energy spectrum. The circular band contour allows only SER to occur; (d) constant energy slice of a hypothetical energy spectrum with boomerang-shaped band contour. The constant energy band contour of the incident states in k-space is convex while that of the reflected states is concave. The opposite band contours between incident and reflected states causes the sign reversal of v_y upon reflection. This results in RER. 99
5.2 (a) Bernal-stacked bilayer graphene lattice structure; (b) the energy spectrum contour plot in phase space, showing three distinct energy regime: Regime (A): $\varepsilon_k < \varepsilon_0/4$, Regime (B): $\varepsilon_0/4 < \varepsilon_k < 10.9\varepsilon_0$ and Regime (C): $\varepsilon_k > 10.9\varepsilon_0$. Retro electron reflection occurs optimally in Regime (B) due to its 'boomerang-like' anisotropic constant energy band contour in k-space. In high energy Regime (C), retro reflection is no longer possible as the band contour becomes parabolic-like; (c) Band contour of an constant energy slice in Regime (B). The green and blue arrows denotes incident and reflected electron direction of motion respectively. The opposite band contour between incident (convex) and reflected states (concave) causes v_y to reverse its direction upon reflection, leading to RER. 100

5.3 (a)-(c) Group velocity component v_x; (d)-(f) group velocity component v_y; and (g)-(i) incident and reflection angles of an incident K valley electron in states k_y. The energies are $\varepsilon_k = 0.5\varepsilon_0$, $\varepsilon_k = 2\varepsilon_0$ and $\varepsilon_k = 5\varepsilon_0$ respectively for column 1, 2 and 3. In (a)-(c), v_x is positive for incident electrons and negative for reflected electrons. The RER regime is enclosed between the dashed lines in (d)-(i). In (d)-(f), sign reversal of v_y corresponds to RER. In (g)-(i), the reflection angle of RER does not change sign since electron is reflected to the same side of the normal. At small ε_k, almost all of the permissible reflections are RER. As E_k increases, more permissible states becomes specular reflection states (which lies outside the RER windows) and the RER angle approaches 0°. 103

5.4 (Left) Regime A1 and (right) Regime A2 excitation spectrum 106

5.5 RER in BLG/S junction. Green, blue and gray arrows indicate incident electron, retro-reflected electron and transmitted quasiparticle respectively. Transmission across the junction is forbidden due to the 2π Berry phase nature of bilayer graphene electron. The junction is hence 100% electron-reflective. 111

5.6 Schematic drawings of (a) Veselago lens with $n_t = -n_i$; and (b) Veselago mirror $n_r \approx -n_i$. In the Veselago lens, a ray emitted from a point source (denoted by yellow triangle) is focused at the transmitted side of the interface. For the Veselago mirror, $n_r \approx -n_i$ is chosen for better visual clarity. The retro-reflected ray is focused at the incident side of the interface. 112

5.7 The electron excitation spectrum of BLG/S at (a) a K valley and (b) a K' valley with $\varepsilon_F = 0.5\varepsilon_0$ and $E_k = \varepsilon_0$. The RER constant energy band contour of the K valley (red dashed curve) is significantly 'smoother' than that of the K' valley (green dashed curve). At large $|k_y|$ (SER regime), K and K' band contours become approximately identical; (c) Reflection angles of K (red curve) and K'(green curve) electrons. K electrons are predominantly focused via smaller angle ($< 20°$) than that of the K' electrons ($\approx 80°$). (d) RER trajectory of electrons emitted from a point source situated at **P** (denoted by yellow triangle). Blue rays represent the incident electrons. The interface acts as a valley-selective dual-focus electron mirror with K electrons (red rays) being focused further away from the interface than the K' electrons (green rays). 114

6.1 Klein effect in condensed matter systems at normal incidence. (a) perfect transmission of massless chiral fermion in SLG and perfect reflection of massive chiral fermion in BLG. (b) Band structure of R2DEG. (c) Simultaneous mixture of massless and massive chiral fermions transport across a potential barrier $V(x)$ in R2EG. The tunneling process (outlined by solid box) mimics massless chiral fermion while the reflection process (outlined by dahsed box) mimics massive chiral fermion. In (a) - (c), the arrows denote the direction of motion of the quasiparticles and electrons. The blue and red branches denote the decoupled branches of opposite pseudospin [(a) and (b)] and real-spin [(c)] at normal incidence. (d) Fermi contours at the incident side ($x < 0$) and at the transmitted side ($x > 0$). 117

6.2 Transmission/reflection probabilites at normal incidence, (a) at different $\mathcal{V}$ with $\mathcal{Z} = 0$, solid line: $T_{-s}^{(s)}(\mathcal{E} = 0.1)$, dashed line: $R_{-s}^{(s)}(\mathcal{E} = 0.1)$, $\circ$: $T_{-s}^{(s)}(\mathcal{E} = 10)$, $\diamond$: $R_{-s}^{(s)}(\mathcal{E} = 10)$; and (b) at different $\mathcal{Z}$ with $\mathcal{E} = 1$, solid line: $T_{-s}^{(s)}(\mathcal{V} = 0.1)$, dashed line: $R_{-s}^{(s)}(\mathcal{V} = 0.1)$, $\circ$: $T_{-s}^{(s)}(\mathcal{V} = 0.9)$, $\diamond$: $R_{-s}^{(s)}(\mathcal{V} = 0.9)$. 124

6.3 Probabilities at finite incident angle ϕ at two incident states $s = \pm 1$ with $\mathcal{Z} = 0.1$ in (a) and (b); and with $\mathcal{Z} = 1$ in (c) and (d). 127

6.4 Dependence of spin-polarization, $\Delta\mathcal{T}$, on $\mathcal{V}$, $\mathcal{E}$ and $\mathcal{Z}$. (a) $\mathcal{V}$-and $\mathcal{E}$-dependence at $\mathcal{Z} = 1$. (b) $\mathcal{V}$-and $\mathcal{Z}$-dependence at $\mathcal{E} = 1$. $\mathcal{E}$-and $\mathcal{Z}$-dependence at (c) $\mathcal{V} = 0.1$; and (d) $\mathcal{V} = 0.9$. 129

7.1 ELR $\varepsilon_{\mathbf{p}}$-sepctrum of electron at T=77K. Unlike electron gas in normal metal, graphene ELR always increases wth increasing $\varepsilon_{\mathbf{p}}$. The ELR is in the arbitrary unit of $\gamma V_0 \varepsilon_v/\hbar$. Inset shows the scattering process. . 135

7.2 $\varepsilon_{\boldsymbol{p}}$-spectrum of $\tau_{\boldsymbol{p}}$ at $T = 77K$. $\tau_{\boldsymbol{p}}$ is plotted in arbitrary unit of $\hbar/2\gamma V_0$ 136

7.3 $\varepsilon_{\boldsymbol{p}}$-spectrum of $D_{\boldsymbol{p}}$ at $T = 77K$. $D_{\boldsymbol{p}}$ is plotted in arbitrary unit of $\hbar\varepsilon_v/4\gamma V_0$ 137

8.1 Outlooks. (a) Angular-dependent optical response; (b) optical response in the presence of an in-plane electric field; (c) electron transport at the trigonal warping warping region where the energy band is split into one central and three sattelite Dirac points; and (d) a gapped-BLG/superconductor/gapped-BLG device. Reversing the polarity of the gate electrodes changes the sign of ΔU and flips the pseudospin magnetization. 142

1 | Introduction

Graphene is a one-atom thick, 2-dimensional honeycomb structure made up of carbon atoms (Fig. 1.1). The single layer was first isolated and systematically studied by Novoselov and Geim in 2004 [1]. The first theoretical study of graphene however dated back to 1947. In his pioneering paper [2], P. R. Wallace found that Graphene is a gapless semiconductor whose valence band touches the conduction band at K and K' points of its Brillouin zone. The most fascinating aspect of this touching point, or the 'Dirac point', is that the energy band is in a linear form of $E_k = \pm\hbar v_F k$ and hence the electrons around the Dirac points behaves like a massless ultra-relativistic fermions, but moving with a much reduced 'speed of light' $v_F \approx c/300$ (c = vacuum speed of light) [3]. This aspect is fundamentally different from the Scrhodinger fermions $E_k = \hbar^2 k^2/2m^*$ in conventional semiconductors. Many unusual physical phenomena arise due to the relativistic quasiparticle dynamics. For example, the K point electrons exhibit anomalous perfect tunneling effect despite the potential barrier height and width [4]. This anomalous tunneling behavior is related to the Klein tunneling of massless spin-1/2 Dirac particles in quantum electrodynamics [5]. The Klein tunneling was thought to be a textbook example to illustrate the bizarre consequence of Dirac equation. The scale-down condensed matter version can now be realized in graphene [6, 7].

Because of the relativistic dynamics, electron scattering in graphene is strongly suppressed, this results in an unusually high electron mobility [8, 9]. It is believed that electron mobility of $100,000$ cm^2/Vs can be achieved in high quality sample [10], suggesting a promising transistor application [11, 12]. The massless Dirac fermions

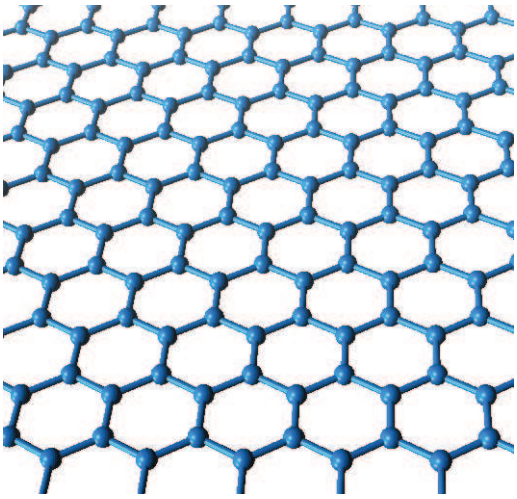

Figure 1.1: Graphene, an atomically thin layer of carbon atoms arranged in honeycomb structure.

exhibits another unusual behavior in the presence of a magnetic field. The quantum Hall conductivity follows half-integer steps $\sigma_{xy} = \pm 4e^2/h(N + 1/2)$ [3, 13, 14] instead of the conventional integer-multiple quantized conductivity in conventional semiconductor. This is again due to the relativistic spectrum of the K electrons where the $E = 0$ Landau level is shared by both electrons and holes. Furthermore, the large energy separation between the two lowest Landau levels allows the quantum Hall effect to survive even at room temperature [15]. The existence of a minimal d.c. conductivity in the absence of charge carrier is another surprising result. The minimal conductivity has a well-established experimental value of $\sigma_{min} = e^2/4h$ [3] yet its physical origin is not well-understood since various theoretical models [4, 16–19] yield very different values of σ_{min}. It has been suggested that the many-body interactions, wrinkling and ripples of the graphene sheet, and the formation of electron-hole puddles [20] could be the possible underlying mechanisms. When interact with photon, the massless Dirac fermion manifests itself as a universal interband optical conductivity of $e^2/4\hbar$ [21–26].

Apart from the unusual electronic and optical properties, electrons in graphene can be manipulated in completely different ways. In graphene, the electron not only has spin, but also possesses two additional degrees of freedom: valley and pseudospin. Such additional degrees of freedom arise from the fact that the low energy electron

resides in two K and K' valleys and their relativistic nature is described by a two-component pseudospinor wavefunction. Although still in the early conceptual stages, the valley and pseusospin degree of freedoms in graphene open up the possibilities of 'valleytroics' and 'pseudospintronics' devices. The concept of 'valleytronics' was first proposed in a nano-constricted device in which two graphene sheets are connected by a narrow zigzag-edge nanoribbon [27]. The electron transport across the junction becomes valley-dependent and the degree of valley polarization is tunable by a gate voltage. Many other strategies has since been proposed. For example, valley-dependent scattering by a line defect [28], spatial splitting of valley current by the trigonally warped band structure at high energy regime [29, 30], tunneling barriers based on gapped graphene and strain-engineered graphene [31–33], and the valley-dependent focusing and de-focusing effect in bilayer graphene n-p junction [34] can all be utilized to produce valley polarization. In addition to the valley degree of freedom, pseudospin magnetization can be generated in graphene with a bandgap [35, 36] or spontaneously generated via electron-electron interaction [37, 38]. More importantly, the pseudospin magnetization can be optically probed [38]. Pseudospin valves in a graphene/superconductor/graphene heterostructure and in a bilayer graphene electrostatic tunneling barrier [36, 39] offer further possibilities to manipulate the transport of the pseudospins.

In terms of device application, graphene is a 'designer' structure whose electronic properties can be tailor-made to meet any device requirement. Graphene can be cut into ribbons or be transformed into superlattices via electrostatic gating. The electronic properties of graphene nanoribbon can be tuned by varying the width and the type of its edges into armchair or zigzag configurations [40–42]. For instance, a bandgap can be opened in armchair graphene nanoribbon and the size of the bandgap is tunable via the nanoribbon width [40, 41]. In the case of graphene superlattices [43–45], elliptical deformation of the Dirac cone can be engineered without breaking the k-linearity of the band structure.

Although it has only been 10 years since the first isolation of graphene [1], myr-

iads of unusual properties, such as the strong suppression of weak localization [46–48], thermoelectric transport [49–51], quantum spin Hall effect [52], chiral superconductivity [53], just to name a few, have been discovered and many more are still continually emerging. It is therefore impossible to fully cover all aspects of graphene in this brief overview. Broader discussions of graphene can be found in several classic review articles [10, 54–57]. Finally, we remark that in a new class of materials, i.e. the topological insulator (TI), the surface states can also described by a Dirac cone. Although it is not the scope of this Thesis to discuss the physics of TI, it is worth-noting that many of the unusual properties of graphene can be directly translated into TI [58]. Together with the emerging single layer honeycomb structures of group IV atoms such as *silicene* [59, 60], *germanene* [61], and *stanene* [62] (single layer silicon, germanium and tin, respectively), it is not unreasonable to speculate that the physics of Dirac fermions shall play an important role in the upcoming developments of condensed matter physics.

1.1 Electronic properties of graphene

1.1.1 Single layer graphene

The crystal structure of single layer graphene is shown in Fig. 1.2(a). The unit cell is formed by two sublattices $\mathcal{A}$ and $\mathcal{B}$. The lattice vectors are given as:

$$\begin{aligned} \mathbf{a}_1 &= \frac{a}{2}(3, \sqrt{3}) \\ \mathbf{a}_2 &= \frac{a}{2}(3, \sqrt{3}) \end{aligned} \tag{1.1}$$

We define a 'hopping' vector: $\delta = -a(1, 0)$ and the sublattices $\mathcal{A}$ and $\mathcal{B}$ are respectively situated at $\mathbf{R}$ and $\mathbf{R} + \delta$. The tight-binding Hamiltonian can be written as [63]:

$$\hat{H} = -t \sum_{\mathbf{R}} |\mathbf{R}\rangle \langle \mathbf{R} + \delta| + |\mathbf{R}\rangle \langle \mathbf{R} + \mathbf{a}_1 + \delta| + |\mathbf{R}\rangle \langle \mathbf{R} + \mathbf{a}_2 + \delta| + h.c. \tag{1.2}$$

We assume that the orbital wavefunction can be represented by the following Bloch functions:

$$\begin{aligned} |\mathbf{k}\rangle_A &= \frac{1}{\sqrt{N}} \sum_{\mathbf{R}} e^{i\mathbf{k}\cdot\mathbf{R}} |\mathbf{R}\rangle \\ |\mathbf{k}\rangle_B &= \frac{1}{\sqrt{N}} \sum_{\mathbf{R}} e^{i\mathbf{k}\cdot\mathbf{R}} |\mathbf{R} + \delta\rangle \end{aligned} \tag{1.3}$$

where N is the number of atom in a unit cell. In the basis of the sublattices $(\mathcal{A}, \mathcal{B})$, the Hamiltonian matrix can then be evaluated as:

$$H_k = \begin{pmatrix} {}_A\langle \mathbf{k}| \hat{H} |\mathbf{k}\rangle_A & {}_A\langle \mathbf{k}| \hat{H} |\mathbf{k}\rangle_B \\ {}_B\langle \mathbf{k}| \hat{H} |\mathbf{k}\rangle_A & {}_B\langle \mathbf{k}| \hat{H} |\mathbf{k}\rangle_B \end{pmatrix} \tag{1.4}$$

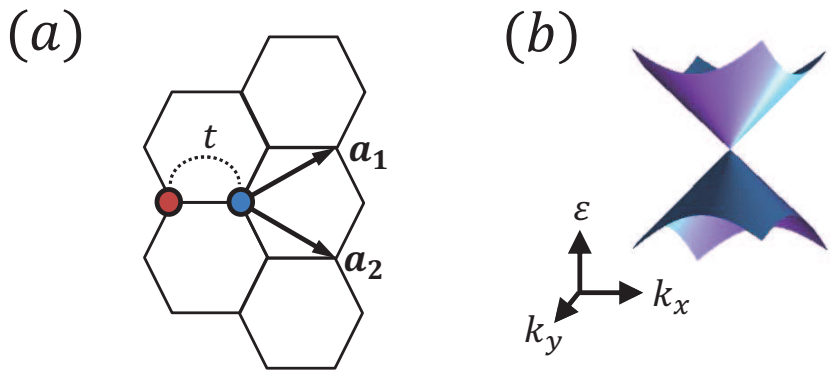

Figure 1.2: Crystal structure of single layer graphene. Blue and red circle denotes sublattices $\mathcal{A}$ and $\mathcal{B}$ respectively.

In the absence of next-nearest neighbour hopping, the matrix elements are given as:

$$\begin{aligned} {}_A\langle \mathbf{k}|\, \hat{H}\, |\mathbf{k}\rangle_A &= {}_B\langle \mathbf{k}|\, \hat{H}\, |\mathbf{k}\rangle_B = 0 \\ {}_A\langle \mathbf{k}|\, \hat{H}\, |\mathbf{k}\rangle_B &= -t(1 + e^{i\mathbf{k}\cdot\mathbf{a}_1} + e^{i\mathbf{k}\cdot\mathbf{a}_2}) = f(\mathbf{k}) \\ {}_B\langle \mathbf{k}|\, \hat{H}\, |\mathbf{k}\rangle_A &= {}_A\langle \mathbf{k}|\, \hat{H}\, |\mathbf{k}\rangle_B^* \end{aligned} \tag{1.5}$$

Therefore, the Hamiltonian matrix becomes:

$$H_k = \begin{pmatrix} 0 & f(\mathbf{k}) \\ f(\mathbf{k})^* & 0 \end{pmatrix} \tag{1.6}$$

and the energy dispersion is given as:

$$\varepsilon_s(\mathbf{k}) = st\sqrt{1 + 4\cos\left(\frac{\sqrt{3}k_x a}{2}\right)\cos\left(\frac{k_y a}{2}\right) + 4\cos^2\frac{k_y a}{2}} \tag{1.7}$$

and eigenstate:

$$\xi_s(\mathbf{k}) = \frac{1}{\sqrt{2}}\begin{pmatrix} 1 \\ e^{-i\phi(\mathbf{k})} \end{pmatrix} \tag{1.8}$$

where $\phi(\mathbf{k})$ is the argument of $f(\mathbf{k})$. We now shift the coordinate with respect to the K point $(2\pi/3a, 2\pi/s\sqrt{3}a)$, i.e. $\mathbf{k}' = \mathbf{k} + \mathbf{K}$. Expand $f(\mathbf{K} + \mathbf{k}')$ up to first order in

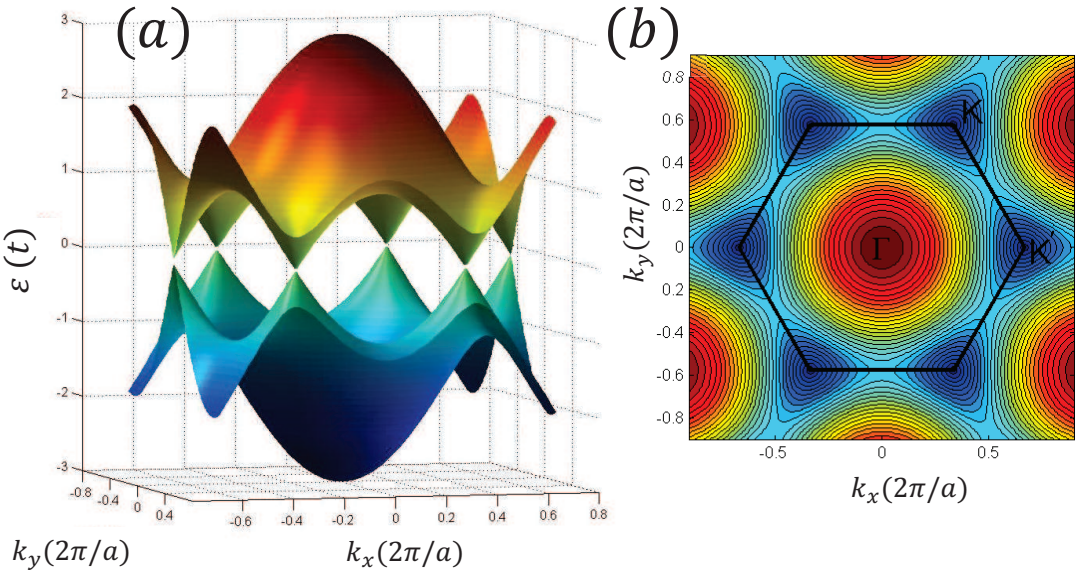

Figure 1.3: (a) Crystal structure of single layer graphene. Blue and red circle denotes sublattices $\mathcal{A}$ and $\mathcal{B}$ respectively. (b) The linear energy spectrum at K and K' point. The valence band touches the conduction band at the Dirac point.

$\mathbf{k}'$, we obtain:

$$H_k = \hbar v_F \begin{pmatrix} 0 & k_- \\ k_+ & 0 \end{pmatrix} = \hbar v_F \sigma \cdot \mathbf{k} \tag{1.9}$$

where $k_\pm = k'_x \pm i k'_y$, $\mathbf{k} = (k_x, k_y)$, $\sigma = (\sigma_x, \sigma_y)$ is the Pauli spin matrix and $v_F = \sqrt{3}ta/2 \approx 10^6$ m/s. and the energy dispersion is $\varepsilon_s(k) = s\hbar v_F k$. Therefore, the low energy electron at the vicinity of the K (and equivalently at K') point is formally equivalent to a spin-1/2 massless Dirac fermion. The Dirac cone is shown in Fig. 1.2(b) and the full band structure is shown in Fig. Fig. 1.3. In deriving Eq. (1.10), we have ignored the next-nearest neighbor (NNN) hopping. The NNN term results in non-zero diagonal elements in the Dirac hamiltonian. This generates an electron-hole asymmetry in the band structure, which becomes important in higher energy regime.

A bandgap can be opened at the Dirac point if an asymmetry between the $\mathcal{A}$ and $\mathcal{B}$ sublattices is introduced. The asymmetry can be done by using a substrate, such as SiC and Boron nitride [64, 65], or by hydrogenation [66]. Intrinsically, the spin-orbit interaction opens a small gap of a few meV [67, 68]. The Hamiltonian matrix

of graphene with a gap is given as:

$$H_k(\Delta) = \hbar v_F \begin{pmatrix} -\Delta & k_- \\ k_+ & \Delta \end{pmatrix} = \hbar v_F + \sigma_z \Delta \tag{1.10}$$

where Δ is the onsite energy difference and it induces a bandgap opening of 2Δ at K-point.

1.1.2 AB-stacked bilayer graphene

Two graphene layers can be stacked to form a bilayer [69]. Two distinct stacking orientations exist: AB-stacking and AA-stacking. We first consider the case of AB-stacking, where $\mathcal{A}_1$ is stacked directly above $\mathcal{B}_2$ [Fig. 1.4(a)] [70]. In the basis of $(\mathcal{A}_1, \mathcal{A}_2, \mathcal{B}_1, \mathcal{B}_2)$, the Hamiltonian matrix at the vicinity of K point is given as[70]:

$$H^{(AB)}(\mathbf{k}) = \begin{pmatrix} 0 & \hbar v_F k_+ & 0 & \hbar v_0 k_- \\ \hbar v_F k_- & 0 & \gamma_1 & 0 \\ 0 & \gamma_1 & 0 & \hbar v_F k_+ \\ \hbar v_0 k_+ & 0 & \hbar v_F k_- & 0 \end{pmatrix} \tag{1.11}$$

where $v_F k_\pm$ represents the intraband $\mathcal{AB}$ hopping, γ_1 represents the direct interlayer hopping between $\mathcal{A}_1 \leftrightarrow \mathcal{B}_2$ and $v_0 = (\sqrt{3}/2)a\gamma_3/\hbar$ where $\gamma_3$represents the weak indirect interlayer hopping between $\mathcal{A}_2 \leftrightarrow \mathcal{B}_1$. Ignoring the weak interlayer hopping, and reducing the basis to $(\mathcal{A}_2, \mathcal{B}_1)$, the four-band Hamiltonian matrix can be simplified to a two-band model [70]:

$$H_0^{(AB)}(k) = -\frac{\hbar^2}{2m} \begin{pmatrix} 0 & k_-^2 \\ k_+^2 & 0 \end{pmatrix} \tag{1.12}$$

where $m = \gamma_1/v_F^2$ indicates an effective mass generation due to the interlayer coupling. The energy dispersion is in a parabolic form of $\varepsilon_s(k) = s\hbar^2k^2/2m$ and the eigenstate is $\xi_s(k) = (1, se^{2i\phi(k)})^T$ where $\phi(k) = \tan^{-1}(k_y/k_x)$. In the two-band approximation,

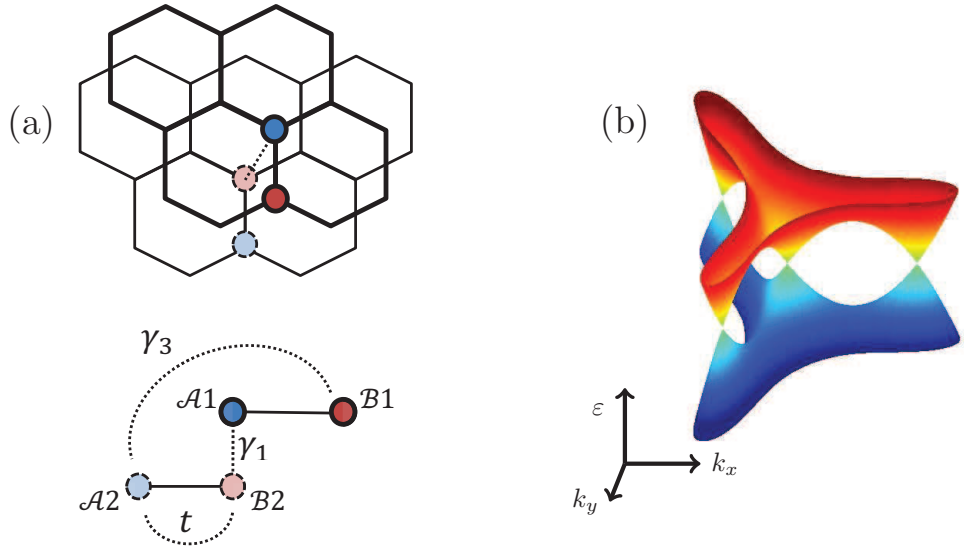

Figure 1.4: (a) Crystal structure of AB-stacked bilayer graphene. (b) Trigonal warping effect of the low energy band structure.

the quasiparticle is analogous to a spin-1 massive chiral fermion [4].

The situation becomes more interesting when the indirect hopping term [i.e. the γ_3 hopping as shown in Fig. 1.4(a)] is included. The indirect hopping term becomes important in the low energy regime as the intermediate energy two-band model in Eq. (1.12) becomes inaccurate. The finite indirect hopping term adds an additional k-linear term to the Hamiltonian matrix [70–72], i.e.

$$\tilde{H}^{(AB)}(\mathbf{k}) = -\frac{\hbar^2}{2m}\begin{pmatrix} 0 & k_-^2 \\ k_+^2 & 0 \end{pmatrix} + \hbar v_0 \begin{pmatrix} 0 & k_+ \\ k_- & 0 \end{pmatrix} \tag{1.13}$$

and the energy dispersion is given as:

$$\varepsilon_s(\mathbf{k}) = s\sqrt{\frac{\hbar^4 k^4}{4m^2} + \hbar^2 v_F^2 k^2 - \frac{\hbar v_F}{m} k^3 \cos 3\phi} \tag{1.14}$$

We first see that the Hamiltonian Eq. (1.13) is a mixture of massless chiral fermion Eq. (1.10) and of massive chiral fermion Eq. (1.12). This mixing creates a $\propto \cos 3\phi$ term in the energy dispersion and it strongly deforms the low energy band structure. The energy band structure is trigonally warped in k-space [Fig. 1.4(b)]. Furthermore, the energy band breaks into one central pocket and three satellite pockets in the very

low energy regime. The trigonal warping effect essentially creates four Dirac points. When the Dirac pockets join together, the trigonally warped energy band exhibits unusual band curvature. This allows an unusual retro type of electron reflection to occur in the low energy regime of bilayer graphene, as we shall discuss in Chapter 5.

It should be noted that in single layer graphene with Rashba spin-orbit interaction [73, 74], the low energy two-band effective Hamiltonian has exactly the same form as Eq. (1.13). Therefore, trigonal warping of the energy band is also present in this system, except that the triangular band is clockwise-rotated by 90-degree in k-space. In bilayer graphene with Rashba spin-orbit interaction, the trigonal warping effect becomes doubled, i.e. the central Dirac point is surrounded by six satellites Dirac points [75].

A bandgap can be generated in bilayer graphene by applying a gate voltage [76–79]. The gate voltage induces a layer asymmetry gap which is in the same spirit as the bandgap opening of single layer graphene in the presence of a $\mathcal{AB}$ sublattice asymmetry. The bandgap can be modeled by including a $-\gamma_0 U_0$ term in Eq. (1.11) where γ_0 is the zero-order gamma matrix and U_0 is the electrostatic potential generated by the gate voltage.

1.1.3 AA-stacked bilayer graphene

We now briefly discuss the electronic properties of AA-stacked bilayer graphene. AA-stacking is achieved by directly stacking $\mathcal{A}_1$ on top of $\mathcal{A}_2$ [Fig. 1.5]. The tight-binding Hamiltonian matrix, in the basis of $(\mathcal{A}_1, \mathcal{B}_2, \mathcal{A}_2, \mathcal{B}_1)^T$, is given as [80, 81]:

$$\hat{H} = \begin{pmatrix} 0 & 0 & \gamma & v_F k_- \\ 0 & 0 & v_F k_+ & \gamma \\ \gamma & v_F k_- & 0 & 0 \\ v_F k_+ & \gamma & 0 & 0 \end{pmatrix}. \tag{1.15}$$

The off diagonal term $\gamma = 0.2$ eV is the interlayer sublattice matching hopping energy. The energy dispersion is given as $\varepsilon_{c,\chi}(\mathbf{k}) = \chi \hbar v_f |\mathbf{k}| + c\gamma$. The band structure

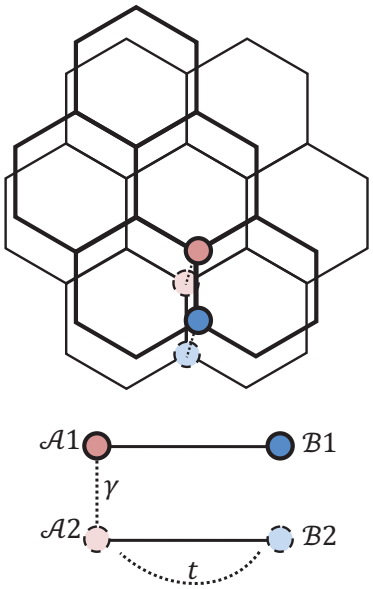

Figure 1.5: Crystal structure of AA-stacked bilayer graphene.

is composed of two Dirac cones, up-down shifted by γ. The eigenstate is:

$$\xi_{c,\chi}(k) = \frac{1}{\sqrt{2}} \begin{pmatrix} \chi e^{-i\phi} \\ c \\ c\chi e^{-i\phi} \\ 1 \end{pmatrix} \tag{1.16}$$

where c and χ represents the cone and chirality indices, respectively. In comparison with the AB-stacked bilayer graphene, AA-stacked bilayers are relatively understudied in current literature. By inspecting the energy dispersion equation, we immediately realize that its Dirac cone band structure make it difficult to be distinguished optically from single layer graphene. However, it was experimentally determined to be a major form of bilayer graphene [82]. One particularly interesting aspect of AA-stacked bilayer graphene is that due to the additional Dirac cone crossing, the electrons and holes can be both electron-like and hole-like. This creates rich particle trajectories in a heterojunction consists of AA-stacked bilayer graphene [83].

Finally, we remark a system which has a similar Hamiltonian as Eq. (1.13), i.e. two-dimensional electron gas with Rashba spin-orbit interaction (R2DEG). Lifted spin-degeneracy in a two-dimensional electron gas can be created spontaneously in

the absence of an external magnetic field if the confining electrostatic potential is asymmetric. Such effect is equivalent to the relativistic case of electron moving through a surface with inhomogeneous electric field. In the rest frame of the electrons, the electric field is relativistically equivalent to a magnetic field. This generates finite Rashba spin-orbit interaction which energetically separating the electron gas into two populations of different spin helicity [84]. In real-spin basis, the Hamiltonian of R2DEG is given as:

$$H^{2D}(k) = \frac{\hbar^2}{2m}\begin{pmatrix} k^2 & 0 \\ 0 & k^2 \end{pmatrix} + i\lambda \begin{pmatrix} 0 & k_- \\ -k_+ & 0 \end{pmatrix} \tag{1.17}$$

This is in a similar form as the bilayer graphene Hamiltonian with trigonal warping effect, Eq. (1.13), except that there is a major difference: the k^2 term is now in the diagonal part. Since there is no mixing of $k_\pm^2$ and $k_\pm$ terms, the band structure is isotropic in k-space. The parabolic 'free' electron bands are left-and right-shifted, and the shifting is characterized by the Rashba coupling strength λ.

1.2 Nonlinear optical properties of graphene

In the first part of this Thesis, we study the nonlinear optical properties of graphene and its sister-structures in terahertz (THz) and far-infrared (FIR) frequencies. The motivation behind these studies arises from two factors. First, not only the THz waves is important in the study of condensed matter where many dynmaical processes occurs in the THz frequency regime (approximately a few meV), it is also an invaluable tool in the field of astrophysics, telecommunication, non-destructive imaging and chemical/bio-molecules identifications [85]. Unfortunately, THz frequency situated right in between the optics and electronic regimes. Efficient generation and detection of THz waves are problematic because it is too high of a frequency via electronic approach and too low of a frequency via photonics approach. The hunt for an efficient mean of THz generation and detection is therefore one of the ongoing

primary objectives. Second, exceptionally strong optical response has been reported in graphene both theoretically and experimentally [86–90]. The third-order nonlinear susceptibility $\chi^{(3)}$ in graphene is 10^8 stronger than that in a bulk insulator [86–88]. Furthermore, Wright et al has found that the THz/FIR interband optical conductivity can be significantly enhanced by 3-photon nonlinear interband optical processes under an electric field strength in the order of 10^3 V/cm. The rather weak 2.3% absorption (corresponding to the universal conductivity $e^2/4\hbar$) can hence be overcome by the nonlinear optical absorption. Although not directly observed in free standing single layer graphene in THz range, giant nonlinear transmittance has experimentally been observed in graphene dispersions [91, 92] and, recently, the third-harmonic generation in graphene on a substrate in near-infrared frequency has been experimentally demonstrated [93]. In bilayer graphene, second harmonic can be generated by breaking the symmetry using an in-plane electric field [94]. Although the 0.2 eV photon energy is well-beyond the THz regime, the unusually large $\chi^{(2)} \approx 10^5$ pm/V highlights the potential of BLG in nonlinear photonics application.

The optical nonlinearity in graphene is directly related to its linear energy spectrum. The energy dispersion of the massless Dirac fermion around the K point is written in the form of $\varepsilon_s = s\hbar v_F |\mathbf{k}|$ and the group velocity is $\mathbf{v}_s = sv_F\hat{\mathbf{k}}$ where $\hat{\mathbf{k}}$ is the unit vector of the wavevector $\mathbf{k}$. The group velocity is completely independent of wavevector k. From a pedagogical point of view, the Dirac fermions is expected to oscillate abruptly between the two values of $+v_F$ and $-v_F$ when driven by an external oscillating electric field,. This gives rise to a series of square-wave optical response. Since a square function is rich in higher-order harmonics, the massless Dirac fermion is expected to exhibit strong nonlinear optical response. This is in contrast to the Schr odinger electrons of $\varepsilon_k = \hbar^2k^2/2m^*$ and group velocity $\mathbf{v} = \hbar\mathbf{k}/m^*$. The k-dependent group velocity allows the optical current response to oscillate continuously with the external electric field and hence the anharmonicity is absent. Although Ishikawa has shown that the highly anharmonic intraband current response (i.e. the square current response as discussed above) is reduced by a interband component

[95], nonlinear optical response such as frequency up-conversion is still expected to be a significant optical process in graphene.

1.2.1 Semiclassical electron transport theory

In this Thesis, the nonlinear optical properties are derived via two conceptually simple formalisms. In the first formalism, the intraband optical response is determined by using a semiclassical electron transport theory in which the electron dynamics is decomposed into terms higher order in the external electric field [96, 97].

Consider a system described by Hamiltonian $\mathcal{H}(\mathbf{p})$ where $\mathbf{p}$ is the electron momentum and the energy eigenvalue is given by $\varepsilon(\mathbf{p})$. The velocity eigenvector is given as $\mathbf{v}(\mathbf{p}) = \frac{\partial\varepsilon(\mathbf{p})}{\partial\mathbf{p}}$. In the presence of an external field $\mathbf{E} = \mathbf{E}_0 e^{i\omega t}$, the photon is coupled to the electron via a Peierls substituion: $\mathbf{p} \to \mathbf{p} - e\mathbf{A}$, i.e. $\mathbf{v}(\mathbf{p}) \to \mathbf{v}(\mathbf{p} - e\mathbf{A})$, where the vector potential $\mathbf{A}$ is related to the external field by $\mathbf{E} = -\partial\mathbf{A}/\partial t$. We can then perform a Taylor expansion in terms of the electric field:

$$\mathbf{v}(\mathbf{p}, \mathbf{E}) = \sum_{i=0} \mathbf{v}^{(i)}(\mathbf{p}, \mathbf{E}) \tag{1.18}$$

where $\mathbf{v}^{(n)}(\mathbf{p}, \mathbf{E})$ represents velocity component proportional to $\mathbf{E}_0^n$. We can then calculate the optical current response via:

$$\mathbf{J}^{(i)} = e \int \mathrm{d}\mathbf{p}\mathbf{v}^{(i)}(\mathbf{p}, \mathbf{E}) f(\varepsilon) \tag{1.19}$$

where $f(\varepsilon)$ is the Fermi-Dirac distribution function. When the external electric field is strong, the equilibrium Fermi-Dirac distribution function is no longer accurate since the electron energy becomes $\varepsilon' = \varepsilon + \Delta\varepsilon$ where $\Delta\varepsilon$ are terms dependent on the external electric field. In this case, we can perform a similar expansion around $\Delta\varepsilon$:

$$f(\varepsilon + \Delta\varepsilon) = f(\varepsilon) + \sum_{i=0} (\Delta\varepsilon)^i \frac{\partial f^{(i)}(\varepsilon)}{\partial\varepsilon} \tag{1.20}$$

This accounts for the population non-equilibrium effect in the presence of a strong

electric field. The optical current density can be obtained by inserting Eq. (1.20) into Eq. (1.19).

1.2.2 n-photon electron coupling wavefunction

In the second formalism, the interband optical response is obtained by recursively constructing the wavefunction when n-photon is coupled to the electron. We first consider the Hamiltonian of the system in the presence of an external electric field:

$$\mathcal{H}(\mathbf{p}) \to \mathcal{H}(\mathbf{p} - e\mathbf{A}) \tag{1.21}$$

We can write the wavefunction of Eq. (1.21) by

$$\Psi(\mathbf{p}) = \sum_{n=0} \phi_n e^{i(n\omega - \varepsilon/\hbar)t} \tag{1.22}$$

where ϕ_n is a $\propto E^n$ coefficient representing the coupling strength of n-photon to the electron and it is the most important ingredient in determining the multiple-photon process of a system. ϕ_n can be obtained by solving the Schr odinger equation:

$$i\hbar \frac{\partial \Psi(\mathbf{p})}{\partial t} = \mathcal{H}\Psi(\mathbf{p}) \tag{1.23}$$

For a two-dimensional system with ($\mathbf{p}$)-dependent off-diagonal term such as graphene, solving the Schr odinger equation gives rise to a set of coupled equations which can be recursively solved to obtain ϕ_n up to any arbitrary order. We can then express the total optical current density as:

$$\begin{aligned} J_\nu^{(n)} &= e \int \mathrm{d}\mathbf{p} \Psi^\dagger \hat{v^\nu} \Psi \\ &= e \int \mathrm{d}\mathbf{p} (\phi_0^\dagger + \phi_1^\dagger + \phi_2^\dagger + \cdots) \hat{v^\nu} (\phi_0 + \phi_1 + \phi_2 + \cdots) \end{aligned} \tag{1.24}$$

where $\hat{v^\nu} = \partial\mathcal{H}/\partial p_\nu$ and $\nu = x, y$ is the ν-component velocity operator. By selecting out terms $\propto E^n$, the n-th order nonlinear optical response can be obtained.

1.3 Klein transport in graphene: band crossing, touching and turning

We now discuss the second theme of this Thesis, i.e. the transport properties in graphene [57, 98]. The transport in graphene cannot be fully appreciated without the discussion of Klein tunneling and Klein reflection in single layer and bilayer graphene [4, 6, 7]. Let's consider the tunneling problem as illustrated in Fig. 1.6(a) and (b). For single layer graphene and bilayer graphene, the incident electron eigenstate is given as:

$$\psi = \begin{pmatrix} 1 \\ e^{-in\phi} \end{pmatrix} \tag{1.25}$$

where $n = 1, 2$ denotes the number of layers. The reflected and transmitted eigenstates are:

$$\psi_r = \frac{r}{\sqrt{2}} \begin{pmatrix} 1 \\ (-1)^n e^{-ni\phi} \end{pmatrix} \tag{1.26}$$

$$\psi_t = \frac{t}{\sqrt{2}} \begin{pmatrix} 1 \\ (-1)^{n+1} e^{-ni\theta} \end{pmatrix} \tag{1.27}$$

where θ is the transmitted angle which is dependent on the incident energy and the potential height. At normal incidence, $\phi = \theta = 0$:

$$t = \frac{1 + (-1)^{n+1}}{2} \tag{1.28}$$

$$r = \frac{1 + (-1)^{n}}{2} \tag{1.29}$$

We immediately see that for transmission is perfect for $n = 1$ and reflection is perfect for $n = 2$, regardless the height of the tunneling barrier [4]. For bilayer graphene, the results is completely the opposite. Electron is perfectly reflected.

Katsnelson relates the perfect transmission of electron in single layer graphene to the Klein tunneling of a relativistic spin-1/2 massless Dirac fermion in quantum

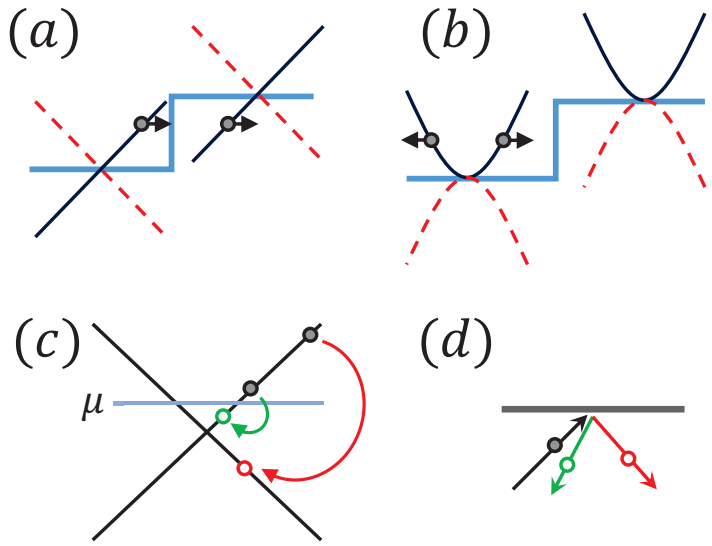

Figure 1.6: Klein transport of (a) single layer graphene; and (b) bilayer graphene. At normal incidence, the branches of opposite pseudospins are decoupled (represented by solid and dashed curve). (c) The band structure in the graphene side of a graphene/superconductor heterojunction. The green (red) arrow denotes the Andreev process involving a conduction (valence) hole. (d) Specular (red) and retro (green) Andreev reflection.

electrodynamics where the perfect tunneling of a Dirac fermion is mediated by a positron creation in the vacuum [4]. For bilayer, the spin-1 massive chiral fermion is non-existent in quantum electrodynamics and the perfect reflection can only be understood from the conservation of pseudospin. Here we adopt a slightly different approach to explain the Klein transport in graphene and bilayer graphene by considering the topology of the band structure. We first show that the energy branches of different pseudospin orientation are de-coupled at normal incidence. The eigenstate of the solid and dashed branches (we represent the pseudospin orientation by $\uparrow$ and $\downarrow$ respectively) in Fig. 1.6 is given by:

$$\psi_{\uparrow(\downarrow)} = \begin{pmatrix} 1 \\ (-)1 \end{pmatrix} \tag{1.30}$$

and $\psi_{\downarrow}^{\dagger}\psi_{\uparrow} = 0$. So the branches are decoupled and inter-branch transition is strictly forbidden.

For graphene, the linear branches of opposite pseudospin cross at the Dirac point [Fig. 1.6(a)]. Since the electron must be confined in its decoupled linear branch,

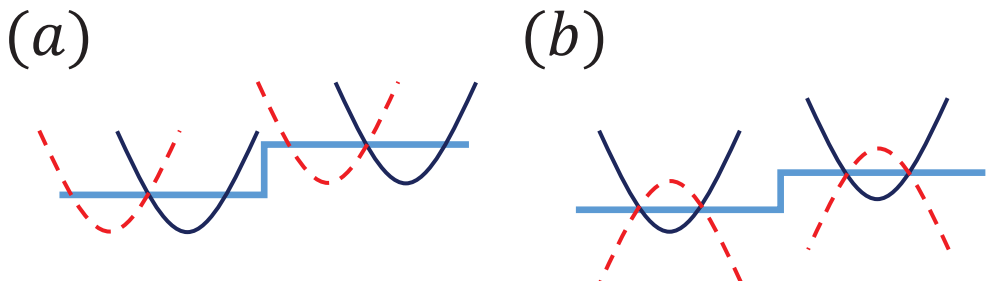

Figure 1.7: Hybrid transport when the decoupled branches both turn and cross: (a) R2DEG; and (b) bilayer graphene with trigonal warping effect.

moving forward across the potential barrier is the only possibility. Electron reflection is entirely impossible because the reflection state is in the decoupled branch of opposite pseudospin orientation (recall that $\psi_{\downarrow}^{\dagger}\psi_{\uparrow} = 0$).

The band topology of bilayer graphene is rather different with that of the graphene. The branches of opposite pseudospin only touch at the Dirac point without any band crossing [Fig. 1.6(b)]. Furthermore, the decoupled parabolic band has a turning point. This essentially creates reflection states within the same pseudospin parabolic branch. Therefore, band touching and band turning in bilayer graphene forces the electron to be fully reflected by a step potential.

We can now link the key feature of Klein transport to the band topology as followed: *Tunneling occurs when there is a band crossing whereas reflection occurs when there is a band turning. If the band crosses without band turning, Klein tunneling takes place. If the band turns and touches without band crossing, Klein reflection takes place.* This observation immediately leads to the following question: what happen if the two decoupled branches of opposite pseudospin *turn and cross*? In Fig. 1.7(a) and 1.7(b), we show two examples. Respectively, they are the band structure of R2DEG and bilayer graphene with trigonal warping effect. In Fig. 1.7(a), the two decoupled *parabolic* branches (note that electrons carry real-spin instead of pseudospin in R2DEG) are left right shifted with one band crossing point whereas in Fig. 1.7(b), the decoupled branches are up-down shifted and with two band crossing point. The transport at the vicinity of the crossing point in these band structure is therefore expected to exhibit hybrids behavior of where both reflection and tunneling can occur. The tunneling problem in Fig. 1.7(a) will be discussed in Chapter 6.

Another interesting transport phenomena occurs at the heterojunction of a single layer graphene and a superconductor [55, 99]. As shown in Fig. 1.6(c), electrons in graphene can couple with another electron below the Fermi level μ to form a Cooper pair, tunnel into the superconducting side, leaving behind a hole [100]. Since the hole is formed in the conduction band, this corresponds to the usual retro Andreev reflection. If the electron energy is much higher than μ, an electron in the *valence* band is captured to form Cooper pair. In this case, the *valence* hole is specularly reflected. The specular Andreev reflection has no counterpart in conventional semiconductor and metal. It is a direct consequence of the linear band structure. The gapless Dirac cones essentially allows the existence of two species of hole excitations: an electron-like excitation whose direction of motion is parallel to the wavevector, and a hole-like excitation whose direction of motion is antiparallel to the wavevector. This leads to the occurrence of both retro and specular types of Andreev reflection [Fig. 1.6(d)].

1.4 Overview of this Thesis

This Thesis follows a two-theme format, i.e.

- Part 1: Nonlinear optical response of graphene and its sister-structures;
- Part 2: Transport properties of bilayer graphene and two-dimensional electron gas with Rashba spin-orbit interaction (R2DEG).

In Part 1, the following graphene and its sister-structures are studied:

- Graphene (Chapter 2)
- Bilayer graphene (Chapter 3)
- Graphene with a bandgap (Chapter 2, 4)
- Graphene with band anisotropy (Chapter 4)
- R2DEG (Chapter 2)

In part 2, the transport properties of the following structures are studied:

- AB-stacked bilayer graphene/superconductor heterojunction (Chapter 5)
- R2DEG heterojunction (Chapter 6)

This is then followed by a brief *coda* in which we discuss the energy loss rate of an external charged particle in graphene (Chapter 7). Finally, the thesis is concluded by Chapter 8: *Conclusion and Outlook*.

2 | Nonlinear optical response in graphene

* The single layer graphene exhibits nonlinear photon-mixing effect in terahertz frequency regime is studied in this Chapter. It is found that the third-order nonlinear current in graphene grows rapidly with increasing temperature. The third-order nonlinear current can be as strong as the linear current under a moderate electric field strength of $10^4 V/cm$. Due to the Dirac dynamics of the graphene quasiparticles, low Fermi-level and electron fillings optimizes the optical nonlinearity. Furthermore, the nonlinear optical response under strong-field condition is also investigated. It is found that the strong-field induced Dirac fermion population redistribution and non-equilibrium carrier heating effects can further amplify the optical nonlinearity of graphene.

2.1 Introduction

The nonlinear intraband optical response of gapless graphene has been previously studied by Mikhailov et al using the semiclassical electron transport equation for two limiting cases: (i) zero doping at finite temperature; and (ii) finite doping at zero temperature [86, 87]. The intermediate regime between (i) and (ii), i.e. doped graphene at finite temperature, is however left open and has not been reported so far. The nonlinear response in this intermediate regime is important since finite

*This Chapter is based on *J. Opt. Soc. Am. B* **29**, 3, 274-279 (2012) and *Infrared, Millimeter and Terahertz Waves* **33**, 8, 816-824 (2012).

doping is usually present due to crystal imperfection and impurities, and the practical implementation of graphene-based device requires finite temperature information. Furthermore, nonlinear response usually occurs under strong external field. The strong-field-drive Dirac fermion (SDF) population redistribution due their externally perturbed dynamics and non-equilibrium carrier heating becomes inevitable in strong-field regime. Optical response of graphene with these strong-field effects considered has however not been reported. In this Chapter, we fill in these gaps by constructing the full temperature spectrum of the nonlinear optical response of a finite-doped ($\mu \neq 0$) graphene single layer in both gapless and gapped cases under both weak-field and strong-field conditions. The dynamics of the quasiparticles when perturbed by a strong electric field are decomposed into linear and nonlinear components, and the optical nonlinearity of the graphene is investigated.

2.2 Optical response of graphene in a weak electric field

The effective Hamiltonian of graphene for low energy carrier expanded around K point is given by

$$\hat{\mathbf{H}} = v_F \begin{bmatrix} 0 & p_- \\ p_+ & 0 \end{bmatrix} \tag{2.1}$$

where the Fermi velocity is $v_F = 3ta/2\hbar \approx 10^6 m/s$, $t \approx 3eV$ is the nearest neighbour hopping bandwidth, $a \approx 0.142nm$ is the carbon-carbon distance, and $p_\pm = p_x \pm ip_y$. The energy eigenvalue of Eq. (2.1) gives rise to the linear energy dispersion $\varepsilon_s = sv_F p$ where $s = \pm 1$. This energy dispersion results in a symmetric upper ($s = +1$) and lower ($s = -1$) Dirac cones, representing electrons and hole states respectively, and is analogue to the charge conjugation symmetry in quantum electrodynamics. The velocity operator is given by $\hat{v} = \partial\hat{\mathbf{H}}/\partial p$. Following Feynman [101], we write the expectation value of $\hat{v}$ as $\langle \hat{v}_s \rangle = \partial\varepsilon_s/\partial p$. This gives velocity eigenvector $\mathbf{v}_s = sv_F\mathbf{p}/p$.

We consider a time-dependent applied electric field in the form of

$$\mathbf{E}(\mathbf{r},t)=\sum_{\eta}\mathbf{E}_{\eta}\exp\left\{i\left(\mathbf{q}_{\eta}\cdot\mathbf{r}-\omega_{\eta}t\right)\right\} \tag{2.2}$$

where $\mathbf{E}_{\eta}$, $\mathbf{q}_{\eta}$ and ω_{η} are the amplitude, wavevector and frequency of the η-th wave of the electric field. Ignoring the weak magnetic component, the external field is minimally coupled to the quasiparticle by performing the substitution $\mathbf{p}\rightarrow\mathbf{p}-e\mathbf{A}(\mathbf{r},t)$ where $\mathbf{E}(\mathbf{r},t)=-\partial\mathbf{A}(\mathbf{r},t)/\partial t$ and e is the electric charge. The velocity becomes:

$$\mathbf{v}_{s}=sv_{F}\frac{\mathbf{p}-e\mathbf{A}}{|\mathbf{p}-e\mathbf{A}|} \tag{2.3}$$

and for simplicity, denote $\mathbf{u}=-e\mathbf{A}(\mathbf{r},t)$, and we arrive at

$$\mathbf{v}_{s}=sv_{F}\frac{\mathbf{p}+\mathbf{u}}{\sqrt{p^{2}+u^{2}+2\mathbf{p}\cdot\mathbf{u}}}=s\frac{v_{F}}{p}\frac{\mathbf{p}+\mathbf{u}}{\sqrt{1+\left(\frac{u}{p}\right)^{2}+\frac{2\mathbf{p}\cdot\mathbf{u}}{p^{2}}}} \tag{2.4}$$

We now perform a Taylor expansion on the quasiparticle velocity $\mathbf{v}_s$ in terms of the externally applied electric field. Assuming that $p\gg u$:

$$\mathbf{v}_{s}=sv_{F}(\mathbf{p}+\mathbf{u})\left\{1-\frac{1}{2}\left[\left(\frac{u}{p}\right)^{2}+\frac{2\mathbf{p}\cdot\mathbf{u}}{p^{2}}\right]+\frac{3}{8}\left[\left(\frac{u}{p}\right)^{2}+\frac{2\mathbf{p}\cdot\mathbf{u}}{p^{2}}\right]^{2}-\frac{5}{2}\left(\frac{\mathbf{p}\cdot\mathbf{u}}{p^{2}}\right)^{3}+O(\mathbf{u}^{4})\right\} \tag{2.5}$$

where $O(\mathbf{u}^4)$ represents terms with fourth and higher order in the external electric field. Grouping terms according to the order of $\mathbf{u}$, we obtain

$$\mathbf{v}_{s}^{(0)}=sv_{F}\left(\frac{\mathbf{p}}{p}\right) \tag{2.6}$$

$$\mathbf{v}_{s}^{(1)}=sv_{F}\left[\frac{\mathbf{u}}{p}-\frac{\mathbf{p}}{p}\left(\frac{\mathbf{p}\cdot\mathbf{u}}{p^{2}}\right)\right] \tag{2.7}$$

$$\mathbf{v}_{s}^{(2)}=sv_{F}\left[\frac{\mathbf{p}}{2p}\left(\frac{u}{p}\right)^{2}+\frac{\mathbf{u}}{p}\left(\frac{\mathbf{p}\cdot\mathbf{u}}{p^{2}}\right)\right] \tag{2.8}$$

$$\mathbf{v}_s^{(3)} = sv_F \left[-\frac{1}{2}\frac{\mathbf{u}}{p}\left(\frac{u}{p}\right)^2 + \frac{3}{2}\frac{\mathbf{p}}{p}\left(\frac{u}{p}\right)^2\left(\frac{\mathbf{p}\cdot\mathbf{u}}{p^2}\right) + \frac{3}{2}\frac{\mathbf{u}}{p}\left(\frac{\mathbf{p}\cdot\mathbf{u}}{p^2}\right)^2 - \frac{5}{2}\frac{\mathbf{p}}{p}\left(\frac{\mathbf{p}\cdot\mathbf{u}}{p^2}\right)^3 \right] \tag{2.9}$$

where $\mathbf{v}_s^{(i)}$ represents i-th order velocity of graphene per spin and per valley degeneracy. The zero-order velocity is equal to the Fermi velocity v_F which is consistent with the unperturbed case. Note that the velocities only reverse their directions for between the two Dirac cones of $s = \pm 1$. The magnitude remains unchanged due to the particle-hole symmetry of the energy band structure.

The i-th order current density is given by

$$\mathbf{J}^{(i)} = \frac{e}{4\pi^2\hbar^2}\sum_s \int_0^{2\pi}\int_{\mu-\varepsilon_{ph}-k_BT}^{\Lambda} \mathrm{d}^2 p \mathbf{v}_s^{(i)} f\left(\varepsilon_s\right) \tag{2.10}$$

where ε_{ph} is the energy of the incoming photons, k_B is the Boltzmann constant, T is the temperature, and $f\left(\varepsilon_s\right)$ is the Fermi-Dirac distribution function. The integration cut-off Λ is equal to the Fermi level μ at $T = 0K$, and is arbitrarily set to a large value of $0.5eV$ for $T > 0K$ and $\mu > 0$ numerical calculation. Up to room temperature, the Fermi-Dirac distribution terminates the momentum integration well before Λ and hence our choice of Λ is well-justified. For $\mu < 0$, Λ cut off the momentum integration at $\mu + k_BT$ to avoid the low momentum regime where $p \gg u$ fails. Deep charge carriers cannot respond to the external perturbation due to the unavailability of higher energy states. We qualitatively approximate this by choosing a lower momentum integration limit of $\mu - \varepsilon_s - k_BT$.

Note that in Eq. (2.10), there is a vector term $\mathbf{v}_s^{(i)}$. Only the component of $\mathbf{p}$ which is parallel to $\mathbf{u}$ will survive in the angular integration part of the current density. Therefore, every $\mathbf{p}$ in $\mathbf{v}_s^{(i)}$ can be replaced by $p\cos\phi$ where ϕ is the angle between $\mathbf{p}$ and the external field. For example, the third-order velocity can be re-written as

$$\begin{aligned} \mathbf{v}_s^{(3)} &= \frac{sv_F}{p^3}\left[-\frac{1}{2} + \frac{3}{2}\cos^2\phi + \frac{3}{2}\cos^2\phi - \frac{5}{2}\cos^4\phi \right]\mathbf{F}_{jkl} \\ &= \frac{sv_F}{p^3}\left[-\frac{1}{2} + 3\cos^2\phi - \frac{5}{2}\cos^4\phi \right]\mathbf{F}_{jkl} \end{aligned} \tag{2.11}$$

where the electric field term is compactly written as:

$$\mathbf{F}_{jkl} = \sum_{jkl} \frac{(\mathbf{E}_j \cdot \mathbf{E}_k)\,\mathbf{E}_l}{\omega_j \omega_k \omega_l} e^{i[(\mathbf{q}_j+\mathbf{q}_k+\mathbf{q}_l)\cdot\mathbf{r}-(\omega_j+\omega_k+\omega_l)t]} \tag{2.12}$$

Third-order nonlinear current density can be obtained by by inserting Eq. (2.11) into Eq. (2.10).

2.2.1 Linear optical response

The linear current density for $\mu > \varepsilon_{ph}$ at $T = 0K$, per spin and per valley, can be obtained by combining Eq. (2.7) and Eq. (2.10):

$$\begin{aligned}
\mathbf{J}^{(1)}_{T=0} &= \frac{e}{4\pi^2\hbar^2}\int \mathrm{d}^2 p \mathbf{v}^{(1)}_s \\
&= -\frac{ie^2 v_F}{(2\pi\hbar)^2}\sum_\eta \frac{\mathbf{E}_\eta}{\omega_\eta} e^{i(\mathbf{q}_\eta\cdot\mathbf{r}-\omega t)} \int \left[\frac{1}{p} - \frac{\cos^2\phi}{p}\right] p dp d\phi \\
&= -\frac{ie^2}{(2\pi\hbar)^2}\sum_\eta \frac{\mathbf{E}_\eta}{\omega_\eta} e^{i(\mathbf{q}_\eta\cdot\mathbf{r}-\omega t)} \int_0^{\hbar\omega_\eta} d\varepsilon_p \int_0^{2\pi} \left[1-\cos^2\phi\right] d\phi \\
&= -\frac{ie^2}{(2\pi\hbar)^2}\sum_\eta \frac{\mathbf{E}_\eta}{\omega_\eta} e^{i(\mathbf{q}_\eta\cdot\mathbf{r}-\omega t)} \times \hbar\omega_\eta \times \int_0^{2\pi} \left[\frac{\phi}{2} - \frac{\sin 2\phi}{4}\right]_0^{2\pi} \\
&= -\frac{ie^2}{4\pi\hbar}\sum_\eta \mathbf{E}_\eta e^{i(\mathbf{q}_\eta\cdot\mathbf{r}-\omega t)}
\end{aligned} \tag{2.13}$$

where $\varepsilon_p = v_F p$. Including spin and valley degeneracy, the zero temperature linear current density is given as

$$\mathbf{J}^{(1)}_{T=0} = -i\frac{e^2}{\pi\hbar}\sum_\eta \mathbf{E}_\eta \exp\left\{i\left(\mathbf{q}_\eta\cdot\mathbf{r}-\omega_\eta t\right)\right\} \tag{2.14}$$

Eq. (2.14) corresponds to a linear conductivity of $\sigma^{(1)}_{T=0} = e^2/\pi\hbar$. This is in agreement with the linear conductivity calculated using Kubo formula [23, 102]. For $\mu < 0$, the current density reverses the direction since it is now contributed by $s = -1$ carriers.

For $T > 0K$, we obtain

$$\begin{aligned}\mathbf{J}_T^{(1)} &= -i\frac{e^2}{\pi\hbar}\frac{k_BT}{\hbar\omega}\ln\left[1+\exp\left(1+\frac{\hbar\omega}{k_BT}\right)\right] \\ &\times\sum_\eta \mathbf{E}_\eta \exp\left\{i\left(\mathbf{q}_\eta\cdot\mathbf{r}-\omega_\eta t\right)\right\}\end{aligned} \tag{2.15}$$

which reduces to *Eq.*(2.14) in the limit of $T \to 0$.

2.2.2 Nonlinear optical response

Due to the inversion symmetry of graphene, it is straightforward to see that the second-order velocity $\mathbf{v}_s^{(2)}$ does not generate any electric current density. In fact, one can immediately see this by examining Eq. (2.8). All of the terms contained in $\mathbf{v}_s^{(2)}$ are proportional to $\cos\phi$ and hence will not survive in the angular-integration of Eq. (2.10).

The third-order nonlinear current density at $T = 0K$ can be obtained by inserting Eq. (2.11) into Eq. (2.10). We obtain:

$$\begin{aligned}\mathbf{J}_{T=0}^{(3)} = -is\frac{e^4v_F^2}{8\pi\hbar^2\mu}\sum_{\eta\nu\xi}\left(\frac{\varepsilon_{\eta\nu\xi}}{\mu-\varepsilon_{\eta\nu\xi}}\right)\frac{\mathbf{E}_\eta\cdot\mathbf{E}_\nu\mathbf{E}_\xi}{\omega_\eta\omega_\nu\omega_\xi} \\ \times\exp\left\{i\left[\left(\mathbf{q}_\eta+\mathbf{q}_\nu+\mathbf{q}_\xi\right)\cdot\mathbf{r}-\left(\omega_\eta+\omega_\nu+\omega_\xi\right)t\right]\right\}\end{aligned} \tag{2.16}$$

where $s = +1(-1)$ for $\mu > 0$ ($\mu < 0$) and $\mu > \varepsilon_{\eta\nu\xi}$ where $\varepsilon_{\eta\nu\xi} = \varepsilon_\eta+\varepsilon_\nu+\varepsilon_\xi$ is the sum of three incoming photon energies. The magnitude of the zero temperature nonlinear current density is the same for electron filling ($\mu > 0$) and hole filling ($\mu < 0$) due to the up-down Dirac cones symmetry. At finite temperature, the nonlinear current density is obtained from

$$\begin{aligned}\mathbf{J}_T^{(3)} = -is\frac{e^4v_F^2}{8\pi\hbar^2}\sum_{\eta\nu\xi}\frac{\mathbf{E}_\eta\cdot\mathbf{E}_\nu\mathbf{E}_\xi}{\omega_\eta\omega_\nu\omega_\xi}\int\frac{\mathrm{d}\varepsilon_p}{\varepsilon_p^2}\frac{1}{1+\exp\left(\frac{\varepsilon_p-\mu}{k_BT}\right)} \\ \times\exp\left\{i\left[\left(\mathbf{q}_\eta+\mathbf{q}_\nu+\mathbf{q}_\xi\right)\cdot\mathbf{r}-\left(\omega_\eta+\omega_\nu+\omega_\xi\right)t\right]\right\}\end{aligned} \tag{2.17}$$

where for simplicity we have suppressed the integration limit. We see that μ plays an important role in the finite temperature current density of graphene. As shown

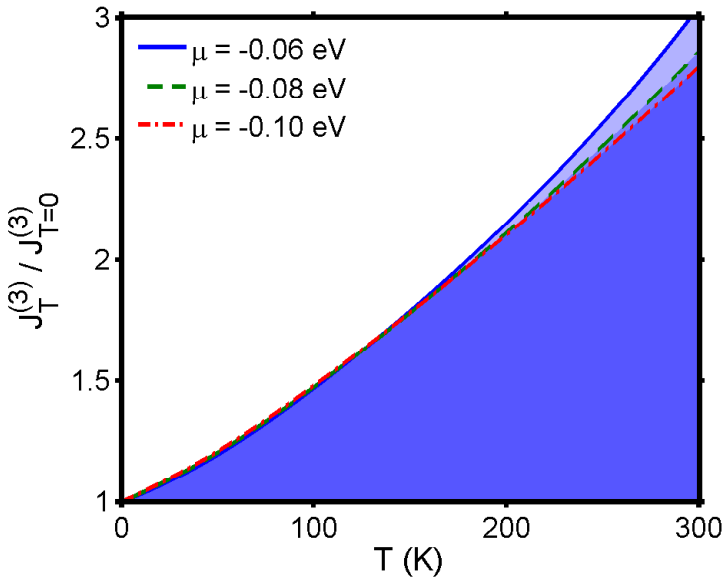

Figure 2.1: Temperature dependence of third order nonlinear current density for $\mu < 0$ at $f = 1$ THz.

in Eq. (2.16), smaller μ generates stronger nonlinear current density. However, the assumption of $p \gg u$ in the derivation of the nonlinear velocities is no longer valid if μ is too small since this will involve charge carriers with momentum comparable to u. For terahertz waves at room temperature, the range of $|\mu| \gtrsim 0.05eV$ will be adequate for $p \gg u$ to hold and we choose $\mu = 60$ meV as the smallest Fermi-level throughout this work. Experimentally, the Fermi level is continuously tunable up to $\pm(1 \sim 2)eV$ by an external gate voltage [103] and hence our choice of μ is practically achievable.

The numerical result of Eq. (2.17) is shown in Fig. 2.1 and Fig. 7.2. The nonlinear current densities are normalized by the zero-temperature current density. The normalization cancels out the electric field dependence.We observe three important and unusual features in the nonlinear optical response: the third-order nonlinear response is: (i) *thermally enhanced* up to room temperature; (ii) approximately *inversely proportional to* μ; and (iii) *asymmetric* between $\mu > 0$ and $\mu < 0$. Feature (i) is due to the thermal extension of the charge carrier lower-limit $\mu - \varepsilon_{\eta\nu\lambda} - k_B T$ at higher temperature. Thermally created vacancy at higher energy level allows more low-lying charge carriers to be excited and this amplifies the nonlinear current den-

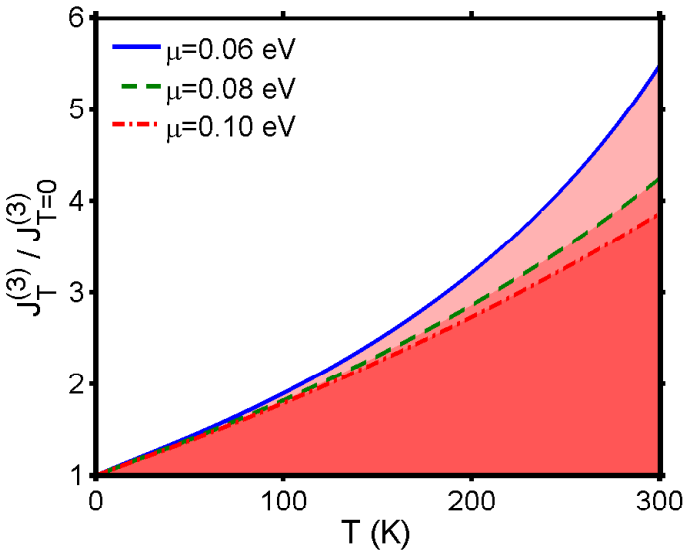

Figure 2.2: Temperature dependence of third order nonlinear current density for $\mu > 0$ at $f = 1$ THz.

sity. However, it should be emphasized that the nonlinear current density does not grow indefinitely with increasing temperature. At much higher temperature, the charge carriers in the opposite Dirac cone contribute to and opposite nonlinear current density generation which eventually reduces in the net nonlinear current density. This reduction is not observed in our case due to the largeness of μ we have chosen, i.e. the nonlinear current density is always contributed by charge carriers in only one Dirac cone. For feature (ii), a small μ results in nonlinear current density contributed by low-momentum charge carriers and this leads to the stronger current density. The combine effect of (i) and (ii) causes the superlinear growth of nonlinear current density at $\mu = 60meV$ and $T > 150K$. Feature (iii) is explained by the finite temperature Dirac fermions population distribution in graphene. Consider the μ is in an arbitrary magnitude of $\mu = \mu_0$. Switching the Fermi-level from $\mu = +\mu_0$ to $\mu = -\mu_0$ is essentially equivalent to the mirror reflection of the upper Dirac cone across the zero energy point into the lower Dirac cone. However, the Fermi-Dirac is not reflected, but is shifted downwards by an amount of $2\mu_0$ and this breaks the overall up-down symmetry of the nonlinear current densities at $\mu = \pm\mu_0$. When $\mu = +\mu_0$, a larger amount of low-lying $s = +1$ electrons becomes excitable at finite temperature and this significantly enhances the nonlinear current density, while in

the case of $\mu = -\mu_0$, larger amount of deep $s = -1$ electrons becomes excitable and the nonlienar current density enhancement is relatively weaker.

It should be emphasized that for small μ or high T, interband nonlinear optical process becomes possible and hence a more complete model including both inter-and intraband contributions to the nonlinear optical current density should be utilized.

The strong nonlinear response of single layer graphene is not surprising if we consider the quasiparticles dynamics in graphene. The massless Dirac fermions around K point is well-described by a 'pseudospin' Hamiltonian Eq. (2.1) and this 'pseudospin' nature mimics the 'real-spin' Rsahba spin-orbit interaction (RSOI) term in 2-dimensionally electron gas confined in a quantum well structure (2DEG) which has previously been shown to exhibit exceptionally strong nonlinear response [97]. In such system, the enhanced nonlinerity is caused by the highly non-parabolic band structure induced by RSOI [96]; while in graphene, the linear (and hence highly non-parabolic) Dirac conic band structure results in the same enhanced optical nonlinearity. The linear optical response is however much smaller in graphene (linear conductivity in the order of quantum conductance e^2/h) and this gives rise to the relatively stronger optical nonlinearity in comparison to 2DEG with RSOI.

Two conclusions can be readily drawn from the above discussions. In order to achieve strong nonlinear optical effect in graphene: (i) small μ is preferred since low-lying electrons is strongly nonlinear; and (ii) electron filling $\mu > 0$ is preferred due to the broken Dirac fermion population symmetry at finite temperature.

We remark that the total optical conductivity should include both intraband and interband contributions. It can however be seen that σ_{inter} is forbidden in few-THz regime due to the largeness of μ. By the virtue of momentum conservation, the requirement for vertical interband transition can be written as $3\varepsilon_{photon} > 2\mu$ (where for simplicity, the three incoming photons are assumed to have the same energy ε_{photon}). For $\mu > 0.06$ eV, each photon has to exceed 0.04 eV, or frequency higher than 10 THz, for vertical interband transition to become possible and this is well beyond the few-THz regime considered here. Therefore, it is reasonable to drop the

σ_{inter} contribution and to consider σ_{intra} as the sole contributor to σ_{total}.

2.2.3 Critical electric field and photon-mixing effect

We now discuss the electric field strength required to create non-negligible photon-mixing effect in graphene. We define a critical field strength such that $|\mathbf{J}^{(3)}|/|\mathbf{J}^{(1)}| = 1$. The physical importance of critical field is that it quantifies the *optical nonlinearity* of a system by comparing both of the linear and nonlinear response. A small critical electric field represents strong optical nonlinearity because the nonlinear response easily dominates over the linear response by only a small electric field.

By combining Eq. (2.14) and Eq. (2.16), we obtain the $T = 0K$ critical field as:

$$E_c(\omega, T = 0K) = \frac{2\omega}{v_F}\left[\frac{2\mu}{e^2}\left(\frac{\mu}{3} - \hbar\omega\right)\right]^{1/2} \tag{2.18}$$

where the three incident fields are assumed to have the same intensity and polarization. For $\omega = 1$ THz and $\mu = 0.1$ eV, the zero temperature critical field is approximately 10^4 V/cm. This electric field strength is about one order of magnitude larger than the critical electric field of the 3-photon nonlinear interband conductivity in intrinsic graphene [89].

At $T > 0$, the critical field is $E_c(\omega, T) = \beta E_c(\omega, T = 0K)$ where the temperature dependence is embedded in the dimensionless parameter β:

$$\beta = \left\{\frac{k_B T}{\hbar\omega}\frac{\ln\left[1 + \exp\left(\frac{\hbar\omega}{k_B T} + 1\right)\right]}{|\mathbf{J}^{(3)}_{T>0}|/|\mathbf{J}^{(3)}_{T=0}|}\right\}^{1/2} \tag{2.19}$$

β describes the temperature dependence of the optical nonlinearity in graphene. The temperature dependence of β is plotted in Fig. 7.3. β exhibits contrasting behavior at low and high temperature regime. At low temperature regime, β increases with increasing temperature due to the stronger linear current density. At higher temperature, the rate of increase of $J^{(3)}$ eventually exceeds $J^{(1)}$ and this leads to the peaking of β, and further increment of temperature results in the lowering of β. For $\mu = 60$ meV, the β peaking is clearly observable at $T \approx 150K$. The room temperature E_c is

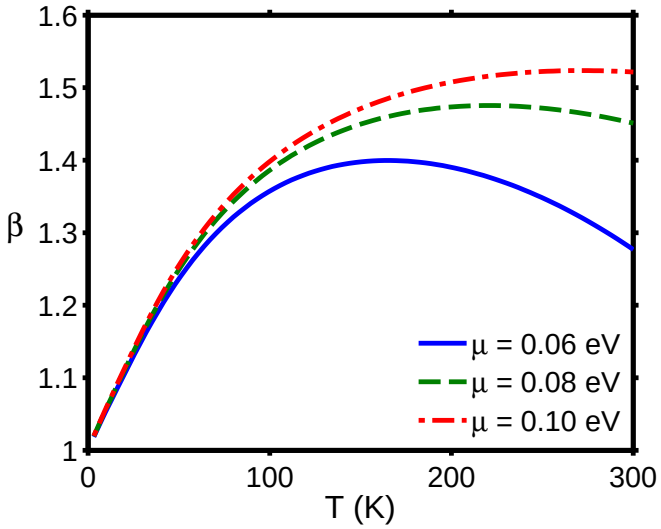

Figure 2.3: Temperature dependence of β at $f = 1$ THz. β exhibits contrasting behavior at low and high temperature regimes.

approximately 10% lower than E_c at $T \approx 150K$. For $\mu = 0.1$ eV and at room temperature, E_c is increased by about 60%, i.e. $E_c \approx 2 \times 10^4 V/cm$ and this is consistent with the experimental electric field strength where gigahertz waves mixing occured [49]. As $E \approx 10^4$ V/cm is a rather strong electric field strength, the redistribution of the charge carrier due to this strong field strength should be taken into account. This will be discussed in detail in Section 2.3.

The nonlinear optical absorption in graphene creates an oscillating current density $J^{(3)}$. This oscillation in turns induces an electromagnetic wave giving rise to the well-known four-wave mixing phenomenon. The strong nonlinear current density in graphene immediately suggests the occurrence of strong four-wave mixing effect. The strength of the electric field $\mathbf{E}^{(3)}$ induced by the nonlinear mixing of $\omega_3 = 2\omega_1 \pm \omega_2$ can be estimated by solving Maxwell's inhomogeneous electromagnetic wave equation $\Box \mathbf{E}^{(3)} = (4\pi/c^2)\partial \mathbf{J}^{(3)}/\partial t$ where $\Box$ is the d'Alembert operator. At distance far away from the graphene single layer, the solution is approximately given by $\partial^2 \mathbf{E}^{(3)}/\partial^2 t \propto \partial \mathbf{J}^{(\mathbf{3})}/\partial t$ and the corresponding third-order polarizability is given as:

$$\chi^{(3)} = \frac{e^4 v_F^2}{8\pi\hbar^2\mu}\left(\frac{\hbar\omega_3}{\mu - \hbar\omega_3}\right)\frac{1}{\omega_2\omega_3}\left(\frac{1}{\omega_1\varepsilon_0}\right)^2 \tag{2.20}$$

2.3 Optical response of graphene in a strong electric field

In previous sections, the optical response is derived by assuming that the Dirac fermion population is well described by $f(\varepsilon_0)$ where $\varepsilon_0 = \mathbf{v}_s^{(0)} \cdot \mathbf{p}$ is the unperturbed linear energy spectrum. Under strong-field condition, the simple assumption of $f(\varepsilon_0)$ is however no longer valid since the externally acquired dynamics $\Delta\varepsilon = (\mathbf{v}_s^{(1)} + \mathbf{v}_s^{(2)} + \mathbf{v}_s^{(3)}) \cdot \mathbf{p}$ is no longer negligible. This additional dynamics causes the Dirac fermions to redistribute themselves via a completely different distribution function of $f(\varepsilon_0) \rightarrow f(\varepsilon_0 + \Delta\varepsilon)$. In this section, we study the optical response of strong-field driven Dirac fermions (SDF) in graphene with the strong-field induced carrier population redistribution taken into account.

2.3.1 Population redistribution due to a strong electric field

The dynamics of the strong-field driven Dirac fermions (SDF) in graphene can be expressed as

$$\mathbf{v}_s^{(0)} \cdot \mathbf{p} \rightarrow (\mathbf{v}_s^{(0)} + \mathbf{v}_s^{(1)} + \mathbf{v}_s^{(2)} + \mathbf{v}_s^{(3)}) \cdot \mathbf{p} = \varepsilon_0 + \Delta\varepsilon \tag{2.21}$$

where $|\mathbf{v}_s^{(0)}| = v_F \approx 10^6 m/s$ is the Fermi velocity, ε_0 is the linear energy dispersion and $\Delta\varepsilon = (\mathbf{v}_s^{(1)} + \mathbf{v}_s^{(2)} + \mathbf{v}_s^{(3)}) \cdot \mathbf{p}$ represents the perturbed dynamics due to the strong field. The Fermi Dirac distribution SDF is given by

$$f(\varepsilon) = \frac{1}{\exp\left(\frac{\varepsilon-\mu}{k_B T}\right) + 1} \tag{2.22}$$

where $\varepsilon = \varepsilon_0 + \Delta\varepsilon$. The distribution function can be expanded for small $\Delta\varepsilon$. Up to third-order, the expansion yields

$$f(\varepsilon) = f_0 + \Delta\varepsilon \frac{\partial f_0}{\partial \varepsilon_0} + \frac{(\Delta\varepsilon)^2}{2!} \frac{\partial^2 f_0}{\partial \varepsilon_0^2} + \frac{(\Delta\varepsilon)^3}{3!} \frac{\partial^3 f_0}{\partial \varepsilon_0^3} \tag{2.23}$$

where f_0 is the Dirac Fermion distribution function. Knowing that $\Delta\varepsilon = (\mathbf{v}_s^{(1)} + \mathbf{v}_s^{(2)} + \mathbf{v}_s^{(3)}) \cdot \mathbf{p}$, the expansion of $f(\varepsilon)$ can be rewritten as

$$\begin{aligned} f(\varepsilon) &= f_0 + [(\mathbf{v}_s^{(1)} + \mathbf{v}_s^{(2)} + \mathbf{v}_s^{(3)}) \cdot \mathbf{p}] \frac{\partial f_0}{\partial \varepsilon_0} \\ &\quad + \frac{[(\mathbf{v}_s^{(1)} + \mathbf{v}_s^{(2)} + \mathbf{v}_s^{(3)}) \cdot \mathbf{p}]^2}{2} \frac{\partial^2 f_0}{\partial \varepsilon_0^2} + \frac{[(\mathbf{v}_s^{(1)} + \mathbf{v}_s^{(2)} + \mathbf{v}_s^{(3)}) \cdot \mathbf{p}]^3}{6} \frac{\partial^3 f_0}{\partial \varepsilon_0^3} \\ &= [(\mathbf{v}_s^{(1)} + \mathbf{v}_s^{(2)} + \mathbf{v}_s^{(3)}) \cdot \mathbf{p}] \frac{\partial f_0}{\partial \varepsilon_0} \\ &\quad + \frac{(\mathbf{v}_s^{(1)} \cdot \mathbf{p})^2 + 2(\mathbf{v}_s^{(1)} \cdot \mathbf{p})(\mathbf{v}_s^{(2)} \cdot \mathbf{p})}{2} \frac{\partial^2 f_0}{\partial \varepsilon_0^2} + \frac{(\mathbf{v}_s^{(1)} \cdot \mathbf{p})^3}{6} \frac{\partial^3 f_0}{\partial \varepsilon_0^3} \\ &= f_0 + \Delta f^{(1)} + \Delta f^{(2)} + \Delta f^{(3)} \end{aligned} \tag{2.24}$$

where we have picked up terms up to third-order in $\mathbf{u}$, and denoted

$$\Delta f^{(1)} = \left(\mathbf{v}_s^{(1)} \cdot \mathbf{p}\right) f_0' \tag{2.25}$$

$$\Delta f^{(2)} = \left(\mathbf{v}_s^{(2)} \cdot \mathbf{p}\right) f_0' + \frac{\left(\mathbf{v}_s^{(1)} \cdot \mathbf{p}\right)^2}{2} f_0'' \tag{2.26}$$

$$\Delta f^{(3)} = \left(\mathbf{v}_s^{(3)} \cdot \mathbf{p}\right) f_0' + \frac{\left(\mathbf{v}_s^{(1)} \cdot \mathbf{p}\right)^3}{6} f_0''' + \left(\mathbf{v}_s^{(1)} \cdot \mathbf{p}\right)\left(\mathbf{v}_s^{(2)} \cdot \mathbf{p}\right) f_0'' \tag{2.27}$$

Eq. (2.25), (2.26) and (2.27) represent the strong field population redistribution of SDF up to third-order of the external electric field. The dot-products in the above equation are found to be

$$\begin{aligned} \mathbf{v}_s^{(1)} \cdot \mathbf{p} &= s v_F \left[\frac{\mathbf{u}}{p} - \frac{\mathbf{p}}{p}\left(\frac{\mathbf{p} \cdot \mathbf{u}}{p^2}\right)\right] \cdot \mathbf{p} \\ &= s v_F \left[\frac{\mathbf{u} \cdot \mathbf{p}}{p} - \frac{\mathbf{p} \cdot \mathbf{p}}{p}\left(\frac{\mathbf{p} \cdot \mathbf{u}}{p^2}\right)\right] \\ &= s v_F \left(u \cos\phi - u \cos\phi\right) \\ &= 0 \end{aligned} \tag{2.28}$$

$$
\begin{aligned}
\mathbf{v}_s^{(2)} \cdot \mathbf{p} &= sv_F \left[\frac{3}{2}\frac{\mathbf{p}}{p}\left(\frac{\mathbf{p}\cdot\mathbf{u}}{p^2}\right)^2 - \frac{1}{2}\frac{\mathbf{p}}{p}\left(\frac{u}{p}\right)^2 - \frac{\mathbf{u}}{p}\left(\frac{\mathbf{p}\cdot\mathbf{u}}{p^2}\right)\right]\cdot\mathbf{p} \\
&= sv_F \left[\frac{3}{2}\frac{\mathbf{p}\cdot\mathbf{p}}{p}\left(\frac{\mathbf{p}\cdot\mathbf{u}}{p^2}\right)^2 - \frac{1}{2}\frac{\mathbf{p}\cdot\mathbf{p}}{p}\left(\frac{u}{p}\right)^2 - \frac{\mathbf{u}\cdot\mathbf{p}}{p}\left(\frac{\mathbf{p}\cdot\mathbf{u}}{p^2}\right)\right] \\
&= sv_F \left[\frac{3}{2}\frac{u^2\cos^2\phi}{p} - \frac{1}{2}\frac{u^2}{p} - \frac{u^2\cos^2\phi}{p}\right] \\
&= sv_F \frac{u^2}{2p}\left(\cos^2\phi - 1\right) \\
&= -sv_F \frac{u^2}{2p}\sin^2\phi
\end{aligned} \tag{2.29}
$$

$$
\begin{aligned}
\mathbf{v}_s^{(3)} \cdot \mathbf{p} &= sv_F \left[-\frac{1}{2}\frac{\mathbf{u}}{p}\left(\frac{u}{p}\right)^2 + \frac{3}{2}\frac{\mathbf{p}}{p}\left(\frac{u}{p}\right)^2\left(\frac{\mathbf{p}\cdot\mathbf{u}}{p^2}\right) + \frac{3}{2}\frac{\mathbf{u}}{p}\left(\frac{\mathbf{p}\cdot\mathbf{u}}{p^2}\right)^2 - \frac{5}{2}\frac{\mathbf{p}}{p}\left(\frac{\mathbf{p}\cdot\mathbf{u}}{p^2}\right)^3\right]\cdot\mathbf{p} \\
&= sv_F \left[-\frac{1}{2}\frac{\mathbf{u}\cdot\mathbf{p}}{p}\left(\frac{u}{p}\right)^2 + \frac{3}{2}\frac{\mathbf{p}\cdot\mathbf{p}}{p}\left(\frac{u}{p}\right)^2\left(\frac{\mathbf{p}\cdot\mathbf{u}}{p^2}\right)\right. \\
&\quad \left. + \frac{3}{2}\frac{\mathbf{u}\cdot\mathbf{p}}{p}\left(\frac{\mathbf{p}\cdot\mathbf{u}}{p^2}\right)^2 - \frac{5}{2}\frac{\mathbf{p}\cdot\mathbf{p}}{p}\left(\frac{\mathbf{p}\cdot\mathbf{u}}{p^2}\right)^3\right] \\
&= sv_F \left[-\frac{1}{2}\frac{u^3}{p^2}\cos\phi + \frac{3}{2}\frac{u^3}{p^2}\cos\phi + \frac{3}{2}\frac{u^3}{p^2}\cos^3\phi - \frac{5}{2}\frac{u^3}{p^2}\cos^3\phi\right] \\
&= sv_F \frac{u^3}{p^2}\cos\phi\left(1 - \cos^2\phi\right) \\
&= sv_F \frac{u^3}{p^2}\cos\phi\sin^2\phi
\end{aligned} \tag{2.30}
$$

These reduces Eq. (2.25), (2.26) and (2.27) to

$$\Delta f^{(1)} = 0 \tag{2.31}$$

$$\Delta f^{(2)} = \left(\mathbf{v}_s^{(2)} \cdot \mathbf{p}\right) f_0' \tag{2.32}$$

$$\Delta f^{(3)} = \left(\mathbf{v}_s^{(3)} \cdot \mathbf{p}\right) f_0' \tag{2.33}$$

It can be seen that up to third-order of the external field, only f_0' contributes to the Δf, higher order expansion f_0'' and f_0''' do not play a role in the population

distribution of SDF. The f_0' is given by

$$f_0' = -\frac{s}{k_B T} \frac{\exp\left(\frac{\varepsilon_s - \mu}{k_B T}\right)}{\left[\exp\left(\frac{\varepsilon_s - \mu}{k_B T}\right) + 1\right]^2} \tag{2.34}$$

2.3.2 Nonlinear optical response of strong field driven massless Dirac Fermion

The total current density of the SDF is given by

$$\begin{aligned} \mathbf{J} &= e \sum_s \int_0^{2\pi} \int_{\mu - \varepsilon_{ph} - k_B T}^{\Lambda} \mathrm{d}^2 p \mathbf{v}_s f\left(\varepsilon_0 + \Delta\varepsilon\right) \\ &= e \sum_s \int_0^{2\pi} \int_{\mu - \varepsilon_{ph} - k_B T}^{\Lambda} \mathrm{d}^2 p \left(\mathbf{v}_s^{(0)} + \mathbf{v}_s^{(1)} + \mathbf{v}_s^{(2)} + \mathbf{v}_s^{(3)}\right) \left(f_0 + \Delta f^{(1)} + \Delta f^{(2)} + \Delta f^{(3)}\right) \end{aligned} \tag{2.35}$$

Splitting the total current density into linear and nonlinear components, we obtain

$$\mathbf{J}^{(1S)} = e \sum_s \int_0^{2\pi} \int_{\mu - \varepsilon_{ph} - k_B T}^{\Lambda} \mathrm{d}^2 p \left(\mathbf{v}_s^{(1)} f_0 + \mathbf{v}_s^{(0)} \Delta f^{(1)}\right) \tag{2.36}$$

$$\mathbf{J}^{(2S)} = e \sum_s \int_0^{2\pi} \int_{\mu - \varepsilon_{ph} - k_B T}^{\Lambda} \mathrm{d}^2 p \left(\mathbf{v}_s^{(2)} f_0 + \mathbf{v}_s^{(0)} \Delta f^{(2)} + \mathbf{v}_s^{(1)} \Delta f^{(1)}\right) \tag{2.37}$$

$$\mathbf{J}^{(3S)} = e \sum_s \int_0^{2\pi} \int_{\mu - \varepsilon_{ph} - k_B T}^{\Lambda} \mathrm{d}^2 p \left(\mathbf{v}_s^{(3)} f_0 + \mathbf{v}_s^{(0)} \Delta f^{(3)} + \mathbf{v}_s^{(1)} \Delta f^{(2)} + \mathbf{v}_s^{(2)} \Delta f^{(1)}\right) \tag{2.38}$$

where the superscript (S) emphasizes the optical response of SDF. Denote $\mathbf{J}^{(iw)} = e \sum_s \int \mathrm{d}^2 p \mathbf{v}_s^{(i)} f_0$ as the *weak-field Dirac fermions* optical response and using $\Delta f^{(1)} = 0$, the optical current density of SDF can be rewritten as

$$\mathbf{J}^{(1S)} = \mathbf{J}^{(1w)} \tag{2.39}$$

$$\mathbf{J}^{(2S)} = \mathbf{J}^{(2w)} + e \sum_s \int_0^{2\pi} \int_{\mu - \varepsilon_{ph} - k_B T}^{\Lambda} \mathrm{d}^2 p \left(\mathbf{v}_s^{(0)} \Delta f^{(2)}\right) \tag{2.40}$$

$$\mathbf{J}^{(3S)} = \mathbf{J}^{(3w)} + e \sum_s \int_0^{2\pi} \int_{\mu - \varepsilon_{ph} - k_B T}^{\Lambda} \mathrm{d}^2 p \left(\mathbf{v}_s^{(0)} \Delta f^{(3)} + \mathbf{v}_s^{(1)} \Delta f^{(2)}\right) \tag{2.41}$$

For $\mathbf{J}^{(2)}$, the integral part is:

$$\begin{aligned} e\sum_s \int_0^{2\pi}\int_{\mu-\varepsilon_{ph}-k_BT}^{\Lambda} \mathrm{d}^2p\left(\mathbf{v}_s^{(0)}\Delta f^{(2)}\right) &= e\sum_s \int_0^{2\pi}\int_{\mu-\varepsilon_{ph}-k_BT}^{\Lambda} \mathrm{d}^2p\left(\mathbf{p}\sin^2\phi\right)[\cdots] \\ &= e\sum_s \int_0^{2\pi}\int_{\mu-\varepsilon_{ph}-k_BT}^{\Lambda} \mathrm{d}^2p\left(\cos\phi\sin^2\phi\right)[\cdots] \\ &= 0 \end{aligned} \tag{2.42}$$

where $[\cdots]$ denotes terms that do no have any angular dependence. We see that the additional terms generated by strong electric field are eliminated by the angular integration. For the third-order nonlinear current density in Eq. (2.41), the first term is the same as the weak field result we derived in previous section. The second-term of in Eq. (2.41) can be evaluated as followed (for simplicity, the integration limit and $e\sum_s$ are dropped):

$$\begin{aligned} \int_0^{2\pi}\int \mathrm{d}^2p\left(\mathbf{v}_s^{(0)}\Delta f^{(3)}+\mathbf{v}_s^{(1)}\Delta f^{(2)}\right) &= -\int \mathrm{d}^2p\frac{v_F^2}{2p}\left[\frac{\mathbf{u}}{p}-\frac{\mathbf{p}}{p}\left(\frac{\mathbf{u}\cdot\mathbf{p}}{p^2}\right)\right]u^2\sin^2\phi f_0' \\ &\quad +\int \mathrm{d}^2p v_F^2\frac{\mathbf{p}}{p}\frac{u^3}{p^2}\cos\phi\sin^2\phi f_0' \\ &= -\int \mathrm{d}^2p\frac{v_F^2}{2p}\left[1-\cos^2\phi\right]\frac{u^3}{p}\sin^2\phi f_0' \\ &\quad +\int \mathrm{d}^2p v_F^2\frac{u^3}{p^2}\cos^2\phi\sin^2\phi f_0' \\ &= -\int \mathrm{d}^2p v_F^2\frac{u^3}{2p^2}\sin^4\phi f_0' + \int \mathrm{d}^2p v_F^2\frac{u^3}{p^2}\cos^2\phi\sin^2\phi f_0' \\ &= v_F^2\int p\mathrm{d}p\int_0^{2\pi}\mathrm{d}\phi\frac{u^3}{p^2}\left(\cos^2\phi\sin^2\phi-\frac{\sin^4\phi}{2}\right)f_0' \\ &= \int \mathrm{d}p\frac{u^3}{p}\left(-\frac{\pi}{8}\right)\left[-\frac{s}{k_BT}\frac{\exp\left(\frac{\varepsilon_s-\mu}{k_BT}\right)}{\left(\exp\left(\frac{\varepsilon_s-\mu}{k_BT}\right)+1\right)^2}\right] \end{aligned} \tag{2.43}$$

Finally, in full units, the strong field term in the third-order current density is:

$$\mathbf{J}^{(3')} = e\mathbf{u}^3\sum_s \frac{sv_F^2}{8\pi\hbar^2k_BT}\int\frac{\mathrm{d}p}{p}\frac{\exp\left(\frac{\varepsilon_s-\mu}{k_BT}\right)}{\left(\exp\left(\frac{\varepsilon_s-\mu}{k_BT}\right)+1\right)^2} \tag{2.44}$$

In summary:

$$\mathbf{J}^{(1S)} = \mathbf{J}^{(1w)} \tag{2.45}$$

$$\mathbf{J}^{(2S)} = 0 \tag{2.46}$$

$$\mathbf{J}^{(3S)} = \mathbf{J}^{(3w)} + \mathbf{J}^{(3')} \tag{2.47}$$

The superscript (S) and (w) emphasize the optical response of SDF and weak-field Dirac fermions respectively. The consequences of (2.45) and (2.46) are quite surprising: the linear and second-order nonlinear optical responses of graphene remain unchanged although the whole SDF population has redistributed themselves. This behavior can be understood by considering the nature of the strong-field induced population redistribution phenomena. Such process is a description of how strongly the Dirac fermions respond to an external perturbation and the degree of redistribution depends on the coupling between the externally acquired dynamics and the unperturbed dynamics of Dirac fermions, i.e. $\mathbf{v}_{external} \cdot \mathbf{p}$. For first-order response, it can be seen that the externally acquired first-order dynamics is completely decoupled from the unperturbed dynamics, i.e. $\mathbf{v}_s^{(1)} \cdot \mathbf{p} = 0$. As a result, this orthogonality ensures that the linear response of graphene is always protected from the strong field effect. For second-order nonlinear response, the second-order coupling $\mathbf{v}_s^{(2)} \cdot \mathbf{p}$ is finite and one would intuitively expect a finite second-order current density to occur. This is however not the case as the additional second-order term vanishes after performing angular integration. In this case, although Dirac fermions are second-order-ly perturbed and redistributed, the crystal itself remains unaffected and retains its inversion symmetry. Therefore, second-order nonlinear response is still zero in the strong-field regime.

We now evaluate the $T = 0$ K third-order nonlinear current density. At $T = 0$

K, the derivative of f_0 is a δ-function: $f_0'(T=0) = -\delta(\varepsilon_s - \mu)$. So

$$\begin{aligned} \mathbf{J}_{T=0}^{(3')} &= e\mathbf{u}^3 \sum_s \frac{s v_F^2}{8\pi\hbar^2} \int \frac{\mathrm{d}p}{p} \delta(\varepsilon_s - \mu) \\ &= e\mathbf{u}^3 \sum_s \frac{s v_F^2}{8\pi\hbar^2} \int \frac{\mathrm{d}\varepsilon_s}{\varepsilon_s} \delta(\varepsilon_s - \mu) \end{aligned} \tag{2.48}$$

Writing the electric field components explicitly, we obtain:

$$\begin{aligned} \mathbf{J}_{T=0}^{(3')} &= -is \sum_{\eta\nu\xi} \frac{\mathbf{E}_\eta \cdot \mathbf{E}_\nu \mathbf{E}_\xi}{\omega_\eta \omega_\nu \omega_\xi} \frac{e^4 v_F^2}{8\pi\hbar^2\mu} \\ &\quad \times \exp\left\{ i \left[(\mathbf{q}_\eta + \mathbf{q}_\nu + \mathbf{q}_\xi) \cdot \mathbf{r} - (\omega_\eta + \omega_\nu + \omega_\xi) t \right] \right\} \end{aligned} \tag{2.49}$$

Finally, in the general case of $T > 0$ K, we have:

$$\mathbf{J}^{(3')} = \mathbf{J}_{T=0}^{(3')} \frac{\mu}{k_B T} \int \frac{\mathrm{d}p}{p} \frac{\exp\left(\frac{\varepsilon_0 - \mu}{k_B T}\right)}{\left(\exp\left(\frac{\varepsilon_0 - \mu}{k_B T}\right) + 1\right)^2} \tag{2.50}$$

2.3.3 Critical electric field in the strong-field regime

At $T = 0$ K, the critical electric field of strongly-driven massless Dirac fermion in graphene can be obtained by directly taking the ratio of the linear and nonlinear current densities derived in previous sections. This gives:

$$E_c^{(S)}(T=0) = \frac{2\omega}{v_F} \left[\frac{2\hbar\omega}{e^2} (\mu - 3\hbar\omega) \right] \tag{2.51}$$

For 1 THz and $\mu = 0.1$ eV, $E_c^{(S)}(T=0) = 3300$ V/cm and is 3 times smaller than that of the weak-field response ($\approx 10^4$ V/cm). At finite temperature, we obtain $E_c^{(S)}(T) = \beta^{(S)}(T) E_c^{(S)}(T=0)$, where the dimensionless strong-field $\beta^{(S)}(T)$ is given as

$$\beta^{(S)}(T) = \left\{ \frac{k_B T}{\hbar\omega} \frac{\ln\left[1 + \exp\left(\frac{\hbar\omega}{k_B T} + 1\right)\right]}{|\mathbf{J}_{T>0}^{(3S)}| / |\mathbf{J}_{T=0}^{(3S)}|} \right\}^{1/2} \tag{2.52}$$

It can be seen in Fig. 2.4 that $E_c^{(S)}$ is significantly lower than weak-field E_c over a wide temperature regime from $T = 0$ K to $T = 600K$. This indicates the stronger

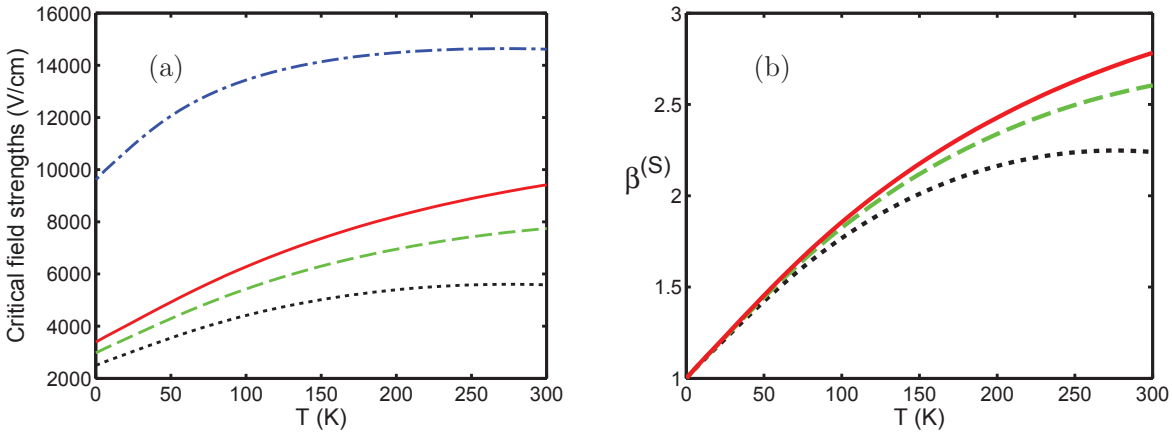

Figure 2.4: (a) Temperature dependence of the strong-field critical fields $E_c^{(S)}$at $f = 1$ THz for $\mu = 0.06$ eV (dotted), $\mu = 0.08$ eV (dashed) and $\mu = 0.1$ eV (solid). The Weak-field critical field E_c for $\mu = 0.1$ eV is also shown (dash-dotted). (b) Temperature dependence of the strong field $\beta^{(S)}$ at $f = 1$ THz for $\mu = 0.06$ eV (dotted), $\mu = 0.08$ eV (dashed) and $\mu = 0.1$ eV (solid).

optical nonlinearity of SDF in comparison to the usual Dirac fermions. The stronger optical nonlinearity of SDF is due to the fact that the third-order nonlinear response is amplified by $\mathbf{J}^{(3')}$ while the linear response remains unchanged.

We now discuss the optical response due to non-equilibrium hot Dirac fermions in graphene. The hot Dirac fermions in graphene are short-lived especially in the case of high lattice temperature where stronger electron-phonon coupling provides efficient pathway for the relaxation [104–106]. Under weak-field condition, Dirac fermions rapidly thermalize themselves with the lattice, i.e. $T = T_{lattice}$. In strong-field regime, the non-equilibrium heating of SDF lifted the SDF temperature from lattice temperature and hence the temperature terms in (2.45) and (2.47) has to be replaced by $T \to T_{hot}$ where T_{hot} is the hot SDF temperature and $T_{hot} > T_{lattice}$. For critical field varies between 10^3 V/cm to 10^4 V/cm, the hot SDF temperature reaches between $T_{hot} = 350K$ to $T_{hot} = 600K$ [107]. In contrast, equilibrium Dirac fermions are relatively 'cold' since the lattice temperature in most of the practical application is only up to $T_{lattice} = 300K$. It can be seen from Fig. 2.5 that the nonlinear current density of hot SDF in $350K < T_{hot} < 600K$ is generally stronger than that of the cold equilibrium Dirac fermions where $T_{lattice} < 300K$.

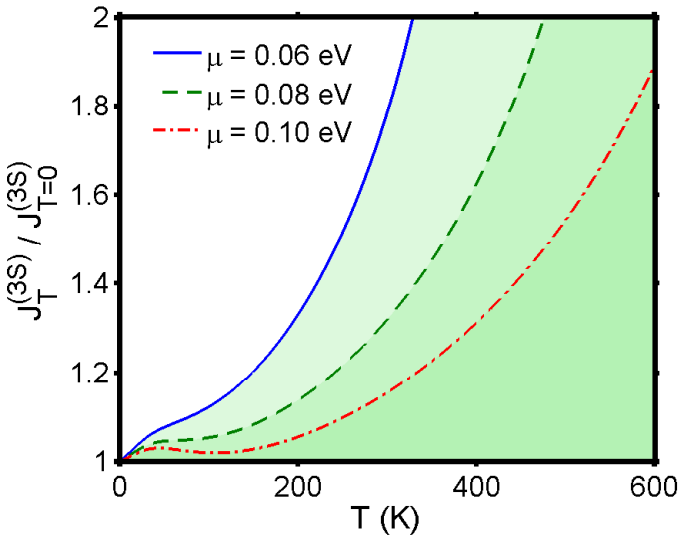

Figure 2.5: Temperature dependence of strong-field third order nonlinear current density at $f = 1$ THz. Note that $T = T_{lattice}$ if non-equilibrium heating is ignored and $T = T_{hot}$ if non-equilibrium heating is considered. Since $T_{hot} > T_{lattice}$, the nonlinear optical response is significantly stronger if carrier heating is considered.

2.4 Optical response of gapped graphene in a strong electric field

For completeness, we briefly discuss the nonlinear intraband conductivity of gapped graphene. The Hamiltonian of gapped graphene in low energy regime is given as

$$\hat{H} = \begin{bmatrix} -\Delta & v_F p_+ \\ v_F p_- & \Delta \end{bmatrix} \tag{2.53}$$

where Δ is the onsite energy difference in the sublattice A and B respectively. The energy eigenvalue is given by $\varepsilon_s = s\sqrt{v_F^2 p^2 + \Delta^2}$ indicating a bandgap opening of 2Δ at the Dirac point. Similarly, up to third-order in external field, the strong-field perturbed carrier velocities can be written as:

$$\mathbf{v}_s^{(0)} = s\frac{v_F \mathbf{p}}{\sqrt{p^2 + \Delta^2}}$$

$$\mathbf{v}_s^{(1)} = s\frac{v_F}{\sqrt{p^2 + \Delta^2}}\left[\mathbf{u} - \mathbf{p}\left(\frac{\mathbf{p}\cdot\mathbf{u}}{p^2 + \Delta^2}\right)\right]$$

$$\mathbf{v}_s^{(2)} = s\frac{v_F}{\sqrt{p^2+\Delta^2}}\left[-\frac{\mathbf{p}}{2}\frac{u^2}{p^2+\Delta^2} - \mathbf{u}\frac{\mathbf{p}\cdot\mathbf{u}}{p^2+\Delta^2} + \frac{3\mathbf{p}}{2}\left(\frac{\mathbf{p}\cdot\mathbf{u}}{p^2+\Delta^2}\right)\right]$$

$$\mathbf{v}_s^{(3)} = s\frac{v_F}{\sqrt{p^2+\Delta^2}}\left[-\frac{\mathbf{u}}{2}\frac{u^2}{p^2+\Delta^2} + \frac{3u^2\mathbf{p}}{2}\frac{\mathbf{p}\cdot\mathbf{u}}{p^2+\Delta^2} + \frac{3\mathbf{u}}{2}\left(\frac{\mathbf{p}\cdot\mathbf{u}}{p^2+\Delta^2}\right)^2 - \frac{5\mathbf{p}}{2}\left(\frac{\mathbf{p}\cdot\mathbf{u}}{p^2+\Delta^2}\right)^3\right] \tag{2.54}$$

The carrier dynamics becomes $\varepsilon = \varepsilon_s + \Delta\varepsilon$ where $\varepsilon_s = s\sqrt{v_F^2p^2+\Delta^2+\Delta^2}$ is the unperturbed energy spectrum and $\Delta\varepsilon = (\mathbf{v}_s^{(1)} + \mathbf{v}_s^{(2)} + \mathbf{v}_s^{(3)})\cdot\mathbf{p}$ is the field-induced energy changed. In strong-field case, the carrier population redistribute themselves according to:

$$f(\varepsilon_s + \Delta\varepsilon) = f_0 + \Delta f_1 + \Delta f_2 + \Delta f_3 \tag{2.55}$$

where

$$\Delta f_1 = (\mathbf{v}_s^{(1)}\cdot\mathbf{p})f_0'$$

$$\Delta f_2 = (\mathbf{v}_s^{(2)}\cdot\mathbf{p})f_0' + \frac{(\mathbf{v}_s^{(1)}\cdot\mathbf{p})^2}{2}f_0''$$

$$\Delta f_3 = (\mathbf{v}_s^{(1)}\cdot\mathbf{p})f_0' + (\mathbf{v}_s^{(1)}\cdot\mathbf{p})(\mathbf{v}_s^{(2)}\cdot\mathbf{p})f_0'' + \frac{(\mathbf{v}_s^{(1)}\cdot\mathbf{p})^3}{6}f_0'''$$

where the dot products are given by

$$\mathbf{v}_s^{(1)}\cdot\mathbf{p} = \frac{sv_Fup\cos\phi}{\sqrt{p^2+\Delta^2}}\left(1 - \frac{p^2}{p^2+\Delta^2}\right)$$

$$\mathbf{v}_s^{(2)}\cdot\mathbf{p} = \frac{sv_F}{\sqrt{p^2+\Delta^2}}\frac{u^2p^2\cos^2\phi}{p^2+\Delta^2}\left(\frac{3}{2}\frac{p^2}{p^2+\Delta^2} - \frac{1}{2} -\right)$$

$$\mathbf{v}_s^{(3)}\cdot\mathbf{p} = \frac{sv_F}{\sqrt{p^2+\Delta^2}}\frac{u^3p^2\cos\phi}{p^2+\Delta^2}\left(\frac{3}{2}\frac{p^2}{p^2+\Delta^2} - \frac{5}{2}\frac{p^4}{(p^2+\Delta^2)^2}\cos^2\phi - \frac{1}{2} + \frac{3}{2}\frac{p^2}{p^2+\Delta^2}\cos^2\phi\right) \tag{2.56}$$

The current density is given by

$$\mathbf{J}^{(1)} = \mathbf{J}^{(1w)} + \mathbf{J}^{(1s)}$$

$$\mathbf{J}^{(2)} = \mathbf{J}^{(2w)} + \mathbf{J}^{(2s)}$$

$$\mathbf{J}^{(3)} = \mathbf{J}^{(3w)} + \mathbf{J}^{(3s)} \tag{2.57}$$

Similarly, the superscript (w) and (s) denote weak-and strong-field term respectively. The weak-field terms can be similarly derived by using the methods discussed in previous section. Here we will focus on the derivation of the strong-field term. The strong-field linear current density is given as

$$\begin{aligned}\mathbf{J}^{(1s)} &= \int \mathrm{d}^2 p \mathbf{v}_s^{(0)} \Delta f_1 \\ &= -s\frac{e^2\mathbf{u}}{\pi\hbar^2}\int \varepsilon \mathrm{d}\varepsilon \left(\frac{\Delta}{\varepsilon}\right)^2 \left(1-\frac{\Delta^2}{\varepsilon^2}\right)\delta(\varepsilon_0-\mu)\end{aligned} \tag{2.58}$$

At $T = 0$K, we obtain

$$\mathbf{J}_{T=0}^{(1s)} = -s\frac{e^2\mathbf{E}}{\pi\hbar}\Delta_\omega\Delta_\mu\left(1-\Delta_\mu^2\right) \tag{2.59}$$

where we have used the fact that $f'(T = 0K) = -\delta(\varepsilon - \mu)$, and denoted $\Delta_\omega = \Delta/\hbar\omega$ and $\Delta_\mu = \Delta/\mu$. The strong-field second-order nonlinear current density is proportional to:

$$\begin{aligned}\mathbf{J}^{(2s)} &\propto \int \mathrm{d}^2 p \left(\mathbf{v}_s^{(0)}\Delta f_2 + \mathbf{v}_s^{(1)}\Delta f_1\right) \\ &= 0\end{aligned} \tag{2.60}$$

since all the terms are contains a single $\cos\phi$, they are eliminated in the angular integration. The second-order response is therefore strictly zero at all temperature as expected. The third-order term consist of multiple terms. At finite temperature, it is given as:

$$\mathbf{J}^{(3w)} = sv_F^2\mathbf{u}^3 8\pi\hbar^2\int\frac{\mathrm{d}\varepsilon}{\varepsilon^2}\left[1+6\left(\frac{\Delta}{\varepsilon}\right)^2-15\left(\frac{\Delta}{\varepsilon}\right)^4\right]\frac{1}{\exp\left(\frac{\varepsilon-\mu}{k_BT}\right)+1} \tag{2.61}$$

$$\begin{aligned}
\mathbf{J}^{(3s)} &= \int \mathrm{d}^2p \left(\mathbf{v}_s^{(0)}\Delta f_3 + \mathbf{v}_s^{(1)}\Delta f_2 + \mathbf{v}_s^{(2)}\Delta f_1\right) \\
&= \frac{sv_F^2\mathbf{u}^3}{8\pi\hbar^2}\int\frac{\mathrm{d}\varepsilon}{\varepsilon}\left(1-\frac{2\Delta^2}{\varepsilon^2}+\frac{33\Delta^4}{\varepsilon^4}\right)f' \\
&\quad +\frac{sv_F^2\mathbf{u}^3}{8\pi\hbar^2}\int\mathrm{d}\varepsilon\left(-\frac{12\Delta^8}{\varepsilon^8}+\frac{21\Delta^6}{\varepsilon^6}-\frac{8\Delta^4}{\varepsilon^4}-\frac{\Delta^2}{\varepsilon^2}\right)f'' \\
&\quad -\frac{sv_F^2\mathbf{u}^3}{8\pi\hbar^2}\int\mathrm{d}\varepsilon\left(\frac{\Delta^6}{\varepsilon^5}-\frac{2\Delta^8}{\varepsilon^7}+\frac{\Delta^{10}}{\varepsilon^9}\right)f'''
\end{aligned} \tag{2.62}$$

where

$$f' = -\frac{1}{k_BT}\frac{\exp\left(\frac{\varepsilon-\mu}{k_BT}\right)}{\left(\exp\left(\frac{\varepsilon-\mu}{k_BT}\right)+1\right)^2} \tag{2.63}$$

$$f'' = \frac{1}{(k_BT)^2}\exp\left(\frac{\varepsilon-\mu}{k_BT}\right)\frac{\exp\left(\frac{\varepsilon-\mu}{k_BT}\right)-1}{\left(\exp\left(\frac{\varepsilon-\mu}{k_BT}\right)+1\right)^3} \tag{2.64}$$

$$f''' = -\frac{1}{k_BT}\frac{\exp\left(\frac{\varepsilon-\mu}{k_BT}\right)}{\left(\exp\left(\frac{\varepsilon-\mu}{k_BT}\right)+1\right)^2} \tag{2.65}$$

At $T = 0$K, $f' = -\delta(\varepsilon-\mu)$, $f'' = -\delta^{(2)}(\varepsilon-\mu)$ and $f''' = -\delta^{(3)}(\varepsilon-\mu)$, where the derivative of the δ-function is defined as:

$$\int f(x)\delta^{(k)}(x-a)\mathrm{d}x = (-1)^k\frac{d^kf}{dx^k}(x=a) \tag{2.66}$$

After some algebra, we obtain the $T = 0$ K result:

$$\mathbf{J}^{(3s)}_{T=0} = \frac{sv_F^2\mathbf{u}^3}{8\pi\hbar^2\mu}\left(1+55\Delta_\mu^4-156\Delta_\mu^6+208\Delta_\mu^8-90\Delta_\mu^{10}\right) \tag{2.67}$$

Finally, the total $T = 0$K response, including both weak-and strong-field terms are given as

$$\mathbf{J}^{(1)}_{T=0} = -s\frac{e^2\mathbf{E}}{\pi\hbar}\left[x+1+\Delta_\omega\Delta_\mu\left(1-\Delta_\mu^2\right)\right] \tag{2.68}$$

$$\mathbf{J}^{(2)}_{T=0} = 0 \tag{2.69}$$

$$\mathbf{J}^{(3)}_{T=0} = \frac{sv_F^2\mathbf{u}^3}{8\pi\hbar^2\mu}\left(y + 1 - \Delta_\mu^2 + 59\Delta_\mu^4 - 177\Delta_\mu^6 + 208\Delta_\mu^8 - 90\Delta_\mu^{10}\right) \quad (2.70)$$

where the weak-field term is represented by x and y, which can be explicitly written as:

$$x = \frac{\frac{\mu}{\hbar\omega}}{\left[1 + \left(\frac{\Delta}{\mu}\right)^2\right]^{1/2}} - \frac{\frac{\mu}{\hbar\omega} - 1}{\left[1 + \left(\frac{\Delta}{\mu - \hbar\omega}\right)^2\right]^{1/2}} \quad (2.71)$$

and

$$y = \frac{\mu}{\mu - \varepsilon_{ph}} \frac{1 + \left(\frac{2\Delta}{\mu_{-ph}}\right)^2}{\left[1 + \left(\frac{\Delta}{\mu_{-ph}}\right)^2\right]^{5/2}} - \frac{1 + \left(\frac{2\Delta}{\mu}\right)^2}{\left[1 + \left(\frac{\Delta}{\mu}\right)^2\right]^{5/2}} \quad (2.72)$$

where ε_{ph} is the energy sum of the three photons. Note that second-order nonlinear current density is again absent in gapped graphene due to the inversion symmetry. One major difference between gapless and gapped graphene is that both of the linear and third-order nonlinear current density are altered by a strong electric field in gapped graphene whereas in gapless graphene, only the third-order nonlinear current density is altered. The third order nonlinear conductivity at finite temperature is evaluated numerically. The temperature and bandgap dependence of the *intraband* third-order nonlinear current density at $\omega = 1.5$ THz and $\mu = 0.12$ eV is shown in Fig. 2.6. Unlike the gapless graphene ($\Delta \to 0$) which exhibits enhanced nonlinear third-order nonlinear optical response at elevated temperature, the third-order nonlinear response of gapped graphene is sensitively influenced by Δ and temperature. Due to the interplay between the bandgap opening and carrier thermal excitation, two distinct nonlinear optical response 'hotspots', in which an amplification factor of ≈ 3.5, are created at two regimes: (i) low temperature with large Δ and; (ii) high temperature with small Δ. These 'hotspots' are linked by an intermediate 'belt' of approximately doubly enhanced nonlinear optical response.

The low temperature hotspot (i) indicates that the bandgap opening in graphene effectively enhances the nonlinear response. The nonlinear response enhancement due to bandgap opening in graphene also occurs in the *interband* nonlinear optical response [108] as we shall show in Chapter 3. This suggests that both of the inter-

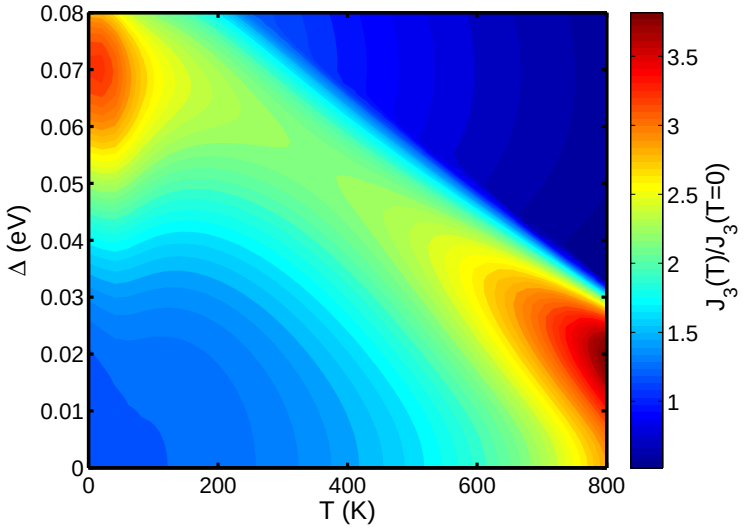

Figure 2.6: Δ and temperature dependence of the third-order nonlinear current density at $f = 1.5$ THz and $\mu = 0.1$eV.

band and the intraband optical absorption are universally enhanced by the bandgap opening in graphene. At very large bandgap, the nonlinear optical response however decreases. This is because the nonlinear velocity components is approximately $\propto p^{-3}$. A large bandgap destroys low momentum states and hence severely degrades the nonlinear optical response. The high temperature hotspot (ii) is a thermal effect. The thermal excitation vacates states beneath the Fermi level, allowing deeper charge carriers to become optically excitable. At very high temperature, the thermally excitable charge carrier population extends to the edge of the bandgap. Any further increment of the temperature does not increase the optically excitable charge carriers. On the other hand, the overall charge carrier momentum are elevated thermally and the p^{-3} reduction of the nonlinear velocity takes place. The combination of these two aspects results the high temperature degradation of the nonlinear optical response.

2.5 Discussion

In summary, the optical response of graphene under strong-field condition exhibits the following interesting behavior: (1) the linear and second-order nonlinear responses are well protected from external field due to the unique Dirac fermions dynamics

and the preservation of crystal inversion symmetry; (2) the third-order nonlinear optical response is enhanced by three distinct mechanisms: (i) third-order response is intrinsically proportional to E^2; (ii) strong-field induces Dirac fermion population redistribution creates an additional contribution to third-order response; and (iii) the non-equilibrium heating raises the carrier temperature to $T_{hot} > T_{lattice}$ and further enhances the nonlinear current density.

Finally, we point out several experiments which can potentially be used to verify our theoretical calculations. Several experimental works emphasizing the visible and near-infrared nonlinear optical response of graphene has been reported recently [88, 91, 109]. Multiple-photon absorption/transmission experiments [91, 109] can be repeated in the THz regime to qualitatively estimate the optical nonlinearity of graphene. The nonlinear wave-mixing effect can be more accurately quantified by irradiating an graphene sample with two THz waves of frequencies ω_1 and ω_2, and selectively filtering the outgoing waves to determine the strength of the mixed wave $(2\omega_1 \pm \omega_2)$ [88]. The temperature dependence of the wave-mixing effect can be probed by performing these experiments under controlled temperature condition. It should be emphasized that our simplistic model presented in this Chapter does not include the effect of disorder and phonon scattering which are inevitably present in experiments. Although the electron-phonon coupling is rather weak in the absence of disorder [110, 111], such coupling can be significantly enhanced via supercollision process in the presence of disorders [112, 113]. Therefore, we expect the nonlinear optical response in the presence of disorder to differ with our theoretical prediction.

In conclusion, we have presented a qualitative and quantitative analysis on the nonlinear effect and its temperature dependence in both gapless and gapped graphene. In graphene, the nonlinear effect is approximately inversely proportional to the Fermi-level and grows rapidly with temperature up to room temperature. The critical electric field required to generate nonlinear effect comparable to linear effect is in a rather moderate value of 10^4 V/cm even in room temperature. Under strong-field condition, the Dirac fermion population redistribution and non-equilibrium carrier

heating effects further enhance the optical non-linearity of graphene. The strong and temperature-robust nonlinear optical nonlinearity suggests that graphene can potentially be an excellent candidate in nonlinear photon-mixing applications. In gapped graphene, the nonlinear optical response is strongly influenced by the bandgap value and the temperature. In order to maximize the nonlinear optical response of a gapped graphene-based photon mixer, the bandgap value and the operating temperature has to be carefully chosen.

3 | Nonlinear optical response in bilayer graphene and 2D electron gas with Rashba spin-orbit coupling

* In this Chapter, we investigate the nonlinear *interband* optical response of two systems whose Hamiltonians are a mixture of terms linear and quadratic in p, namely bilayer graphene (BLG) with low energy trigonal warping effect and two dimensional electron gas in the presence of Rashba spin-orbit interaction (R2DEG). We show that not only these systems exhibits strong nonlinear optical response in the terahertz frequency regime the optical nonlinearity is well-preserved at elevated temperature.

3.1 Nonlinear optical response of bilayer graphene

In this Section, we study the nonlinear *interband* optical response in bilayer graphene (BLG) in the frequency regime of terahertz to far-infrared. The interband optical response is obtained by using a quantum mechanical treatment that couples the BLG quasiparticle to a time-dependent electric field [89]. We expressed the light-dressed electron wavefunction as an infinite sum in terms of the number of photons coupled to the massless Dirac fermion. This allows us to explicitly construct the nonlinear

*This Chapter is based on *Appl. Phys. Lett.* **97**, 243110 (2010) and *Eur. Phys. J. B* **87**, 2, 1-7 (2014).

optical current density up to any arbitrary order in the external electric field.

We show that the optical response of BLG is significantly enhanced due to the third-order nonlinear process. The nonlinear effects are particularly strong in the low frequency regime, which covers the technologically important frequency band of terahertz to far-infrared. More importantly, the field intensity required for the onset of nonlinear response is rather low, indicating that BGL is an excellent material for nonlinear optics and photonics application. The third-order nonlinear optical response is composed of two terms: (i) single-frequency term which corresponds to the simultaneous absorption of two photons and the emission of one photon; and (ii) triple-frequency term which corresponds to the simultaneous absorption of three photons. Both of (i) and (ii) become comparable to the linear optical response at very moderate electric field of 10^3 V/cm which is well within the experimental achievable range in laboratories. Furthermore, we investigate the temperature dependence of the nonlinear optical response. At room temperature, we found that the electric field required to produce nonlinear optical response comparable to the linear one is reduced to 10^2 V/cm. This thermally enhanced optical nonlinearity is not found in single layer graphene. This suggest that BLG is a preferred structure for developing graphene-based nonlinear photonics and optoelectronics device.

3.1.1 Recursion equations for n-photon-electron coupling

We consider the case where a time-dependent electric field $\mathbf{E}(t) = \mathbf{E}e^{i\omega t}$ is applied along the x-axis. We start with the low energy effective Hamiltonian of BLG in K valley [70–72]:

$$H = \alpha \begin{pmatrix} 0 & (p_- + eA)^2 \\ (p_+ + eA)^2 & 0 \end{pmatrix} - \beta \begin{pmatrix} 0 & p_+ eA \\ p_- + eA & 0 \end{pmatrix} \tag{3.1}$$

where $p_\pm = p_x \pm ip_y$, $A = \frac{E}{i\omega}e^{i\omega t}$, $\alpha = 1/(2m^*)$, $m^* = 0.033m_e$, and $\beta = v_F \approx 10^5$ m/s [70]. Note that in Eq. (3.1), we have performed a Peierls substitution of $p + eA$.

The Hamiltonian can be rearranged to the following form

$$H = \begin{bmatrix} 0 & Y_- + \frac{eE}{i\omega} X_- e^{i\omega t} - \alpha \frac{e^2E^2}{\omega^2} e^{i2\omega t} \\ Y_+ + \frac{eE}{i\omega} X_+ e^{i\omega t} - \alpha \frac{e^2E^2}{\omega^2} e^{i2\omega t} & 0 \end{bmatrix} \tag{3.2}$$

where for simplicity, we denote

$$X_\pm = 2\alpha p_\pm - \beta \tag{3.3}$$

$$Y_\pm = \alpha p_\pm^2 - \beta p_\mp \tag{3.4}$$

The electron-photon coupled wavefunction can be written as an infinite sum in terms of the number of photons:

$$\psi(\vec{p}, n) = \sum_{n=0}^{\infty} \begin{pmatrix} a_n(\vec{p}) \\ b_n(\vec{p}) \end{pmatrix} e^{i(n\omega - \varepsilon/\hbar)t} \tag{3.5}$$

where $(a_n(\vec{p}), b_n(\vec{p}))^T$ are the spinor components representing n-photon coupling of the electron. The time derivatives of the wavefunction is

$$\frac{\partial \psi}{\partial t}(\vec{p}, n) = \sum_{n=0}^{\infty} i(n\omega - \varepsilon/\hbar) \begin{pmatrix} a_n(\vec{p}) \\ b_n(\vec{p}) \end{pmatrix} e^{i(n\omega - \varepsilon/\hbar)t} \tag{3.6}$$

The spinor components can be obtained by solving the Schr odinger equation $i\hbar \frac{\partial \psi}{\partial t} = H\psi$. Combining Eq. (3.1) and (3.6) with the Schr odinger equation, we have:

$$\sum_{n=0}^{\infty} \begin{bmatrix} 0 & Y_- + \frac{eE}{i\omega} X_- e^{i\omega t} - \alpha \frac{e^2E^2}{\omega^2} e^{i2\omega t} \\ Y_+ + \frac{eE}{i\omega} X_+ e^{i\omega t} - \alpha \frac{e^2E^2}{\omega^2} e^{i2\omega t} & 0 \end{bmatrix} \begin{pmatrix} a_n(\vec{p}) \\ b_n(\vec{p}) \end{pmatrix} e^{i(n\omega - \varepsilon/\hbar)t}$$
$$= \sum_{n=0}^{\infty} (\varepsilon - n\hbar\omega) \begin{pmatrix} a_n(\vec{p}) \\ b_n(\vec{p}) \end{pmatrix} e^{i(n\omega - \varepsilon/\hbar)t} \tag{3.7}$$

The $e^{i\omega t}$ and $e^{i\omega 2t}$ terms cane be absorbed into the spinor components to obtain a_{n-1}, a_{n-2} and b_{n-1}, b_{n-2}, respectively. Due to the off-diagonal nature of the Hamiltonian

in Eq. (3.1), the upper and the lower spinor components a_n and b_n are coupled and two recursion equations can be obtained:

$$\begin{aligned}(\varepsilon - n\hbar\omega)a_n &= Y_- b_n + \frac{eE}{i\omega}X_- b_{n-1} - \alpha\frac{e^2E^2}{\omega^2}b_{n-2} \\ (\varepsilon - n\hbar\omega)b_n &= Y_+ a_n + \frac{eE}{i\omega}X_+ a_{n-1} - \alpha\frac{e^2E^2}{\omega^2}a_{n-2}\end{aligned} \tag{3.8}$$

The above equation contains information of all multiple photon processes in intrinsic graphene. The recursion relation couples the n photon processes to the $n-1$ photon processes. In general, we can write

$$n\hbar\omega(n\hbar\omega - 2\varepsilon)a_n = \frac{eE}{i\omega}[X_-(\varepsilon - n\hbar\omega)b_{n-1} + X_+Y_-a_{n-1}] - \alpha\frac{e^2E^2}{\omega^2}[Y_-a_{n-2} + (\varepsilon - n\hbar\omega)b_{n-2}] \tag{3.9}$$

$$n\hbar\omega(n\hbar\omega - 2\varepsilon)b_n = \frac{eE}{iw}[X_-Y_+b_{n-1} + X_+a_{n-1}(\varepsilon - n\hbar\omega)] - \alpha\frac{e^2E^2}{\omega^2}[(\varepsilon - n\hbar\omega)a_{n-2} + Y_+b_{n-2}] \tag{3.10}$$

For $n = 0$, there is no photon. The spinor components can be solved to obtain:

$$a_0 = \frac{Y_-}{\varepsilon\sqrt{2}} \tag{3.11}$$

$$b_0 = \frac{1}{\sqrt{2}} \tag{3.12}$$

where ε is the energy dispersion as given by

$$\varepsilon = \sqrt{Y_+Y_-} = \pm\sqrt{\alpha^2p^4 - 2\alpha\beta p^3\cos 3\theta + \beta^2p^2} \tag{3.13}$$

The $n = 0$ no-photon spinor components are in agreement with the single particle eigenfunction of BLG [70]. For n=1, we obtain

$$a_1 = \frac{eE}{i\sqrt{2}\hbar\omega^2\varepsilon(\hbar\omega - 2\varepsilon)}\left[\varepsilon(\varepsilon - \hbar\omega)X_- + X_+Y_-^2\right] \tag{3.14}$$

$$b_1 = \frac{eE}{i\sqrt{2}\hbar\omega^2\varepsilon(\hbar\omega - 2\varepsilon)}\left[\varepsilon X_-Y_+ + (\varepsilon - \hbar\omega)X_+Y_-\right] \tag{3.15}$$

This gives the spinor components of one-photon coupling. The two-photon terms can be recursively built by combining a_0, b_0 and a_1, b_1 into Eq. (3.8), and so on.

3.1.2 Optical current operator and density

We now construct the current density created by the external time-dependent electric field. The velocity operator in x-direction, $v_x = \partial H/\partial p_x$, is given by

$$\hat{v}_x = 2\alpha \begin{pmatrix} 0 & (p_- + eA) \\ (p_+ + eA) & 0 \end{pmatrix} - \beta \begin{pmatrix} 0 & 1 \\ 1 & 0 \end{pmatrix} = \hat{v}_A + \hat{v}_B \tag{3.16}$$

where

$$\hat{v}_A = 2\alpha \begin{pmatrix} 0 & (p_- + eA) \\ (p_+ + eA) & 0 \end{pmatrix} \tag{3.17}$$

$$\hat{v}_B = -\beta \begin{pmatrix} 0 & 1 \\ 1 & 0 \end{pmatrix} \tag{3.18}$$

where $\hat{v}_A$ originates from the p quadratic term of the Hamiltonian Eq. (3.1) and $\hat{v}_B$ originates from the p linear term. In single layer graphene, the velocity operator is only contains $\hat{v}_B$. In BLG, the interlayer coupling craetes an additional $\hat{v}_B$.

The total x directional optical current operator is given by

$$\hat{j} = -e\psi^\dagger \hat{v}\psi = -e(\psi^\dagger \hat{v}_A \psi + \psi^\dagger \hat{v}_B \psi) \tag{3.19}$$

where the wavefunction is given by Eq. (3.6). The total current density can be obtained by integrating Eq. (3.19) in p-space, i.e.

$$J = \frac{1}{(2\pi\hbar)^2} \Re \int \mathrm{d}\mathbf{p} \hat{j} N(\varepsilon) \tag{3.20}$$

where the temperature dependence of the total current density is encoded in $N(\varepsilon) = f(-\varepsilon) - f(\varepsilon) = \tanh \varepsilon / 2k_B T$. Since ψ in in Eq. (3.19) is a linear superposition of the spinor components n-th order, we can selectively construct J_n in any arbitrary

order n in the external electric field. For example, the $n = 1$ linear optical current operator is:

$$j_1 = \hat{j}_1^{(A)} + \hat{j}_1^{(B)} + \hat{j}_1' \tag{3.21}$$

where

$$\hat{j}_1^{(A)} = -2e\alpha \left[(a_1 b_0^* p_+ + b_1 a_0^* p_-) + (a_1^* b_0 p_+ + b_1^* a_0 p_-)\right] \tag{3.22}$$

$$\hat{j}_1^{(B)} = e\beta(a_0^* b_0 + b_0^* a_0) \tag{3.23}$$

and

$$\hat{j}_1' = \frac{E}{i\omega}\left(a_0^* b_1 + b_0^* a_1\right) + c.c. \tag{3.24}$$

The single-photon linear optical current density is hence given by

$$J_1 = \frac{1}{4\pi^2\hbar^2}\Re \int \hat{j}_1 p \mathrm{d}p \mathrm{d}p \mathrm{d}\theta \tag{3.25}$$

It is obvious that the linear optical current is made up of the multiples of $n = 1$ and $n = 0$ spinor components (e.g. $a_0^* b_1$ since it is a one-photon process. For the third-order nonlinear optical response, the three-photon process can be either composed of the multiples of $n = 0$ and $n = 3$ spinor components or the $n = 1$ and $n = 2$ spinor components. These respectively represent optical processes of simultaneous three-photon absorption and the simultaneous two-photon absorption followed by one-photon emission. J_3 is therefore composed of a single-frequency term $\propto e^{i\omega t}$ and a triple-frequency term $\propto e^{3i\omega t}$.

In order to avoid flooding this Chapter with too many algebra, only the linear optical current density is shown in the subsequent section. The derivation of third-order results is included in the Appendix A.

3.1.3 Linear optical response: derivation

In this section, we derive the linear optical current density. We first look at the optical current density corresponding to the $j_1^{(A)}$ component of Eq. (3.22).:

$$J_1^{(A)} = \frac{1}{4\pi^2\hbar^2}\Re\int j_1^{(A)} p\mathrm{d}p\mathrm{d}\theta \tag{3.26}$$

To ensure convergence of the integral, an infinitesimally small part δ is added to the $(\hbar\omega - 2\varepsilon)$denominator carried by the $n = 1$ spinor component. We obtain:

$$J_1^{(A)} = \frac{-1}{4\pi^2\hbar^2}\frac{e^2E}{2\omega^2\hbar}\Re\left(\int \frac{1}{i\varepsilon(\omega\hbar - 2\varepsilon - i\delta)}[\cdots]p\mathrm{d}p\mathrm{d}\theta\right) \tag{3.27}$$

where for simplicity $[\cdots]$ contains the spinor products in Eq. (3.22). Explicitly, it is given as

$$\varepsilon(\omega\hbar - \varepsilon)(X_-p_+ + X_+p_-) + (X_-Y_+^2p_+X_- + Y_-^2p_+) \tag{3.28}$$

Note that $[\cdots]$ is purely real. For $\delta \to 0$, we have:

$$\begin{aligned}
J_1^{(A)} &= \frac{-1}{4\pi^2\hbar^2}\frac{e^2E}{2\omega^2\hbar}\Re\left(\int \frac{1}{i\varepsilon}\delta(\omega\hbar - 2\varepsilon)[\cdots]p\mathrm{d}p\mathrm{d}\theta\right) \\
&= \frac{1}{4\pi^2\hbar^2}\frac{e^2E}{2\omega^2\hbar}\int Im\left(\frac{1}{i\varepsilon}\right) Im\left(\delta(\omega\hbar - 2\varepsilon)\right)[\cdots]p\mathrm{d}p\mathrm{d}\theta \\
&= \frac{-1}{4\pi^2\hbar^2}\frac{e^2E}{2\omega^2\hbar}\int \frac{\pi}{\varepsilon}\delta(\omega\hbar - 2\varepsilon)[\cdots]p\mathrm{d}p\mathrm{d}\theta \\
&= \frac{-1}{4\pi^2\hbar^2}\frac{e^2E}{2\omega^2\hbar}\int \frac{\pi}{\varepsilon}\delta(g(\theta))[\cdots]p\mathrm{d}p\mathrm{d}\theta
\end{aligned} \tag{3.29}$$

where $g(\theta) = \hbar\omega - \varepsilon$. Convert the delta function (originally delta function of $(\omega\hbar)$) in to a new delta function of θ:

$$\delta(\hbar\omega - 2\varepsilon) = \frac{\delta(\theta - \theta_0)}{|g'(\theta_0)|} \tag{3.30}$$

where θ_0 is the root of $g(\theta) = 0$, i.e.

$$\frac{\hbar^2\omega^2}{4} = \alpha^2p^4 - 2\alpha\beta p^3\cos\theta_0 + \beta^2p^2 \tag{3.31}$$

$$\theta_0 = \frac{1}{3}\cos^{-1} X(p) \tag{3.32}$$

and

$$X(p) = \frac{\alpha^2 p^4 + \beta^2 p^2 - \omega^2\hbar^2/4}{2\alpha\beta p^3} \tag{3.33}$$

The derivative of $g(\theta)$ with respect to θ is given as

$$g'(\theta) = \frac{6\alpha\beta p^3 \sin\frac{1}{3}\theta}{\sqrt{\alpha^2 p^4 - 2\alpha\beta p^3\cos\theta + \beta^2 p^2}} \tag{3.34}$$

substitute θ_0, we obtain

$$g'(\theta_0) = \frac{6\alpha\beta p^3 \sin\cos^{-1}(X(p))}{\hbar\omega/2} = \frac{6\alpha\beta p^3\sqrt{1-X^2(p)}}{\omega\hbar/2} \tag{3.35}$$

Therefore, the first order current density becomes

$$\begin{aligned} J_1^{(A)} &= \frac{-\pi}{4\pi^2\hbar^2}\frac{e^2E}{2\hbar\omega^2}\int\frac{\hbar\omega/2}{\varepsilon}\frac{\delta(g(\theta-\theta_0))}{6\alpha\beta p^3\sqrt{1-X^2(p)}}[\cdots]p\mathrm{d}p\mathrm{d}\theta \\ &= \frac{-e^2E}{4(\omega\hbar)^2h}\frac{1}{6\alpha\beta}\int\frac{\omega\hbar/2}{\omega\hbar/2}\frac{[\cdots]_{\theta=\theta_0}}{p^2\sqrt{1-X^2(p)}}\mathrm{d}p \end{aligned} \tag{3.36}$$

where ε at the denominator inside the integral is replaced by $\hbar\omega/2$ and $[\cdots]_{\theta=\theta_0}$ signifies that all θ terms in $[\cdots]$ are to be replaced by θ_0. Recovering the SI units, we obtain:

$$J_1^{(A)} = \frac{-e^2E}{6(\omega\hbar)^2hv_F}\int\frac{[\cdots]_{\theta=\theta_0}}{p^2\sqrt{1-X^2(p)}}\mathrm{d}p \tag{3.37}$$

We now determine the p-integration limit, which is determined by θ_0. From Eq. (3.32) we see that $X(p)$ can only take the values of $[-1, 1]$. Outside this range, θ_0 will be imaginary. Hence, p-integration limits can be obtained from:

$$-1 \leq X(p) \leq 1 \tag{3.38}$$

which can be solved to give four end points

$$p_{l(u)} = \frac{(-)\beta + \sqrt{\beta^2 + 2\alpha\hbar\omega}}{2\alpha} \tag{3.39}$$

$$p'_{l(u)} = \frac{\beta - (+)\sqrt{\beta^2 - 2\alpha\hbar\omega}}{2\alpha} \tag{3.40}$$

The region $p_l \leftrightarrow p'_l$ represents the the first integrable region in the momentum space while $p'_u \leftrightarrow p_u$ represents the second integrable region. This splits the linear optical current density into two parts:

$$J_1^{(A)} = \int_{p_l \leftrightarrow p'_l} [\cdots] \mathrm{d}p\mathrm{d}\theta + \int_{p'_u \leftrightarrow p_u} [\cdots] \mathrm{d}p\mathrm{d}\theta \tag{3.41}$$

Note that the limit $p'_{l(u)}$ exists only when $\hbar\omega < \beta^2/2\alpha$. Beyond this condition, Eq. (3.40) becomes imaginary, and the p-integration runs continuously from $p_l \rightarrow p_u$. Physically, the integration limit in Eq. (3.40) corresponds to the separated Dirac pockets in the the low energy regime of the BLG energy band structure with trigonal warping effect. The p-integration within $p_l \leftrightarrow p'_l$ corresponds to the optical response generated by the central Dirac pocket while that within $p'_u \leftrightarrow p_u$ corresponds to the optical current density generated by the satellite pockets. When $\hbar\omega$ is large, the optical transition occurs in high energy regime where the Dirac pockets merge into a single energy band and hence the optical current density is formed by the continuous integration through the limits of Eq. (3.39). This allows us to separate the low frequency optical response into the central Dirac pocket contribution and the satellite Dirac pockets contribution.

We now derive the second term of Eq. (3.21), i.e. $J_1^{(B)}$. The spinor components are given as:

$$a_1 b_0^* + b_1 a_0^* = \frac{eE}{2i\omega^2\hbar\varepsilon(\omega\hbar - 2\varepsilon)}[\varepsilon(\varepsilon - \omega\hbar)(X_- + X_+) + (X_- Y_+^2 + X_+ Y_-^2)] \tag{3.42}$$

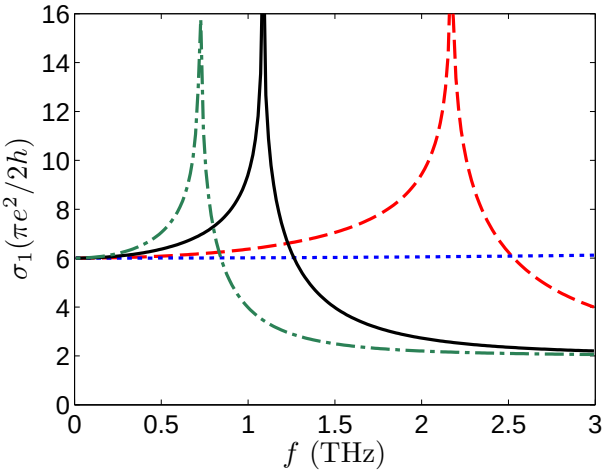

Figure 3.1: Frequency dependence of the linear optical conductivity at different interlayer coupling strength. Dotted curve: 0.1α, dashed curve: 0.5α, solid curve: α, dash-dotted curve: 1.5α, where $\alpha = 1/2m^*$ and $m^* = 0.33m_e$ [70]. The low frequency conductivity always approach $6\sigma_0$ regardless the strength of the interlayer coupling.

Following similar algebraic manipulation we performed for $J^{(A)}$, we obtain:

$$J_1^{(B)} = \frac{e^2 E m^*}{6(\hbar\omega)^2 h} \int \frac{[\cdots]^*_{\theta=\theta_0}}{p^2\sqrt{1-X^2(p)}} \mathrm{d}p \tag{3.43}$$

where $[\cdots]'_{\theta=\theta_0}$ represents the following terms

$$[\cdots]'_{\theta=\theta_0} = [\varepsilon(\hbar\omega-\varepsilon)(X_- p_+ + X_+ p_-) + (X_- Y_+^2 p_- + X_+ Y_-^2 p_+)]_{\theta=\theta_0} \tag{3.44}$$

We remark that the component in Eq. (3.21) is a seemingly anomalous term since it does not contain any photon. However, this term is eventually canceled out by the same term of opposite sign in K' valley and hence will not contribute to the final optical current density. Finally, the full linear optical current *conductivity* is

$$\sigma_1 = \frac{J_1}{E} = \frac{-e^2}{6(\omega\hbar)^2 h v_F} \int \frac{[\cdots]_{\theta=\theta_0}}{p^2\sqrt{1-X^2(p)}} \mathrm{d}p + \frac{e^2 m^*}{6(\omega\hbar)^2 h} \int \frac{[\cdots]'_{\theta=\theta_0}}{p^2\sqrt{1-X^2(p)}} \mathrm{d}p \tag{3.45}$$

where the p-integration limit is determined by Eq. (3.39) and Eq. (3.40). The frequency dependence of the linear optical conductivity is plotted in Fig. 3.1. There is a conductivity peak corresponding to the singularity in the density of states when

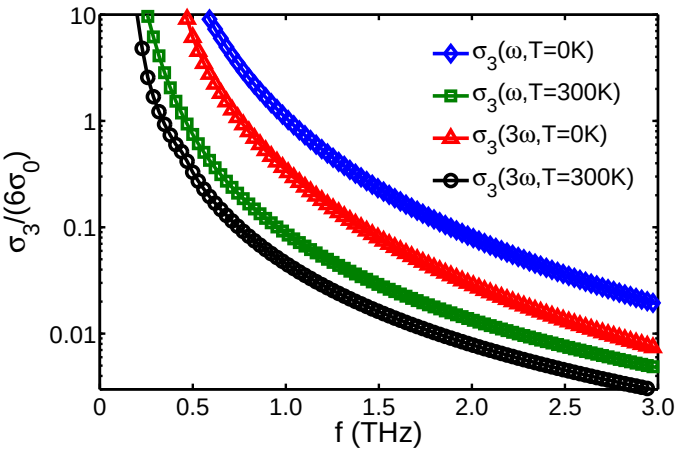

Figure 3.2: Frequency dependence of the third-order nonlinear optical conductivities at zero and room temperatures. The electric field strength is 1000 V/cm.

the low energy Dirac pockets joint together [72]. Furthermore, it can be seen that in the limit of $\omega \to 0$, the conductivity approaches $6\sigma_0$ where $\sigma_0 = \pi e^2/2h = e^2/4\hbar$. This is in agreement with the linear response result obtained from the Kubo formula [19]. Several values of the interlayer coupling strength α is chosen, and the low frequency conductivity is always $6\sigma_0$. As suggested by Cserti et al, the universal minimum conductivity of $6\sigma_0$ regardless the interlayer coupling strength is of topological origin [19].

3.1.4 Nonlinear optical response

The nonlinear optical response is numerically evaluated. In Fig. 3.2 we plot the nonlinear conductance versus frequency in unit of $6\sigma_0$ for two different temperatures. The electric field is 1000 V/cm. All nonlinear terms decrease rapidly with frequency. This is expected as linear response dominates at high frequencies in almost all systems. For BLG, the nonlinear response at single frequency is about five times stronger than frequency tripled terms.

Fig. 3.3 shows the temperature dependent nonlinear conductance at a field of 600 V/cm and at a frequency of 1 THz. At low temperature, the nonlinear conductance exceeds the linear conductance. The $\sigma_3(\omega)$ is greater than the linear conductance in the whole temperature regime. The all important $\sigma_3(3\omega)$ stays as the same as the

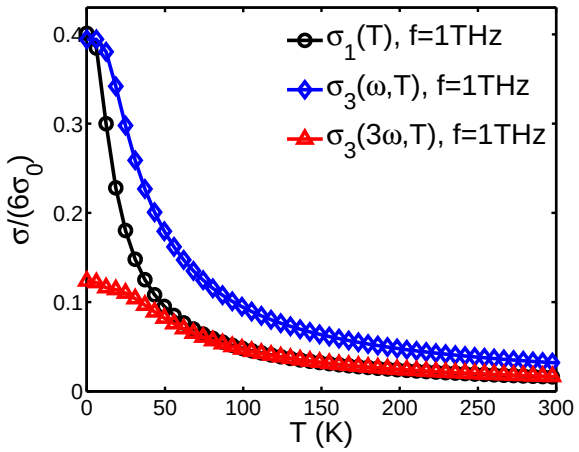

Figure 3.3: Linear and nonlinaer conductances vs. temperature for frequency of 1 THz. The electric field is 600 V/cm

linear conductance even at room temperatures. In comparison with the intraband nonlinear optical response of SLG, it is immediately obvious that the interband nonlinear optical response of BLG exhibits a contrasting temperature dependence. The intraband nonlinear optical current density of SLG grows with temperature (Fig. 2.5) while that of the BLG decreases with temperature.

The quantity that characterizes nonlinearity of an electronic material is the field required for the nonlinear current to equal the linear current. We refer this field to be the critical field E_c. In the present case, there are two critical fields, $E_c(\omega)$ and $E_c(3\omega)$. Fig. 3.4 shows the frequency dependence of the critical fields at zero and room temperature. Within the frequency range 0-3 THz the critical fields are well within the field strength achievable in a laboratory. At $f = 1$ THz, $E_c(\omega) = 1100$ V/cm at zero temperature and 800 V/cm at room temperature, and $E_c(3\omega) = 4700$ V/cm at zero temperature and 3000 V/cm at room temperature. This is comparable to the nonlinear effect in single layer graphene [89]. This result suggests that interlayer coupling and doubling the carrier numbers in BLG do not reduce the nonlinear effect. If this trend is maintained up to a few layers, the potential for developing graphene-based nonlinear devices can be significantly expanded. The small cusp at low frequency is due to a singularity in the density of states [72], which gives rise to a large value of linear current.

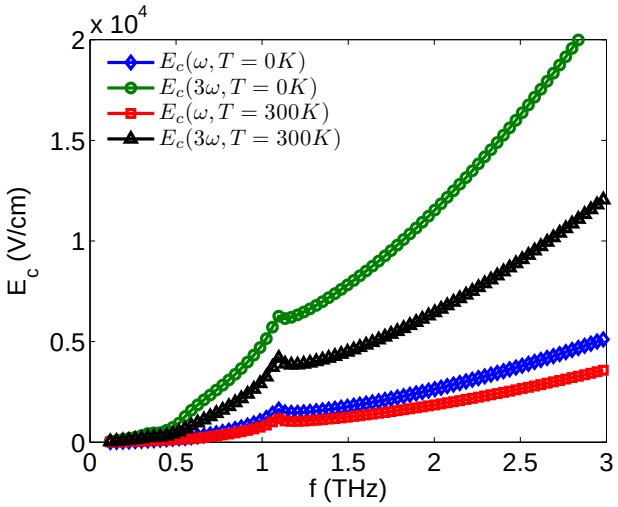

Figure 3.4: Frequency dependent critical fields at zero and room temperatures.

In Fig. 3.5, we present the temperature dependence of the critical field. The rapid decrease in the critical field at low temperature is mainly due to the decrease in linear current. The sole contribution to the linear current is the direct transition from the valence band to the conduction band via one photon absorption. As temperature increases, the bottom part of the conduction band and the top part of the valence band are thermally occupied. This reduces the carriers available for the optical transition and thus reduces the linear current. Three photon processes are less affected by thermal effect at low temperatures due to the availability of the intermediate states.

To obtain further insight on the nonlinear effect in BGL, we estimate the contribution to the nonlinear current from regions around different Dirac points. The reason that BLG exhibits a strong nonlinear effect at low energy is due to a unique property of BLG, i.e., the trigonal warping. At low frequencies, the contribution to the total nonlinear current from the central Dirac points and the three satellite Dirac points can be separated by breaking the integration limits into two parts via Eq. (3.39) and Eq. (3.39) (as discussed in the paragraph immediately after Eq. (3.41)). We found that for both $\sigma_3(\omega)$ and $\sigma_3(3\omega)$, the contribution from the central Dirac point is less than 10% while each satellite Dirac point contributes around 30% of the total nonlinear current. This is a clear indication on the connection between the trigonal warping and nonlinear optical processes in BLG since the existence of the satellite Dirac point is a unique signature of the low energy trigonal warping effect.

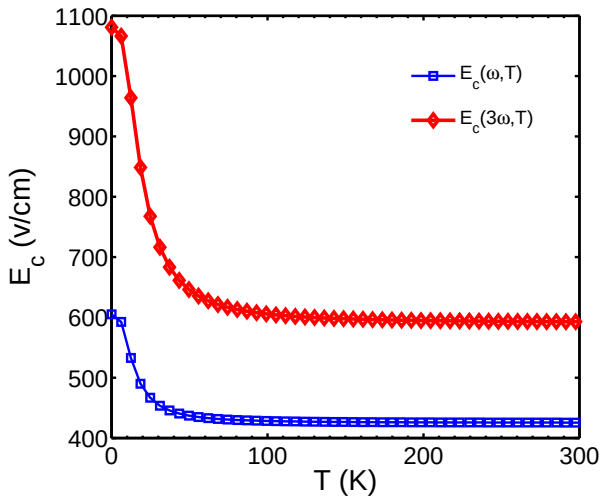

Figure 3.5: Temperature dependent critical fields for frequency of 1 THz.

3.1.5 Discussion

The results of this Chapter demonstrate that BLG is a rather strong nonlinear material. This nonlinear effect is robust from low to room temperatures. The frequency tripling nonlinear term is comparable to the linear term in the terahertz frequency regime. This term's relative strength suggests that BLG has a potential in a terahertz emitter/detector at frequencies, which are traditionally difficult to obtain by using an existing emitter at one-third the frequency.

The nonlinear optical response of BLG can be severely altered if electron-phonon coupling is strong at room temperature. It is, therefore, constructive to provide a brief discussion on the role of phonon excitation in BLG. In the temperature range of up to room temperature, the dominant electron-phonon coupling is via longitudinal acoustic (LA) phonons since either the couplings to other graphene lattice phonon modes are too weak or the energy scales of these optical phonon modes are far too high [114] The velocity of the LA phonon is around 2×10^4 m/s [114]. Under an electric field around 1000 V/cm with a frequency of 1 THz, the energy of the photoexcited electron is around 1 THz. These electrons are located very close to the Dirac point, and the electron velocity is around 0.6×10^6 m/ s. In the absence of other disorders and due to the energy conversation, the probability of single phonon emission is negligible. The multiple phonon excitation is possible but the probability is also very

low due to the high order electron-phonon coupling. Therefore we do not expect that phonon excitation will play a significant role in altering the nonlinear electrical current in this energy regime.

In conclusion, we have shown that BLG exhibits a strong nonlinear effect in the terahertz to far-infrared regime under an electric field of around 10^3 V/cm. In particular, a moderate field can induce the frequency tripling term at room temperature. This suggests a potential for developing graphene-based optics and photonics applications.

3.2 Nonlinear optical response in 2D semiconductor with Rashba spin-orbit interaction

The BLG Hamiltonian, Eq. (3.1) contains a p-quadratic and a p-linear term. We now consider the case of a two-dimensional semiconductor with Rashba spin-orbit interaction (R2DEG) whose Hamiltonian has a similar structure as BLG except that the p-quadratic term is in the diagonal position. It is the aim of this Section to study how the optical response of this system differs from that of the SLG. The interband optical responses occurs via the electronic transition between the two spin-split subbands. We obsever the occurrence of multiple sharp edges in the nonlinear conductivity frequency spectrum, which correspond to the cut-off effect produced by the multiple-photon processes. Furthermore, the free electron term H_0 raises the optical nonlinearity at room temperature. This aspect is not found in the nonlinear optical response of a purely linear system such as graphene.

3.2.1 Recursion equations of R2DEG in an external electric field

We apply the same strategy to derive recursion equations and hence the optical response under an external field. We consider a two-dimensionally confined electron gas in x-y plane with RSOI (such as asymmetrically confined electron gas in InAs

quantum well [115, 116] or surface states of metals, semiconductor and surface alloys [117–119]). We consider the case where electrons occupy only the $s = -1$ band with Fermi level situated at the band-crossing point at $T = 0$ K(i.e. Fermi level $\varepsilon_F = 0$). The Hamiltonian is a combination of a parabolic free electron term H_0 and a linear Rashba term H_R:

$$\begin{aligned} \mathcal{H}(p) &= H_0(p) + H_R(p) \\ &= \alpha \begin{bmatrix} p_x^2 + p_y^2 & 0 \\ 0 & p_x^2 + p_y^2 \end{bmatrix} + v_R \begin{bmatrix} 0 & p_y + ip_x \\ p_y - ip_x & 0 \end{bmatrix}, \end{aligned} \tag{3.46}$$

where $\alpha = 1/2m^*$ and $v_R = \lambda_R/\hbar$. m^* and λ_R are the free electron effective mass and Rashba coupling parameter respectively. α and v_R are related to the Rashba splitting energy via $E_R = v_R^2/4\alpha$. p_x and p_y denotes the x-and y-directional momentum component respectively. Note that Eq. (3.46) is similar to that of the bilayer graphene (BLG) in Eq. (3.1) with low energy trigonal warping, except that in R2DG the parabolic term is diagonal while in BLG the parabolic term is off-diagonal [70, 72]. The eigenvalue is given as

$$\varepsilon_s = \alpha p^2 + s v_R p, \tag{3.47}$$

where $s = \pm 1$ distinguishes the two chiral subband. The band structure is shown in Fig. 3.6(a). The eigenfunction is

$$\xi_0(p) = \frac{1}{\sqrt{2}} \begin{bmatrix} sp_+/p \\ 1 \end{bmatrix}, \tag{3.48}$$

where $p_\pm = p_y \pm ip_x$ and $p = (p_x^2 + p_y^2)^{1/2}$. We consider an external electric field in the form of $\mathbf{E} = \hat{x}Ee^{i\omega t}$ along the x-direction. The vector potential is given as $\mathbf{A} = \mathbf{E}/i\omega$. We can minimally couple the electron to the photon via $p_x \to p_x + eA$. This gives $\mathcal{H}' = \mathcal{H}(p_x \to p_x + eA)$. The eigenfunction is:

$$\Psi(p) = \sum_{n=0}^{\infty} e^{i(n\omega - \varepsilon_+/\hbar)t} \psi_n(p), \tag{3.49}$$

where $\psi_n(p) = (a_n(p), b_n(p))^T$ is the n-photon spinor components, representing the n-photon coupling to electron. By solving the Schr oedinger equation $i\hbar\partial\Psi(p)/\partial t = \mathcal{H}'\Psi(p)$, we obtain a set of recursive equations connecting nth-order spinor components with $(n-1)$th order spinor components

$$\begin{aligned} a_n &= \frac{1}{n\hbar\omega(n\hbar\omega - 2v_R p)} \left\{ -\mathcal{F}\left[2i\alpha\left(v_R p - n\hbar\omega\right)p_x + v_R^2 p_+\right] a_{n-1} \right. \\ &+ \left. v_R\mathcal{F}\left[\left(v_R p - n\hbar\omega\right) - 2i\alpha p_x p_+\right] b_{n-1} - \alpha\mathcal{F}^2\left(v_R p - n\hbar\omega\right) a_{n-2} - \alpha v_R\mathcal{F}^2 p_+ b_{n-2} \right\} \end{aligned} \tag{3.50}$$

$$\begin{aligned} b_n &= \frac{1}{n\hbar\omega(n\hbar\omega - 2v_R p)} \left\{ -\mathcal{F}\left[2i\alpha\left(v_R p - n\hbar\omega\right)p_x - v_R^2 p_-\right] b_{n-1} \right. \\ &- \left. v_R\mathcal{F}\left[\left(v_R p - n\hbar\omega\right) + 2i\alpha p_x p_-\right] a_{n-1} - \alpha\mathcal{F}^2\left(v_R p - n\hbar\omega\right) b_{n-2} - \alpha v_R\mathcal{F}^2 p_- a_{n-2} \right\} \end{aligned} \tag{3.51}$$

where $\mathcal{F} = eE/\omega$. By recursively applying Eq. (3.50) and Eq. (3.50), we can construct spinor components to any order in electron-photon coupling. For $n = 0$, the zero-order spinor components are found to be $a_0 = p_+/\sqrt{2}p$ and $b_0 = 1/\sqrt{2}$, respectively, which is in agreement with the single electron eigenfunction Eq. (3.48). For $n = 1$, we obtain:

$$a_1 = \frac{\mathcal{F}}{\sqrt{2}\hbar\omega(\hbar\omega - 2v_R p)} \left\{ -2i\alpha\left(v_R p - \hbar\omega\right)\frac{p_+}{p} + v_R\left[\left(v_R p - \hbar\omega\right) - 2i\alpha p_x p_+\right] \right\}, \tag{3.52}$$

$$b_1 = \frac{\mathcal{F}}{\sqrt{2}\hbar\omega(\hbar\omega - 2v_R p)} \left\{ -2i\alpha\left(v_R p - \hbar\omega\right) - v_R\left[\left(v_R p - \hbar\omega\right)\frac{p_+}{p} + +2i\alpha p_x p\right] \right\}, \tag{3.53}$$

where $\omega = \omega - i0$. The velocity operator $\hat{v}_x = \partial\mathcal{H}(p_x + eA)/\partial p_x$ is given as

$$\hat{v}_x = \begin{bmatrix} 2\alpha(p_x + eA) & iv_R \\ -iv_R & 2\alpha(p_x + eA) \end{bmatrix}. \tag{3.54}$$

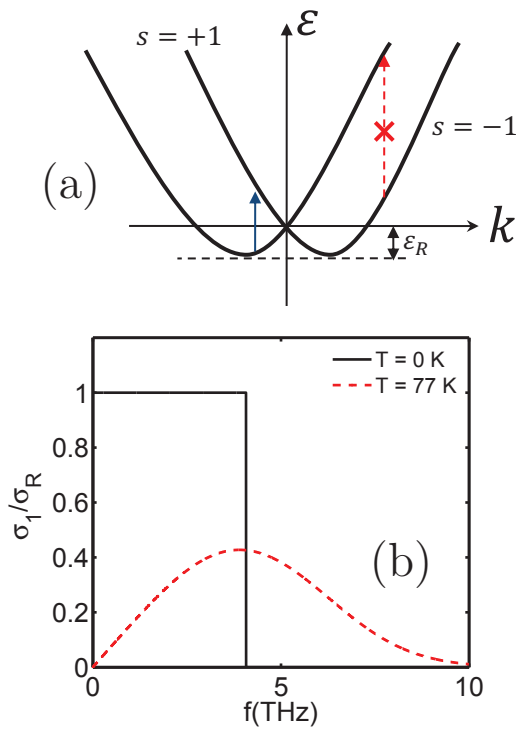

Figure 3.6: (a) Band structure of R2DG. The Fermi energy is at $\varepsilon_F = 0$. The red (dashed) arrow denote forbidden interband transition. The blue (solid) arrow denote permissible interband transition; (b) Linear conductivity. Rashba energy of $E_R = 2.1$ meV is used. The conductivity is normalized by $\sigma_R = e^2/8\hbar$.

From Eq. (3.19) and Eq. (3.20), the linear and nonlinear optical conductivities can be obtained.

3.2.2 Linear optical conductivity

Following the same strategy outlined in previous section, we derive the linear optical conductivity as:

$$\sigma_1(\omega) = \frac{e^2}{8\hbar}\mathcal{N}(\hbar\omega/2) \tag{3.55}$$

which is consistent with the results calculated using Kubo formalism [120]. The temperature dependence is encoded in:

$$\mathcal{N}(x) = \frac{1}{e^{\frac{\alpha p^2 - x}{k_B T}} + 1} - \frac{1}{e^{\frac{\alpha p^2 + x}{k_B T}} + 1} \tag{3.56}$$

The linear conductivity is shown in Fig. 3.6. At $T = 0$ K, the linear conductivity is a square function of incident photon frequency. The linear conductivity becomes

zero when a maximum frequency $\hbar f_{max} = 4v_R^2/\alpha = 8E_R$ is exceeded. This happens because the energy spacing between $s = +1$ and $s = -1$ subbands is insufficient to accommodate high frequency optical transition of the electron [see Fig. 3.6(a)]. For $E_R = 2.1$ meV, $f_{max} \approx 4$ THz. At $T = 77$ K, states in $s = -1$ subband with energy $E > 0$ are thermally populated and also contributes to the linear conductivity. These results in the smearing of the linear conductivity up to about $f = 10$ THz.

3.2.3 Third-order nonlinear optical conductivity

The single-frequency and triple-frequency third-order nonlinear optical conductivities are given, respectively, as

$$\sigma_3(\omega) = \sigma_R \frac{e^2E^2}{\hbar\omega^3}\left[\frac{v_R^2}{\hbar\omega}(2+x)\mathcal{N}(\hbar\omega) + \frac{\alpha}{8}\mathcal{N}\left(\frac{\hbar\omega}{2}\right)\right] \tag{3.57}$$

$$\sigma_3(3\omega) = \sigma_R \frac{e^2E^2}{\hbar\omega^3}\left[\frac{v_R^2}{\hbar\omega}(g_1+g_2+g_3) + \alpha(g_4+g_5)\right] \tag{3.58}$$

where $\sigma_R = e^2/8\hbar$ and

$$\begin{aligned} x &= \frac{\hbar\omega}{4E_R} \\ g_1 &= \left(\frac{13}{48} + \frac{x}{8} + \frac{x^2}{2}\right)\mathcal{N}\left(\frac{\hbar\omega}{2}\right) \\ g_2 &= \left(-\frac{2}{3} + 2x\right)\mathcal{N}(\hbar\omega) \\ g_3 &= \frac{15}{16}\mathcal{N}\left(\frac{3\hbar\omega}{2}\right) \\ g_4 &= -\frac{1}{3}\mathcal{N}\left(\frac{\hbar\omega}{2}\right) \\ g_5 &= \left(\frac{1}{6} + x\right)\mathcal{N}\left(\frac{3\hbar\omega}{2}\right) \end{aligned} \tag{3.59}$$

The frequency dependence of the third-order nonlinear conductivities is shown in Fig. 3.7. We have chosen a moderate Rashba splitting energy of $E_R = 2.1$ meV

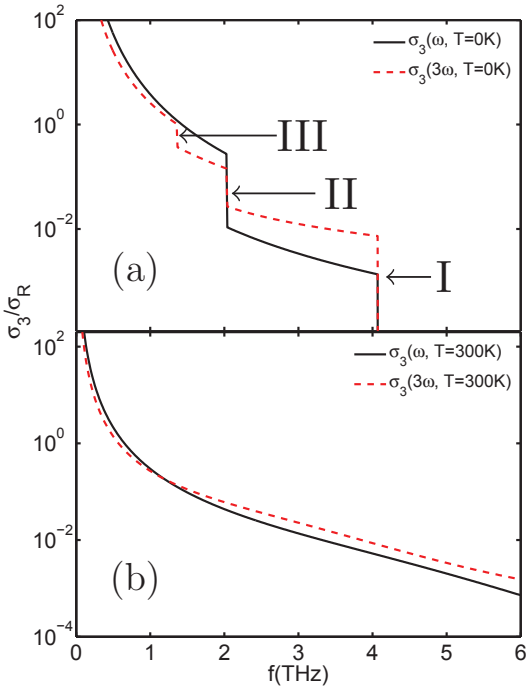

Figure 3.7: Third order nonlinear optical conductivities $\sigma(\omega)$ (solid curve) and $\sigma(3\omega)$ (dashed curve) at $E = 1000$ V/cm. (a) $T = 0$ K, the sharp edges marks the cut-off of 1-photon edge (I), 2-photon edge (II) and 3-photon edge (III); (b) $T = 300K$.

and 'Rashba velocity' of $v_R = 5.026 \times 10^4$ m/s [117]. At $T = 0$ K three step-like edges are clearly observable for both $\sigma(\omega)$ and $\sigma(3\omega)$. These steps are related to the existence of three distinct Dirac delta functions $\delta(n\hbar\omega - 2v_R p)$ with $n = 1, 2, 3$ when evaluating the optical current density integration. The separation between $s = +1$ and $s = -1$ subbands at a fixed $\hbar\omega$ is $\Delta = \varepsilon_+ - \varepsilon_- = 2v_R p$. The delta functions therefore physically represents the cut-off of an optical process when electron absorb n-photon to transit from $s = -1$ to $s = +1$ subband is no longer possible. At low temperature, electrons are mostly residing in $s = -1$ subband. Since the maximum permissible frequency-width for interband transition is $hf_{max} = 8\varepsilon_R$, $\delta(n\hbar\omega - 2v_R p)$ truncates any n-photon process at ω_{max}/n, giving rise to a 'n-photon edge' in Fig. 3.7(a). Albeit the similarity of graphene Dirac Hamiltonian and H_R, such truncation does not occur in graphene because in graphene the $s = -1$ subband does not 'bend-up' in k-space. There is no f_{max} and hence the permissible frequency for optical absorption can increases as far as the linear Dirac-cone approximation still holds. The $T = 300$ K nonlinear conductivities are plotted in Fig. 3.7(b). The thermal

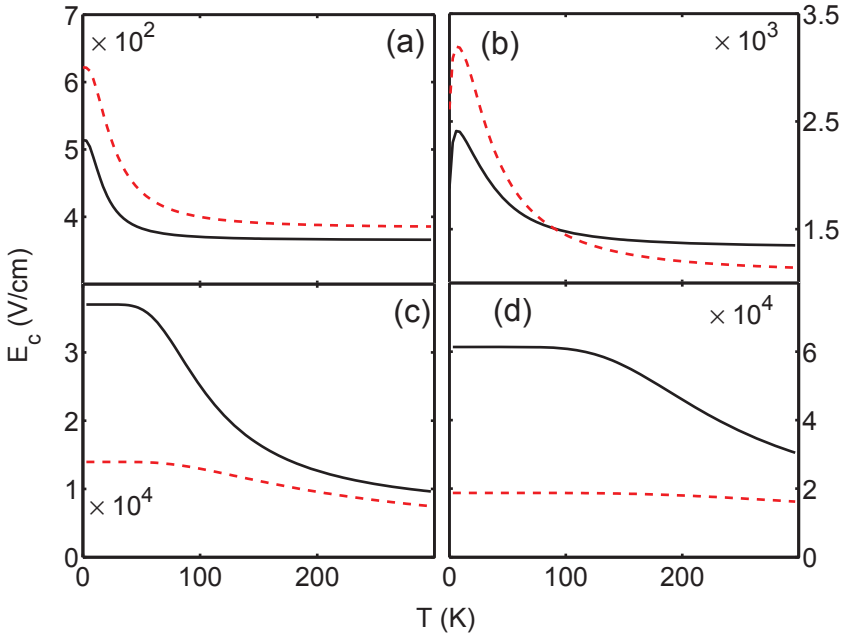

Figure 3.8: Temperature dependence of critical electric field strength $E_c(\omega)$ (solid curve) and $E_c(3\omega)$ (dashed curve) at various frequency: (a) 1 THz, (b) 2 THz, (c) 5 THz, and (d) 7 THz. The low temperature nonlinear conductivities are mainly contributed by 1-photon edge. At higher temperature, the smearing of 2-photon and 3-photon edges enhances the NOR, resulting in gradually decreasing critical field strength.

excitation of electrons to higher lying states washes out the n-photon edges. At low frequency, the nonlinear response is initially large but decreases with temperature since low lying conducting states are thermally depopulated. At higher frequency, the nonlinear response however behaves in a contrasting way: it is initially small and increases with temperature. This is because the $s = -1$ electrons are thermally excited to states with higher energy and are capable of performing large-frequency interband transition. The optical response of R2DG is hence sensitively influenced by temperature. At approximately $f > 1$ THz, the $\sigma_3(3\omega) > \sigma_3(\omega)$.

The temperature dependence of the single-frequency $E_c(\omega)$ and triple-frequency $E_c(3\omega)$ is shown in Fig. 3.8. At low frequency ($f = 1$ THz), E_c decreases with increasing temperature since σ_1 decreases very rapidly as a result of its stronger temperature dependence in comparison with the nonlinear terms [Fig. 3.8(a)]. At $f = 2$ [Fig. 3.8(b)] THz, a sharp E_c-peak at low temperature regime can be seen. This happens because $f = 2$ THz is situated at the vicinity of the 2-photon edge. Thermal smearing of the 2-photon edge decreases the nonlinear optical response,

resulting in an initial rapid rise of E_c. As the temperature is further increased, the thermal smearing of the 3-photon edge replenishes the nonlinear response and this reduces the E_c, resulting in a E_c peak structure. At higher frequency [$f = 5$ THz in Fig. 3.8(c) and $f = 7$ THz in Fig. 3.8(d)], the E_c behaves rather differently. A low-temperature plateau regime occurs before the gradual decrease of E_c. This can be explained by the fact that when $f > f_{max}$ (which is about 4 THz in this case), the low temperature nonlinear conductivities are mainly contributed by the smearing of the 1-photon edge, which, coincidentally, has the same $\mathcal{N}(\hbar\omega/2)$ temperature dependence as the $\sigma_1(\omega)$. The temperature dependence of E_c, which is the ratio of linear and nonlinear term, is therefore a constant. As temperature increases, the smearing of 2-photon and 3-photon edges extend towards the higher frequencies. This enhances the nonlinear response, resulting in the gradual decrease of E_c. Interestingly, for $f < 5$ THz, both $E_c(\omega)$ and $E_c(3\omega)$ show very little variation as $T > 150$ K. Therefore, in few THz regime, the optical nonlinearity of R2DEG is very stable against temperature variation.

3.2.4 Effects of v_R and m^* on R2DG Nonlinear Optical Response

We now investigate the effects of RSOI coupling parameter λ_R and electron effective mass m^* on the optical response of R2DEG. λ_R and m^* represents the relative weighting of parabolic 'free' electron term H_0 and linear H_R term in the R2DG Hamiltonian Eq. (3.46). Varying λ_Rm (or equivalently v_R) and m^* is essentially equivalent to the tuning of R2DEG into a non-relativistic, 'free' electron-like system (when H_0 dominates) or into a relativistic, massless Dirac fermion-like system (when H_R dominates). The v_R of the nonlinear conductivities are plotted for $T = 0$ K in Fig. 3.9(a) and for $T = 300$ K for Fig. 3.9(b) (with $f = 1$ THz, $E = 1000$ V/cm and the effective mass is $m^* = 0.05m_e$). As $v_R \to 0$ (i.e. RSOI is completely absent), the nonlinear responses are completely removed as we expect. At $T = 0$ K, we again see the n-photon edges. Since $\omega_{max} \propto v_R$, v_R has to be sufficiently large in order to produce subband-splitting

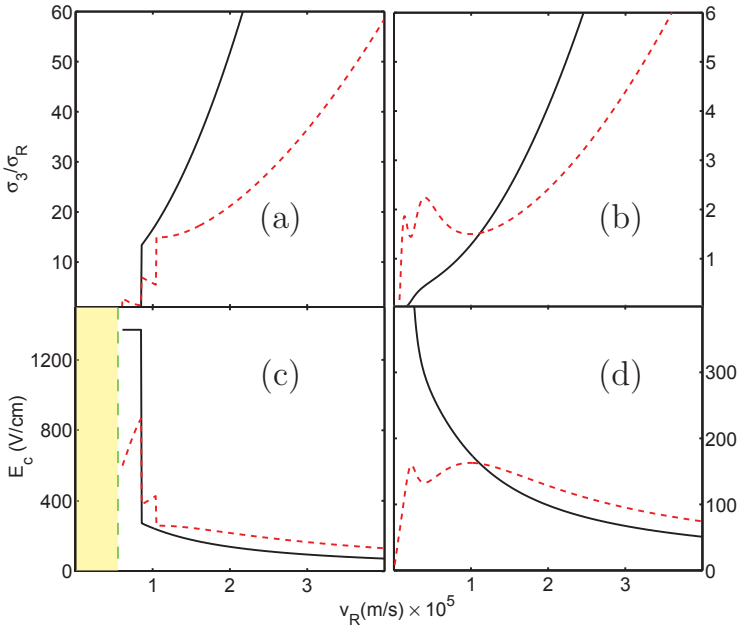

Figure 3.9: v_R-dependence of the nonlinear conductivities, $\sigma_3(\omega)$ (solid curve) and $\sigma_3(3\omega)$ (dashed curve), at: (a) $T = 0$ K; (b) $T = 300$ K with $E = 1000$ V/cm. v_R-dependence of the critical electric fields, $E_c(\omega)$ (solid curve) and $E_c(3\omega)$ (dashed curve), at: (c) $T = 0$ K; and (d) $T = 300$ K. The frequency is set to 1 THz and effective mass $m^* = 0.05m_e$. The shaded region in the (a) and (c) denotes the regime when the Rashba splitting is too small to accommodate the optical transition of electrons.

of adequate frequency-width to accommodate the electronic transition from $s = -1$ to $s = +1$ subband. The first edge corresponds to the onset of single-photon process. Multiple-photon processes become possible as v_R increases, creating the subsequent 2-and 3-photon edges. At $T = 300$ K, the edges are thermally washed out. The smeared edges shifts towards smaller v_R since thermally excited electrons allows the onset of the photon-edges at smaller v_R. The v_R dependence of E_c at $T = 0$ K and $T = 300$ K are plotted in Fig. 3.9(c) and Fig. 3.9(d), respectively. Note that E_c is undefined in the yellow-shaded region Fig. 3.9 since both linear and nonlinear responses are zero at small v_R. We found that the critical electric field E_c can be reduced by large v_R, i.e. strong RSOI strength.

Unlike v_R which is externally tunable, the effective electron mass m^* is an intrinsic properties of the crystal structure and cannot be tuned externally. However, it is still constructive to study the m^* dependency in order to understand the nonlinear behavior of R2DEG. Although the velocity operator Eq. 3.54 is independent of m^*,

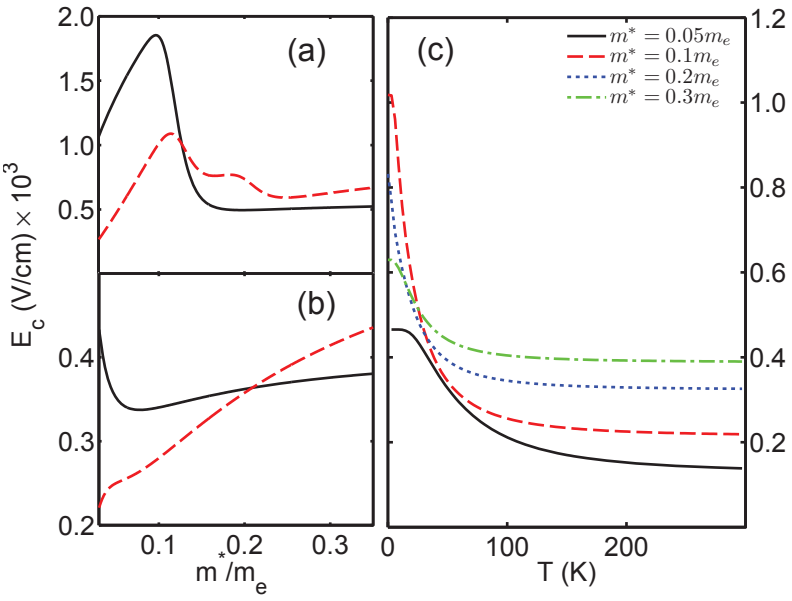

Figure 3.10: m^* dependence of the critical electric field strengths, $E_c(\omega)$ (solid curve) and $E_c(3\omega)$ (dashed curve), of the frequency tripling term at 1 THz: (a) $T = 4$ K and (b) $T = 15$ K ($v_R = 5 \times 10^4$ m/s). (c) Temperature dependence of $E_c(3\omega)$ at various values of m^*. At low temperature, $E_c(3\omega)$ is a complicated function of m^* but is, in general, smaller for larger m^* (except $m^* = 0.05m_e$) due to the photon-edges. At high temperature regime, $E_c(3\omega)$ is smaller for small m^*. The parabolic term H_0 is therefore an important component in achieving strong optical nonlinearity at elevated temperature.

the spinor components Eq. (3.50) and Eq. (3.50) are influenced by m^*. The effective mass therefore play a role in the nonlinear optical response of R2DG albeit the fact that the subband spin-splitting is chiefly a consequence of the RSOI. In Fig. 3.10(a) and 3.10(b), the m^* dependence of E_c is plotted for m^*/m ranging from 0.03 to 0.35 at $T = 4$ K and $T = 15$ K, respectively. Since $hf_{max} = 4m^*v_F^2$, the photon-edges also occurs in the m^* dependence plot when m^* is just right for the onset of n-photon process (i.e. when f_{max} is a multiple of the incoming photon's frequency). However, at $T = 15$ K [Fig. 3.10(b)], the edges are almost completely removed by thermal excitation. In Fig. 3.10(c), we plot the temperature dependence of $E_c(3\omega)$ at various m^* values. In general, $E_c(3\omega)$ decreases rapidly at higher temperature. Since $H_0 \propto 1/2m^*$, the result suggests that large H_0 significantly raises the optical nonlinearity.

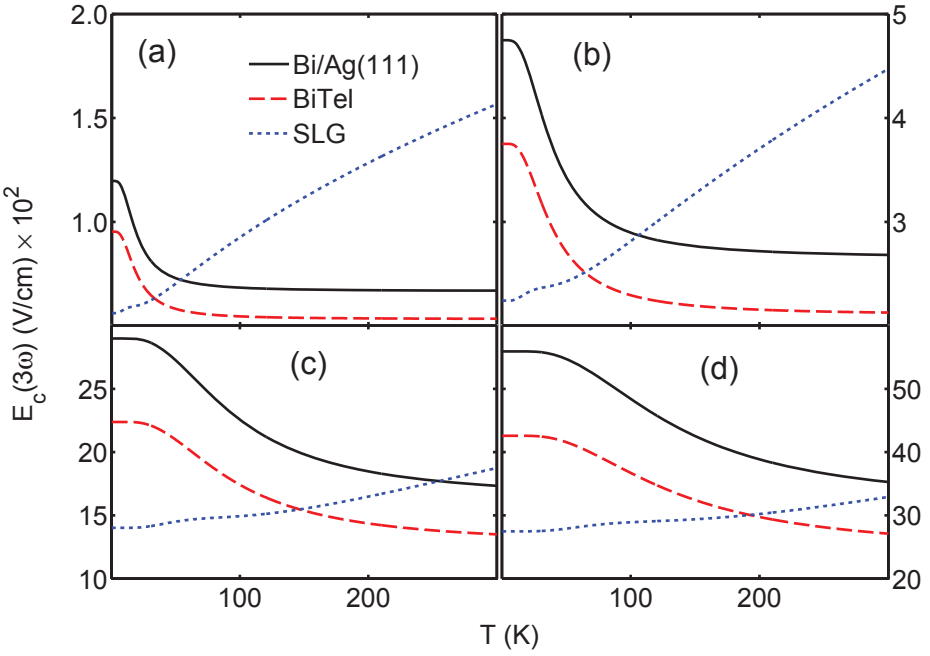

Figure 3.11: (Color online) Comparison between $E_c(3\omega)$ of graphene [89] and R2DG in BiTeI layered semiconductor and Bi/Ag(111) surface alloys: (a) 1 THz; (b) 2 THz; (c) 5 THz; and (d) 7 THz. Although at low temperature regime single layer graphene (SLG) has stronger optical nonlinearity (lower E_c), this optical nonlinearity does not survive at higher temperature. In contrast, R2DG shows stronger optical nonlinearity at elevated temperature.

3.2.5 Discussion

Finally, we compare the nonlinear optical response of R2DG with that of a single layer graphene in Fig. 3.11. Experimentally, strong RSOI in the order of $v_R = 4.6\times10^5$ m/s and $v_R = 5.8 \times 10^5$ m/s are achieved in Bi/Ag(111) surface state and layered polar semiconductor BiTeI respectively [119, 121]. Using these realistic experimental values, we calculate the important triple-frequency term $E_c(3\omega)$ of these R2DEG systems and comparison with graphene is made. For R2DEG, $E_c(3\omega)$ decreases as $T \to 300$ K. In contrast, $E_c(3\omega)$ of graphene increases with increasing temperature [89]. At room temperature, and assuming that the RSOI is preserved, the optical nonlinearity of R2DEG can be 3 times stronger than graphene at 1 THz. The temperature enhanced optical nonlinearity in R2DEG pinpoints a major difference between the optical nonlinearity of a electronic system with purely linear Hamiltonian and that of a system with mixed linear and parabolic terms in its Hamiltonian. Recently, the R2DG in Ir(111) surface covered by graphene single layer has found to be well-protected from

ambient atmosphere, and yet maintaining a strong RSOI in the order of $\lambda_R \approx 10^{-10}$ eVm [122]. This provides a potential platform to experimentally probe the nonlinear optical properties of R2DEG without the need of an ultra-vacuum environment. However, extra care has to be taken in separating out the nonlinear optical response from graphene since graphene is also a strongly nonlinear medium.

4 | Nonlinear optical response in graphene: bandgap opening and band anisotropy

* In this Chapter, we calculate the nonlinear optical spectrum of single layer graphene: (i) with a bandgap and (ii) with band anisotropy. We use semihydrogenated graphene (SHG) as a model to illustrate the nonlinear optical response of single layer graphene with a bandgap. We found that there exists a strong nonlinear optical response for energies lower than the bandgap where the linear response is forbidden. At low temperature, there exists two well separated linear response and nonlinear response peaks. This suggests that SHG can have a unique potential as a two-color nonlinear material in the terahertz frequency region where the relative intensity of the two colors can be tuned with the electric field. In a graphene superlattice structure of Kronig-Penney type periodic potential, the Dirac cone is elliptically deformed. We found that not only the optical nonlinearity is preserved in such a system, the total optical response is further enhanced by a factor proportional to the band anisotropy. This suggests that graphene superlattice is another potential candidate in terahertz device application.

*This Chapter is based on *Appl. Phys. Lett.* **98**, 042107 (2011) and *J. Phys. D: Appl. Phys.* **45**, 395303 (2012).

4.1 Subgap nonlinear conductivity in semihydrogenated graphene

We first investigate the optical response in semihydrogenated graphene (SHG) in terahertz frequency regime. In general, for systems with a finite gap, the linear response, or one photon process for frequency below the bandgap Δ, is forbidden. However, multiphoton processes can still occur for frequencies below the gap. The strength of such nonlinear response is usually very weak. We found that the opening of a band gap at the Dirac point leads to a very strong nonlinear response below the gap. In fact the low frequency nonlinear conductance can be as strong as the universal conductance in intrinsic graphene under a rather moderate electric field of the order of 10^3 V/cm. This result is particularly useful for developing applications in nonlinear optics and nonlinear photonics since the linear process is fully suppressed in this frequency regime. Furthermore, we found that the nonlinear optical response at the onset frequency of the nonlinear subgap conductivity peak is universally enhanced by a factor of $31/13 \approx 2.38$ regardless the value of Δ. This suggests that this enhancement is related to the topological changes in the energy band structure of Dirac quasiparticles when a bandgap is created.

4.1.1 Recursion equations and linear optical current density

The interband optical conductivity is calculated by recursively solving the n-photon coupled spinor components in the presence of an external electric field. We first construct the recursion equations for the n-photon coupled spinor components. In the tight-binding approximation, the Hamiltonian for SHG under a time-dependent electric field along the x-axis $Ee^{-i\omega t}$ can be written as

$$H = \begin{pmatrix} -\Delta/2 & v_0(p_- + eA) \\ v_0(p_+ + eA) & \Delta/2 \end{pmatrix} \tag{4.1}$$

where $p_\pm = p_x \pm ip_y$, and $A = \frac{E}{i\omega}e^{i\omega t}$. The on-site energies of the A-sublattice and B-sublattice are $-\Delta/2$ and $\Delta/2$, respectively. This creates a bandgap opening of Δ at the Dirac point. The quasiparticle is equivalent to a *massive* Dirac fermion in this case.

We now write the two-component wavefunction in terms of two spinor components $a_n(\mathbf{p})$, and $b_n(\mathbf{p})$:

$$\psi(\vec{p}) = \sum_{n=0}^{\infty} \begin{pmatrix} a_n(\vec{p}) \\ b_n(\vec{p}) \end{pmatrix} e^{i(n\omega - \varepsilon/\hbar)t} \tag{4.2}$$

The time derivatives of the wavefunction is

$$\frac{\partial \psi}{\partial t}(\vec{p}, n) = \sum_{n=0}^{\infty} i(n\omega - \varepsilon/\hbar) \begin{pmatrix} a_n(\vec{p}) \\ b_n(\vec{p}) \end{pmatrix} e^{i(n\omega - \varepsilon/\hbar)t} \tag{4.3}$$

The Schrodinger's equation can be solved as followed:

$$\begin{aligned} \sum_{n=0}^{\infty} (\varepsilon - n\omega\hbar) \begin{pmatrix} a_n(\vec{p}) \\ b_n(\vec{p}) \end{pmatrix} e^{i(n\omega - \varepsilon/\hbar)t} &= \sum_{n=0}^{\infty} \begin{pmatrix} -\Delta/2 & v_0(p_- + eA) \\ v_0(p_+ + eA) & \Delta/2 \end{pmatrix} \begin{pmatrix} a_n(\vec{p}) \\ b_n(\vec{p}) \end{pmatrix} e^{i(n\omega - \varepsilon/\hbar)t} \\ &= \sum_{n=0}^{\infty} \begin{pmatrix} \frac{-\Delta}{2} a_n + V_0 p_- b_n + \frac{eEv_0}{i\omega} b_{n-1} \\ \frac{\Delta}{2} b_n + v_0 a_n + \frac{eEv_0}{i\omega} a_{n-1} \end{pmatrix} e^{i(n\omega - \varepsilon/\hbar)t} \end{aligned} \tag{4.4}$$

This gives the coupled recursion equations:

$$\begin{aligned} \left(\varepsilon - n\hbar\omega + \frac{\Delta}{2}\right) a_n &= v_0 p_- b_n + \frac{eEv_0}{i\omega} b_{n-1} \\ \left(\varepsilon - n\hbar\omega - \frac{\Delta}{2}\right) b_n &= v_0 p_+ a_n + \frac{eEv_0}{i\omega} a_{n-1} \end{aligned} \tag{4.5}$$

For $n = 0$, there is no photon. The spinor components are coupled by the following equations

$$\begin{aligned} \varepsilon_+ a_0 &= v_0 p_- b_0 \\ \varepsilon_- b_0 &= v_0 p_+ a_0 \end{aligned} \tag{4.6}$$

where the for simplicity we denote $\varepsilon_\pm = (\varepsilon \pm \Delta/2)$. Solving the coupled equations, we obtain:

$$a_0 = \frac{v_0 p_-}{\varepsilon_+ \sqrt{2}} C(\varepsilon) \tag{4.7}$$

$$b_0 = \frac{C(\varepsilon)}{\sqrt{2}} \tag{4.8}$$

where $C(\varepsilon(s,p))$ is a normalization factor, which can be determined as followed:

$$|C(\varepsilon(s,p))|^2 \begin{pmatrix} a_0^* & b_0^* \end{pmatrix} \begin{pmatrix} a_0 \\ b_0 \end{pmatrix} = \frac{v_0^2 p^2}{2\varepsilon_+^2} + \frac{1}{2} = 1 \tag{4.9}$$

$$\begin{aligned} \frac{1}{|C(\varepsilon(s,p))|^2} &= \frac{v_0^2 p^2 + \varepsilon_+^2}{2\varepsilon_+^2} \\ C(\varepsilon(s,p)) &= \sqrt{\frac{2\varepsilon_+^2}{v_0^2 p^2 + \varepsilon_+^2}} \end{aligned} \tag{4.10}$$

and hence the normalized single electron eigenstate is:

$$\psi_s(p) = \sqrt{\frac{\varepsilon_+^2}{v_0 p^2 + \varepsilon_+^2}} \begin{bmatrix} \frac{v_0 p_-}{\varepsilon_+} \\ 1 \end{bmatrix} \tag{4.11}$$

which is consistent with the results in [123]. The energy dispersion is given as

$$\varepsilon(s,p) = s\sqrt{v_0^2 p^2 + \left(\frac{\Delta}{2}\right)^2} \tag{4.12}$$

In general, any n-th order process is coupled to $(n-1)$-th process by the following recursion formula:

$$n\omega\hbar(n\omega\hbar - 2\varepsilon)a_n = \frac{eEv_0}{i\omega}\left[\left(\varepsilon - n\omega\hbar - \frac{\Delta}{2}\right) b_{n-1} + v_0 p_- a_{n-1}\right] \tag{4.13}$$

$$n\omega\hbar(n\omega\hbar - 2\varepsilon)b_n = \frac{eEv_0}{i\omega}\left[\left(\varepsilon - n\omega\hbar + \frac{\Delta}{2}\right) a_{n-1} + v_0 p_+ b_{n-1}\right] \tag{4.14}$$

We now construct the $n = 1$ spinor components:

$$a_1 = \frac{eEv_0C(\varepsilon)}{\sqrt{2}i\omega^2\hbar(\omega\hbar - 2\varepsilon)\varepsilon_+}\left[\varepsilon_+\left(\varepsilon - \omega\hbar - \frac{\Delta}{2}\right) + v_0^2p_-^2\right] \tag{4.15}$$

$$b_1 = \frac{eEv_0C(\varepsilon)}{\sqrt{2}i\omega^2\hbar(\omega\hbar - 2\varepsilon)\varepsilon_+}\left[\left(\varepsilon - \omega\hbar + \frac{\Delta}{2}\right)v_0p_- + v_0p_+\varepsilon_+\right] \tag{4.16}$$

Any higher order spinor components can then be recursively constructed.

4.1.2 Linear optical response

As discussed in Chapter 3, optical current operator and current density can be constructed using Eq. (3.19) and (3.20). The velocity operator $\hat{v}$ is given by

$$\hat{v} = v_0\begin{pmatrix} 0 & 1 \\ 1 & 0 \end{pmatrix} \tag{4.17}$$

Therefore, from Eq. (3.19) and (3.20), the optical current operator is given as

$$\begin{aligned} j_1 &= -ev_0(a_1b_0^* + b_1a_0^*) \\ &= \frac{-e^2Ev_0^2}{2i\omega^2\hbar(\omega\hbar - 2\varepsilon)\varepsilon_+}\left[\varepsilon_+\left(\varepsilon - \omega\hbar - \frac{\Delta}{2}\right) + v_0^2p_-^2 + \frac{\left(\varepsilon - \omega\hbar + \frac{\Delta}{2}\right)}{\varepsilon_+}v_0^2p^2 + v_0^2p_+^2\right] \\ &= \frac{-e^2Ev_0^2}{2i\omega^2\hbar(\omega\hbar - 2\varepsilon)\varepsilon_+^2}\left[\varepsilon_+^2\left(\varepsilon - \omega\hbar - \frac{\Delta}{2}\right) + \left(\varepsilon - \omega\hbar + \frac{\Delta}{2}\right)v_0^2p^2 + \varepsilon_+v_0^2(p_-^2 + p_+^2)\right] \end{aligned} \tag{4.18}$$

where we have used the fact that the spinor-products are given by

$$a_1b_0^* = \frac{eEv_0}{2i\omega^2\hbar(\omega\hbar - 2\varepsilon)\varepsilon_+}\left[\varepsilon_+\left(\varepsilon - \omega\hbar - \frac{\Delta}{2}\right) + v_0^2p_-^2\right] \tag{4.19}$$

$$b_1a_0^* = \frac{eEv_0}{2i\omega^2\hbar(\omega\hbar - 2\varepsilon)\varepsilon_+}\left[\frac{\left(\varepsilon - \omega\hbar + \frac{\Delta}{2}\right)}{\varepsilon_+}v_0^2p^2 + v_0^2p_+^2\right] \tag{4.20}$$

Note that in Eq. (4.18) we have dropped the energy-dependent normalization factor C for simplicity. This term will be recovered in the end. The optical current density

is given by

$$\begin{aligned} J_1 &= \frac{-e^2 E v_0^2}{2\omega^2\hbar}\frac{1}{4\pi^2\hbar^2}\Re\left(\int p\mathrm{d}p\mathrm{d}\theta\frac{1}{i(\omega\hbar-2\varepsilon)\varepsilon_+^2}\right. \\ &\quad \left.\times\left[\varepsilon_+^2\left(\varepsilon-\omega\hbar-\frac{\Delta}{2}\right)+\left(\varepsilon-\omega\hbar+\frac{\Delta}{2}\right)v_0^2p^2+\varepsilon_+v_0^2(p_-^2+p_+^2)\right]\right) \\ &= \frac{-e^2 E v_0^2}{8\pi\omega^2\hbar^3}\int p\mathrm{d}p\mathrm{d}\theta\frac{1}{\varepsilon_+^2}\delta(\omega\hbar-2\varepsilon) \\ &\quad \times\left[\varepsilon_+^2\left(\varepsilon-\omega\hbar-\frac{\Delta}{2}\right)+\left(\varepsilon-\omega\hbar+\frac{\Delta}{2}\right)v_0^2p^2+\varepsilon_+v_0^2(p_-^2+p_+^2)\right] \end{aligned} \tag{4.21}$$

The delta function is converted to momentum space via

$$\delta(\omega\hbar-2\varepsilon)=\frac{\delta(p-p_0)}{\left|\frac{\partial(\omega\hbar-2\varepsilon)}{\partial p}\right|_{p=p_0}} \tag{4.22}$$

where

$$p_0=\frac{1}{v_0}\sqrt{\frac{\omega^2\hbar^2}{4}-\left(\frac{\Delta}{2}\right)^2} \tag{4.23}$$

and

$$\left|\frac{\partial(\omega\hbar-2\varepsilon)}{\partial p}\right|_{p=p_0}=\frac{2v_0^2p_0}{(\omega\hbar/2)} \tag{4.24}$$

Substitute the Eq. (4.22) into Eq. (4.21), we obtain

$$\begin{aligned}
J_1 &= \frac{-e^2Ev_0^2}{8\pi\omega^2\hbar^3}\int p\mathrm{d}p\mathrm{d}\theta\frac{\delta(p-p_0)}{2v_0^2p_0}\frac{(\omega\hbar/2)}{\varepsilon_+^2} \\
&\quad\times\left[\varepsilon_+^2\left(\varepsilon-\omega\hbar-\frac{\Delta}{2}\right)+\left(\varepsilon-\omega\hbar+\frac{\Delta}{2}\right)v_0^2p^2+\varepsilon_+v_0^2(p_-^2+p_+^2)\right] \\
&= \frac{-e^2E}{16\pi\omega^2\hbar^3}\int_0^{2\pi}\mathrm{d}\theta\frac{(\omega\hbar/2)}{\varepsilon_+^2} \\
&\quad\times\left[\varepsilon_+^2\left(\omega\hbar/2-\omega\hbar-\frac{\Delta}{2}\right)+\left(\omega\hbar/2-\omega\hbar+\frac{\Delta}{2}\right)v_0^2p_0^2+\varepsilon_+2v_0^2p_0^2\cos(2\theta)\right] \\
&= \frac{-e^2E}{8\omega^2\hbar^3}\frac{(\omega\hbar/2)}{(\omega\hbar/2+\Delta/2)^2}\left[\left(\frac{\omega\hbar}{2}+\frac{\Delta}{2}\right)^2\left(\frac{-\omega\hbar}{2}-\frac{\Delta}{2}\right)+\left(\frac{-\omega\hbar}{2}+\frac{\Delta}{2}\right)\left[\frac{\omega^2\hbar^2}{4}-\left(\frac{\Delta}{2}\right)^2\right]\right] \\
&= \frac{e^2E}{8\omega^2\hbar^3}\frac{(\omega\hbar/2)}{(\omega\hbar/2+\Delta/2)}\left[\left(\frac{\omega\hbar}{2}+\frac{\Delta}{2}\right)^2+\left(\frac{-\omega\hbar}{2}+\frac{\Delta}{2}\right)^2\right] \\
&= \frac{e^2E}{8\omega^2\hbar^3}\frac{\omega\hbar}{\omega\hbar+\Delta}\left[\frac{\omega^2\hbar^2}{2}+\frac{\Delta^2}{2}\right] \\
&= \frac{e^2E}{16\hbar}\frac{\omega\hbar}{\omega\hbar+\Delta}\left[1+\frac{\Delta^2}{\omega^2\hbar^2}\right]
\end{aligned} \tag{4.25}$$

We now evaluate the normalization factor C. Since all ε and p in C has to be replaced by $\omega\hbar/2$ and p_0, respectively, we have:

$$\begin{aligned}
C &= \sqrt{\frac{2\left(\varepsilon+\frac{\Delta}{2}\right)^2}{\left[v_0^2p^2+\left(\varepsilon+\frac{\Delta}{2}\right)^2\right]}} \\
&= \sqrt{\frac{2\left(\frac{\omega\hbar}{2}+\frac{\Delta}{2}\right)^2}{\left[v_0^2p_0^2+\left(\frac{\omega\hbar}{2}+\frac{\Delta}{2}\right)^2\right]}} \\
&= \sqrt{\frac{2\left(\frac{\omega\hbar}{2}+\frac{\Delta}{2}\right)^2}{(\omega\hbar/2)^2-(\Delta/2)^2+\left(\frac{\omega\hbar}{2}+\frac{\Delta}{2}\right)^2}} \\
&= \sqrt{\frac{2\left(\frac{\omega\hbar}{2}+\frac{\Delta}{2}\right)}{2(\omega\hbar/2)^2+2\omega\hbar\left(\frac{\Delta}{2}\right)^2}} \\
&= \sqrt{\frac{\omega\hbar+\Delta/2}{\omega\hbar}}
\end{aligned} \tag{4.26}$$

Note that in general, if the integral carry a delta function of $\delta(x\omega\hbar-y\varepsilon)$, then the

normalization factor C becomes:

$$C = \sqrt{\frac{\left(\frac{x}{y}\right)\omega\hbar + \frac{\Delta}{2}}{\left(\frac{x}{y}\right)\omega\hbar}} \tag{4.27}$$

Including the normalization factor, we obtain:

$$J_1 = \frac{\omega\hbar + \Delta}{\omega\hbar} \times \frac{e^2 E}{16\hbar} \frac{\omega\hbar}{\omega\hbar + \Delta} \left[1 + \frac{\Delta^2}{\omega^2\hbar^2}\right] \tag{4.28}$$

Finally, the linear optical conductivity, σ_1, in SI unit is given by

$$\sigma_1(\omega) = \frac{e^2}{4\hbar} \left[1 + \frac{\Delta^2}{\omega^2\hbar^2}\right] \tanh\left(\frac{\omega\hbar}{4k_B T}\right) \Theta(\omega\hbar - \Delta) \tag{4.29}$$

Note that the step-function $\Theta(\omega\hbar - \Delta)$ function forbids any linear optical process to occur in the subgap regime.

4.1.3 Nonlinear optical response of semihydrogenated graphene

The third-order nonlinear optical conductivities are derived according to the procedures outlined in Chapter 3. We found that:

$$\begin{aligned} \sigma_3(\omega) &= \sigma_0 \frac{e^2 E^2 v_0^2}{\omega^3 \hbar \left(\omega\hbar + \frac{\Delta}{2}\right)} \left[2 + \frac{\Delta}{\omega\hbar} + \frac{\Delta^2}{(\omega\hbar)^2} + \frac{\Delta^3}{2(\omega\hbar)^3} - \frac{3(\Delta)^4}{8(\omega\hbar)^4} - \frac{3\Delta^5}{16(\omega\hbar)^5}\right] \\ &\quad \times \tanh\left(\frac{\omega\hbar}{2k_B T}\right) \Theta(\omega\hbar - \Delta) \end{aligned} \tag{4.30}$$

and

$$\sigma_3(3\omega) = \sigma_0 \frac{e^2 E^2 v_0^2}{\omega^4 \hbar^2} \left[X_1 \tanh\left(\frac{\omega\hbar}{4k_B T}\right) + X_2 \tanh\left(\frac{\omega\hbar}{2k_B T}\right) + X_3 \tanh\left(\frac{3\omega\hbar}{4k_B T}\right)\right] \Theta(3\omega\hbar - \Delta) \tag{4.31}$$

where $\sigma_0 = e^2/4\hbar$ and

$$X_1 \equiv -\frac{1}{48}\left[13 + \frac{2\Delta^2}{(\omega\hbar)^2} + \frac{\Delta^4}{(\omega\hbar)^4}\right] \tag{4.32}$$

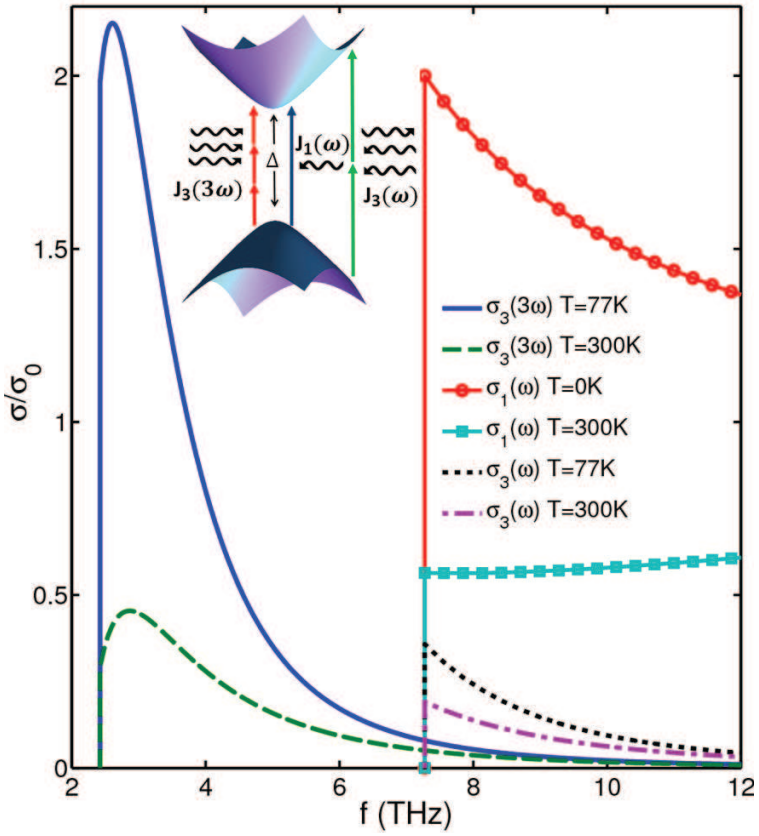

Figure 4.1: The frequency dependent optical conductance in the low frequency regime for two temperatures. The electric field is 3600 V/cm. The absorption edge for the frequency tripled response is shifted to $\Delta/3$. The inset is a schematic showing different optical processes.

$$X_2 \equiv \frac{1}{3}\left[2 - \frac{\Delta^2}{(\omega\hbar)^2} + \frac{\Delta^4}{8(\omega\hbar)^4}\right] \tag{4.33}$$

$$X_3 \equiv -\frac{1}{48}\left[45 - \frac{14\Delta^2}{(\omega\hbar)^2} + \frac{\Delta^4}{(\omega\hbar)^4}\right] \tag{4.34}$$

When $\Delta \to 0$, the above equations reduces to the usual graphene conductivities [89], i.e.

$$\sigma_3(\omega) \to \sigma_0 \frac{e^2E^2v_0^2}{\omega^4\hbar^2} \tanh\left(\frac{\omega\hbar}{2k_BT}\right) \times 2 \tag{4.35}$$

$$\sigma_3(3\omega) = \sigma_0 \frac{e^2E^2v_0^2}{\omega^4\hbar^2}\left[-\frac{13}{48}\tanh\left(\frac{\omega\hbar}{4k_BT}\right) + \frac{2}{3}\tanh\left(\frac{\omega\hbar}{2k_BT}\right) - \frac{45}{48}\tanh\left(\frac{3\omega\hbar}{4k_BT}\right)\right] \tag{4.36}$$

In Fig. 4.1, we plot the optical conductance versus frequency for a typical value of $\Delta = 0.03eV$. The on-site energy due to semihydrogenation removes the universal conductance. For $\hbar\omega < \Delta$, the linear conductance is zero for any temperature by the

virtue of energy conservation. The third-order current at single frequency, $\sigma_3(\omega)3$, is also zero for $\hbar\omega < \Delta$. The triple-frequency third-order term $\sigma_3(\omega)3$ persists to a low frequency of $\hbar\omega = \Delta/3$. The nonlinear effect in SHG is unique in that the response peak of the linear term and frequency tripled term is well separated by $\delta\hbar\omega = 2\Delta/3$. This provides a useful mechanism for two-color excitation and detection, one color is associated with the linear response and the other is associated with the nonlinear response. The relative intensities of the two colors can be tuned with the electric field. At a rather moderate electric field of 3600 V/cm, the magnitude of two peaks is roughly the same at 77 K. At room temperature, the peak in linear conductance disappears while the nonlinear conductance still exhibits a resonance.

We now discuss one interesting behavior of the nonlinear response peak. We compare the $\sigma_3(3\omega)$ at the optical response peak with that of the gapless graphene at the same frequency. The ratio at T=0K is given by

$$\frac{\sigma_3(3\omega)_\Delta}{\sigma_3(3\omega)} = \frac{31}{13} \approx 2.38 \tag{4.37}$$

This 2.38 times enhanced optical response at the onset frequency of $\sigma_3(3\omega)$ is universal for any value of Δ. This suggests that the 2.38 enhancement is related to the topological changes in the band structure of the Dirac fermion when a bandgap created. The 2.38 enhancement ratio is a unique signature of the interband nonlinear optical response of SHG and is not present in the intraband nonlinear optical response of gapped graphene (Chapter 2).

At the frequencies close to the energy gap, the onset linear conductance is twice the universal conductance [103] $\sigma_{1c} = 2\sigma_0$. The onset triple-frequency nonlinear conductivity $\sigma_3(3\omega) = \sigma_{1c}$ at $\hbar\omega = \Delta/3$ requires an applied field of E=3600 V/cm. This is a rather weak field for typical experimental conditions. On the other hand, the onset single-frequency nonlinear conductivity $\sigma_3(\omega) = \sigma_{1c}$ at $\hbar\omega = \Delta$ requires an electric field of around three times greater. Therefore, the potential of using the frequency tripled nonlinear effect in the frequency below the gap is very significant. The electric field required for $\sigma_3(\omega) = \sigma_{1c}$ at the vertical absorption edge can be

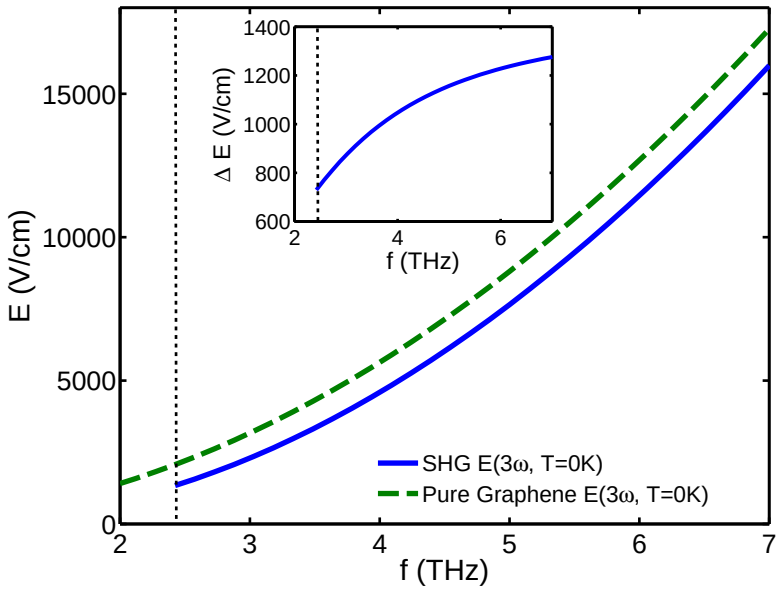

Figure 4.2: The frequency dependence of the critical field $E(3\omega)$ for SHG and pure (gapless) graphene. The inset shows the reduction of the critical field in SHG. Note that there exists a cut-off frequency $f_c = \Delta/3h \approx 2.4$ THz since $\sigma_3(3\omega) = 0$ at frequency smaller than f_c.

determined,

$$E_c(\hbar\omega = \Delta/3) = \frac{\Delta^2}{9e\hbar v_F}\left[\frac{24}{56\tanh\left(\frac{\Delta}{12k_BT}\right) - 25\tanh\left(\frac{\Delta}{6k_BT}\right)}\right]^{1/2} \tag{4.38}$$

In Fig. 4.2, we show the frequency dependence of the critical field at which $\sigma_3(3\omega)/\sigma_{1c} = 1$. This field measures the nonlinearity of the system at a given frequency. In the entire low frequency regime, $\Delta/3 < \hbar\omega < \Delta$, we found that the critical field for SHG is smaller than that in pure graphene by around 10%-40%. This indicates that SHG is a strong nonlinear system at low frequencies and low temperatures. The reason for this is that the density of states near the band edge has a van Hove-like singularity, $D(\varepsilon) \approx \varepsilon^{\hat{a}\acute{L}\check{S}1/2}$. This is qualitatively different from the case of normal two-dimensional semiconductors. In normal semiconductors, the energy dispersion near the band edge is parabolic and the density of states is constant. Here in SHG the large density of state near the band edge leads to a strong nonlinear effect.

In Fig. 4.3 we show the temperature dependence of the critical field $E_c(3\omega)$ at two different frequencies. At low temperature $E_c(3\omega)$ is nearly constant and is

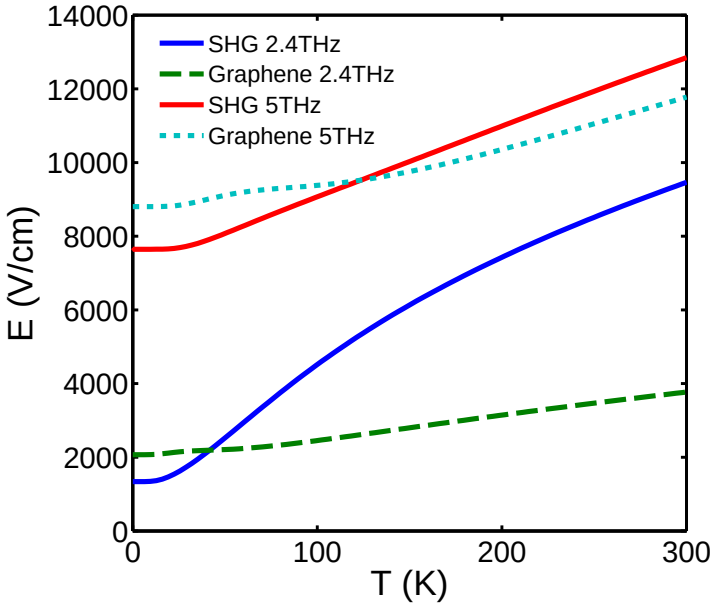

Figure 4.3: The temperature dependence of the critical field at two different frequencies of 2.4 and 5 THz.

smaller than that required in pure graphene. At high temperature, $E_c(3\omega)$ in SHG is larger than that required in pure graphene. As temperature increases, the Van Hove singularity becomes weaker and the critical field increases. At high temperature, $E_c(3\omega)$ increases with temperature as $E_c(3\omega) \approx T^{1/2}$. It should be pointed out that a high critical field in SHG at room temperature will not remove the key property of two-color optical response in SHG. In pure graphene, the response maximum of the linear term and frequency tripled term is not resolved.

The nonlinear effect reported is more general than that in SHG. Many effects can lead to a finite gap in the Dirac point in graphene. For example, the spin-orbit coupling can result in a gap of the size of $\Delta \approx 0.2$ meV. This is a very small gap but will produce qualitatively the same nonlinear effect as in SHG. Impurity scattering included gap which is also in the form of Eq. (4.38). The critical field mentioned earlier for $\sigma_3(3\omega)$ is proportional to Δ^2. Therefore, in general, the smaller the gap, the weaker the critical field at the onset frequency of the nonlinear response peak. If the gap can be controlled by external means, then the distance between the two peaks also becomes tunable. However, smaller gaps will result in a smaller distance

between the peaks of linear response and frequency tripled response and the linear and nonlinear response peaks becomes less resolved.

In conclusion, it is found that graphene with a bandgap in its Dirac point exhibits strong nonlinear optical response at frequency range of $\Delta/3 < \omega\hbar < \Delta$. In this frequency range the optical response is solely contributed by three-photon nonlinear process and hence has a zero critical field. The nonlinear response peak and the linear response peaks are well-separated giving rise to a two-color characteristic. Furthermore, the triple-frequency nonlinear optical response is universally enhanced by a factor of $31/13 \approx 2.38$, suggesting a topological origin due to the bandgap opening in the Dirac fermion energy spectrum. Finally, we remark that the band gap opening in graphene not only enhances the intraband nonlinear optical response (as discussed in Chapter 2), but also the interband nonlinear optical response.

4.2 Optical spectrum of graphene superlattice

We now study the optical response of a Kronig-Penney type graphene superlattice. The superlattice structure is made up of a graphene sheet placed on top of a spatially and periodically gated substrate. The Fermi levels of graphene is periodically raised and lowered and this produces a superlattice tunneling structure. Since the model consider only the isotropic low energy Dirac cone, the relative position and orientation between graphene crystal structure and the gated substrate is unimportant. In this structure, the band structure of the massless Dirac fermion is no longer symetrical in k-space. The effect of anisotropy on the optical response in terahertz frequency regime is investigated. It is found that the optical absorption, both linear and nonlinear response, are universally enhanced by the anisotropy when the external field aligns with the superlattice periodicity. Since both linear and nonlinear response are enhanced by the same amount, the optical nonlinearity (i.e. the relative magnitude between linear and nonlinear responses) is unexpectedly preserved regardless how strong the band structure anisotropy is. The enhanced optical absorption and the preserved optical nonlinearity reveals that anisotropy has transformed graphene superlattice into

a stronger nonlinear material which produces larger nonlinear optical current than isotropic case under the same critical electric field strength. Such enhanced optical absorption and well-preserved optical nonlinearity also occurs in gapped graphene in which the quasiparticle is in the form of *massive* Dirac fermions. The anisotropic *massive* Dirac femrion is a bizzare quasiparticle not only with non-uniform 'light speed' but also non-uniform mass dependent of the propagation direction. The results suggest that the enhanced electron-single-photon and electron-multiple-photon couplings are a universal feature of relativistic Dirac fermions of both massless or massive types, and the band structure isotropy is not a pre-requisite for the strong optical nonlinearity in graphene.

4.2.1 Recursion equations of anisotropic massless Dirac fermion

In a graphene superlattice created by applying a Kronig-Penney potential [43, 44], the K-point electrons no longer travels with uniform v_F in all direction. Instead, the group velocity in the direction perpendicular to the periodicity of the Kronig-Penney potential is reduced by a factor of λ dependent on the strength and periodicity of the potential. The group velocity of the wavevector k is renormalized according to its relative direction with respect to the direction of the 1D superlattice. The renormalization of the wavevector is given by[43, 44]:

$$\frac{v_{\hat{k}} - v_0}{v_0} = -\left[\frac{U^2 L^2}{\pi^4 v_0^2} \sum_{n>0} \frac{1}{4n^2} \sin^2 \frac{n\pi w}{L}\right] \sin^2 \theta_{\mathbf{k},\hat{x}} \tag{4.39}$$

where n is a positive integer, $v_{\hat{k}}$ is the renormalized group velocity in the direction of the wavevector $\mathbf{k}$, and v_0 is the unrenormalized group velocity. w, L and U are the superlattice parameters: barrier width, superlattice periodicity and barrier height respectively. The angle $\theta_{k,\hat{x}}$ is the angle between $\mathbf{k}$ and the direction of the superlattice $\hat{x}$. Rearrange Eq. (4.39) and substituting $\theta_{k,\hat{x}} = \pi/2$, we obtain the renormalization

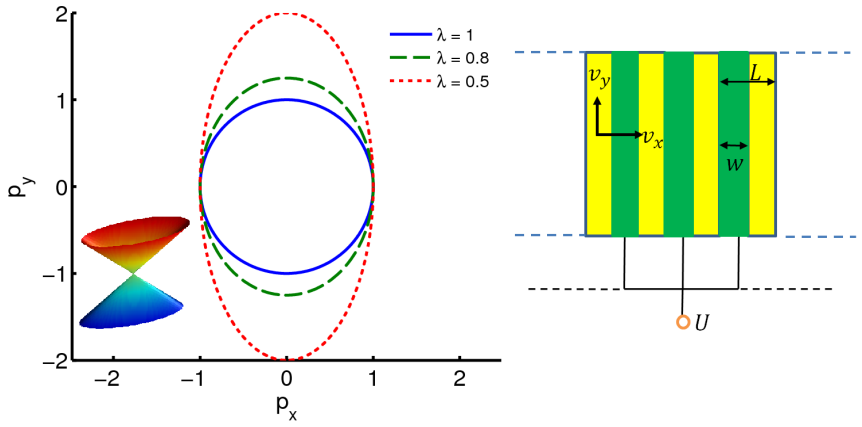

Figure 4.4: Band structure of graphene superlattice (inset). In the p_x-p_y plan, the Dirac cone is elongated elliptically in the y-direction. L, w and U are the superlattice periodicity, potential width and potential height, respectively, of the Kronig-Penney type graphene superlattice.

factor, *lambda*, of the y-directional group velocity as:

$$\lambda \equiv \frac{v_y}{v_0} = -\left[\frac{U^2L^2}{\pi^4 v_0^2}\sum_{n>0}\frac{1}{4n^2}\sin^2\frac{n\pi w}{L}\right]\sin^2\theta_{\mathbf{k},\hat{x}} + 1 \tag{4.40}$$

λ represents the degree of anisotropy of the band structure. The band structure of the superlattice is no longer circular, but is deformed to an elliptic cone. Such quasiparticle nature is analogue to a massless Dirac fermion traveling in anisotropic spacetime [43, 44, 124]. In topological insulator (TI), the quasiparticle residing in its surface state is also in the massless Dirac form with Fermi velocity approximately half of the graphene [58]. Interestingly, the anisotropic massless Dirac fermion can also be found in the $(2, 2, 1)$ side-surface state of Bi_2Se_3 TI with a rather strong anisotropy of $v_x = 3.1 \times 10^5$ m/s and $v_y = 1.4 \times 10^5$ m/s [125]. In a Bi square net of $SrMnBi_2$ TI, highly anisotropic Fermi velocity differs by a factor of 8 was experimentally observed [126].

The anisotropy can be modeled by defining an *anisotropy parameter*, λ, which modifies the y-direction group velocity by $v_y = \lambda v_F$ where $v_F = 10^6$ m/s is the Fermi velocity, and the anisotropy parameter is continuously tunable, $0 \leq \lambda \leq 1$, by varying the superlattice periodicity L, potential width w and potential height U (Fig. 4.4) [43, 44]. For a superlattice barrier height of $U = 0.3$ eV, $\lambda = 0$ occurs

when $w = 10$ nm and $L = 25$ nm [43]. In this case, the group velocity in y-direction completely vanishes and the electron is confined to move in the direction along the superlattice structure. This allows the non-destructive transformation of the 2D graphene sheet into a 1D electronic system equivalent to a graphene nanoribbon. The graphene superlattice Hamiltonian is written as $\hat{\mathcal{H}} = \sigma_x p_x + \lambda \sigma_y p_y$ where the λ term has created the desired anisotropy in y-direction. The energy dispersion is given as $\varepsilon_s(p, \theta) = s v_F p \sqrt{\cos^2\theta + \lambda^2 \sin^2\theta}$ where $s = \pm 1$ denotes electron and hole state. The group velocity in θ-direction is given as

$$v = v_F \sqrt{\cos^2\theta + \lambda^2 \sin^2\theta} \tag{4.41}$$

which gives the expected x- and y-components of $v(\theta = 0) = v_F = v_x$ and $v(\theta = \pi/2) = \lambda v_F = v_y$. The eigenfunction is given as $\psi_0(s, p) = \frac{1}{\sqrt{2}}(1, v_F(p_x + i\lambda p_y)/\varepsilon_s)^T$ where T denotes transpose. The band structure is plotted in Fig. 4.4. It can be seen that due to the reduced group velocity in y-direction, the conic Dirac cone is elongated in y-direction, forming an anisotropic elliptic Dirac cone. When an external field $\mathbf{E} = \mathbf{E}_0 e^{i\omega t}$ is applied along the x-direction, the quasiparticle is minimally coupled to the photon according to $p_x \to p_x - eA$ where $\mathbf{A} = -\partial\mathbf{E}/\partial t$. The Hamiltonian is then given by

$$\hat{H} = v_F \begin{bmatrix} 0 & p_x - \lambda i p_y - eA \\ p_x + \lambda i p_y - eA & 0 \end{bmatrix} \tag{4.42}$$

The energy dispersion is given as

$$\varepsilon_s(p, \phi) = s v_F p \sqrt{\cos^2\theta + \lambda^2 \sin^2\theta} \tag{4.43}$$

where $s = \pm 1$. The single electron eigenstate is given as

$$\psi_0(s, p) = \frac{1}{\sqrt{2}} \begin{bmatrix} 1 \\ s v_F \frac{p_x + i\lambda p_y}{\varepsilon} \end{bmatrix} \tag{4.44}$$

where $\varepsilon = |\varepsilon_s|$. The wavefunction in the presents of an external electric field is written

as

$$\psi_n(p) = \sum_n \begin{bmatrix} a_n \\ b_n \end{bmatrix} e^{i(\frac{\varepsilon_s}{\hbar} - n\omega)t} \tag{4.45}$$

The Schrodinger's equation $H\psi = i\hbar\partial\psi/\partial t$ can then be solved:

$$-\hbar\sum_n \left(\frac{\varepsilon}{\hbar} - n\omega\right) \begin{bmatrix} a_n \\ b_n \end{bmatrix} e^{i(\frac{\varepsilon_s}{\hbar} - n\omega)t} = v_F \sum_n \begin{bmatrix} 0 & p_x - \lambda i p_y \\ p_x + \lambda i p_y & 0 \end{bmatrix} \begin{bmatrix} a_n \\ b_n \end{bmatrix} e^{i(\frac{\varepsilon_s}{\hbar} - n\omega)t} \tag{4.46}$$

which gives coupled equations

$$(\varepsilon - n\hbar\omega)a_n = v_F\tilde{p}_- b_n + \frac{eEv_F}{i\omega} b_{n-1} \tag{4.47}$$

$$(\varepsilon - n\hbar\omega)b_n = v_F\tilde{p}_+ a_n + \frac{eEv_F}{i\omega} a_{n-1} \tag{4.48}$$

where $\tilde{p}_\pm = p_x \pm i\lambda p_y$. For $n = 0$, we have:

$$a_0 = \frac{1}{\sqrt{2}} \tag{4.49}$$

$$b_0 = \frac{v_F\tilde{p}_+}{\sqrt{2}\varepsilon} \tag{4.50}$$

For $n = 1$, we have:

$$a_1 = \frac{eEv_F}{\sqrt{2}i\hbar\omega^2(\hbar\omega - 2\varepsilon)} \left[(\varepsilon - \hbar\omega)\frac{v_F\tilde{p}_+}{\varepsilon} + v_F\tilde{p}_-\right] \tag{4.51}$$

$$b_1 = \frac{eEv_F}{\sqrt{2}i\hbar\omega^2(\hbar\omega - 2\varepsilon)} \left[(\varepsilon - \hbar\omega) + \frac{v_F^2\tilde{p}_+^2}{\varepsilon}\right] \tag{4.52}$$

4.2.2 Linear optical response

We now derive the optical current density

$$\begin{aligned}
J_1 &= \frac{1}{(2\pi\hbar)^2}\int pdpd\phi \hat{j}_x^{(1)} \\
&= \frac{-ev_F}{(2\pi\hbar)^2}\int pdpd\phi(a_1 b_0^* + b_1 a_0^*) \\
&= -\frac{e^2 E v_F^2}{4i\pi^2\hbar^3\omega^2}\int \frac{pdpd\phi}{\hbar\omega - 2\varepsilon}\left[(\varepsilon - \hbar\omega) + \frac{v_F^2}{\varepsilon}(\tilde{p}_+^2 + \tilde{p}_-^2)\right] \\
&= -\frac{e^2}{4\hbar}\frac{v_F^2 E}{i\pi^2\hbar^2\omega^2}\int \frac{pdpd\phi}{\hbar\omega - 2\varepsilon}\left[(\varepsilon - \hbar\omega) + \frac{v_F^2 p^2}{\varepsilon}(\cos^2\phi - \lambda^2\sin^2\phi)\right] \\
&= -\sigma_0\frac{v_F^2 E}{i\pi^2\hbar^2\omega^2}\int \frac{pdpd\phi}{\hbar\omega - 2\varepsilon}\left[(\varepsilon - \hbar\omega) + \frac{v_F^2 p^2}{\varepsilon}(\cos^2\phi - \lambda^2\sin^2\phi)\right] \qquad (4.53)
\end{aligned}$$

where $\sigma_0 = e^2/4\hbar$ is the universal minimum conductance in graphene. Write $\omega \to \omega + i\eta$ with $\eta \to 0$, the denominator is transformed into a Dirac delta function:

$$\lim_{\eta\to 0} Im\left(\frac{1}{\omega \pm i\eta}\right) = \mp\pi\delta(\omega) \qquad (4.54)$$

Furthermore,

$$\left|\frac{d(\omega - 2\varepsilon)}{dp}\right|_{p_0} = \frac{2v_F^2 p_0 R_+(\phi)}{\frac{\hbar\omega}{2}} \qquad (4.55)$$

$$p_0 = \frac{\hbar\omega}{2v_F R_+(\phi)^{1/2}} \qquad (4.56)$$

where $R_\pm(\phi) \equiv \cos^2\phi \pm \lambda^2\sin^2\phi$. We can then write:

$$\begin{aligned}
J_1 &= -\sigma_0\frac{v_F^2 E}{\pi\hbar^2\omega^2}\int pdpd\phi\frac{\delta(p - p_0)}{2v_F^2 p_0 R(\phi)_+}\frac{\hbar\omega}{2}\left[(\varepsilon - \hbar\omega) + \frac{v_F^2 p^2}{\varepsilon}R_-(\phi)\right] \\
&= -\sigma_0\frac{v_F^2 E}{\pi\hbar^2\omega^2}\int \frac{p_0 d\phi}{2v_F^2 p_0 R_+(\phi)}\frac{\hbar\omega}{2}\left[-\frac{\hbar\omega}{2} + \frac{v_F^2}{\frac{\hbar\omega}{2}v_F^2 R_+(\phi)}\left(\frac{\hbar\omega}{2}\right)^2 R_-(\phi)\right] \\
&= -\sigma_0\frac{E}{2\pi\hbar^2\omega^2}\int \frac{d\phi}{R_+(\phi)}\left(\frac{\hbar\omega}{2}\right)^2\left[-1 + \frac{R_-(\phi)}{R_+(\phi)}\right] \\
&= \frac{\sigma_0 E}{4}\frac{1}{2\pi}\int \frac{d\phi}{R_+(\phi)}\left[1 - \frac{R_-(\phi)}{R_+(\phi)}\right] \qquad (4.57)
\end{aligned}$$

This gives the linear conductivity as:

$$\sigma_x^{(1)}(T) = \sigma_0 \times \frac{1}{2\pi} \int \frac{d\phi}{\cos^2\phi + \lambda^2 \sin^2\phi} \left[1 - \frac{\cos^2\phi - \lambda^2 \sin^2\phi}{\cos^2\phi + \lambda^2 \sin^2\phi}\right] \tanh\left(\frac{\hbar\omega}{2}\right) \quad (4.58)$$

Now, the integrals can be evaluated as:

$$\int_0^{2\pi} \frac{d\phi}{\cos^2\phi + \lambda^2 \sin^2\phi} = \frac{2\pi}{\lambda} \quad (4.59)$$

$$\int_0^{2\pi} d\phi \frac{\cos^2\phi - \lambda^2 \sin^2\phi}{(\cos^2\phi + \lambda^2 \sin^2\phi)^2} = \frac{\tan x}{1 + \lambda^2 \tan x}\Big|_0^{2\pi} = 0 \quad (4.60)$$

Finally, we obtain:

$$\sigma_1(\omega) = \frac{\sigma_0}{\lambda} \tanh\left(\frac{\hbar\omega}{2}\right) \quad (4.61)$$

where the spin and valley degeneracies have been included (a factor of 4).

The second order and third order spinors can be constructed similarly using the recursion equation, Eq. (4.47). Following exactly the same procedures, we found that:

$$\sigma_3(\omega) = 2\sigma_0 \frac{E^2 v_F^2 e^2}{\hbar^2\omega^4} \frac{1}{2\pi} \int \frac{d\phi}{R_+} \left(1 - \frac{R_-}{R_+}\right) \tanh\left(\frac{\hbar\omega}{k_B T}\right) \quad (4.62)$$

$$\sigma_3(\omega) = 2\frac{\sigma_0}{\lambda} \frac{E^2 v_F^2 e^2}{\hbar^2\omega^4} \tanh\left(\frac{\hbar\omega}{k_B T}\right) \quad (4.63)$$

For the third-order triple-frequency (TF) conductivity, we obtain:

$$\sigma_3(3\omega) = \sigma_0 \frac{E^2 v_F^2 e^2}{\hbar^2\omega^4} \left(\frac{X}{48} \tanh\left(\frac{\hbar\omega}{2k_B T}\right) + \frac{Y}{3} \tanh\left(\frac{\hbar\omega}{k_B T}\right) + \frac{3Z}{16} \tanh\left(\frac{3\hbar\omega}{2k_B T}\right)\right) \quad (4.64)$$

where the dimensionless parameters X, Y and Z are given as

$$X = \frac{1}{2\pi} \int \frac{d\phi}{R_+} \left(13 - 12\frac{R_-}{R_+} - \frac{R'}{R_+^2}\right) \quad (4.65)$$

$$Y = \frac{1}{2\pi} \int \frac{d\phi}{R_+} \left(-2 + \frac{R'}{R_+^2}\right) \quad (4.66)$$

$$Z = \frac{1}{2\pi} \int \frac{d\phi}{R_+} \left(5 + 4\frac{R_-}{R_+} - 9\frac{R'}{R_+^2}\right) \quad (4.67)$$

$$R' = \cos^4\phi - 6\lambda^2\cos^2\phi\sin^2\phi + \lambda^4\sin^4\phi \tag{4.68}$$

Using the integral:

$$\int_0^{2\pi}\frac{R'}{R_+^3} = \frac{\tan x}{1+\lambda^2\tan^2 x} + \frac{2\tan x}{(1+\lambda^2\tan^2 x)^2}\Bigg|_0^{2\pi} = 0 \tag{4.69}$$

and together with previous Eq. (4.59) and (4.60), we obtain:

$$\sigma_3(3\omega) = \frac{\sigma_0}{\lambda}\frac{E^2v_F^2e^2}{\hbar^2\omega^4}\left(\frac{13}{48}\tanh\left(\frac{\hbar\omega}{2k_BT}\right) - \frac{2}{3}\tanh\left(\frac{\hbar\omega}{k_BT}\right) + \frac{15}{16}\tanh\left(\frac{3\hbar\omega}{2k_BT}\right)\right) \tag{4.70}$$

In Fig. 4.5, the nonlinear optical conductivities at different band anisotropy λ is shown. We see that $\sigma_1(\omega)$, $\sigma_3(\omega)$ and $\sigma_3(3\omega)$ are all universally enhanced by a factor of $1/\lambda$, in comparison with that of the isotropic case [89]. For $\lambda = 0.1$, which can be achieved by applying spatial period of $L \approx 20nm$, potential width of $w = 10$ nm and potential height of $U = 0.3$ eV, the total optical absorption is enhanced by 10 times. In the extremely anisotropic case of $\lambda = 0.01$, which can be achieved by $L \approx 25$ nm, $w = 10$nm and $U = 0.3$ eV [43], 100 times amplification is achieved. The $1/\lambda$ enhanced optical absorption is quite a surprising result. Intuitively, one might expect a *reduced* optical response in the anisotropic case since the y-component of the group velocity $v_y = \lambda v_F$ is reduced by a factor of λ and the resulting 'slower' charge carrier should degrade the optical current. This is however not the complete picture since $\mathbf{E}$ is directed along x-direction and the x-directional optical response is only minimally affected by the reduced y-directional group velocity $v_y = \lambda v_F$. On the other hand, when $\lambda < 1$ the p_y components in a equi-energy slice actually becomes *larger* in comparison to the isotropic Fermi velocity case because of the smaller slope (or equivalently the reduced v_y) in y-direction (see Fig. 1). The overall *larger momentum* of the charge carrier across an equi-energy surface is the underlying reason of the anisotropy-induced enhancement of the *interband* optical absorption in the Kronig-Penney type graphene superlattice. As the anisotropy increases, i.e. $\lambda \to 0$, the band structure becomes more y-directionally elongated across an equienergy surface and

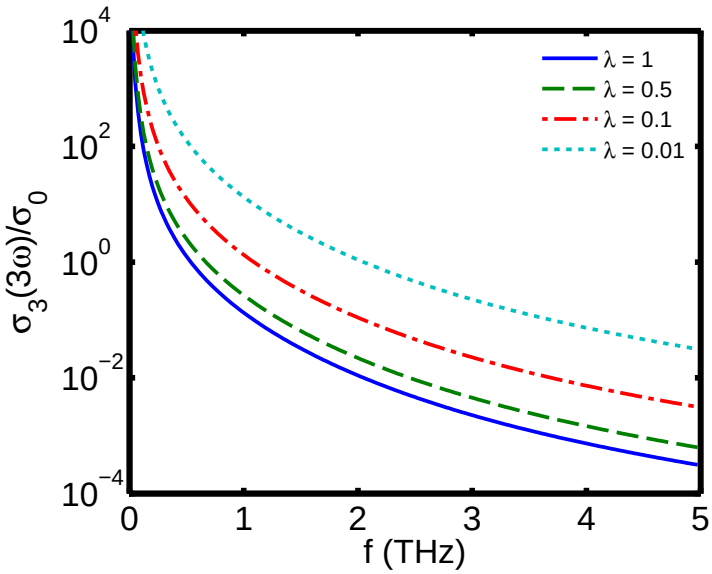

Figure 4.5: The frequency dependence of $\sigma_3(3\omega)$ at $E = 1000$ V/cm and 300 K.

this results in the $1/\lambda$ dependence.

The critical field strength E_c remains the same regardless the level of anisotropy since both linear and nonlinear response are enhanced by the same factor of $1/\lambda$. Therefore, just like normal graphene, graphene superlattice is also an exceptionally strong nonlinear material with $E_c \approx 10^3$ V/cm for up to room temperature at $f = 1$ THz. The strong optical nonlinearity observed in normal graphene and graphene superlattice is a general feature of of the *relativistic* behavior of the quasiparticle. The band structure isotropy is not necessarily required to achieve the strong optical nonlinearity. As long as the quasiparticle energy dispersion maintain its linear form, the strong optical nonlinearity is always guaranteed and is well protected from any band structure anisotropy. The total integrated optical absorption is given as $\Sigma(\lambda) = \int \sigma(\omega, \lambda) d\omega$ and it can be immediately seen that the total nonlinear absorption is increased by a factor $1/\lambda$ for all THz frequency regime as shown in Fig. 4.5. Although graphene superlattice is equally advantageous as normal graphene in terms of the smallness of E_c, the $1/\lambda$ increased total response indicates that the nonlinear optical current output of graphene superlattice is still larger than that of the normal graphene at a given electric field strength. This suggests the improved THz photon detection and THz frequency up-conversion in graphene superlattice which are po-

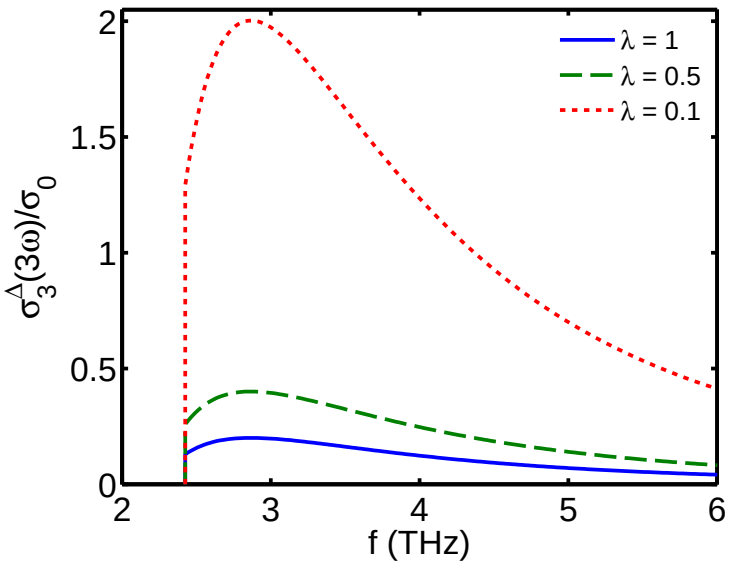

Figure 4.6: Anisotropic gapped graphene frequency-tripling conductivity at 300 K and $E = 3400$ V/cm and $\Delta = 0.03$ eV.

tentially useful in the development of graphene-based THz optical device. Finally, we briefly discuss the optical response of gapped graphene with anisotropic band structure. We found that the linear and nonlinear optical conductivity is in the same form as Eq. (4.29), Eq. (4.35) and Eq. (4.35) multiplied by a factor of $1/\lambda$. The band anisotropy enhanced subgap triple-frequency conductivity is plotted in Fig. 4.6). We conclude that the $1/\lambda$ enhancement is universal in both gapped and gapless cases in the presence of band anisotropy.

4.2.3 Discussion

We now discuss the importance of the fifth order nonlinear term. The nth-order conductance is proportional to a dimensionless parameter $Z = (eEv_F/\hbar\omega^2)^{n-1}$ and an overlap integral of eigenstates of different orders $< \phi_{n-m}|\phi_m >$. Because the overlap integral decreases very rapidly with n, the third-order nonlinear effect persists for $Z > 1$ while the fifth-order term is negligible. At frequency around 1 THz, the critical field (the field at which the third-order current equals the linear current) is around 2000 V/cm [89]. For $V_F = 10^6$ m/s, $\omega = 1$ THz, and $E = 2000$ V/cm, the resulting $Z = 50$. At this value of Z, the third-order current equals approximately the

linear current, but the fifth-order current is about 10^{-5} of the linear current, totally negligible [127].

Finally, we discuss the substrate effect on the graphene superlattice structure. Firstly, the substrate effect in single layer graphene is sample dependent [128]. It has been shown that the substrate effect is negligible for graphene prepared by micromechanical cleavage; on the other hand, epitaxial graphene on SiC substate exhibits significant altered electronic properties. An interesting substrate effect is the coupling of Dirac electrons with the surface polar phonons formed on the substrate. It has been shown that such coupling can significantly influence the optical [129] and transport properties [130] of single graphene layer. Therefore, we expect the nonlinear optical response of the superlattice to be different in the presence of such coupling effect.

In conclusion, the anisotropic Dirac fermion in the graphene superlattice tunes up the total optical conductance while maintaining the same critical electric field. This also occurs in anisotropic graphene with a gap. Furthermore, the optical nonlinearity is perfectly protected from band anisotropy while the total optical response, including both linear and nonlinear processes, are enhanced by a factor of $1/\lambda$. Since λ is dependent on the superlattice parameters, a graphene superlattice can potentially be used as a tunable terahertz source/detector. Finally, as a weak sinusoidal term can be added to a graphene via holographic illumination [131] or by patterning the substrate, possible experimental verification of the results could be performed with direct measurement of the optical conductivity of such a system.

5 | Retro reflection of electrons at the interface of bilayer graphene and superconductor

* Electron reflection at an interface is a fundamental quantum transport phenomenon. The most famous electron reflection is the electron→hole Andreev reflection (AR) at a metal/superconductor interface. While AR can be either specular or retro-type, electron→electron reflection is limited to only the specular type. In this Chapter, we show that electrons can undergo retro electron reflection (RER) in bilayer graphene (BLG). The underlying mechanism for this previously unknown process is the anisotropic constant energy band contour of BLG. The electron group velocity is fully reversed upon reflection, causing electrons to be retro-reflected. Utilizing a BLG/superconductor junction (BLG/S) as a model structure, we show that the unique low energy quasiparticle nature of BLG not only allows RER to occur, but also gives rise to two additional features: (1) AR is completely absent, making BLG/S 100% electron reflective; (2) electrons are valley-selectively focused upon retro-reflection.

5.1 Specular reflection and retro reflection

Specular reflection of a particle by smooth solid wall is a classic textbook illustration on the principle of conservation of momentum [132]. Because the particle motion is

*This Chapter is based on *Sci. Rep.* **2**, 1013 (2012).

intrinsically 'locked' to the direction of the momentum, the conservation of momentum parallel to the interface, k_y, automatically implies the group velocity component parallel to the interface, v_y, to remain unchanged upon reflection. This results in specular reflection [Fig. 5.1(a)]. In the quantum mechanical case, retro reflection can occur at a superconducting interface via Andreev reflection (AR) [100]. AR is a two particle process in which an incident electron in the normal metal couples with another electron below the Fermi level to form a Cooper pair, crossing the interface into the superconductor [133] and leaving behind a hole. Since the hole is a time reversed version of the incident electron, its v_y is anti-parallel with k_y. The conservation of k_y requires a sign reversal of v_y upon reflection. This results in electron→hole retro reflection. In graphene [55, 99] and a 2D semiconductor with Rashba spin-orbit coupling [134], the pseudo-spin (graphene) and real-spin (Rashba semiconductor) nature of the two systems creates an additional 'spin'-split branch: up-down Dirac cones in graphene and left-right sub-bands in the Rashba semiconductor. When forming an interface with a superconductor, the split branches form two 'flavors' of holes: one with k_y parallel with v_y and one with k_y anti-parallel with v_y. This allows both retro and specular AR to occur in these systems.

Retro reflection of electrons at an interface remains elusive. For retro electron reflection (RER) to occur, reversal of v_y is required but this, however, violates the momentum conservation principle. To achieve RER, v_y needs to be 'unlocked' from k_y such that the direction of v_y can be freely reversed upon reflection while conserving k_y [Fig. 5.1(b)]. We define a *constant energy band contour* as the outline of the energy spectrum across a constant energy slice in k-space. The concept of constant energy band contours will be useful in the qualitative understanding of the electron reflection trajectory, since it is directly related to the electron group velocity. Fig 5.1(c) shows the circular band contour of a parabolic (or linear) energy spectrum. In this case, specular electron reflection (SER) is the only permissible electron→electron reflection process since v_y does not change sign upon reflection. We articulate that (i) anisotropic and (ii) *opposite* band contour for incident and

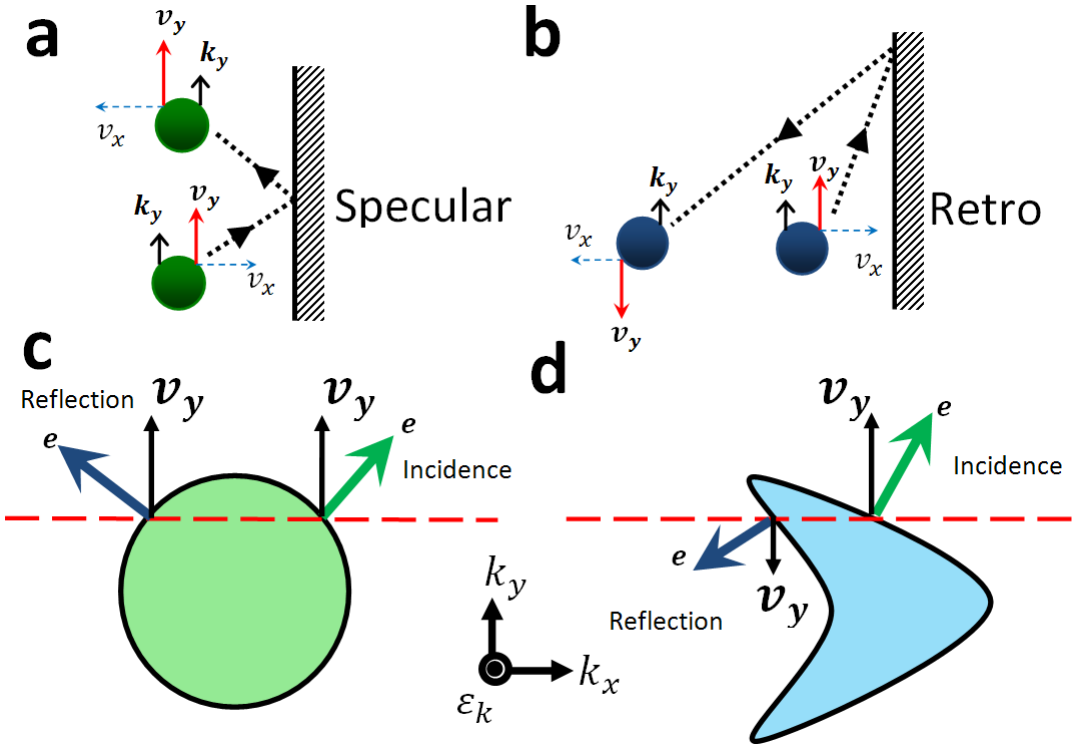

Figure 5.1: (a) Since electron group velocity component v_y is locked to the momentum component k_y, conservation of k_y allows only specular electron reflection (SER) to occur; (b) retro electron reflection (RER) requires v_y to be 'unlocked' from k_y such that reversal of v_y can still occur while conserving k_y; (c) constant energy slice of a parabolic (or linear) energy spectrum. The circular band contour allows only SER to occur; (d) constant energy slice of a hypothetical energy spectrum with boomerang-shaped band contour. The constant energy band contour of the incident states in k-space is convex while that of the reflected states is concave. The opposite band contours between incident and reflected states causes the sign reversal of v_y upon reflection. This results in RER.

reflected electron states are the fundamental criteria for an electron to be retro-reflected. Criterion (i) allows the electron motion to be unlocked from the direction of momentum since in an anisotropic band contour, the momentum no longer aligns with the group velocity while the direction of the group velocity is solely determined by the contour of the band via $\vec{v} = (v_x, v_y) = \hbar^{-1}\nabla_k \varepsilon_k$. Criterion (ii) allows the direction of v_y to be reversed upon reflection. In Fig. 5.1(d), a hypothetical energy spectrum with boomerang-shaped constant energy band contour in k-space is shown. The boomerang-shaped constant energy band contour is highly anisotropic in k-space. The constant energy band contour of the incident states is convex while that of the reflected states is concave. Along a constant line of k_y, the reflected electron motion is completely reversed in both x- and y-direction. v_y is reversed while conserving k_y.

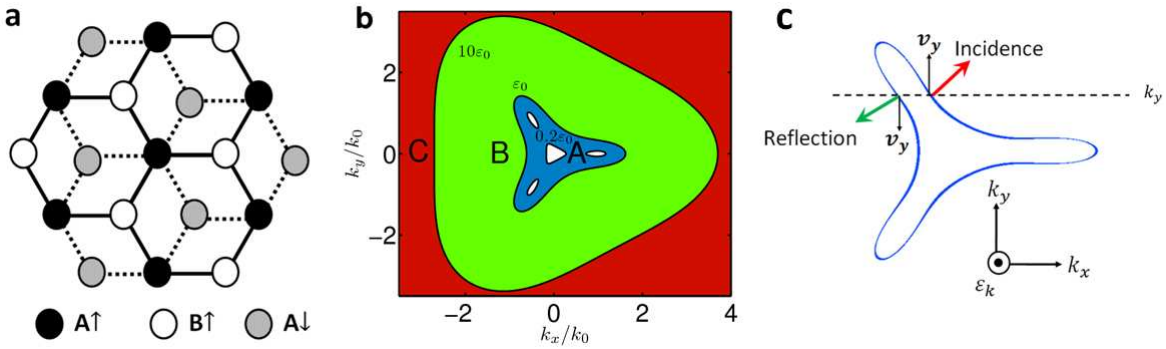

Figure 5.2: (a) Bernal-stacked bilayer graphene lattice structure; (b) the energy spectrum contour plot in phase space, showing three distinct energy regime: Regime (A): $\varepsilon_k < \varepsilon_0/4$, Regime (B): $\varepsilon_0/4 < \varepsilon_k < 10.9\varepsilon_0$ and Regime (C): $\varepsilon_k > 10.9\varepsilon_0$. Retro electron reflection occurs optimally in Regime (B) due to its 'boomerang-like' anisotropic constant energy band contour in k-space. In high energy Regime (C), retro reflection is no longer possible as the band contour becomes parabolic-like; (c) Band contour of an constant energy slice in Regime (B). The green and blue arrows denotes incident and reflected electron direction of motion respectively. The opposite band contour between incident (convex) and reflected states (concave) causes v_y to reverse its direction upon reflection, leading to RER.

The reflection process is hence RER.

The boomerang-shaped constant energy band contour occurs in a Bernal-stacked bilayer graphene (BLG). The low energy spectrum of BLG exhibits the trigonal warping effect (TW), i.e. the energy spectrum splits into four discrete low energy pockets which join to form a single-band at higher energy [70]. The TW has resulted in highly anisotropic constant energy band contour which fulfills both of the RER criteria. In the tight-binding framework, the low energy effective Hamiltonian is given as

$$\mathcal{H}_\xi = \varepsilon_0 \left(- \begin{bmatrix} 0 & k_-^2 \\ k_+^2 & 0 \end{bmatrix} + \xi \begin{bmatrix} 0 & k_+ \\ k_- & 0 \end{bmatrix} \right) \tag{5.1}$$

where $\xi = 1(-1)$ for K (K') valley, $\varepsilon_0 = (v_3/v_F)^2\gamma_1$, $k_\pm = k_x \pm ik_y$. The wave vectors are normalized by k_0 and are dimensionless, i.e. $k_x \equiv k_x/k_0$, $k_y \equiv k_y/k_0$ where $k_0 = v_3\gamma_1/(\hbar v_F^2)$. The hopping parameters are $\gamma_1 = 0.3$ eV, $v_3/v_F = 0.1$ and $v_F = 10^6$ m/s [70]. The characteristic wave vector k_0 defines the phase-space separation between central and satellite Dirac points. The low energy pockets join to form a single trigonally warped band structure at $\varepsilon_k = \varepsilon_0/4$. The quadratic term

in Eq. (5.1) represents the indirect electron hopping between B↑ and A↓ sublattices (↑ and ↓ denote upper and lower layer respectively) mediated by A↑-B↓ dimer pair while the linear term represents the weak direct electron hopping between the B↑ and A↓ side [Fig. 5.2(a)].

The inclusion of the linear term anisotropically deforms the low energy dispersion into:

$$\varepsilon_{k,\xi} = \varepsilon_0\sqrt{k^4 + k^2 - 2\xi k^3 \cos 3\phi} \tag{5.2}$$

where ϕ is the momentum angle and $\xi = \pm$ is the valley-index. For simplicity, we denote $\varepsilon_k \equiv \varepsilon_{k,+}$ for the K-valley. The BLG energy spectrum exhibits three distinct categories of band contour [Fig. 5.2(b)]: (A) the band structure splits into four distinct low energy 'pockets' at $\varepsilon_k < \varepsilon_0/4$; (B) the pockets join to form a single band with 'three-leaf'-like contour at $\varepsilon_0/4 < \varepsilon_k < 10.9\varepsilon_0$; and (C) the band contour becomes parabolic-like in the high energy regime of $\varepsilon_k > 10.9\varepsilon_0$. Regime (B) is the most interesting since the reflection process is dominantly RER. The 'three-leaf'-shaped band contour is highly anisotropic. The incident electron states residing on the right-pointing 'leaf' and the right-edges of the upper and lower leaves has a *convex* constant energy band contour while the reflected electron residing on the left-hand edge of the upper and lower leaves has a *concave* constant energy band contour. As shown in Fig. 5.2(c), an incident electron with direction of motion pointing upwardly-right (red arrow) is reflected as an electron pointing downwardly-left (green arrow) along a constant line of k_y. The reversal of v_y while conserving k_y results in RER. SER occurs only at large $|k_y|$ in which criteria (ii) no longer holds (incident and reflected electrons has the same constant energy band contour and hence v_y does not change sign upon reflection). The very low energy regime (A) and high energy regime (C) are less ideal for RER. In Regime (A), RER occurs only minimally in the upper and lower pockets. In regime (C), the quadratic term in Eq. (5.1) dominates and the constant energy band contour loses the required boomerang-shaped constant energy band contour.

5.2 Retro electron reflection in bilayer graphene

In the usual cases (parabolic or linear band structure), quasi-momentum angle $\phi = \tan^{-1}(k_y/k_x)$ is commonly used to described particle trajectory. Each ϕ uniquely defines a particle traveling in the direction of ϕ. In BLG, ϕ is no longer locked to the electron motion due to the constant energy band contour anisotropy. Instead, the electron trajectory is more accurately described by group velocity angle $\theta = \tan^{-1}(v_y/v_x)$. Unlike ϕ, the uniqueness of θ is lost. Each θ can simultaneously represent several electron states and hence becomes ambiguous. We therefore characterize the reflection problem by momentum component k_y instead of the incident quasi-momentum angle θ or incident group velocity angle ϕ.

The group velocity is given as $v_\nu = \hbar^{-1}\partial\varepsilon_k^{(e)}/\partial k_\nu$ where $\nu = x, y$ denotes x- and y-directional group velocity respectively. We consider the case where the reflection interface is placed along the y-direction. Explicitly, we can write

$$v_x(k,\xi) = \frac{2}{\hbar^{-1}\varepsilon_{k,\xi}}\left[2k_x^3 + (2k_y^2+1)k_x + 3\xi(k_y^2 - k_x^2)\right] \tag{5.3}$$

$$v_y(k,\xi) = \frac{2}{\hbar^{-1}\varepsilon_{k,\xi}}\left(2k_x^2k_y + 2k_y^3 + k_y + \xi k_x k_y\right) \tag{5.4}$$

In the following discussion, we focus on $\xi = +1$ (i.e. electrons in K valley). In Fig. 5.3(a)-(c), v_x of incident and reflected electrons across a constant energy slice are shown. v_x has the opposite sign between incident electron and reflected electron and is highly asymmetric due to the broken left-right symmetry of the BLG band contour.

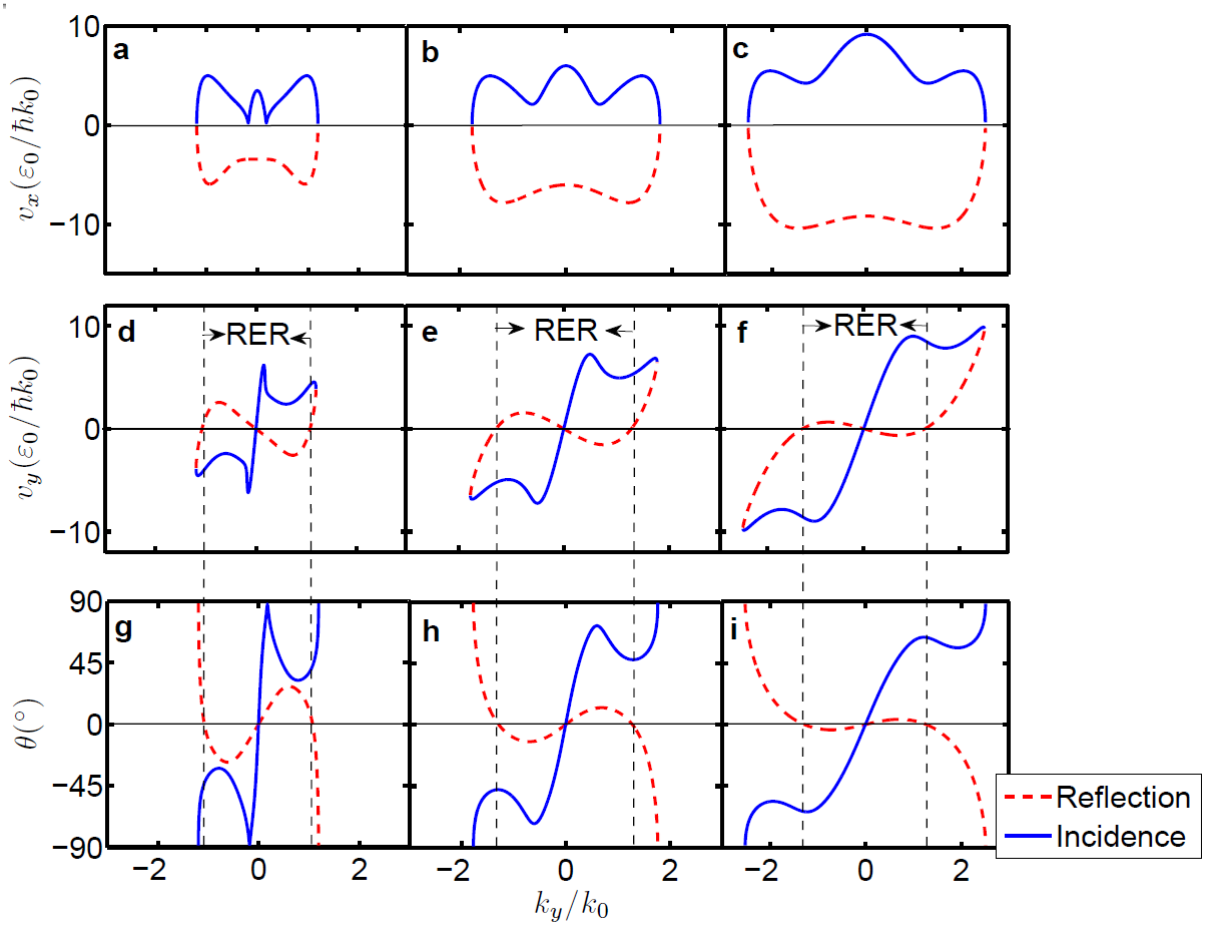

Figure 5.3: (a)-(c) Group velocity component v_x; (d)-(f) group velocity component v_y; and (g)-(i) incident and reflection angles of an incident K valley electron in states k_y. The energies are $\varepsilon_k = 0.5\varepsilon_0$, $\varepsilon_k = 2\varepsilon_0$ and $\varepsilon_k = 5\varepsilon_0$ respectively for column 1, 2 and 3. In (a)-(c), v_x is positive for incident electrons and negative for reflected electrons. The RER regime is enclosed between the dashed lines in (d)-(i). In (d)-(f), sign reversal of v_y corresponds to RER. In (g)-(i), the reflection angle of RER does not change sign since electron is reflected to the same side of the normal. At small ε_k, almost all of the permissible reflections are RER. As E_k increases, more permissible states becomes specular reflection states (which lies outside the RER windows) and the RER angle approaches 0°.

The group velocity component v_y is the most important quantity in determining the electron reflection type [Fig. 5.3(d)-(f)]. Sign reversal of v_y at a fixed k_y indicates RER (enclosed by dotted lines in the Fig. 5.3(d)-(i). The incident electron v_y reaches a sharp maximum when the band contour is flattened as k_y increases. At $k_y \gtrsim 1.3k_0$, v_y no longer changes sign upon reflection and the reflection becomes specular. At small ε_k, almost all permissible reflection states are within the RER window and hence RER is dominant. The specular reflection states (outside the RER window) expands as ε_k increases, making RER relatively less profound. At $\varepsilon_k = 5\varepsilon_0$ [Fig. 5.3(f)], more than half of the permissible k_y corresponds to specular reflection.

The *non-uniqueness* of θ is obvious in Fig. 5.3(g)-(i), i.e. multiple sets of v_x and v_y produce the same θ. In contrast to v_y, RER requires the sign of θ to remain unchanged upon reflection since in an retro reflection the electron is reflected to the same side of the normal of incidence. Due to the asymmetric constant energy band contour in k-space, the retro-reflected electrons do not trace back the incident path. Instead, they are mostly retro-reflected with smaller angle, maximally about 20°. The reflection angle approaches zero with increasing ε_k as the constant energy band contour becomes 'smoother' and loses the anisotropic band contour required to effectively produce large-angle RER. At $\varepsilon_k > 10.9\varepsilon_0$, the reflection θ drops below zero, i.e. reflected electrons are placed on the opposite side of the incident normal, and therefore all electron reflection becomes specular-type.

Since the BLG energy spectrum is highly anisotropic, the relative orientation between BLG and the superconductor is expected to crucially affect the electron reflection. In the case of a BLG-heterojunction oriented along the *zigzag* direction of BLG, the RER completely disappears. This is because the band structure is rotated by 90°. The constant energy band contour of the incident states becomes identical to that of the reflected states. This violates the RER criteria (ii)as mentioned above. This signifies the importance of criteria (ii) as a fundamental RER requirement.

5.3 Absence of Andreev reflection in a BLG/S junction

In this section, we utilize a hybrid junction made up of a bilayer graphene and a superconductor (BLG/S) to demonstrate the unusual RER phenomena. We consider a ballistic BLG/S junction at low temperature where the BLG is in the region $x < 0$ and the superconductor is in the region $x > 0$. The interface locates at $x = 0$ (along the y-axis). We assume that the Fermi wavelength λ_F is much shorter than the BCS coherence length and the London penetration depth. In general, the relevant dimensions of the NS device are of the same order of magnitude as λ_F. The Fermi levels of them align in line if no bias is applied across the junction. Thus, the physics on the scale of λ_F can be described by Bogoliubov-de Genne (BdG) equations, $H\Psi(\mathbf{r}) = \varepsilon\Psi(\mathbf{r})$, where H is the Hamiltonian describing the excitation in the BLG/S junction. Explicitly, it is written as

$$H = \begin{bmatrix} \mathcal{H}_\xi - \varepsilon_F & \Delta \\ \Delta^* & \varepsilon_F - \mathcal{H}_\xi \end{bmatrix} \tag{5.5}$$

where ε_F is the Fermi energy and $\Delta = \Delta^*$ is the isotropic superconductor pair potential of s-wave type. We further assumed that the superconductivity is induced intrinsically in BLG via the proximity effect [135], and thus avoiding lattice mismatch problems. The reflection coefficients can then be obtained by solving the BdG equation and matching the wavefunctions at the boundary [136]. We first obtained the excitation spectrum of the BLG/S junction from Eq. 5.5:

$$E_k = \sqrt{\Delta^2 + (\varepsilon_F \pm \varepsilon_k)^2} \qquad \tilde{E}_k = \sqrt{\Delta^2 + (\varepsilon_F \pm \tilde{\varepsilon}_k)^2} \tag{5.6}$$

for K and K' valley respectively. In BLG side ($x < 0$), the pair potential vanishes, and the excitation spectrum is given as $E_k = \varepsilon_F \pm \varepsilon_k$ where upper (lower) sign denotes hole (electron) branch. Similarly, for K' valley, we have $\tilde{E}_k = \varepsilon_F \pm \tilde{\varepsilon}_k$. When an incident electron from K valley incidents on the interface, it must couple with a K' electron

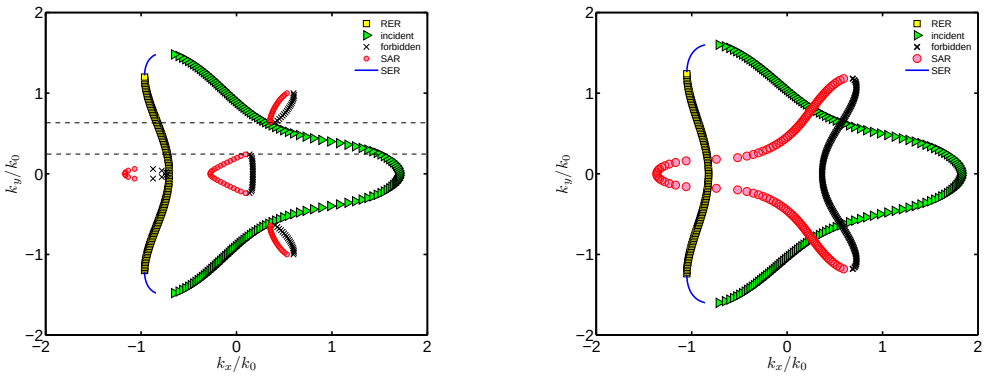

Figure 5.4: (Left) Regime A1 and (right) Regime A2 excitation spectrum

so that the total momentum of the Cooper pair is zero. Therefore, the Andreev holes must originate from the K' valley.

The following assumption will be used: (i) There is no lattice mismatch, the superconductor part is induced by proximity effect on BLG [135]; (ii) there is a large Fermi wavevector mismatch between BLG and S, i.e. $\lambda_F \gg \lambda'_F$, so that the transmitted mode in S is always perpendicular to the BLG/S interface; and (iii) $\varepsilon_F > \varepsilon_0/4$ is considered. In low energy regime of $\varepsilon_F < \varepsilon_0/4$, the conduction electron bands are split into four energy pockets. Such low energy regime is practically impossible unless extremely pure sample is used, and hence it will not be considered in this work.

The energy regimes can be subdivided into four regimes: (A1) and (B1) $\varepsilon_F + \frac{\varepsilon_0}{4} > E_k > \varepsilon_F$ where electron branch is continuous and hole branch is sperated into pockets; (A2) and (B2) $E_k > \varepsilon_F + \frac{\varepsilon_0}{4}$ where both eletron and hole branches are continuous. The holes in (A1) and (A2) cases are valence holes while those in (B1) and (B2) cases are conduction holes. In Fig. 5.4, the excitation spectrum of Regime (A1) and (A2) are shown. The types of reflection are also labeled. It can be seen that since valence holes are involved, the Andreev reflection in these Regimes are solely specular type.

Regimes (A2) and (B2) are the simpler cases since the hole branch are continuous and the coefficients can be solved from a simple 4×4 matrix. Results for regimes (A1) and (B1) can be obtained via similar calculations. We use k to denote x-component of the wavevector and q to denote y-component of the wavevector. The incident ($\circ$), reflected electron (e), and reflected hole (h) wavefunctions are given

as $\psi_0 = \exp(ik_0x+iqy)\begin{bmatrix}1\\ \zeta_0\\ 0\\ 0\end{bmatrix}$ $\psi_e = \exp(ik_ex+iqy)\begin{bmatrix}1\\ \zeta_e\\ 0\\ 0\end{bmatrix}$ $\psi_h = \exp(ik_hx+iqy)\begin{bmatrix}0\\ 0\\ 1\\ -\zeta_h\end{bmatrix}$ The k's can be solved from the excitation energy at a given q and $E_k^{(e,h)}$. The hole reflection is *inter*-valley in order to form zero-momentum Cooper pair in superconducting side. The ζ's are given as

$$\zeta_0 = \varepsilon_0 \frac{-(k_0 - iq)^2 + (k_0 + iq)}{\varepsilon_F + E_k} \tag{5.7}$$

$$\zeta_e = \varepsilon_0 \frac{-(k_e - iq)^2 + (k_e + iq)}{\varepsilon_F + E_k} \tag{5.8}$$

$$\zeta_h = \varepsilon_0 \frac{-(k_h + iq)^2 - (k_h - iq)}{E_k - \varepsilon_F} \tag{5.9}$$

The K' valley states are given as $\tilde{\psi}_0 = \exp(i\tilde{k}_0x + iqy)(1, \tilde{\zeta}_0, 0, 0)^T$, $\tilde{\psi}_e = \exp(i\tilde{k}_ex + iqy)(1, \tilde{\zeta}_e, 0, 0)^T$ and $\tilde{\psi}_h = \exp(i\tilde{k}_hx + iqy)(0, 0, 1, -\tilde{\zeta}_h)^T$, where $\tilde{k}$ can be solved from the $\tilde{E}_k$. The $\tilde{\zeta}$'s are given as:

$$\tilde{\zeta}_0 = \varepsilon_0 \frac{-(\tilde{k}_0 + iq)^2 - (\tilde{k}_0 - iq)}{\varepsilon_F + \tilde{E}_k} \tag{5.10}$$

$$\tilde{\zeta}_e = \varepsilon_0 \frac{-(\tilde{k}_e + iq)^2 - (\tilde{k}_e - iq)}{\varepsilon_F + \tilde{E}_k} \tag{5.11}$$

$$\tilde{\zeta}_h = \varepsilon_0 \frac{-(\tilde{k}_h - iq)^2 + (\tilde{k}_h + iq)}{\tilde{E}_k - \varepsilon_F} \tag{5.12}$$

The *total* wavefunction in BLG for each electron/hole states is the superposition of K and K' states, i.e. $\Psi_{(n)} = \frac{\psi_{(n)} + \tilde{\psi}_{(n)}}{2}$ where $n = (0, e, h)$ for incident, electron and hole respectively. The K and K' valley total wavefunction, $\Psi_{(n)}$, is not required in the case of single layer graphene calculation because the two valleys are isotropic in k-space [99]. It is, however, mandatory in BLG/s case since the constant energy band contour between the two valleys are *inequivalent* in k-space. In the superconducting side, the electron-like and hole-like wavefunctions are given as

$$\phi_e = \exp(ik_e^{(S)}x + iq^{(S)}y)\begin{bmatrix} u \\ u\chi_e \\ v \\ v\chi_e \end{bmatrix} \qquad \phi_e = \exp(ik_h^{(S)}x + iq^{(S)}y)\begin{bmatrix} v \\ v\chi_h \\ u \\ u\chi_h \end{bmatrix}$$

and the χ's are given as

$$\chi_m = \varepsilon_0 \frac{-(X_m - iY)^2 + (X_m + iY)}{|-(X_m - iY)^2 + (X_m + iY)|} \tag{5.13}$$

where $m = (e, h)$ for electron and holes respectively and $X_m = k_m^{(s)}/k_0$, $Y = q^{(S)}/k_0$ are the wavevectors in superconducting side. For K' valley,

$$\tilde{\phi}_e = \exp(i\tilde{k}_e^{(S)}x + iq^{(S)}y)\begin{bmatrix} u \\ u\tilde{\chi}_e \\ v \\ v\tilde{\chi}_e \end{bmatrix} \qquad \tilde{\phi}_e = \exp(i\tilde{k}_h^{(S)}x + iq^{(S)}y)\begin{bmatrix} v \\ v\tilde{\chi}_h \\ u \\ u\tilde{\chi}_h \end{bmatrix}$$

where

$$\tilde{\chi}_m = \varepsilon_0 \frac{-(\tilde{X}_m + iY)^2 - (\tilde{X}_m - iY)}{|-(\tilde{X}_m + iY)^2 - (\tilde{X}_m - iY)|} \tag{5.14}$$

and $\tilde{X}_m = \tilde{k}_m^{(s)}/k_0$. Assume that the transmitted modes are just above Δ in the superconductor, then $k_m^{(S)} = k_{F,m}\cos\theta^{(S)}$ where $k_{F,m}$ are the two real solutions of k from $E_k = \Delta$. Due to the large Fermi mismatch $\varepsilon_F^{(S)} \gg \varepsilon_F$, it can be safely assumed that $\theta^{(S)} = 0$ and hence $q^{(S)} = 0$, $k_m^{(S)} = k_{F,m}$. The spinor component can then be solved to obtain $\chi_e = \chi_h = \tilde{\chi}_e = \tilde{\chi}_h = -1$. This equality relation between the transmitted spinor components is the key condition that leads the dissapearance of Andreev reflection. Matching the wavefunction at the interface between BLG and

the superconductor, i.e. $\Psi_0 + r_e\Psi_e + r_h\Psi_h = a\Phi_e + b\Phi_h$ at $x = 0$, we obtained

$$\begin{bmatrix} 1 & 0 & -u & -v \\ \frac{\zeta_e+\tilde{\zeta}_e}{2} & 0 & u & v \\ 0 & 1 & -v & -u \\ 0 & -\frac{\zeta_h+\tilde{\zeta}_h}{2} & v & u \end{bmatrix} \begin{bmatrix} r_e \\ r_h \\ a \\ b \end{bmatrix} = \begin{bmatrix} -1 \\ -\frac{\zeta_0+\tilde{\zeta}_0}{2} \\ 0 \\ 0 \end{bmatrix} \tag{5.15}$$

where the coefficients are arranged in the order of $(r_e, r_h, a, b)^T$ respectively for electron, hole reflections, electron- and hole-like transmission. Since $\chi_e = \chi_h = \tilde{\chi}_e = \tilde{\chi}_h = -1$, r_e can be immediately decoupled from the other coefficients:

$$r_e = -\frac{1 + \frac{\zeta_0+\tilde{\zeta}_0}{2}}{1 + \frac{\zeta_e+\tilde{\zeta}_e}{2}} \tag{5.16}$$

The ζ's are interlinked by $\zeta_0 = \tilde{\zeta}_e$ and $\zeta_e = \tilde{\zeta}_0$ due to the reversed constant energy band contour of the electron branches. Hence, $r_e = -1$ and $r_h = 0$. The normalized electron reflection *probability* is given as

$$R_e = \frac{v_x^{(r)} + \tilde{v}_x^{(r)}}{v_x^{(i)} + \tilde{v}_x^{(i)}} |r_e|^2 \tag{5.17}$$

where $v_x^{(i,r)}$ are the incident and reflected x-direction group velocities respectively in K valley, and $\tilde{v}_x^{(i,r)}$ are the incident and reflected x-direction group velocity in K' valley. Since the constant energy band contour of the K and K' electron in k-space are reversed, it can be immediately seen that $\tilde{v}_x^{(i,r)} = v_x^{(r,i)}$. Therefore, the normalized electrons and hole reflection probabilities are:

$$R_e = 1 \tag{5.18}$$

and

$$R_h = 0 \tag{5.19}$$

We see that AR is completely absent in a BLG/S junction. The absence of AR is related to the Klein reflection in BLG. In the case of BLG modeled by isotropic

and parabolic energy dispersion, electrons incident normal to a potential barrier are backscattered with unit-probability since the transmission mode normal to the interface is evanescent as encoded in the 2π Berry phase of its spinor wavefunction [4, 137]. Although direct transport measurement on the 2π backscattering of electrons in BLG has not been reported up to date, quantum Hall measurements on bilayer graphene has clearly indicated that it has a 2π Berry phase [137]. The 2π Berry phase is also retained when the low energy anisotropy is included [138]. Due to the large Fermi mismatch at the junction ($\varepsilon_F^{(S)} \gg \varepsilon_F^{(BLG)}$), the transmission modes are always perpendicular to the interface for any incident angles and hence instead of perfect electron *backscattering* at only normal incidence, electrons reflect with unit probability at any incident angles in a BLG/S junction. Mathematically, this can be seen from the spinor-form of the BLG low energy electron wavefunctions. The transmitted spinor-wavefunction in the superconductor side for electron-like and hole-like excitations are, respectively,

$$\phi_e = (u, v) \otimes (\psi_{A\uparrow}^{(i)}, \psi_{B\downarrow}^{(i)})$$

$$\phi_h = (v, u) \otimes (\psi_{A\uparrow}^{(r)}, \psi_{B\downarrow}^{(r)}) \tag{5.20}$$

where u and v are the BCS coherence factors, $\psi_{A\uparrow}^{(i,r)}, \psi_{B\downarrow}^{(i,r)}$ corresponds to the wavefunction amplitude at sub-lattice $A\uparrow$ and $B\downarrow$ respectively. The superscript (i, r) denotes incidence and reflection states respectively.

Upon transmission, the normal-transmitted spinor follows the equality $\psi_{B\downarrow}^{(i)} = \psi_{B\downarrow}^{(r)}$. This essentially uncouples the electron-reflection coefficient from the other transmission/hole-reflection coefficients, resulting in our angular-independent result: $R_e = 1$ (Fig. 5.5). This aspect is in contrast to the single layer graphene/superconductor junction (SLG/S) where electrons reflect in an entirely opposite way: AR occurs with unit-probability only at normal incidence [99]. The perfect transmission of electrons at normal incidence is a signature of the π Berry phase of the massless Dirac fermions [4, 139]. The superconducting wavefunction in SLG/S is in the form of $\psi_A^{(i,r)}, \psi_B^{(i,r)}$

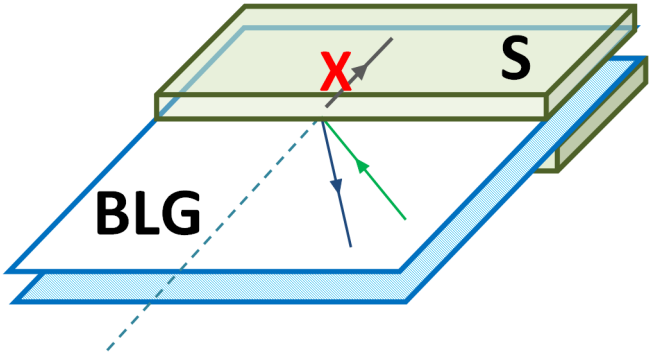

Figure 5.5: RER in BLG/S junction. Green, blue and gray arrows indicate incident electron, retro-reflected electron and transmitted quasiparticle respectively. Transmission across the junction is forbidden due to the 2π Berry phase nature of bilayer graphene electron. The junction is hence 100% electron-reflective.

where subscripts A and B correspond to the wavefunction amplitudes at the two inequivalent sub-lattices A and B respectively. Upon transmission, the spinor follows a rather different relation of $\psi_B^{(i)} = -\psi_B^{(r)}$. The hole and electron reflection coefficients are coupled with each others in this case and hence the AR reflection coefficient has a incident angle dependence.

5.4 BLG/S junction as a valley-selective Veselago electron-mirror

The nature of RER in BLG/S is related to Veselago optics [140]. A Veselago electron-lens based on single layer graphene (SLG) and BLG p-n junctions has previously been reported [34, 141]. Such junctions are Veselago electron-lenses because of the negative electron refractive index. In SLG, the negative electron refractive index originates from the existence of a lower Dirac sub-band which has opposite quasiparticle dynamics in comparison with the upper Dirac sub-band [141]. In BLG, the negative electron refractive index originates from its anisotropic constant energy band contour [34]. In contrast to a Veselago electron-*lens*, BLG/S is equivalent to a Veselago electron-*mirror*.

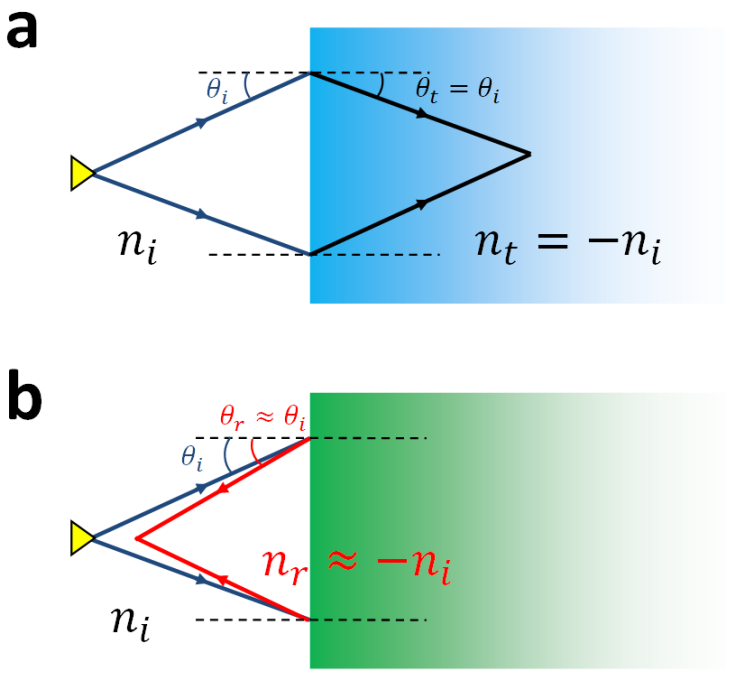

Figure 5.6: Schematic drawings of (a) Veselago lens with $n_t = -n_i$; and (b) Veselago mirror $n_r \approx -n_i$. In the Veselago lens, a ray emitted from a point source (denoted by yellow triangle) is focused at the transmitted side of the interface. For the Veselago mirror, $n_r \approx -n_i$ is chosen for better visual clarity. The retro-reflected ray is focused at the incident side of the interface.

In optics, ray refraction is governed by Snell's Law

$$n_i \sin\theta_i = -n_t \sin\theta_t \tag{5.21}$$

where n_i and n_t are the refractive index at the incident side and at the transmitted side respectively. A negative sign is added to the right hand side of Eq. (5.21) since we define the reflection angle θ_r to have the same sign as the incident angle θ_i if the reflected ray is on the same side of the normal of incidence as the incident ray. For simplicity, we consider a Veselago *lens* with $n_t = -n_i$. Since $\theta_i = \theta_r$ the transmitted ray is placed at the 'wrong' side of the normal of incidence and this results in the transmitted ray, originating from a point source, being re-focused after propagating a certain distance in the transmission side of the interface [Fig. 5.6(a)]. The Veselago lens is therefore a flat lens with ray-focusing behavior. For the *reflection* problem, a reflection 'Snell's Law' can also be written as $n_i \sin\theta_i = -n_r \sin\theta_r$ where n_r is the refractive index on the reflected side. The reflection 'Snell's Law' is however

redundant in the usual case, since reflection occurs in the same medium where $n_r = n_i$ and hence $\theta_r = -\theta_i$. To construct a Veselago *mirror*, we consider a hypothetical *anisotropic* medium with $n_r = -n_i$, i.e. the refractive index of the medium undergoes a sign change when a ray travels in the opposite direction with respect to the incident ray. This leads to the retro-reflection condition of $\theta_r = \theta_i$. The reflection interface is Veselago-like since the reflected ray is placed at the 'wrong' side of the incident normal. The retro-reflected rays, emitted from a point source, trace back their original incident path and are re-focused at the incident side of the interface [Fig. 5.6(b)]. The interface can therefore be regarded as a flat Veselago *mirror* with ray-focusing behavior. It becomes obvious that the RER effect in BLG/S is equivalent to a Veselago electron-mirror. In BLG/S, the absence of AR makes the interface a perfect electron-mirror and the RER process is Veselago-like. BLG/S is therefore a flat Veselago electron-mirror with electron focusing ability.

In BLG, the low energy electrons reside in two inequivalent K and K' valleys. Intervalley scattering is strongly suppressed [142]. Devices utilizing this robust valley degree of freedom in graphene, *valleytronics*, have been proposed [27]. The first step towards valleytronics is a valley polarizer. The RER phenomena of BLG/S junction offers another simple way to separate electrons from different valleys without the need of cutting [27], straining [143], terahertz laser-irradiating [144] or selective-damaging [28] graphene. The K and K' electron excitation spectrum of BLG/S has an opposite constant energy band contour [Fig. 5.7(a) and Fig. 5.7(b)]. The reflection states in the K valley have a much 'smoother' constant energy band contour [Fig. 5.7(a)] than the reflection states in the K' valley [Fig. 5.7(b)]. This immediately suggest that the electron reflection in BLG/S is valley-selective. In Fig. 5.7(c), it can be seen that the K electrons are predominantly retro-reflected with small angle $\theta < 20°$ while the K' electrons are predominantly retro-reflected with large angle $50° < \theta < 70°$. SER occurs only at the upper and lower tips of the constant energy band contour when $|k_y|$ is large. It should be emphasized that valley-selective reflection is only possible when electrons undergo retro-reflection. The specularly reflected electrons are always

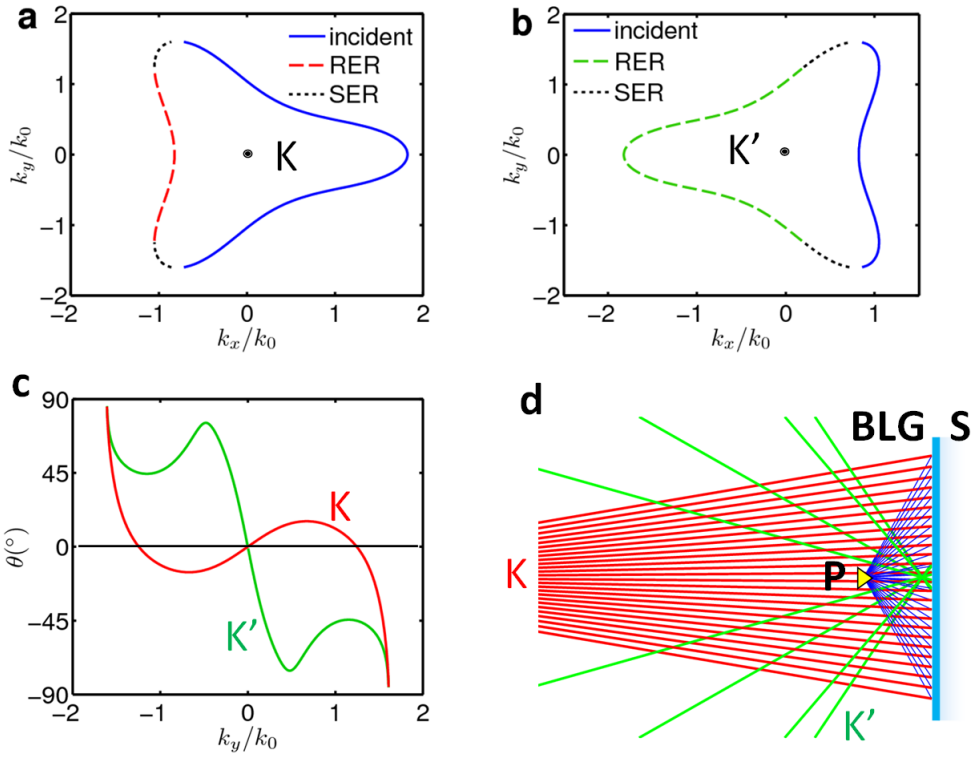

Figure 5.7: The electron excitation spectrum of BLG/S at (a) a K valley and (b) a K' valley with $\varepsilon_F = 0.5\varepsilon_0$ and $E_k = \varepsilon_0$. The RER constant energy band contour of the K valley (red dashed curve) is significantly 'smoother' than that of the K' valley (green dashed curve). At large $|k_y|$ (SER regime), K and K' band contours become approximately identical; (c) Reflection angles of K (red curve) and K'(green curve) electrons. K electrons are predominantly focused via smaller angle ($< 20^\circ$) than that of the K' electrons ($\approx 80^\circ$). (d) RER trajectory of electrons emitted from a point source situated at **P** (denoted by yellow triangle). Blue rays represent the incident electrons. The interface acts as a valley-selective dual-focus electron mirror with K electrons (red rays) being focused further away from the interface than the K' electrons (green rays).

divergently reflected and the valley states are mixed since the upper and lower 'tips' of the constant energy band contour at large $|k_y|$ are approximately identical for both K and K' valleys. In Fig. 5.7(d), the RER trajectory of electrons injected from a point source is shown. The BLG/S junction acts as a valley-selective dual focusing electron mirror with K electrons being focused further away from the junction due to the 'smoother' constant energy band contour of K reflection states while K' electrons are focused closer to the junction due to the 'sharper' constant energy band contour of K' reflection states.

5.5 Discussion

It should be emphasized that the RER is more profound in the low energy regime of $\varepsilon_k \approx \varepsilon_0$. This requires high quality samples with carrier concentrations $n \approx 10^{11}\text{cm}^{-2}$ [70] which is experimentally achievable [145]. RER does not survive in energy regimes higher than $\varepsilon_k > 10.9\varepsilon_0$ since the reversal of v_y upon reflection can no longer occur as the anisotropy of the constant energy band contour is lost.

The absence of AR in a BLG/S junction at low energy regimes is in agreement with previous study on BLG/S junction utilizing a four-band model without low energy band anisotropy [102]. It was shown that AR in BLG is a small effect in the order of E_k/γ_1. Here we further demonstrate that AR is not only a small effect but is completely absent in the low energy regime.

RER and the Veselago mirror effect discussed in this Chapter shall occur in any BLG-based heterojunction as long as the quasiparticle energy involved is in the trigonal warping regime of the BLG energy dispersion. One obvious advantage of utilizing BLG/superconductor junction as a model structure to demonstrate RER is that electron transmission is strictly forbidden in this junction. This provides a purely reflective interface which serves as a very ideal platform to demonstrate the RER and Veselago mirror effect.

In conclusion, we theoretically show the existence of RER in BLG. The RER represents one last missing piece in the quantum transport phenomena of a superconducting interface where specular reflection of electrons, and retro and specular reflection of holes have all been demonstrated [99, 134, 146–150]. In a BLG/S hybrid junction, AR is expected to be completely absent in the low Fermi level regime due to the 2π Berry phase of the BLG quasiparticles. The valley-inequivalent RER in BLG/S is analogous to a valley-selective Veselago electron-mirror. The valley-selective dual-focusing behavior suggests a potential application in the field of valleytronics.

6 | Chiral-like tunneling in 2D semiconductors with Rashba spin-orbit coupling

* In this Chapter, we study the quantum tunneling of electron in a two-dimensional semiconductor with Rashba spin-orbit coupling (R2DEG). In SLG, the linear energy band of opposite pseudospin crosses at the Dirac point whereas in BLG, the opposite pseudospin bands are parabolic (and hence there exists a band turning point) and they touch at the Dirac point without any band crossing. In R2DEG, parabolic branch of opposite spin crosses at a Dirac-like point and has a band turning point. The quantum transport in this system therefore shows hybrid behavior of both *massless* chiral fermion (mCF) and *massive* chiral fermion (MCF) and we observe transport properties not found in usual two-dimensional electron gas. Albeit its π Berry phase, electron backscattering is present in R2DEG.

6.1 Real spin chiral-like tunneling of electrons in R2DEG

When a massless chiral fermion encounter a potential barrier, reflection is completely suppressed due the forbidden spin-flip transition, a phenomenon known as Klein tunneling [5]. The conservation of spin therefore leads to the perfect transmission of

*This Chapter is based on *Sci. Rep.* **4**, 3780 (2013)

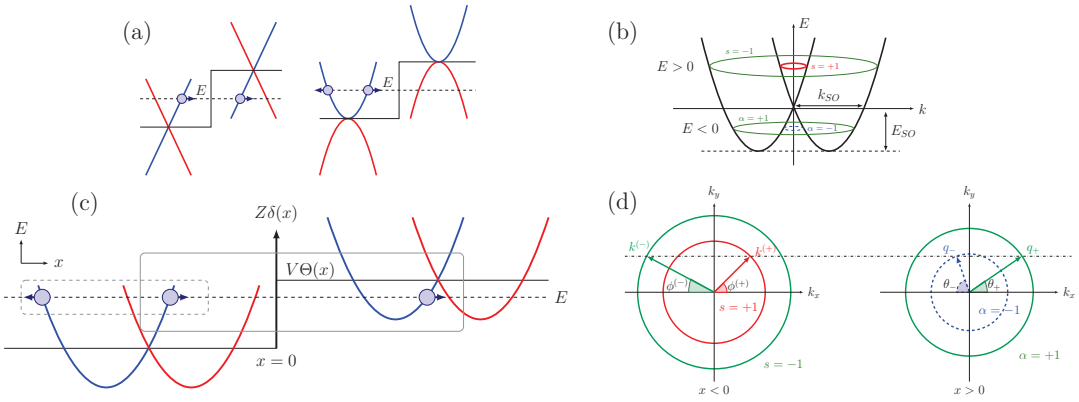

Figure 6.1: Klein effect in condensed matter systems at normal incidence. (a) perfect transmission of massless chiral fermion in SLG and perfect reflection of massive chiral fermion in BLG. (b) Band structure of R2DEG. (c) Simultaneous mixture of massless and massive chiral fermions transport across a potential barrier $V(x)$ in R2EG. The tunneling process (outlined by solid box) mimics massless chiral fermion while the reflection process (outlined by dahsed box) mimics massive chiral fermion. In (a) - (c), the arrows denote the direction of motion of the quasiparticles and electrons. The blue and red branches denote the decoupled branches of opposite pseudospin [(a) and (b)] and real-spin [(c)] at normal incidence. (d) Fermi contours at the incident side ($x < 0$) and at the transmitted side ($x > 0$).

electrons through a high and wide potential barrier at normal incidence [Fig. 6.1(a)]. The 'Klein tunneling' was first described by Klein as a paradoxical behavior of a relativistic electron [5]. In single layer graphene (SLG), electrons at the vicinity of K-point follows linear energy dispersion and are chiral in the sense that the pseudospin, which represents the relative contribution from the sublattices, is locked to the direction of electron motion [54]. The low energy electron in SLG is equivalent to a spin-1/2 massless chiral fermion in relativistic quantum mechanics [3]. Due to the relativistic description of the Dirac quasiparticle, SLG serves as an ideal scaled-down platform to demonstrate the anomalous Klein tunneling in condensed matter systems [4, 6, 7]. In bilayer graphene (BLG), the low energy electrons mimic spin-1 massive chiral fermions. In contrast to SLG, electrons in BLG are reflected perfectly by a potential barrier at normal incidence [Fig. 6.1(a)]. Since such a perfect reflection of electrons is chiral in nature, it can be regarded as a 'Klein reflection' effect which has no counterpart in relativistic quantum mechanics.

In R2DEG, the crossing of the two spin-split subbands generates a Dirac-like point. Furthermore, the subbands are parabolic in k and has a band turning point.

We therefore expect the transport phenomena at the vicinity of the subband crossing point to exhibit hybrid behavior of mCF and MCF. It is the main objective of this Chapter to investigate the quantum tunneling of electron at the vicinity of the band-crossing point. We first consider the R2DEG Hamiltonian [84, 115, 116]:

$$H = \frac{p^2}{2m^*} + \frac{\lambda}{\hbar}(\sigma \times \mathbf{p}) \cdot \mathbf{e}_z. \tag{6.1}$$

Here λ is the Rashba spin-orbit coupling parameter and m^* is the electron effective mass. The eigenvalue is given as $E_s(k) = \hbar^2 k^2/2m^* + s\lambda k$ ($s = \pm 1$). The band structure of R2DEG is shown in Fig. 6.1(b). The parabolic band of electrons with opposite spin are left-right shifted by $k_{SO}m^*\lambda/\hbar^2$ in phase-space, giving rise to a subband crossing point (X-point) at $k = 0$. The energy difference between X-point and the subband minima is characterized by $E_{SO} = m^*\lambda^2/2\hbar^2$. The chirality of the quasiparticle in SLG and BLG is usually defined as the projection of the pseudospin on the direction of motion of the particle [4, 151], i.e. $\hat{v} \cdot \hat{\sigma}$, where $\hat{v}$ and $\hat{\sigma}$ are the unit vector of the group velocity and pseudospin direction. In R2DEG, the spin polarization lies in the plane of the electron gas and is perpendicular to the electron wavevector. It is not possible to define 'chirality' using the same dot product method. However, all electrons residing in a particular Fermi circle do follow a fixed $\hat{v} \times \hat{P}$ relation where $\hat{P}$ is the direction of real-spin and hence the electrons can be regarded as 'chiral-like'. Such description allows us to link the real-spin chiral-like tunneling phenomena in R2DEG directly with the pseudospin chiral tunneling effect in SLG and BLG. Furthermore, the two branches of opposite pseudospins crosses and touches, respectively, in SLG and BLG. The crossing and touching points are commonly known as the 'Dirac point' due to the relativistic dynamics of the quasiparticles. In R2DEG, the spin splitting, and hence the formation of the X-point, has its root from the relativistic effect of the electrically confined electrons (which manifests itself as a Rashba Hamiltonian linear in k). This justifies the interpretation of the electron tunneling across the Dirac-like X-point in R2DEG as a chiral-like tunneling phenomena.

The energy dispersion of electrons at the vicinity of the X-point is nearly linear

and therefore closely resembles the mCF in SLG. Additionally, electrons at the vicinity of the subband minima are furthest away from the linear X-point and exhibits the strongest parabolicity. As a result, these electrons mimic the MCF in BLG. As shown in Fig. 1(c), an incident electron can only be scattered by a potential barrier to states lying in the same spin-split subband in order to conserve real-spin. For transport electron of a given energy with respect to the X-point, two possibilities arise: (1) electron transmission to a spin non-flipping state below the X-point or (2) electron reflection to a spin non-flipping state above the X-point. Phenomenally, process (1) is in the same spirit as the Klein tunneling of mCF in SLG while process (2) is more akin to the Klein reflection of MCF in BLG. The quantum transport of electron across a potential barrier in R2DEG can thus exhibit both mCF-like and MCF-like behaviors.

The electron transport across a potential barrier $V(x)$ in R2DEG is governed by the Hamiltonian

$$H(x,k) = \begin{pmatrix} \frac{\hbar^2 k^2}{2m^*} + V(x) & \lambda(k_y + ik_x) \\ \lambda(k_y - ik_x) & \frac{\hbar^2 k^2}{2m^*} + V(x) \end{pmatrix}. \tag{6.2}$$

We model the potential barrier by $V(x) = \Theta(x)V_0 + \delta(x)Z$, where $\Theta(x)$ is a Heaviside step function, $\delta(x)$ is a Dirac delta function, V_0 and Z denotes the height of the step potential and the strength of an interface potential respectively [Fig. 6.1(c)].

In order to make parallel comparison with the chiral tunneling of electrons in SLG and BLG, we consider only the case where incident state lies above the X-point with $E > 0$ and the transmitted state lies below the X-point with $E < 0$. This sets up an incident energy condition of $V_0 > E > V_0 - E_{SO}$. For electrons incident from the left of the junction with $x < 0$, an $E > 0$ constant energy surface intersects both $s = \pm 1$ branches at two concentric circles of radius $k^{(s)} = \sqrt{2m/\hbar^2(E_{SO} + E)} - sk_{SO}$. For transmitted electron at $x > 0$, an $E < 0$ constant energy surface intersects only the $s = -1$ branch. However, due to the existence of a subband turning point (i.e. the subband minimum), the constant energy surface again intersects two concentric circles of radius $q_\alpha = k_{SO} + \alpha\sqrt{2m/\hbar^2(E_{SO} + E - V)}$ where $\alpha = \pm 1$ [Fig. 6.1(d)].

Unlike SLG and BLG where $s = -1$ states are always hole-like in the sense that the motion of electron is antiparallel to its wavevector, the $s = -1$ branch states of R2DEG are electron-like in the outer circle $\alpha = +1$ and hole-like in the inner circle $\alpha = -1$. The existence of hole-like states in the $s = -1$ branch suggests that negative electron refraction and electron focusing effect [152, 153], previously reported in SLG [43], BLG [141] and topological insulator [34, 154], can also be realized in R2DEG via transmission of electrons to $\alpha = -1$ circle of the $s = -1$ branch.

6.2 Transmission and reflection probabilities

In this section, we briefly derive the transmission and reflection probabilities. The probabilities are obtained using the standard wavefunction matching formalism [155].The eigenstates of Eq. (6.2) for the electrons in $x < 0$ and $x > 0$ are given as $\xi^{(s)} = 1/\sqrt{2}(1, -sie^{i\phi^{(s)}})^T$ and $\xi_\alpha^{(-)} = 1/\sqrt{2}(1, ie^{i\theta_\alpha})^T$, respectively. Generally, an electron in s-state incident from $x < 0$ to $x > 0$ can be reflected to s and $-s$ branches in the region $x < 0$, or be transmitted to $\alpha = \pm 1$ states in the region $x > 0$. The reflection and transmission angles, ϕ's and θ's, are related by the conservation of momentum component parallel to the interface, i.e. $k^{(s)} \sin\phi^{(s)} = k^{(-s)} \sin\phi^{(-s)} = q_\alpha \sin\theta_\alpha^{(-)}$ where $k^{(s)}$ and $\phi^{(s)}$ are the incident wavevector and angle respectively. We construct the total LHS and RHS wavefunctions: Ψ_L and Ψ_R, and the transmission/reflection probabilities can be obtained by connecting Ψ_L and Ψ_R via the boundary conditions: $\Psi_L|_{x=0} = \Psi_R|_{x=0}$ and $\Psi'_R|_{x=0} - \Psi'_L|_{x=0} = (2mZ/\hbar^2)\,\Psi_R\,|_{x=0}$.

On the incident side where $x < 0$, the total wavefunction is given as

$$\Psi_L = \xi^{(s)} e^{ik^{(s)}\cos\phi^{(s)}x} + \sum_{s'=\pm 1} r_{s'}^{(s)} \xi^{(s')*} e^{-ik^{(s')}\cos\phi^{(s')}x} \tag{6.3}$$

where $s = \pm 1$, $*$ denotes complex conjugate, $\phi^{(s)}$ is the angle of incidence of an electron from s-branch and $r_{s'}^{(s)}$ denotes the reflection coefficients of $s \to s'$ reflection

process. The eigenstate is explicitly written as

$$\xi^{(s)} = \begin{bmatrix} 1 \\ -ise^{-i\phi^{(s)}} \end{bmatrix} \tag{6.4}$$

On the transmitted side where $x > 0$, the total wavefunction is given as

$$\Psi_R = t_+^{(s)} \xi_+ e^{iq_+ \cos\theta_+ x} + t_-^{(s)} \xi_-^* e^{-iq_- \cos\theta_- x} \tag{6.5}$$

where $t_\pm^{(s)}$ is the transmission coefficients to $\alpha = \pm 1$ state. The second term of Eq. (8) is a hole-like transmitted state whose direction of motion is antiparallel with its wavevector and hence it carries a factor of $e^{-iq_- \cos\theta_- x}$. The eigenstate is given as

$$\xi_\pm = \begin{bmatrix} 1 \\ \mp ise^{\pm i\theta_\alpha} \end{bmatrix} \tag{6.6}$$

Due to the conservation of y-component wavevector, k_y, the $s \to s'$ reflection angles can be obtained via $\psi^{(s')} = \sin^{-1}(k^{(s)}/k^{(s')} \sin\phi^{(s)})$ and the transmission angles in α branch can be obtained via $\theta_\alpha = \sin^{-1}(k^{(s)}/q_\alpha \sin\phi^{(s)})$, where $\phi^{(s)}$ and $k^{(s)}$ are the incident angle and wavevector respectively and $s' = \pm 1$. Ψ_L and Ψ_R can be connected by the boundary conditions at $x = 0$, i.e. $\Psi_L|_{x=0} = \Psi_R|_{x=0}$ and $d_x\Psi_R|_{x=0} - d_x\Psi_L|_{x=0} = 2mZ/\hbar^2$. This leads to a set of simultaneous equations

$$\begin{pmatrix} 1 & 1 & -1 & -1 \\ e^{i\phi^{(+)}} & -e^{i\phi^{(-)}} & -e^{i\theta_+} & e^{-i\theta_-} \\ -k^{(+)}\cos\phi^{(+)} & -k^{(-)}\cos\phi^{(-)} & -Q_+ & Q_- \\ k^{(+)}\cos\phi^{(+)} e^{i\phi^{(+)}} & -k^{(-)}\cos\phi^{(-)} e^{i\phi^{(-)}} & Q_+ e^{i\theta_+} & Q_- e^{-i\theta_-} \end{pmatrix} \begin{pmatrix} r_+^{(s)} \\ r_-^{(s)} \\ t_+^{(s)} \\ t_-^{(s)} \end{pmatrix} = \begin{pmatrix} -1 \\ se^{i\phi^{(s)}} \\ -k^{(s)}\cos\phi^{(s)} \\ -sk^{(s)}\cos\phi^{(s)} e^{i\phi^{(s)}} \end{pmatrix} \tag{6.7}$$

where $Q_\pm = q_\pm \cos\theta_\pm \pm i2mZ/\hbar^2$. The transmission and reflection coefficients can

then be solved and the probabilities are determined from

$$\begin{aligned} R_{s'}^{(s)} &= \frac{v_{s'}}{v_s}|r_{\pm}^{(s)}|^2 \\ T_{\alpha}^{(s)} &= \frac{u_{\alpha}}{v_s}|r_{\pm}^{(s)}|^2 \end{aligned} \tag{6.8}$$

where $s = \pm 1$ and $s' = \pm 1$. v_s, $v_{s'}$ and $u_{\pm}$ are the x-directional component of the incident and reflected electron group velocity at $x < 0$ and of the transmitted electron group velocity at $x > 0$ respectively, i.e.

$$\begin{aligned} v_s &= \sqrt{\frac{2}{m^*}\left(E_{SO} + E\right)}\cos\phi^{(s)} \\ v_{s'} &= \sqrt{\frac{2}{m^*}\left(E_{SO} + E\right)}\cos\phi^{(s')} \\ u_{\alpha} &= \sqrt{\frac{2}{m^*}\left(E_{SO} + E - V\right)}\cos\theta_{\alpha} \end{aligned} \tag{6.9}$$

At normal incidence, Eq. (10) reduces to

$$\begin{pmatrix} 1 & 1 & -1 & -1 \\ 1 & -1 & -1 & 1 \\ -k^{(+)} & -k^{(-)} & -Q'_{+} & Q'_{-} \\ k^{(+)} & -k^{(-)} & Q'_{+} & Q'_{-} \end{pmatrix} \begin{pmatrix} r_{+}^{(s)} \\ r_{-}^{(s)} \\ t_{+}^{(s)} \\ t_{-}^{(s)} \end{pmatrix} = \begin{pmatrix} -1 \\ s \\ -k^{(s)} \\ -sk^{(s)} \end{pmatrix} \tag{6.10}$$

where $Q'_{\pm} = q_{\pm} \pm i2mZ/\hbar^2$. Eq. (13) can be decoupled into two sets of equations:

$$\begin{cases} r_{+}^{(s)} - t_{+}^{(s)} = \frac{s-1}{2} \\ k^{(+)}r_{+}^{(s)} + Q'_{+}t_{+}^{(s)} = \frac{1-s}{2}k^{(s)} \end{cases} \tag{6.11}$$

$$\begin{cases} r_{-}^{(s)} - t_{-}^{(s)} = \frac{-1-s}{2} \\ k^{(+)}r_{-}^{(s)} + Q'_{+}t_{-}^{(s)} = \frac{-1-s}{2}k^{(s)} \end{cases} \tag{6.12}$$

Solving the above equation, we obtain

$$r_s^{(s)} = t_s^{(s)} = 0$$

$$r_{-s}^{(s)} = \frac{k^{(s)} + sQ'_{-s}}{k^{(-s)} - sQ'_{-s}}$$

$$t_{-s}^{(s)} = \frac{k^{(+)} + k^{(-)}}{k^{(-s)} - sQ'_{-s}} \tag{6.13}$$

Combine Eq. (6.8), Eq. (6.9) and Eq. (6.13), we obtain:

$$\begin{aligned} R_s^{(s)}(\phi^{(s)} = 0) &= T_{\alpha=s}^{(s)}(\phi^{(s)} = 0) = 0, \\ R_{-s}^{(s)}(\phi^{(s)} = 0) &= \frac{\left(\sqrt{1+\mathcal{E}} - \sqrt{1-\mathcal{V}}\right)^2 + 4\mathcal{Z}^2}{\left(\sqrt{1+\mathcal{E}} + \sqrt{1-\mathcal{V}}\right)^2 + 4\mathcal{Z}^2}, \\ T_{\alpha=-s}^{(s)}(\phi^{(s)} = 0) &= \frac{4\sqrt{1+\mathcal{E}}\sqrt{1-\mathcal{V}}}{\left(\sqrt{1+\mathcal{E}} + \sqrt{1-\mathcal{V}}\right)^2 + 4\mathcal{Z}^2}, \end{aligned} \tag{6.14}$$

where we define dimensionless parameters $\mathcal{E} = E/E_{SO}$, $\mathcal{V} = (V - E)/E_{SO}$ and $\mathcal{Z} = Z/\lambda$. $R_{s'}^{(s)}$ denotes the reflection probability of $s \to s'$ reflection process and $T_\alpha^{(s)}$ denotes the transmission of an s incident state into α state of $s = -1$ branch. The spinors are states of a spin component orthogonal to $\mathbf{k}$ so that the spin orientation always points in perpendicular direction to $\mathbf{k}$. At normal incidence, $R_s^{(s)}$ and $T_{\alpha=s}^{(s)}$ are strictly zero since the cross-subband processes of $s \to s$ reflection and s to $\alpha = s$ transmission requires reversal of spin orientation. Therefore only the spin non-flipping transitions of $s \to -s$ reflection and $\alpha = -s$ transmission are permissible, leading to non-zero $R_{-s}^{(s)}$ and $T_{-s}^{(s)}$ at normal incidence.

Eq. (6.14) reveals that the two parabolic branches of opposite spin are decoupled. Such decoupling is also evident in SLG and BLG at normal incidence. In fact, the decoupling of branches of opposite pseudospin is the most important condition for the Klein tunneling and the Klein reflection to occur. In SLG, the mDF energy spectrum decouples into two independent linear branches of opposite pseudospin crosses at the Dirac point whereas in BLG, the MDF energy spectrum decouples into two independent parabolic branches touching at the Dirac point. Due to this decoupling,

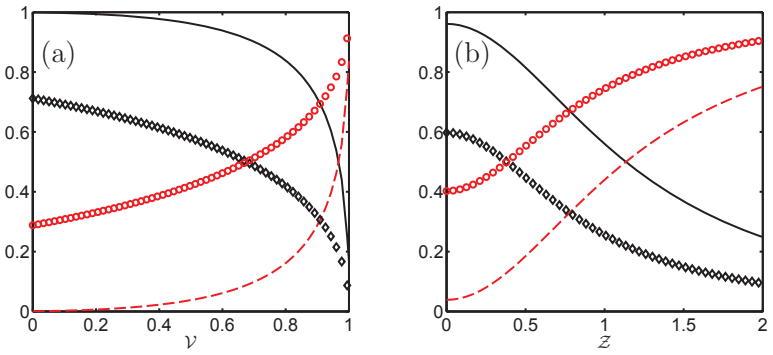

Figure 6.2: Transmission/reflection probabilites at normal incidence, (a) at different $\mathcal{V}$ with $\mathcal{Z} = 0$, solid line: $T_{-s}^{(s)}(\mathcal{E} = 0.1)$, dashed line: $R_{-s}^{(s)}(\mathcal{E} = 0.1)$, $\circ$: $T_{-s}^{(s)}(\mathcal{E} = 10)$, $\diamond$: $R_{-s}^{(s)}(\mathcal{E} = 10)$; and (b) at different $\mathcal{Z}$ with $\mathcal{E} = 1$, solid line: $T_{-s}^{(s)}(\mathcal{V} = 0.1)$, dashed line: $R_{-s}^{(s)}(\mathcal{V} = 0.1)$, $\circ$: $T_{-s}^{(s)}(\mathcal{V} = 0.9)$, $\diamond$: $R_{-s}^{(s)}(\mathcal{V} = 0.9)$.

the mDF must be confined in its own pseudospin branch and this leads to the Klein tunneling of mDF across a potential barrier. In BLG, the decoupled pseudospin branch only touches at the Dirac point without any band crossing. Since there is a band turning in the parabolic pseudospin branch, the confinement of electron within a decoupled pseudospin branch requires to electron to be reflected. In R2DEG, the decoupled real-spin branches are parabolic and has a band turning point (as in the case of BLG), and they also cross each other at the X-point (as in the case of SLG). The electron transport is therefore a hybrid of the tunneling phenomena in SLG and BLG. In Eq. (6.14), it is seen that the transmission and reflection within the same real-spin branches are both finite. This further elucidate the hybrid behavior of mCF and MCF behaviour in R2DEG.

Whether an incident electron is preferably transmitted or reflected depends on the properties of the incidence and transmission states in the R2DEG band structure and is influenced by $\mathcal{E}$ and $\mathcal{V}$. The energy parameter $\mathcal{E}$ characterizes the 'Dirac-ness' of the incident electron, with $\mathcal{E} \to 0$ representing a mCF-like incident state at the vicinity of the X-point. The potential parameter $\mathcal{V}$, ranging from 0 to 1, characterizes the 'Dirac-ness' of the transmitted electron. In the trivial case when $\mathcal{V} \to 0$, transmission state is at the vicinity of the X-point and the electrons mimic mCF of SLG. In contrast to $\mathcal{V} \to 0$, when $\mathcal{V} \to 1$, the transmission state is at the vicinity of the subband minima and the electrons is MCF-like, as in the case of BLG.

In Fig. 6.2(a), we show the crossover of the transmission/reflection probabilities from mCF-like behavior to the MCF-like behavior when $\mathcal{V}$ varies from 0 to 1 with $\mathcal{Z} = 0$. We first restrict ourselves to the extreme case of Dirac-like incident state at an energy $\mathcal{E} = 0.1$ with (i) $\mathcal{V} \to 0$ and (ii) $\mathcal{V} \to 1$. Case(i) is the trivial case where the mismatch between the incident and transmitted states is vanishingly small. In this case, electron transport occurs around the X-point and is dominated by very high transmission. For case (ii), transmission state is furthest away from the X-point and is MCF-like. We obtain completely opposite results where electrons are reflected with high probability. Therefore, the highly transmitting mCF-like behavior and the highly reflective MCF-like behavior are both present in R2DEG. At any intermediate $\mathcal{E}$ and $\mathcal{V}$, the quantum transport phenomena is a mixture of the mCF and MCF tunneling effects where both transmission and reflection are possible. We emphasize that the electron transport in R2DEG is a hybrid of the massless Dirac fermion in SLG (where band crossing is present) and the massive Dirac fermion in BLG (where band turning point is present) where transmission and reflection of electron are always simultaneously present. Perfect Klein tunneling and Klein reflection of electrons do not occur in R2DEG unless in the above mentioned trivial cases.

6.3 π Berry phase electron backscattering

When $\mathcal{V} \to 1$, reflection dominates because of the vanishing Fermi radius of the transmitted states. We point out a phenomenally interesting situation when $\mathcal{E} \to 0$ and $\mathcal{V} \to 1$. The incident electron is mCF-like while the transmitted state is at the proximity of the subband minima and is MCF-like. The 'massless' incident state prefers transmission while the 'massive' transmitted state forbids transmission. This is loosely analogous to the situation of 'an unstoppable object meeting an impenetrable barrier'. In fact, the chiral tunneling of electron at normal incidence can be interpreted as the absence of $s \to s$ reflection process due to the spin non-flipping requirement. In graphene, there is only one possible pseudospin non-flipping transmission mode while in R2DEG there exists an additional spin non-flipping reflection

state in the $s = -s$ branch. The electron transport condition can be re-stated as: (i) no $s \to s$ reflection as required by the incident state; and (ii) no $\alpha = -s$ transmission as required by the transmitted state. This leaves the incident electron with only one choice, i.e. reflection to the $-s$ branch. In Fig. 6.2(b), we show the transmission/reflection probabilities in the presence of an interface potential $\mathcal{Z} > 0$. Reflection of $s \to s$ and transmission to $\alpha = -s$ are always forbidden regardless the strength of $\mathcal{Z}$. The interface potential in the present structure is non-magnetic and the spin-orbit coupling is not due to spin accumulation. As a result the chiral tunneling in R2DEG is well protected from the interface potential. The effect of $\mathcal{Z}$ is that it enhances $R_{-s}^{(s)}$ reflection while suppressing $T_{-s}^{(s)}$ transmission as can be seen in Fig. 6.2(b). In the extreme case of $\mathcal{Z} \to \infty$, it can be shown from Eq. (6.14) that $R_{-s}^{(s)} = 1$ and $T_{-s}^{(s)} = 0$.

When electrons are transported around a closed loop adiabatically in k-space, the wavefunction acquires an additional Berry phase of geometric nature: $\gamma = \oint_c \mathrm{d}\mathbf{k} \cdot \mathcal{A}$, where the Berry connection is $\mathcal{A} = i\xi_s^\dagger(\mathbf{k})\nabla_{\mathbf{k}}\xi_s(\mathbf{k})$ [156]. The Berry phase is closely related to the transport phenomena. One classic example being graphene where the π Berry phase associated with the pseudospin rotation leads to the absence of electron backscattering [138, 139]. In R2DEG, $\mathcal{A} = -1$ and the Berry phase is also π [157]. Electron backscattering is, however, permissible in R2DEG. To illustrate this peculiar result, we consider the spin polarization: $\mathbf{P}_s = \xi_s^\dagger \sigma \xi_s$ where σ is the Pauli spin matrix. Because of $\mathbf{P}_s \cdot (\mathbf{k}/k) = 0$, the spin is perpendicular to the electron wavevector $\mathbf{k}$. Furthermore, spin polarization is contained entirely in the plane of R2DEG and it rotates, with respect to $\mathbf{k}$, in opposite directions along the $s = \pm 1$ Fermi circles ($\mathbf{P}_s$ rotates in clockwise direction along the $s = +1$ Fermi circle and in anti-clockwise direction along the $s = -1$ Fermi circle) as dictated by $\mathbf{P}_s \times (\mathbf{k}/k) = s\hat{z}$. For an incident electron with incident angle $\phi^{(s)}$, the spin polarization is $\mathbf{P}_s^{(i)} = s(\hat{\mathbf{x}} \sin\phi^{(s)} - \hat{\mathbf{y}} \cos\phi^{(s)})$. The reflected electron spin polarization is

$$\mathbf{P}_{\pm s}^{(r)} = \pm s(\hat{\mathbf{x}} \sin\phi^{(s)} + \hat{\mathbf{y}} \cos\phi^{(s)}), \tag{6.15}$$

for $s \to s$ and $s \to -s$ reflection respectively. At normal incidence, the spin polar-

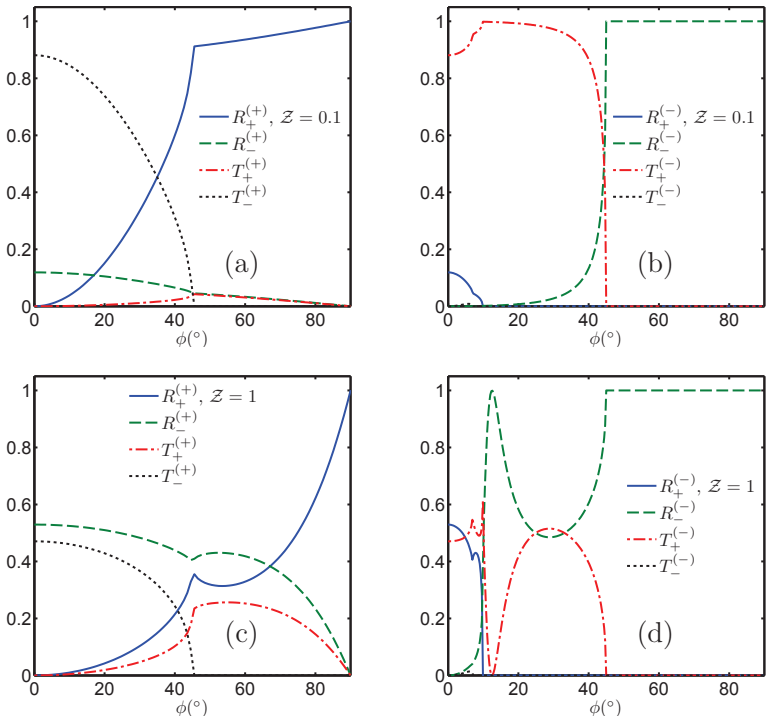

Figure 6.3: Probabilities at finite incident angle ϕ at two incident states $s = \pm 1$ with $\mathcal{Z} = 0.1$ in (a) and (b); and with $\mathcal{Z} = 1$ in (c) and (d).

izations of both incident and reflected electrons are purely y-directional: $\mathbf{P}_s^{(i)} = -s\hat{\mathbf{y}}$ and $\mathbf{P}_{\pm s}^{(r)} = \pm s\hat{\mathbf{y}}$. Correspondingly, $\mathbf{P}_s^{(i)} = \mp\mathbf{P}_{\pm s}^{(r)}$ and this implies that the spin orientation is reversed in $s \to s$ reflection while it remains unchanged in $s \to -s$ reflection. During the spin-flipping $s \to s$ reflection, electron acquires and additional π Berry phase and, as in the case of the psudospin chiral tunneling in graphene, $s \to s$ backscattering is forbidden. However, in the spin non-flipping $s \to -s$ reflection process, the electron does not acquire additional Berry phase. Consequently, the $s \to -s$ backscattering is permissible and this leads to the rather surprising result that electron backscattering is *present* in R2DEG albeit its π Berry phase.

6.4 Spin-polarized transmission through a n-p junction

The numerical results of finite incident angle transmission/reflection probabilities are shown in Fig. 6.3 for two incident states $s = \pm 1$ with $\mathcal{E} = 1$ and $\mathcal{V} = 0.5$. At finite

incident angle, $R_s^{(s)}$ and $T_s^{(s)}$ are no longer zero since the spins are mixed. The transmission and reflection probabilities sum up to one because there is only one incident electron and the electron current moving across the heterojunction has to be conserved as required by the charge continuity condition. For $s = -1$ to $s = 1$ reflection process, there exists a critical incident angle of $\phi^{(-),c} = \sin^{-1}\left(k^{(+)}/k^{(-)}\right)$. The critical angle for the transmission of s incident state is given as $\phi_\alpha^{(s),c} = \sin^{-1}\left(q_\alpha/k^{(s)}\right)$. The transmission/reflection probabilities vanishes when the critical incident angle is exceeded. In Fig. 6.3(a), $T_-^{(-)}$ dominates when incident angle is small. For incident angle greater than $\phi_-^{(+),c}$, $T_+^{(+)}$ becomes the only permissible transmission process. For $s = -1$ incident state, the $\alpha = -1$ branch has a relatively small radius in k-space. Due to the smallness of $\phi_-^{(-),c}$, $T_-^{(-)}$ process is nearly absent as shown in Fig. 6.3(b). At small and intermediate incident angle, the $s = -1$ incident electron prefers $R_+^{(-)}$ reflection and $T_+^{(-)}$ tunneling where the mismatching of spin orientation is not too severe. Once the incident angle exceeds $\phi^{(-),c}$, $T_+^{(-)}$ tunneling becomes the only favorable process and hence $T_+^{(-)} \approx 1$ up to the intermediate incident angle regime. At larger incident angle, the mismatching of spin polarization of the $R_-^{(-)}$ reflection decreases and $R_-^{(-)}$ rapidly peaks to unity. The effects of the interface potential $\mathcal{Z}$ on the transmission/reflection probabilities are shown in Fig. 6.3(c) and 6.3(d). For $s = +1$ incident state, $\mathcal{Z}$ suppresses transmission and amplifies reflection at small incident angle. At larger incident angle, $\mathcal{Z}$ however promotes the transmission to $\alpha = +1$ [Fig. 6.3(c)]. For $s = -1$ incident state, transmission is always suppressed. $R_+^{(-)}$ briefly peaks to unity well before the termination of $T_+^{(-)}$ [Fig. 6.3(d)].

Since the electron transport across a potential barrier in R2DEG is sensitively influenced by $\mathcal{E}$, $\mathcal{V}$ and $\mathcal{Z}$, controllable tuning of these quantities offers a possibility of manipulating the spin polarization of the transmitted electrons. We further investigate the spin-polarized electron transport by defining

$$\Delta\mathcal{T}(\mathcal{E},\mathcal{V}) = \sum_s \int_0^{\frac{\pi}{2}} \left(\frac{T_+^{(s)}(\phi,\mathcal{E},\mathcal{V}) - T_-^{(s)}(\phi,\mathcal{E},\mathcal{V})}{T_+^{(s)}(\phi,\mathcal{E},\mathcal{V}) + T_-^{(s)}(\phi,\mathcal{E},\mathcal{V})} \right) \mathrm{d}\phi. \tag{6.16}$$

Here, $\Delta\mathcal{T} > 0$ ($\Delta\mathcal{T} < 0$) represents the excess transmission of electrons to

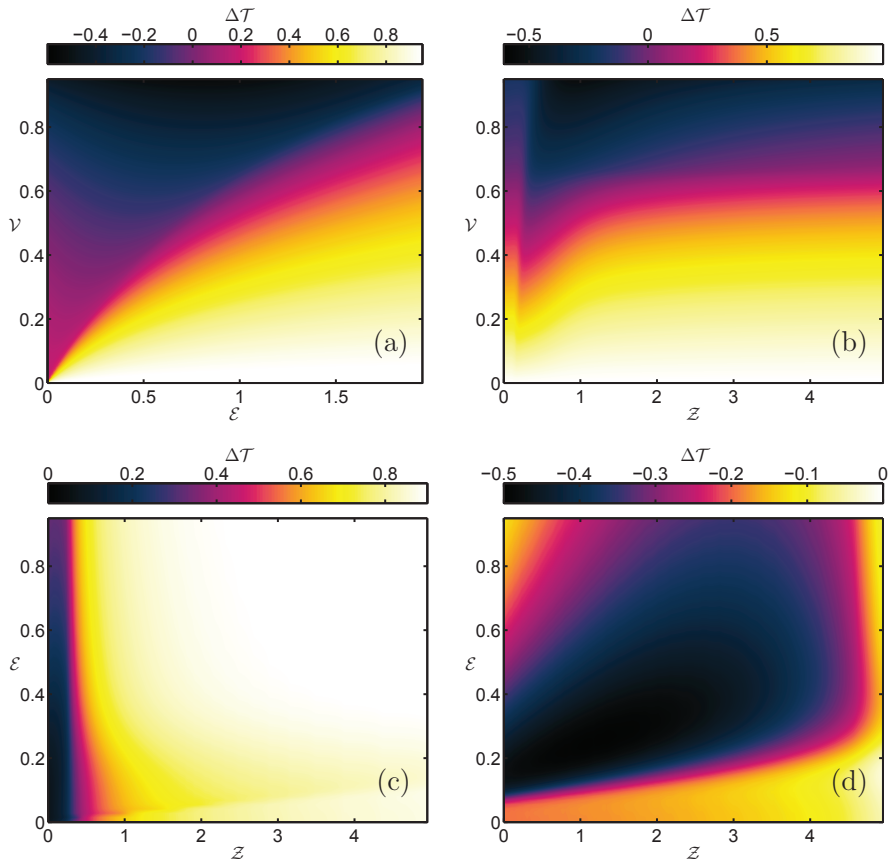

Figure 6.4: Dependence of spin-polarization, $\Delta\mathcal{T}$, on $\mathcal{V}$, $\mathcal{E}$ and $\mathcal{Z}$. (a) $\mathcal{V}$-and $\mathcal{E}$-dependence at $\mathcal{Z} = 1$. (b) $\mathcal{V}$-and $\mathcal{Z}$-dependence at $\mathcal{E} = 1$. $\mathcal{E}$-and $\mathcal{Z}$-dependence at (c) $\mathcal{V} = 0.1$; and (d) $\mathcal{V} = 0.9$.

$\alpha = +1$ ($\alpha = -1$) branch. In Fig. 6.4(a), $\Delta\mathcal{T} > 0$ dominates when $\mathcal{V} \to 0$ due to the smallness of the critical angles of $T_{-}^{(\pm)}$. $\Delta\mathcal{T} < 0$ dominates when $\mathcal{V} \to 1$ where the radius of the $\alpha = -1$ branch in phase-space is large enough to accommodate more electron transmissions. In general, $\mathcal{Z}$ does not significantly modify $\Delta\mathcal{T}$ with the exception that at large $\mathcal{V}$, transmission to $\alpha = -1$ state is strongly enhanced by small $\mathcal{Z} \approx 0.2$ as shown in Fig. 6.4(b). Fig. 6.4(a) and Fig. 6.4(b) suggest that $\mathcal{V}$ plays an important role in determining the sign of $\Delta\mathcal{T}$. We verified this by examining the $\mathcal{Z}$-and $\mathcal{E}$-dependence of $\Delta\mathcal{T}$ at two contrasting choices of $\mathcal{V} = 0.1$ in Fig. 6.4(c) and $\mathcal{V} = 0.9$ in Fig. 6.4(d). At $\mathcal{V} = 0.1$, $\Delta\mathcal{T} > 0$ in the entire ranges of $0 < \mathcal{E} < 2$ and $0 < \mathcal{Z} < 5$ [Fig. 6.4(c)]. The polarization is completely reversed to $\Delta\mathcal{T} < 0$ at $\mathcal{V} = 0.9$ as shown in Fig. 6.4(d). This immediately suggests that electrons are preferably transmitted to $\alpha = +1$ ($\alpha = -1$) branch if the transmission state mimics massless (massive) chiral fermion. The R2DEG junction thus works as

a spin-polarizer which polarizes electrons into $\alpha = \pm 1$ branches depending on the choice of $\mathcal{V}$.

6.5 Discussion

We have calculated the electron transport across a step potential in R2DEG. We demonstrated the simultaneous occurrence of both mCF- and MCF-like tunneling behavior in a non-relativistic Schrödinger system. The Rashba spin-orbit coupling can give rise to adjustable transparency for electron transport at a semiconductor junction. Apart from the non-relativistic nature of the R2DEG system, there is another interesting distinction between the chiral tunneling in the present system and the chiral tunneling in a relativistic system or in graphene. In graphene, incident electrons are in the conduction band and transmitted electrons are in the valence band. In the present system, the states on the two sides of the junction are both in the conduction band and the valence band is completely irrelevant.

The results presented in this work is in the ballistic transport regime where the sample size is assumed to be smaller than the electron mean free path. In the diffusive regime where disorder and interaction is important, localization of 2DEG is expected to occur [158, 159]. Weak localization of electrons in R2DEG has been experimentally observed in Zn doped p-type InAs single crystal [160]. We therefore expect our results to be quantitatively different with that of the diffusive regime. However, as long as the impurity is not spin-flipping, the chiral-like transport phenomena at normal incidence will remain valid. To observe the R2DEG electron transport and its crossover between mCF and MCF behavior, a large E_{SO} is preferred since it allows a larger tuning range for $\mathcal{V}$. Experimental results on layered semiconductor BiTeI [121] and surface state of Bi/Ag(111) [119] have revealed giant RSOI with E_{SO} in the order of 10^2 meV. A junction based on these materials may be a suitable system to experimentally study the the crossover from mCF-like and MCF-like tunneling phenomena.

7 | Energy loss rate of a fast charged particle in graphene

* We study the energy loss rate of a fast charged particle in this Chapter. We found that the energy-loss rate always increases with increasing incident particle energy, which is quite unusual when compared to electron gas in normal metal. Graphene exhibits a 'discriminating' behavior where there exists a low energy cut-off below which the scattering process is strictly forbidden, leads to lossless traverse of an external particle in graphene. This low energy cutoff is of the order of nearest neighbor hopping bandwidth. The scattering calculation shows that not only backscattering is absent intrinsically between two massless Dirac fermions, it also absent in the external charged particle scattering off graphene.

7.1 Introduction

In previous chapters, we study the intrinsic scattering of electrons in bilayer graphene and R2DEG by a electrostatic potential. In this Chapter, we study the extrinsic case in which an external particle is scattered by a single layer graphene sheet by calculating its energy loss rate (ELR) in graphene. ELR is an important quantity since it is directly related to electron energy loss spectroscopy (EELS). EELS is an useful tools in probing the electronic band structure, phonon excitation, plasmon excitation [161, 162], and surface properties of condensed matter. Consequently, the ELR spectrum of an external particle scattered off graphene is an important quantity

*This Chapter is based on *Appl. Phys. Lett.* **99**, 053111 (2011).

in order to fully extract the physics behind the experimental EELS results. The ELR of a particle in marginal Fermi liquid[163] and ELR of positron in metal[164] has been theoretically studied. In this Chapter, we apply the formalism in [163, 164] to the case of an intrinsic ($\mu = 0$) graphene.

7.2 Absence of backscattering of an external charged particle scattering

We consider a particle with initial momentum $\boldsymbol{p}$ and energy $\varepsilon_{\boldsymbol{p}}$ is fired onto a graphene single layer (see inset in Fig. 7.1). The particle transfers a momentum of $\Delta\mathbf{p} = \boldsymbol{q}$ and energy $\Delta\varepsilon = \omega = \varepsilon_{\boldsymbol{p}} - \varepsilon_{\boldsymbol{p-q}}$ to the graphene and emerges with a reduced momentum of $\boldsymbol{p-q}$ and energy $\varepsilon_{\boldsymbol{p-q}}$ ($\hbar \triangleq 1$). For non-relativistic case, $\omega = pq\cos\phi/m - q^2/2m$ where ϕ is the angle between $\boldsymbol{p}$ and $\boldsymbol{q}$, and m is the particle mass. The energy loss rate can be written as

$$\frac{d\varepsilon_{\boldsymbol{p}}}{dt} = \int \frac{d^2q}{(2\pi)^2} W_q(\omega) \tag{7.1}$$

where $W_q(\omega)$ is the transition probability and is given by

$$W_q(\omega) = \frac{2g_q}{1 - e^{-\beta\omega}} Im\left[\frac{1}{\epsilon_q(\omega)}\right] \tag{7.2}$$

where g_q is the coupling constant representing the interaction between the incident particle and graphene, β is the inverse temperature $(k_B T)^{-1}$. $\epsilon_q(\omega) = 1 - \nu_q \Pi(q,\omega)$ is the dielectric function under self-consistent field approximation where ν_q is the strength of electron-electron interaction and $\Pi(q,\omega)$ is the polarizability function of graphene. The imaginary part of the inverse dielectric function in Eq. (7.2) signifies the incident particle energy-loss in graphene. The polarizability function can be evaluated from the bare bubble diagrams [165] and is given by

$$\Pi(q,\omega) = \sum_{\boldsymbol{k},s,s'} F_{s,s'}(\theta_{\boldsymbol{k},\boldsymbol{k+q}}) \frac{f_{\boldsymbol{k+q},s'} - f_{\boldsymbol{k},s}}{v_F(s'|\boldsymbol{k}+\boldsymbol{q}| - s|\boldsymbol{k}|) - \omega'} \tag{7.3}$$

where $\omega' = \omega + i\eta$ with $\eta \to 0$, the wavefunction overlap is $F_{s,s'}(\theta_{\boldsymbol{k},\boldsymbol{k}+\boldsymbol{q}}) = (1 + ss'\cos\theta_{\boldsymbol{k},\boldsymbol{k}+\boldsymbol{q}})/2$ where $\theta_{\boldsymbol{k},\boldsymbol{k}+\boldsymbol{q}}$ is the angle between $\boldsymbol{k}$ and $\boldsymbol{k}+\boldsymbol{q}$ and $f_{\boldsymbol{k},s}$ is the Fermi-Dirac distribution function with $E_{\boldsymbol{k},s} = sv_F|\boldsymbol{k}|$ where $s = \pm 1$. The plasmon oscillation has been ignored since it is damped in intrinsic graphene. For intrinsic ($\mu = 0$) graphene at $T = 0K$, the imaginary polarizability function is given by [165, 166]

$$Im\left[\Pi(q,\omega)\right] = \frac{1}{4v_F}\frac{q^2}{(\omega^2/v_F^2 - q^2)^{1/2}}\Theta(\omega - qv_F) \tag{7.4}$$

where both spin and valley degeneracies has been included. Combining Eq. (7.1), Eq. (7.2) and Eq. (7.4) and evaluate the integral in polar coordinate, we obtain

$$\frac{d\varepsilon_{\boldsymbol{p}}}{dt} \propto \int_0^{2\pi} d\phi \int_0^{\Lambda} \frac{g_q \nu_q}{|\epsilon_q(\omega)|^2}\frac{dq}{1 - e^{\omega\beta}}\frac{q^3\omega}{(\omega^2 - q^2)^{1/2}}\Theta(\omega - q) \tag{7.5}$$

where for simplicity, yet without losing physics, we have dropped the leading constant terms, and denote $\hbar = v_F = k_B = m = 1$. The q-integration is limited by the step-function in Eq. (7.5). This sets up an upper limit Λ above which the imaginary polarizability function becomes zero.

In order to simplified Eq. (7.5), we make the following assumptions: (i) the electron-electron interaction is Coulomb, i.e. $\nu_q = e^2/\varepsilon_0 q$; (ii) the energy loss is small and hence the screening can be treated as static, i.e. $\epsilon_q(\omega) \to \epsilon_q(\omega = 0)$; and (iii) the coupling constant g_q between incident particle and quasiparticle excitation in graphene can be assumed to be of short range and hence is q-independent. It is obvious from Eq. (7.4) that the static $\epsilon_q(\omega = 0)$ will be contributed solely by the real part of the polarizability function, which can be conveniently evaluated from Eq. (7.4) using Kramers-Kronig relation[166] and is also q-independent.

The graphene ELR is given by

$$\begin{aligned}\frac{\partial\varepsilon_{\boldsymbol{p}}}{\partial t} &= \frac{\hbar g e^2}{4mv_F\varepsilon_0\epsilon_0^2}\int \frac{\omega dq d\phi}{1 - e^{\hbar\omega\beta}}\frac{q^2}{\left(\frac{\omega^2}{v_F^2} - q^2\right)^{1/2}}\Theta\left(\frac{\omega}{v_F} - q\right) \\ &= \frac{\hbar g e^2}{4mv_F\varepsilon_0\epsilon_0^2}\int_0^{2\pi}\int_0^{\Lambda} \frac{\hbar\omega dq d\phi}{1 - e^{\hbar\omega\beta}}\frac{q^2}{\left(\frac{\hbar^2\omega^2}{v_F^2} - \hbar^2 q^2\right)^{1/2}}\Theta\left(\frac{\omega}{v_F} - q\right)\end{aligned} \tag{7.6}$$

where ε_0 is the free space permittivity, ϵ_0 is the static approximated dielectric function, and Λ is the q-integral cut-off, which can be optained by solving

$$\frac{\omega}{v_F} - q^2 = 0 \tag{7.7}$$

where $\omega = \hbar(2pq\cos\phi - q^2)/2m$. It was found that $\Lambda = 2(p\cos\phi - p_0)$ where $p_0 = mv_F/\hbar$. Since the Λ must be positive, this requires that $p > p_0$, ie., in order to deposit energy in graphene, the incident particle must at least has an energy of

$$\varepsilon_p^{critical} = \frac{\hbar^2 p_0^2}{2m} = \frac{mv_F^2}{2} = \frac{\varepsilon_v}{2} \approx 2.8eV \tag{7.8}$$

where we defined $\varepsilon_v = mv_F^2$. This limits the maximum momentum transfer during the scattering process. In normal scattering process, the maximum momentum transfer is $2p$, while in graphene, the step-function from the imaginary polarizability function has limited the maximum momentum transfer to $2(p - p_0)$. Since nonzero q-integration requires $\Lambda > 0$, or equivalently $p > p_0$, this sets up a critical incident particle energy $\varepsilon_{\boldsymbol{p}}^c = mv_F/2$, below which the scattering process will be strictly forbidden. This discriminating behavior of graphene is quite unusual. Graphene seems to 'discriminate' the incident particle according to their energy and scatter only those with energies higher than $\varepsilon_{\boldsymbol{p}}^c$, regardless the amount of energy transfer ω. Interestingly, $\varepsilon_{\boldsymbol{p}}^c$ for an incident electron is approximately equal to the nearest neighbor hopping bandwidth in graphene $t \approx 2.8eV$. This implies that a slow charged particle with parabolic energy dispersion can travel through without loss of energy, i.e. graphene is completely transparent if for a slow incident charged particle.

7.3 Energy loss rate, mean scattering time and diffusion constant

We make the following substitution to transform Eq. 7.6 into a dimensionless integration: where we define $p_0 = mv_F$, $\tilde{q} = q/p_0$, $\tilde{p} = p/p_0$, $\tilde{\omega} = 2\tilde{p}\tilde{q}\cos\phi - \tilde{q}^2$, $\beta' = \beta/2$

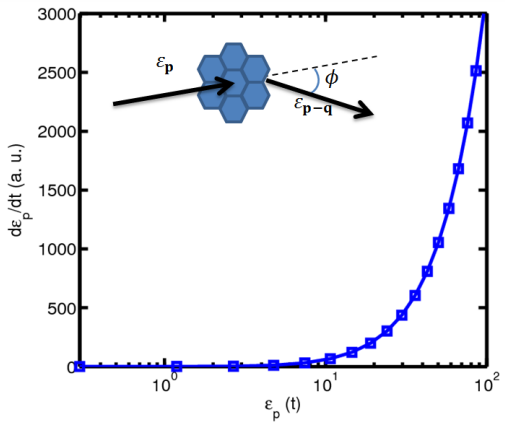

Figure 7.1: ELR $\varepsilon_{\mathbf{p}}$-sepctrum of electron at T=77K. Unlike electron gas in normal metal, graphene ELR always increases wth increasing $\varepsilon_{\mathbf{p}}$. The ELR is in the arbitrary unit of $\gamma V_0 \varepsilon_v/\hbar$. Inset shows the scattering process.

and $\varepsilon_v = mv_F^2$. The ELR can then be rewritten as

$$\begin{aligned}\frac{\partial \varepsilon_{\boldsymbol{p}}}{\partial t} &= \frac{\hbar g e^2}{4mv_F\varepsilon_0\epsilon_0^2}\int_0^{2\pi} d\phi \int_0^{2(\tilde{p}-1)} \frac{p_0^3}{2\sqrt{m}} \frac{\varepsilon_v \tilde{\omega}\tilde{q}^2 d\tilde{q}}{\left(1-e^{\frac{\varepsilon_v\tilde{\omega}}{2k_BT}}\right)\left(\frac{\varepsilon_v^2\tilde{\omega}^2}{4mv_F^2}-\frac{\hbar^2 p_0^2}{m}\tilde{q}^2\right)} \\ &= \frac{\hbar g e^2}{4mv_F\varepsilon_0\epsilon_0^2}\int_0^{2\pi} d\phi \int_0^{2(\tilde{p}-1)} \frac{p_0^3\sqrt{\varepsilon_v}}{\sqrt{m}} \frac{\tilde{\omega}\tilde{q}^2 d\tilde{q}}{\left(1-e^{\frac{\varepsilon_v\tilde{\omega}}{2k_BT}}\right)(\tilde{\omega}^2-4\tilde{q}^2)}\end{aligned} \tag{7.9}$$

The constant terms can be grouped to give

$$\frac{\hbar g e^2}{4mv_F\varepsilon_0\epsilon_0^2}\frac{p_0^3\sqrt{\varepsilon_v}}{\sqrt{m}} = \frac{\hbar^2 p_0^2}{2m}\frac{g}{2\hbar\epsilon_0^2}\frac{\sqrt{\varepsilon_v}}{\sqrt{mv_F^2}}\frac{e^2 p_0}{\varepsilon_0^2} = \frac{\varepsilon_v}{2}\frac{g}{\epsilon_0^2}\frac{V_0}{2\hbar} \tag{7.10}$$

where $V_0 = e^2 p_0/\varepsilon_0$ and is in the units of $[Js^{-1}]$. Finally, we write the ELR in SI unit as

$$\frac{d\varepsilon_{\boldsymbol{p}}}{dt} = \gamma\frac{V_0\varepsilon_v}{\hbar}\int_0^{2\pi}\frac{\tilde{\omega}}{1-e^{\varepsilon_v\beta'\tilde{\omega}}}d\phi\int_0^{\Lambda}\frac{\tilde{q}^2 d\tilde{q}}{(\tilde{\omega}^2-4\tilde{q}^2)^{1/2}} \tag{7.11}$$

where $\gamma = \frac{g}{4\epsilon_0^2}$ is a dimensionless constant representing the strength of incident particle-graphene interaction.

The $\varepsilon_{\boldsymbol{p}}$-spectrum is evaluated numerically and plotted in Fig. 7.1. For electron gas in normal metal, the ELR is known to be proportional to $\varepsilon_{\boldsymbol{p}}^2$ for slow particle and proportional to $\sim \ln(\varepsilon_{\boldsymbol{p}})/\varepsilon_{\boldsymbol{p}}^2$ for fast particles[164]. This however does not occur in graphene in which the ELR always increases with increasing $\varepsilon_{\boldsymbol{p}}$. It is also evident

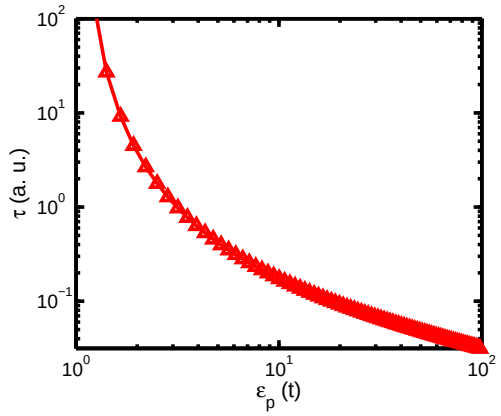

Figure 7.2: $\varepsilon_{\boldsymbol{p}}$-spectrum of $\tau_{\boldsymbol{p}}$ at $T = 77K$. $\tau_{\boldsymbol{p}}$ is plotted in arbitrary unit of $\hbar/2\gamma V_0$

that ELR is zero for $\varepsilon_{\boldsymbol{p}} < 2.8eV$. The temperature dependence is generally very weak for particle of all speeds. This is expected since from Eq. (7.11), the temperature factor carries $\varepsilon_v\beta' \approx 33000K/T$, which ensures that $[1 - exp(-\varepsilon_v\beta'\tilde{\omega})]^{-1} \approx 1$ for all moderate temperatures. It is however still obvious that the temperature dependence of slow particle is much stronger than that of the fast particle. Here we should notice two points. (i) The maximum momentum transfer is determined by simultaneous requirement of energy and momentum conservation of the incident electron in the scattering process. Furthermore the initial and the final state of the graphene are determined by the spectral function of the graphene, given by Eq. (7.4) which is related to the Dirac fermion nature. Since the scattering involves two particles (the incident electron and the Dirac electron in graphene) the maximum momentum transfer of the incident electron is intrinsically related to the allowed momentum transfer of the Dirac electron. That the back scattering for the Dirac electron in graphene (maximum momentum transfer) is forbidden leads to a reduced maximum momentum transfer of the incident electron. (ii) The dielectric function of the graphene is calculated with the linear energy dispersion approximation, i.e., in the Dirac regime. For this reason the energy transfer in a scattering event between the incident electron and the Dirac electrons should be within the linear regime. This is the case here since the maximum momentum transfer is limited by Λ and p_0 is large. In all figures, different quantities are plotted against the incident energy, not the energy of Dirac electrons.

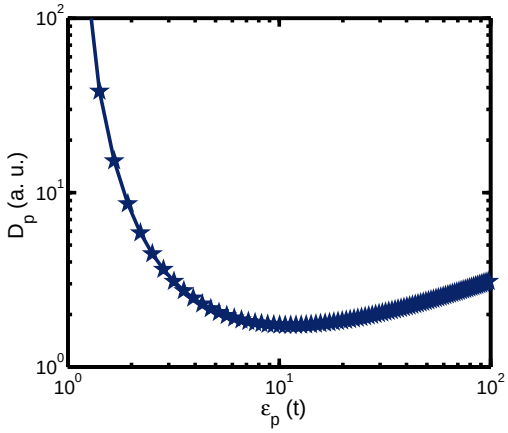

Figure 7.3: $\varepsilon_{\boldsymbol{p}}$-spectrum of $D_{\boldsymbol{p}}$ at $T = 77K$. $D_{\boldsymbol{p}}$ is plotted in arbitrary unit of $\hbar\varepsilon_v/4\gamma V_0$

The ELR is related to mean scattering time $\tau_{\boldsymbol{p}}$ by $\tau_{\boldsymbol{p}} = \varepsilon_{\boldsymbol{p}}(d\varepsilon_{\boldsymbol{p}}/dt)^{-1}$. In Fig. 7.2, we plot the $\varepsilon_{\boldsymbol{p}}$-spectrum of the mean scattering time. The temperature dependence is also very weak for the mean scattering time, but in general increasing scattering is observed at higher temperatures. $\tau_{\boldsymbol{p}}$ decreases very rapidly with increasing $\varepsilon_{\boldsymbol{p}}$, indicating energetic particles experience more profound scatterings in graphene. Note that the low energy tail of the $\varepsilon_{\boldsymbol{p}}$-spectrum blows up to infinity since it would take almost forever for an extremely slow ($\varepsilon_{\boldsymbol{p}} \to 0$) particle to be scattered.

The diffusion constant is given by $D_{\boldsymbol{p}} \sim (mp)^2\tau_{\boldsymbol{p}} \sim \varepsilon_{\boldsymbol{p}}\tau_{\boldsymbol{p}}$. The $\varepsilon_{\boldsymbol{p}}$-spectrum $D_{\boldsymbol{p}}$ is plotted in Fig. 7.3. In contrast to $\tau_{\boldsymbol{p}}$, $D_{\boldsymbol{p}}$ is a non-monotonic function of energy. It is interesting to note that in the high energy regime, there exists a diffusion minimum. The minimum diffusion length is the result of interplay between the incident energy and the scattering time. In the low energy regime $|d\tau_p/d\varepsilon_{\boldsymbol{p}}| > 1$. and in the high energy regime $|d\tau_p/d\varepsilon_{\boldsymbol{p}}| < 1$. The boundary of these two distinct energy regimes is $\varepsilon_{\boldsymbol{p}} \approx 10t$. As a result, there is a diffusion minimum around $\varepsilon_{\boldsymbol{p}} \approx 10t$.

7.4 Discussion

We remark that our calculation on the ELR in intrinsic graphene is limited by the temperature dependence of Eq. (7.4). The step-function-like zero temperature Fermi-Dirac distribution function will be smeared out at finite temperature. The smearing

is however quite small and will not significantly alter the results up to temperature in the order of few hundreds K. Therefore, Eq. (7.4) is reasonably adequate for our current purposes. For higher temperature where the smearing of the Fermi-Dirac distribution is no longer negligible and the full polarizability function, including both inter- and intraband transitions, should be used.

In conclusion, the energy-loss rate of a charged particle in graphene has been calculated. We present the energy dependence of the energy loss rate, scattering time and the diffusion constant. It is found that slow particles suffer no energy loss at all in graphene. For fast particles, a diffusion minimum has been detected. Our theoretical results can be verified in the diffraction of electrons through a graphene sheet [167]. The incident energy dependence of the scattered electron energy loss can be measured and compared with our theoretical results.

8 | Conclusion and outlooks

In conclusion, we have systematically studied the nonlinear optical response of SLG and several of its sister-structures, and the transport properties of BLG and R2DEG.

We first see that single layer graphene exhibits a strong intraband nonlinear optical response, requiring a moderate field strength in the order of 10^4 V/cm. In the presence of non-equilibrium population, the third-order nonlinear current density is raised at elevated temperature. The situation becomes more complicated when a bandgap is opened. Due to the two hot-spots feature of the nonlinear optical response, at a specific temperature, only a matching bandgap value can produce a maximal nonlinear optical response.

For interband nonlinear optical response, the presence of the k-parabolic term in the BLG and R2DEG Hamiltonian not only preserve the nonlinear optical response, but also induces a temperature robustness. These systems exhibit enhanced optical nonlinearity at higher temperature. This suggests that BLG, in comparison to SLG, could be a preferred structure for nonlinear THz device applications. In gapped graphene, i.e. such as the semihydrogenated graphene (SHG), the three-photon interband nonlinear optical process generates a sub-gap nonlinear response peak at frequencies where linear response is forbidden. In the moderate electric field strength of 10^3 V/cm, SHG can be transformed into a two-color material. We also found a $1/\lambda$ enhancement of both linear and nonlinear optical current in the elliptically deformed Dirac cone of a graphene superlattice.

In the transport study of BLG/S heterojunction, we obtained two main results: (i) retro electron reflection; and (ii) absence of Andreev reflection. The retro-reflection

of electron is the most unusual. It represents the last missing pieces of the quantum transport phenomena in a superconductor heterojunction, where specular electron reflection, retro and specular Andreev reflections have all been previously found:

- Specular electron reflection: semiconductor, metal, SLG, BLG, R2DEG
- Retro electron reflection: BLG (with trigonal warping effect), R2DEG
- Specular Andreev reflection: SLG, BLG, R2DEG
- Retro Andreev reflection: semiconductor, metal, SLG, BLG, R2DEG

In addition to the band anisotropy retro electron reflection in BLG, another retro reflection mechanism involving the hole-like electron states below the band crossing point has been found in R2DEG [153]. This type of retro reflection is a direct consequence of the band topology in R2DEG where band crossing and turning are both present. We further study the consequences of band topology on the electron transport this two-band system. We found that because of the band turning and crossing, the electron transport in R2DEG is a hybrid situation of massless and massive chiral fermions. The hybrid behavior is phenomenally important in the understanding of electron transport of the pseudospin or real-spin branches. Furthermore, the tunneling at the vicinity of the band crossing point exhibits a spin-polarizing effect.

Finally, we calculated the energy loss rate of a fast charged particle scattering off graphene. We found that the absence of backscattering is not only an intrinsic property between two massless Dirac fermions, but is also present in the case of an external charged particle scattering. Because of this, only fast charged particle can deposit energy in graphene. Graphene becomes completely transparent to slow incident charged particle at a low energy cutoff of approximately 3 eV.

Outlooks

The BLG nonlinear optical response in Chapter 3 is performed via a very minimal model. We first notice that due to the band anisotropy in k-space, the optical response

should exhibit an angular dependence with respect to the orientation of the external electric field [Fig. 8.1(a)]. Furthemore, the interband optical response calculated in Chapter 3 are indistinguishable for K and K' valleys. In the presence of an in-plane electric field, i.e. a bias voltage [Fig. 8.1(b)], will the optical response from K and K' valleys become distinguishable? It will be interesting to see if a nonlinear valley-current can be generated in this configuration.

Due to the band turning and band touching, electron undergoes Klein reflection in AB-stacked BLG as long as the two-band model is valid. In low energy regime, the trigonal warping effect shifts the parabolic bands and leads to the band crossing [Fig. 8.1(c)]. It is certain that Klein reflection no longer holds in this energy regime and the transmission becomes finite. A systematic investigation can be performed to study the tunneling of electrons between the separated energy pockets in the low energy trigonal warping regime.

The gapped-BLG/superconductor/gapped-BLG heterostructure [Fig. 8.1(d)] is another interesting structure which has not been studied in detail. In the presence of a bandgap, there exists a transmission regime with only hole excitation and the electron excitation is completely absent. In this case, transmission can only occur via cross Andreev process. However, Andreev reflection in BLG is a rather weak process [102]. There can be a competition between the electron reflection and the cross-Andreev reflection. It is therefore not clear if a significant cross-Andreev reflection can still be found in this structure. Also, it has been demonstrated that a tunneling barrier in gapped BLG is a pseudospin-valve [36]. In gapped SLG/superconductor/gapped SLG structure, pseudospin valve effect has been reported [39]. Can the gapped-BLG/S/gapped-BLG structure be similarly utilized as a pseudospin-valve device? One obvious advantage of gapped-BLG is that the bandgap is easily tunable by gate voltage. Reversing the gate polarity changes the sign of ΔU, and this immediately flips the pseudospin magnetization. One can therefore speculate that some interesting pseudospin transport phenomena could possibily be found in a gapped-BLG/S/gapped-BLG heterostructure.

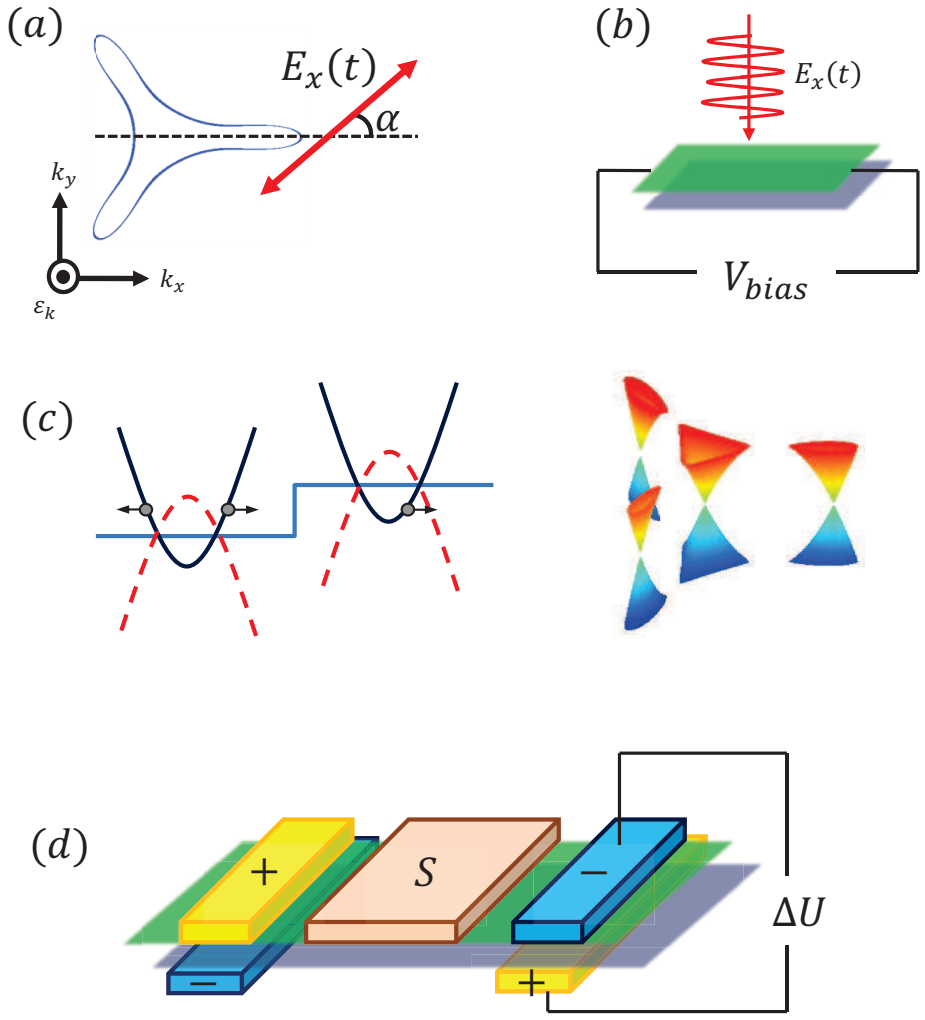

Figure 8.1: Outlooks. (a) Angular-dependent optical response; (b) optical response in the presence of an in-plane electric field; (c) electron transport at the trigonal warping warping region where the energy band is split into one central and three sattelite Dirac points; and (d) a gapped-BLG/superconductor/gapped-BLG device. Reversing the polarity of the gate electrodes changes the sign of ΔU and flips the pseudospin magnetization.

Bibliography

[1] K. S. Novoselov et al. *Science* 306 (2004), 666–669 (in pp. 1, 3).

[2] P. R. Wallace. *Phys. Rev.* 71, 9 (1947), 622–634 (in p. 1).

[3] K. S. Novoselov et al. *Nature* 438 (2005), 197–200 (in pp. 1, 2, 117).

[4] M. I. Katsnelson, K. S. Novoselov, and A. K. Geim. *Nature Phys.* 2 (2006), 620–625 (in pp. 1, 2, 9, 16, 17, 110, 117, 118).

[5] O. Klein. *Z. Phys.* 53, 3-4 (1929), 157–165 (in pp. 1, 116, 117).

[6] A. F. Young and P. Kim. *Nature Phys.* 5 (2009), 222–226 (in pp. 1, 16, 117).

[7] N. Stander, B. Huard, and D. Goldhaber-Gordon. *Phys. Rev. Lett.* 102 (2009), 026807 (in pp. 1, 16, 117).

[8] K. I. Bolotin et al. *Solid State Commun.* 146 (2008), 351–355 (in p. 1).

[9] J. Chen et al. *Nature Nanotech.* 3 (2008), 206 (in p. 1).

[10] A. K. Geim and K. S. Novoselov. *Nature Mater.* 6 (2007), 183–191 (in pp. 1, 4).

[11] F. Schwierz. *Nature Nanotech.* 5 (2010), 487–496 (in p. 1).

[12] F. Xia et al. *Nano Lett.* 10 (2010), 715–718 (in p. 1).

[13] Y. Zhang et al. *Nature* 438 (2005), 201–204 (in p. 2).

[14] V. P. Gusynin and S. G. Sharapov. *Phys. Rev. Lett.* 95 (2005), 146801 (in p. 2).

[15] K. S. Novoselov et al. *Science* 315 (2007), 1379 (in p. 2).

[16] K. Zeigler. *Phys. Rev. B* 75 (2007), 233407 (in p. 2).

[17] I. F. Herbut, V. Juricic, and O. Vafek. *Phys. Rev. Lett.* 100 (2008), 045403 (in p. 2).

[18] N. M. R. Peres, F. Fuinea, and A. H. Castro Neto. *Phys. Rev. B* 73 (2006), 125411 (in p. 2).

[19] J. Cserti, A. Csordas, and G. David. *Phys. Rev. Lett.* 99 (2007), 066802 (in pp. 2, 58).

[20] J. A. Martin et al. *Nature Phys.* 4 (2008), 144–148 (in p. 2).

[21] A. B. Kuzmenko et al. *Phys. Rev. Lett.* 100 (2008), 117401 (in p. 2).

[22] R. R. Nair et al. *Science* 320 (2008), 1308 (in p. 2).

[23] C. Zhang, L. Chen, and Z. Ma. *Phys. Rev. B* 77 (2008), 241402(R) (in pp. 2, 25).

[24] L. A. Falkovsky and S. S. Pershogub. *Phys. Rev. B* 76 (2007), 153410 (in p. 2).

[25] V. P. Gusynin, S. G. Sharapov, and J. P. Carbotte. *Phys. Rev. Lett.* 96 (2006), 256802 (in p. 2).

[26] Z. Q. Li et al. *Nature Phys.* 4 (2008), 532–535 (in p. 2).

[27] A. Rycerz, J. Tworzydo, and C. W. J. Beenakker. *Nature Phys.* 3 (2007), 172–175 (in pp. 3, 113).

[28] D. Gunlycke and C. T. White. *Phys. Rev. Lett.* 106 (2011), 136806 (in pp. 3, 113).

[29] J. L. Garcia-Pomar, A. Cortijo, and M. Nieto-Vesperinas. *Phys. Rev. Lett.* 100 (2008), 236801 (in p. 3).

[30] J. M. Pereira et al. *J. Phys.: Condens. Matter* 21 (2009), 045301 (in p. 3).

[31] F. Zhai and K. Chang. *Phys. Rev. B* 85 (2012), 115415 (in p. 3).

[32] D. Moldovan et al. *Phys. Rev. B* 86 (2012), 115431 (in p. 3).

[33] A. Chaves et al. *Phys. Rev. B* 82 (2010), 205430 (in p. 3).

[34] C. G. Peterfalvi et al. *New J. Phys.* 14 (2013), 063028 (in pp. 3, 111, 120).

[35] L. Majidi and M. Zareyan. *Phys. Rev. B* 83 (2011), 115422 (in p. 3).

[36] P. San-Jose et al. *Phys. Rev. Lett.* 102 (2009), 247204 (in pp. 3, 141).

[37] H. Min et al. *Phys. Rev. B* 77 (2008), 041407(R) (in p. 3).

[38] M. Trushin and J. Schlieman. *Phys. Rev. Lett.* 107 (2011), 156801 (in p. 3).

[39] L. Majidi and M. Zareyan. *Phys. Rev. B* 86 (2012), 075443 (in pp. 3, 141).

[40] M. Y. Han et al. *Phys. Rev. Lett.* 98 (2007), 206805 (in p. 3).

[41] L. Brey and H. A. Fertig. *Phys. Rev. B* 73 (2006), 235411 (in p. 3).

[42] M. Ezawa. *Phys. Rev. B* 73 (2006), 045432 (in p. 3).

[43] C.-H. Park et al. *Nature Phys.* 4 (2008), 213–217 (in pp. 3, 87–89, 93, 120).

[44] C.-H. Park et al. *Phys. Rev. Lett.* 101 (2008), 126804 (in pp. 3, 87, 88).

[45] C.-H. Park et al. *Nano Lett.* 8 (2008), 2920–2924 (in p. 3).

[46] H. Suzuura and T. Ando. *Phys. Rev. Lett.* 89 (2002), 266603 (in p. 4).

[47] S. V. Morozov. *Phys. Rev. Lett.* 97 (2006), 016801 (in p. 4).

[48] D. V. Khveschenko. *Phys. Rev. Lett.* 97 (2006), 036802 (in p. 4).

[49] D. Dragoman and M. Dragoman. *Appl. Phys. Lett.* 91 (2007), 203116 (in pp. 4, 31).

[50] P. Wei et al. *Phys. Rev. Lett.* 102 (2009), 166808 (in p. 4).

[51] Balandin et al. *Nano Lett.* 8 (2008), 902–907 (in p. 4).

[52] C. L. Kane and E. J. Mele. *Phys. Rev. Lett.* 95 (2005), 226801 (in p. 4).

[53] R. Nandkishore, L. S. Levitov, and A. V. Chubukov. *Nature Phys.* 8 (2012), 158–163 (in p. 4).

[54] A. H. Castro Neto et al. *Rev. Mod. Phys.* 81 (2009), 109–162 (in pp. 4, 117).

[55] C. W. J. Beenakker. *Rev. Mod. Phys.* 80 (2008), 1337 –1354 (in pp. 4, 19, 98).

[56] F. Bonaccorso et al. *Nature Photon.* 4 (2010), 611–622 (in p. 4).

[57] S. D. Sarma, S. Adam, and E. H. Hwang. *Rev. Mod. Phys.* 83, 2 (2011), 407–439 (in pp. 4, 16).

[58] M. Z. Hasan and C. L. Kane. *Rev. Mod. Phys.* 82 (2010), 3045–3067 (in pp. 4, 88).

[59] P. Vogt et al. *Phys. Rev. Lett.* 108 (2012), 155501 (in p. 4).

[60] A. Fleurence et al. *Phys. Rev. Lett.* 108 (2012), 245501 (in p. 4).

[61] E. Bianco et al. *Nano Lett.* 7, 5 (2013), 4414–4421 (in p. 4).

[62] Y. Xu. *Phys. Rev. Lett.* 111 (2013), 136804 (in p. 4).

[63] C. Thomsen S. Reich J. Maultzsch and P. Ordejon. *Phys. Rev. B* 66 (2002), 035412 (in p. 5).

[64] G. Giovannetti et al. *Phys. Rev. B* 76 (2007), 073103 (in p. 7).

[65] S. Y. Zhou et al. *Nature Mater.* 6 (2007), 770–775 (in p. 7).

[66] D. C. Elias et al. *Science* 323, 5914 (2009), 610–613 (in p. 7).

[67] A. H. Castro Neto and F. Guinea. *Phys. Rev. Lett.* 103 (2004), 026804 (in p. 7).

[68] H. Min et al. *Phys. Rev. B* 74 (2006), 165310 (in p. 7).

[69] J. Nilsson et al. *Phys. Rev. B* 78 (2008), 045405 (in p. 8).

[70] C. McCann, D. S. L. Abergel, and V. I. Fal'ko. *Solid State Commun.* 143 (2007), 110–115 (in pp. 8, 9, 49, 51, 57, 63, 100, 115).

[71] E. McCann and V. I. Fal'ko. *Phys. Rev. Lett.* 96 (2006), 086805 (in pp. 9, 49).

[72] M. Koshino and T. Ando. *Phys. Rev. B* 73 (2006), 245403 (in pp. 9, 49, 58, 59, 63).

[73] B. Wang, C. Zhang, and Z. Ma. *J. Phys.: Condens. Matter* 24 (2012), 485303 (in p. 10).

[74] P. Rakyta, A. Kormanyos, and J. Cserti. *Phys. Rev. B* 82 (2010), 113405 (in p. 10).

[75] B. Wang, C. Zhang, and Z. Ma. *J. Phys.: Condens. Matter* 24 (2011), 035303 (in p. 10).

[76] E. V. Castro et al. *Phys. Rev. Lett.* 99 (2007), 216802 (in p. 10).

[77] Y. Zhang. *Nature* 459 (2009), 820–823 (in p. 10).

[78] J. Oostinga et al. *Nature Mater.* 7 (2007), 151–157 (in p. 10).

[79] K. F. Mak et al. *Phys. Rev. Lett.* 101 (2008), 196405 (in p. 10).

[80] A. L. Rakhmanov et al. *Phys. Rev. Lett.* 109 (2012), 206801 (in p. 10).

[81] C. J. Tabert and E. J. Nicol. *Phys. Rev. B* 86 (2012), 075439 (in p. 10).

[82] Z. Liu et al. *Phys. Rev. Lett.* 102 (2009), 015501 (in p. 11).

[83] M. Sanderson, Y. S. Ang, and C. Zhang. *Phys. Rev. B* 88 (2013), 245404 (in p. 11).

[84] Y. A. Bychkov and E. I. Rashba. *JETP Lett.* 39 (1984), 78 (in pp. 12, 118).

[85] P. H. Siegel. *IEEE Trans. Microw. Theory Techn.* 50, 3 (2002), 910–928 (in p. 12).

[86] S. A. Mikhailov. *Euro. Phys. Lett.* 79 (2007), 27002 (in pp. 13, 21).

[87] S. A. Mikhailov and K. Ziegler. *J. Phys.: Condens. Matter* 20 (2008), 384204 (in pp. 13, 21).

[88] E. Hendry et al. *Phys. Rev. Lett.* 105 (2010), 097401 (in pp. 13, 46).

[89] A. R. Wright et al. *Appl. Phys. Lett.* 95 (2009), 072101 (in pp. 13, 30, 48, 59, 72, 82, 93, 95).

[90] M. Dragoman et al. *Appl. Phys. Lett.* 97 (2010), 093101 (in p. 13).

[91] G.-K Lim et al. *Nature Photon.* 5 (2011), 554–560 (in pp. 13, 46).

[92] J. Wang et al. *Adv. Mater.* 23 (2009), 2430–2435 (in p. 13).

[93] S.-Y Hong et al. *Phys. Rev. X* 3 (2013), 021014 (in p. 13).

[94] S. Wu et al. *Nano Lett.* 12, 4 (2012), 2032–2036 (in p. 13).

[95] K. L. Ishikawa. *Phys. Rev. B* 82 (2010), 201402(R) (in p. 14).

[96] P. A. Wolff and G. A. Pearson. *Phys. Rev. Lett.* 17 (1966), 1015–1017 (in pp. 14, 29).

[97] F. Gao, G. Wang, and C. Zhang. *Nanotech.* 19 (2008), 465401 (in pp. 14, 29).

[98] A. F. Young and P. Kim. *Annu. Rev. Condens. Matter Phys.* 2 (2011), 101–120 (in p. 16).

[99] C. W. J. Beenakker. *Phys. Rev. Lett.* 97 (2006), 067007 (in pp. 19, 98, 107, 110, 115).

[100] A. F. Andreev. *Zh. Eksp. Teor. Fiz.* 46 (1964), 1823 (in pp. 19, 98).

[101] R. P. Feynman. *Phys. Rev.* 56 (1939), 340–343 (in p. 22).

[102] T. Ludwig. *Phys. Rev. B* 79 (2007), 195322 (in pp. 25, 115, 141).

[103] Chen et al. *Nature* 471 (2011), 617–620 (in pp. 27, 83).

[104] H. M. Dong, W. Xu, and R. B. Tan. *Solid State Comm.* 150 (2010), 1770–1773 (in p. 39).

[105] D. Sun et al. *Phys. Rev. Lett.* 101 (2008), 157402 (in p. 39).

[106] S. Butscher et al. *Appl. Phys. Lett.* 91 (2007), 203103 (in p. 39).

[107] W. S. Bao, S. Y. Liu, and X. L. Lei. *Phys. Lett. A* 374 (2010), 1266–1269 (in p. 39).

[108] Y. S. Ang and C. Zhang. *Appl. Phys. Lett.* 98 (2011), 042107 (in p. 44).

[109] X. F. Wang, P. Vasilopoulos, and F. M. Peeters. *Phys. Rev. B* 65 (2002), 165217 (in p. 46).

[110] C.-L. Song et al. *Phys. Rev. Lett.* 109 (20132), 137004 (in p. 46).

[111] S. Ulstrup et al. *Phys. Rev. B* 86 (2012), 161402(R) (in p. 46).

[112] A. C. Betz et al. *Nature Phys.* 9 (2013), 109–112 (in p. 46).

[113] M. W. Graham et al. *Nature Phys.* 9 (2013), 103–108 (in p. 46).

[114] E. H. Hwang and S. Das Sarma. *Phys. Rev. B* 77 (2008), 115449 (in p. 61).

[115] D. Grundler. *Phys. Rev. Lett.* 84, 26 (2000), 6074–6077 (in pp. 63, 118).

[116] J. Nitta, T. Akazaki, and H. Takayanagi. *Phys. Rev. Lett.* 78, 7 (1997), 1335–1338 (in pp. 63, 118).

[117] S. LaShell, B. A. McDougall, and E. Jensen. *Phys. Rev. Lett.* 77, 16 (1996), 3419–3422 (in pp. 63, 67).

[118] K. Yaji et al. *Nature Comm.* 1 (2010), 17 (in p. 63).

[119] C. R. Ast et al. *Phys. Rev. Lett.* 98 (2007), 186807 (in pp. 63, 72, 130).

[120] D. Yuan et al. *Phys. Rev. B* 72 (2005), 033320 (in p. 65).

[121] K. Ishizaka et al. *Nature Mater.* 10 (2011), 521–526 (in pp. 72, 130).

[122] A. Varykhalov. *Phys. Rev. Lett.* 108 (2012), 066804 (in p. 73).

[123] L. Chen, Z. Ma, and C. Zhang. *Appl. Phys. Lett.* 96 (2010), 023107 (in p. 77).

[124] W. F. Edwards. *Am. J. Phys.* 31, 7 (1963), 482 (in p. 88).

[125] C. Y. Moon et al. *Phys. Rev. B* 84 (2011), 195425 (in p. 88).

[126] J. Park et al. *Phys. Rev. Lett.* 107 (2011), 126402 (in p. 88).

[127] X. G. Xu and J. C. Cao. *Mod. Phys. Lett. B* 24 (2010), 2243 (in p. 96).

[128] Y. Y. Wang et al. *J. Phys. Chem. C* 112.29 (2008), 10637–10640 (in p. 96).

[129] B. Scharf et al. *Phys. Rev. B* 87 (2013), 035414 (in p. 96).

[130] X. Li et al. *Appl. Phys. Lett.* 97 (2010), 232105 (in p. 96).

[131] D. Weiss et al. *Phys. Rev. B* 39 (1989), 13020 (in p. 96).

[132] H. Goldstein, C. P. Poole, and J. L. Safko (2002) (in p. 97).

[133] P. G. de Gennes (1966) (in p. 98).

[134] B. Lv, C. Zhang, and Z. Ma. *Phys. Rev. Lett.* 108 (2012), 077002 (in pp. 98, 115).

[135] H. B. Heersche et al. *Nature* 446 (2012), 56–59 (in pp. 105, 106).

[136] G. E. Blonder, M. Tinkham, and T. M. Klapwijk. *Phys. Rev. B* 25 (1982), 4515 (in p. 105).

[137] K. S. Novoselov et al. *Nat. Phys.* 2 (2006), 177–180 (in p. 110).

[138] G. P. Miktik and Y. V. Sharlai. *Low Temp. Phys.* 34 (2008), 794 (in pp. 110, 126).

[139] T. Ando, T. Nakanishi, and R. Saito. *J. Phys. Soc. Jpn.* 67 (1998), 2857–2862 (in pp. 110, 126).

[140] V. G. Veselago. *Sov. Phys. Usp.* 10 (1968), 509–514 (in p. 111).

[141] V. V. Cheianov, V. Fal'ko, and B. L. Altshuler. *Science* 315 (2007), 1252–1255 (in pp. 111, 120).

[142] S. V. Morozov et al. *Phys. Rev. Lett.* 97 (2006), 016801 (in p. 113).

[143] Z. Wu et al. *Phys. Rev. Lett.* 106 (2011), 176802 (in p. 113).

[144] D. S. L. Abergel and T. Chakraborty. *Appl. Phys. Lett.* 95 (2009), 062107 (in p. 113).

[145] B. E. Feldman, J. Martin, and A. Yacoby. *Nature Phys.* 5 (2009), 889–893 (in p. 115).

[146] I. Zutic and S. Das Sarma. *Phys. Rev. B* 60 (1999), R16322 (in p. 115).

[147] M. J. M. De Jong and C. W. J. Beenakker. *Phys. Rev. Lett.* 74 (1995), 1657 (in p. 115).

[148] T. Yokoyama, Y. Tanaka, and J. Inoue. *Phys. Rev. B* 74 (2006), 035318 (in p. 115).

[149] A. Dimoulas. *Phys. Rev. B* 61 (2000), 9729 (in p. 115).

[150] Y. Tanaka and S. Kashiwaya. *Phys. Rev. Lett.* 74 (1995), 3451 (in p. 115).

[151] A. H. MacDonald, J. Jung, and F. Zhang. *Phys. Scr.* T146 (2012), 014012 (in p. 118).

[152] X. Zhang. *Appl. Phys. Lett* 88 (2006), 052114 (in p. 120).

[153] B. Lv and Z. Ma. *Phys. Rev. B* 87 (2013), 045305 (in pp. 120, 140).

[154] F. Hassler, A. R. Akhmerov, and C. W. J. Beenakker. *Phys. Rev. B* 82 (2010), 125423 (in p. 120).

[155] D. J. Griffiths (2004) (in p. 120).

[156] M. V. Berry. *Proc. R. Soc. Lond. A* 1802 (1984), 45–57 (in p. 126).

[157] S.-Q Shen. *Phys. Rev. B* 70 (2004), 081311(R) (in p. 126).

[158] D. K. Ferry and S. M. Goodnick (1999) (in p. 130).

[159] T. Ando, A. B. Fowler, and F. Stern. *Rev. Mod. Phys.* 54, 2 (1982), 437–672 (in p. 130).

[160] C. Schierholz et al. *Phys. Rev. B* 70 (2004), 233311 (in p. 130).

[161] T. Eberlein et al. *Phys. Rev. B* 77 (2008), 233406 (in p. 131).

[162] J. Lu et al. *Phys. Rev. B* 80 (2009), 113410 (in p. 131).

[163] C. Zhang and Y. Takahashi. *Phys. Rev. B* 46 (1992), 9247 (in p. 132).

[164] C. Zhang, N. Tzoar, and P. M. Platzman. *Phys. Rev. B* 37 (1988), 7326 (in pp. 132, 135).

[165] E. H. Hwang and S. Das Sarma. *Phys. Rev. B* 75 (2007), 205418 (in pp. 132, 133).

[166] B. Wunsch et al. *New J. Phys.* 8 (2006), 318 (in p. 133).

[167] J. C. Meyer et al. *Solid State Comm.* 143, 1-2 (2007), 101–109 (in p. 138).

Appendices

Appendix A

Derivation of $\sigma(\omega)$ and $\sigma(3\omega)$ of bilayer graphene

A.1 $n = 2$ and $n = 3$ spinor components

From Eq. (3.8), we write the $n = 2$ spinor components:

$$a_2 = \frac{eE}{4i\omega^2\hbar(\omega\hbar-\varepsilon)}[X_-(\varepsilon-2\omega\hbar)b_1 + X_+Y_-a_1] - \alpha\frac{e^2E^2}{4\omega^3\hbar(\omega\hbar-\varepsilon)}\left[Y_-a_0 + \frac{(\varepsilon-2\omega\hbar)}{\sqrt{2}}\right]$$

$$b_2 = \frac{eE}{4i\omega^2\hbar(\omega\hbar-\varepsilon)}[X_-Y_+b_1 + X_+(\varepsilon-2\omega\hbar)a_1] - \alpha\frac{e^2E^2}{4\omega^3\hbar(\omega\hbar-\varepsilon)}\left[(\varepsilon-2\omega\hbar)a_0 + \frac{Y_+}{\sqrt{2}}\right] \tag{A.1}$$

where a_0, b_0, a_1 and b_1 are given by Eq. (3.11), (3.12), (3.14) and (3.15), respectively. Explicitly, we write:

$$\begin{aligned} a_2 &= \frac{-e^2E^2}{4\sqrt{2}\omega^4\hbar^2\varepsilon(\omega\hbar-\varepsilon)(\omega\hbar-2\varepsilon)}\left[2(\varepsilon-\omega\hbar)^2\Gamma Y_- + \varepsilon(\varepsilon\hbar-2\omega)X_-^2Y_+ + X_+^2Y_-^3\right] \\ &\quad -\frac{\alpha e^2E^2}{4\sqrt{2}\omega^3\hbar\varepsilon(\omega\hbar-\varepsilon)}\left[\varepsilon(\varepsilon-2\omega\hbar) + Y_-^2\right] \end{aligned} \tag{A.2}$$

$$\begin{aligned} b_2 &= \frac{-e^2E^2}{4\sqrt{2}\omega^4\hbar^2\varepsilon(\omega\hbar-\varepsilon)(\omega\hbar-2\varepsilon)}\left[2\varepsilon(\varepsilon-\omega\hbar)^2\Gamma + \varepsilon X_-^2Y_+ + (\varepsilon-2\omega\hbar)X_+^2Y_-^2\right] \\ &\quad -\frac{\alpha e^2E^2}{4\sqrt{2}\omega^3\hbar\varepsilon(\omega\hbar-\varepsilon)}\left[\varepsilon Y_+ + (\varepsilon-2\omega\hbar)Y_-\right] \end{aligned} \tag{A.3}$$

where Γ is defined as $\Gamma = X_+X_-$.

In the following calculations, the following short-form are used for simplicity:

$$a_1 = \frac{eE}{i\sqrt{2}\omega^2\hbar\varepsilon(\omega\hbar - 2\varepsilon)}[\cdots a_1 \cdots] \tag{A.4}$$

$$b_1 = \frac{eE}{i\sqrt{2}\omega^2\hbar\varepsilon(\omega\hbar - 2\varepsilon)}[\cdots b_1 \cdots] \tag{A.5}$$

and similarly we replaced the terms in the square bracket of Eq. (A.2) and Eq. (A.3) by the short-form notations, i.e.

$$a_2 = \frac{-e^2E^2}{4\sqrt{2}\omega^4\hbar^2\varepsilon(\omega\hbar - \varepsilon)(\omega\hbar - 2\varepsilon)}[\cdots a_2^{(1)} \cdots] - \frac{\alpha e^2E^2}{4\sqrt{2}\omega^3\hbar\varepsilon(\omega\hbar - \varepsilon)}[\cdots a_2^{(2)} \cdots] \tag{A.6}$$

$$b_2 = \frac{-e^2E^2}{4\sqrt{2}\omega^4\hbar^2\varepsilon(\omega\hbar - \varepsilon)(\omega\hbar - 2\varepsilon)}[\cdots b_2^{(1)} \cdots] - \frac{\alpha e^2E^2}{4\sqrt{2}\omega^3\hbar\varepsilon(\omega\hbar - \varepsilon)}[\cdots b_2^{(2)} \cdots] \tag{A.7}$$

A.2 Derivation of $\sigma_3(\omega)$

The *single-frequency* optical current operator j_3 can be split into

$$j_3 = j_3^{(A)} + j_3^{(B)} \tag{A.8}$$

where

$$\begin{aligned} j_3^{(A)} &= j_3^{\prime(A)} + j_3^{\prime\prime(A)} \equiv -e\phi_0^\dagger \hat{v}_A \phi_2 - e\phi_2^\dagger v_A \phi_0 \\ j_3^{(B)} &= j_3^{\prime(B)} + j_3^{\prime\prime(B)} \equiv -e\phi_0^\dagger \hat{v}_B \phi_2 - e\phi_2^\dagger v_B \phi_0 \end{aligned} \tag{A.9}$$

where $\phi_n = (a_n, b_n)^T$. We now solve $j_3^{(B)}$. The spinor product $a_2 b_1^*$ is given as

$$a_2 b_1^* = \frac{-e^2E^2}{4\sqrt{2}\omega^4\hbar^2\varepsilon(\omega\hbar - \varepsilon - i\delta)(\omega\hbar - 2\varepsilon - i\delta)} \times \frac{-eE}{i\sqrt{2}\omega^2\hbar\varepsilon(\omega\hbar - 2\varepsilon + i\delta)}[\ldots a_2^{(1)} \ldots][\ldots b_1^* \cdots]$$

$$- \frac{\alpha e^2E^2}{4\sqrt{2}\omega^3\hbar\varepsilon(\omega\hbar - \varepsilon - i\delta)} \times \frac{-eE}{i\sqrt{2}\omega^2\hbar\varepsilon(\omega\hbar - 2\varepsilon + i\delta)}[\cdots a_2^{(2)} \cdots][\cdots b_1^* \cdots] \tag{A.10}$$

which is simplified to:

$$a_2 b_1^* = \frac{e^3 E^3}{8i\omega^6\hbar^3\varepsilon^2 \left|\omega\hbar - 2\varepsilon\right|^2 (\omega\hbar - \varepsilon - i\delta)} [\dots a_2^{(1)} \dots][\dots b_1^* \cdots]$$

$$+ \frac{\alpha e^3 E^3}{8i\omega^5\hbar^2\varepsilon^2(\omega\hbar - \varepsilon - i\delta)(\omega\hbar - 2\varepsilon + i\delta)} [\cdots a_2^{(2)} \cdots][\cdots b_1^* \cdots] \tag{A.11}$$

and hence

$$a_2 b_1^* + b_2 a_1^* = \frac{e^3 E^3}{8i\omega^6\hbar^3\varepsilon^2 \left|\omega\hbar - 2\varepsilon\right|^2 (\omega\hbar - \varepsilon - i\delta)} \left\{[\dots a_2^{(1)} \dots][\dots b_1^* \cdots] + [\dots b_2^{(1)} \dots][\dots a_1^* \cdots]\right\}$$

$$+ \frac{\alpha e^3 E^3}{8i\omega^5\hbar^2\varepsilon^2(\omega\hbar - \varepsilon - i\delta)(\omega\hbar - 2\varepsilon + i\delta)} \left\{[\cdots a_2^{(2)} \cdots][\cdots b_1^* \cdots] + [\cdots b_2^{(2)} \cdots][\cdots a_1^* \cdots]\right\} \tag{A.12}$$

where the product $[\dots a_2^{(1)} \dots][\dots b_1^* \cdots]$ is explicitly given by

$$[\varepsilon X_+ Y_+ - (\varepsilon - \omega\hbar) X_- Y_+] \left[2(\varepsilon - \omega\hbar)^2 \Gamma Y_- + \varepsilon(\varepsilon\hbar - 2\omega) X_-^2 Y_+ + X_+^2 Y_-^3\right]$$

$$= 2\varepsilon(\varepsilon - \omega\hbar)^2 \Gamma X_+ Y_-^2 + \varepsilon^4(\varepsilon - 2\omega\hbar)\Gamma X_- + \varepsilon X_+^3 Y_-^4 + 2(\varepsilon - \omega\hbar)^3 \varepsilon^2 \Gamma X_-$$

$$+ \varepsilon(\varepsilon - \omega\hbar)(\varepsilon - 2\omega\hbar) X_-^3 Y_+^2 + (\varepsilon - \omega\hbar)\varepsilon^2 \Gamma X_+ Y_-^2$$

$$= \varepsilon(\varepsilon - \omega\hbar)(3\varepsilon - 2\omega\hbar)\Gamma X_+ Y_-^2 + \varepsilon^2[\varepsilon^2(\varepsilon - 2\omega\hbar) + 2(\varepsilon - \omega\hbar)^3]\Gamma X_-$$

$$+ \varepsilon(\varepsilon - \omega\hbar)(\varepsilon - 2\omega\hbar) X_-^3 Y_+^2 + \varepsilon X_+^3 Y_-^4 \tag{A.13}$$

and $[\cdots a_2^{(2)} \cdots][\cdots b_1^* \cdots]$ is given by:

$$[\varepsilon X_+ Y_+ - (\varepsilon - \omega\hbar) X_- Y_+] \left[\varepsilon(\varepsilon - 2\omega\hbar) + Y_-^2\right]$$

$$= \varepsilon^2(\varepsilon - 2\omega\hbar) X_+ Y_- + \varepsilon X_+ Y_-^3 + \varepsilon(\varepsilon - \omega\hbar)(\varepsilon - 2\omega\hbar) X_- Y_+ + \varepsilon^2(\varepsilon - \omega\hbar) X_- Y_-$$

Since $[\dots b_2^{(1)}\dots][\dots a_1^*\cdots]$ is the complex conjugate of $[\dots a_2^{(1)}\dots][\dots b_1^*\cdots]$, the sum of them, denoted by $\{I\}$ is:

$$\begin{aligned}\{I\} &= \varepsilon(\varepsilon-\omega\hbar)(3\varepsilon-2\omega\hbar)\Gamma(X_+Y_-^2+X_-Y_+^2)+\varepsilon^2[\varepsilon^2(\varepsilon-2\omega\hbar)+2(\varepsilon-\omega\hbar)^3]\Gamma(X_-+X_+)\\ &\quad+\varepsilon(\varepsilon-\omega\hbar)(\varepsilon-2\omega\hbar)(X_-^3Y_+^2+X_+^3Y_-^2)+\varepsilon(X_+^3Y_-^4+X_-^3Y_+^4)\end{aligned} \tag{A.14}$$

and similarly, we have:

$$\begin{aligned}\{II\} &= \left\{[\cdots a_2^{(2)}\cdots][\cdots b_1^*\cdots]+[\cdots b_2^{(2)}\cdots][\cdots a_1^*\cdots]\right\}\\ &= \varepsilon(X_+Y_-^3+X_-Y_+^3)+\varepsilon^2(\varepsilon-\omega\hbar)(X_-Y_-+X_+Y_+)\\ &\quad+\varepsilon(\varepsilon-2\omega\hbar)(2\varepsilon-\omega\hbar)(X_+Y_-+X_-Y_+)\end{aligned} \tag{A.15}$$

Therefore, the $j_3^{\prime(B)}=-e\phi_0^\dagger\hat{v}_B\phi_2$ can be written as:

$$j_3^{\prime(B)}=e\beta\left[\frac{e^3E^3}{8i\omega^6\hbar^3\varepsilon^2\left|\omega\hbar-2\varepsilon\right|^2(\omega\hbar-\varepsilon-i\delta)}\{I\}+\frac{\alpha e^3E^3}{8i\omega^5\hbar^2\varepsilon^2(\omega\hbar-\varepsilon-i\delta)(\omega\hbar-2\varepsilon+i\delta)}\{II\}\right] \tag{A.16}$$

The optical current density $J_3^{\prime(B)}$ is given by

$$\begin{aligned}J_3^{\prime(B)} &= \frac{e\beta}{4\pi^2\hbar^2}\Re\int pdpd\theta\left[\frac{e^3E^3}{8i\omega^6\hbar^3\varepsilon^2\left|\omega\hbar-2\varepsilon\right|^2(\omega\hbar-\varepsilon-i\delta)}\{I\}+\right.\\ &\quad\left.+\frac{\alpha e^3E^3}{8i\omega^5\hbar^2\varepsilon^2(\omega\hbar-\varepsilon-i\delta)(\omega\hbar-2\varepsilon+i\delta)}\{II\}\right]\end{aligned} \tag{A.17}$$

The first term can be evaluated as followed:

$$\begin{aligned}
& \frac{-e\beta}{4\pi^2\hbar^2}\int\{I\}Im\left(\frac{e^3E^3}{8i\omega^6\hbar^3\varepsilon^2\left|\omega\hbar-2\varepsilon\right|^2}\right)Im\left(\frac{1}{(\omega\hbar-\varepsilon-i\delta)}\right)pdpd\theta \\
= & \frac{e^4E^3\beta}{32\pi^2\omega^6\hbar^5}\int\frac{\{I\}}{\varepsilon^2\left|\omega\hbar-2\varepsilon\right|^2}\pi\delta(\omega\hbar-\varepsilon)pdpd\theta \\
= & \frac{e^4E^3\beta}{32\pi\omega^6\hbar^5}\int\frac{\{I\}}{\varepsilon^2\left|\omega\hbar-2\varepsilon\right|^2}\frac{\omega\hbar\times\delta(\theta-\theta_0)}{3\alpha\beta p^3\sqrt{1-X(p)^2}}pdpd\theta \\
= & \frac{e^4E^3}{96\alpha\pi\omega^6\hbar^5}\int\frac{\{I\}_{\theta=\theta_0}}{\omega\hbar\left|\omega\hbar-2\omega\hbar\right|^2p^2\sqrt{1-X(p)^2}}dp \\
= & \frac{e^4E^3\hbar}{96\alpha\pi(\omega\hbar)^9}\int\frac{\{I\}_{\theta=\theta_0}}{p^2\sqrt{1-X(p)^2}}dp
\end{aligned} \tag{A.18}$$

where θ_0 is the root of $(\omega\hbar-\varepsilon)$ and is given by

$$\theta_0=\frac{1}{3}\cos^{-1}\left(X(p)\right) \tag{A.19}$$

and

$$X(p)\equiv\frac{\alpha^2p^4+\beta^2p^2-\omega^2\hbar^2}{2\alpha\beta p^3} \tag{A.20}$$

The second term is given by

$$\begin{aligned}
& \frac{-e\beta}{4\pi^2\hbar^2}\int Im\left(\frac{\alpha e^3E^3}{8i\omega^5\hbar^2\varepsilon^2}\right)Im\left(\frac{1}{(\omega\hbar-\varepsilon-i\delta)(\omega\hbar-2\varepsilon+i\delta)}\right)\{II\}pdpd\theta \\
= & \frac{e\beta}{4\pi^2\hbar^2}\int\frac{\alpha e^3E^3}{8\omega^5\hbar^2\varepsilon^2}Im\left(\frac{1}{(\omega\hbar-\varepsilon-i\delta)(\omega\hbar-2\varepsilon)}+\frac{1}{(\omega\hbar-\varepsilon)(\omega\hbar-2\varepsilon+i\delta)}\right)\{II\}pdpd\theta \\
= & \frac{e^4E^3\alpha\beta}{32\pi^2\omega^5\hbar^4}\left(\int\frac{\pi\delta(\omega\hbar-\varepsilon)\{II\}pdpd\theta}{\varepsilon^2(\omega\hbar-2\varepsilon)}-\int\frac{\pi\delta(\omega\hbar-2\varepsilon)\{II\}pdpd\theta}{\varepsilon^2(\omega\hbar-\varepsilon)}\right) \\
= & \frac{e^4E^3\alpha\beta}{32\pi\omega^5\hbar^4}\left(\int\frac{\omega\hbar\times\delta(\theta-\theta_0)\{II\}pdpd\theta}{3\alpha\beta\varepsilon^2(\omega\hbar-2\varepsilon)p^3\sqrt{1-X(p)^2}}-\int\frac{\omega\hbar/2\times\delta(\theta-\theta_0')\{II\}pdpd\theta}{6\alpha\beta p^3\varepsilon^2(\omega\hbar-\varepsilon)\sqrt{1-X'(p)^2}}\right) \\
= & \frac{e^4E^3}{96\pi\omega^5\hbar^4}\left(\int\frac{\{II\}_{\theta=\theta_0}dp}{\omega\hbar(-\omega\hbar)p^2\sqrt{1-X(p)^2}}-\int\frac{\{II\}_{\theta=\theta_0'}dp}{\omega\hbar(\omega\hbar/2)p^2\sqrt{1-X'(p)^2}}\right) \\
= & \frac{-e^4E^3\hbar}{96\pi(\omega\hbar)^7}\left(\int\frac{\{II\}_{\theta=\theta_0}dp}{p^2\sqrt{1-X(p)^2}}+\int\frac{2\times\{II\}_{\theta=\theta_0'}dp}{p^2\sqrt{1-X'(p)^2}}\right)
\end{aligned} \tag{A.21}$$

where θ_0' is the root of $(\omega\hbar - 2\varepsilon)$ and is given by

$$\theta_0' = \frac{1}{3}\cos^{-1}\left(X'(p)\right) \tag{A.22}$$

and

$$X'(p) \equiv \frac{\alpha^2 p^4 + \beta^2 p^2 - \frac{\omega^2\hbar^2}{4}}{2\alpha\beta p^3} \tag{A.23}$$

Therefore, from $J_3^{(B)} = J_3'^{(B)} + J_3''^{(B)}$, we obtain:

$$\begin{aligned} J_3^{(B)} &= \frac{e^4E^3\hbar}{48\alpha\pi(\omega\hbar)^9}\int\frac{\{I\}_{\theta=\theta_0}}{p^2\sqrt{1-X(p)^2}}dp - \frac{e^4E^3\hbar}{48\pi(\omega\hbar)^7}\left(\int\frac{\{II\}_{\theta=\theta_0}dp}{p^2\sqrt{1-X(p)^2}}\right. \\ &\left. + \int\frac{2\{II\}_{\theta=\theta_0'}dp}{p^2\sqrt{1-X'(p)^2}}\right) \end{aligned} \tag{A.24}$$

Note that a factor of two is added since $J_3'^{(B)} = J_3''^{(B)}$ and another factor of 2 is added when both spin degeneracy. Finally, we write the single-frequency conductivity corresponding to $\hat{v}_B$ as:

$$\sigma_3^{(B)}(\omega) = \frac{e^4E^2\hbar}{24\alpha\pi(\omega\hbar)^9}\int\frac{\{I\}_{\theta=\theta_0}}{p^2\sqrt{1-X(p)^2}}dp - \frac{e^4E^3\hbar}{24\pi(\omega\hbar)^7}\left(\int\frac{\{II\}_{\theta=\theta_0}dp}{p^2\sqrt{1-X(p)^2}} + \int\frac{2\{II\}_{\theta=\theta_0'}dp}{p^2\sqrt{1-X'(p)^2}}\right) \tag{A.25}$$

Using the same procedures, the optical current density corresponding to velocity operator $\hat{v}_A$ can be determined:

$$\sigma_3^{(A)}(\omega) = \frac{e^4E^2\hbar}{12\pi(\omega\hbar)^9}\int\frac{\{I\}^{(A)}_{\theta=\theta_0}}{p^2\sqrt{1-X(p)^2}}dp - \frac{e^4E^3\hbar\alpha}{12\beta\pi(\omega\hbar)^7}\left(\int\frac{\{II\}^{(A)}_{\theta=\theta_0}dp}{p^2\sqrt{1-X(p)^2}} + \int\frac{2\{II\}^{(A)}_{\theta=\theta_0'}dp}{p^2\sqrt{1-X'(p)^2}}\right) \tag{A.26}$$

where $\{I\}^{(A)}$ and $\{II\}^{(A)}$ are the 'bracket terms' originating from $\phi_0^\dagger\hat{v}_A\phi_2$ and $\phi_2^\dagger\hat{v}_A\phi_0$ (i.e. $a_0^*p_+b_2 + b_0^*p_-a_2$, and so on). Finally, the total single-frequency third-oder nonlinear optical conductivity is:

$$\sigma_3(\omega) = \sigma_3^{(A)}(\omega) + \sigma_3^{(B)}(\omega) \tag{A.27}$$

σ_3 is calculated numerically and is one of the main results of Chapter 3.

A.3 Derivation of $\sigma_3(3\omega)$

The n=3 spinor components are given by

$$a_3 = \frac{eE}{3i\omega^2\hbar(3\omega\hbar-2\varepsilon)}[X_-(\varepsilon-3\omega\hbar)b_2+X_+Y_-a_2]-\alpha\frac{e^2E^2}{3\omega^3\hbar(3\omega\hbar-2\varepsilon)}[Y_-a_1+(\varepsilon-3\omega\hbar)b_1]$$

$$b_3 = \frac{eE}{3i\omega^2\hbar(3\omega\hbar-2\varepsilon)}[X_-Y_+b_2+X_+a_2(\varepsilon-3\omega\hbar)]-\alpha\frac{e^2E^2}{3\omega^3\hbar(3\omega\hbar-2\varepsilon)}[(\varepsilon-3\omega\hbar)a_1+Y_+b_1] \tag{A.28}$$

Substitute Eq. (3.14), (3.14), (A.2) and (A.3), we obtain

$$\begin{aligned} a_3 = &\frac{-e^3E^3}{12\sqrt{2}i\omega^6\hbar^3\varepsilon(\omega\hbar-\varepsilon)(\omega\hbar-2\varepsilon)(3\omega\hbar-2\varepsilon)}[\cdots a_3^{(1)}\cdots] \\ &-\frac{\alpha e^3E^3}{12\sqrt{2}i\omega^5\hbar^2\varepsilon(\omega\hbar-\varepsilon)(3\omega\hbar-2\varepsilon)}[\cdots a_3^{(2)}\cdots] \\ &-\frac{\alpha e^3E^3}{3\sqrt{2}i\omega^5\hbar^2\varepsilon(\omega\hbar-2\varepsilon)(3\omega\hbar-2\varepsilon)}[\cdots a_3^{(3)}\cdots] \end{aligned} \tag{A.29}$$

$$\begin{aligned} b_3 = &\frac{-e^3E^3}{12\sqrt{2}i\omega^6\hbar^3\varepsilon(\omega\hbar-\varepsilon)(\omega\hbar-2\varepsilon)(3\omega\hbar-2\varepsilon)}[\cdots b_3^{(1)}\cdots] \\ &-\frac{\alpha e^3E^3}{12\sqrt{2}i\omega^5\hbar^2\varepsilon(\omega\hbar-\varepsilon)(3\omega\hbar-2\varepsilon)}[\cdots b_3^{(2)}\cdots] \\ &-\frac{\alpha e^3E^3}{3\sqrt{2}i\omega^5\hbar^2\varepsilon(\omega\hbar-2\varepsilon)(3\omega\hbar-2\varepsilon)}[\cdots b_3^{(3)}\cdots] \end{aligned} \tag{A.30}$$

The third order current operator $j_3(3\omega)$ is be composed of:

$$j_3(3\omega) = j_3'(3\omega) + j_3''(3\omega) \tag{A.31}$$

where we can split it into $\hat{v}_A$ and $\hat{v}_B$ parts, i.e.

$$j_3' = -e\phi_0^\dagger\hat{v}_A\phi_3 - e\phi_3^\dagger\hat{v}_B\phi_0 \equiv j_3^{'(A)} + j_3^{'(B)} \tag{A.32}$$

$$j_3'' = -e\phi_0^\dagger\hat{v}_A\phi_3 - e\phi_3^\dagger\hat{v}_B\phi_0 \equiv j_3^{''(A)} + j_3^{''(B)} \tag{A.33}$$

where we dropped the argument and write $j_3 = j_3(3\omega)$ for notational simplicity. For $j_3^{\prime(B)}$, we find:

$$a_3 b_0^* = \frac{-e^3E^3}{24i\omega^6\hbar^3\varepsilon(\omega\hbar-\varepsilon)(\omega\hbar-2\varepsilon)(3\omega\hbar-2\varepsilon)}[\cdots a_3^{(1)}\cdots]$$

$$-\frac{\alpha e^3E^3}{24i\omega^5\hbar^2\varepsilon(\omega\hbar-\varepsilon)(3\omega\hbar-2\varepsilon)}[\cdots a_3^{(2)}\cdots]$$

$$-\frac{\alpha e^3E^3}{6i\omega^5\hbar^2\varepsilon(\omega\hbar-2\varepsilon)(3\omega\hbar-2\varepsilon)}[\cdots a_3^{(3)}\cdots]$$

where $b_0^* = 1/\sqrt{2}$. The sum of $a_3 b_0^* + b_3 a_0^*$ is then given by

$$a_3 b_0^* + b_3 a_0^* = \frac{-e^3E^3}{24i\omega^6\hbar^3\varepsilon(\omega\hbar-\varepsilon)(\omega\hbar-2\varepsilon)(3\omega\hbar-2\varepsilon)}\{I\}$$

$$-\frac{\alpha e^3E^3}{24i\omega^5\hbar^2\varepsilon(\omega\hbar-\varepsilon)(3\omega\hbar-2\varepsilon)}\{II\}$$

$$-\frac{\alpha e^3E^3}{6i\omega^5\hbar^2\varepsilon(\omega\hbar-2\varepsilon)(3\omega\hbar-2\varepsilon)}\{III\}$$

where

$$\{I\} \equiv [\cdots a_3^{(1)}\cdots] + [\cdots b_3^{(1)}\cdots]$$

$$\{II\} \equiv [\cdots a_3^{(2)}\cdots] + [\cdots b_3^{(2)}\cdots]$$

$$\{III\} \equiv [\cdots a_3^{(3)}\cdots] + [\cdots b_3^{(3)}\cdots] \tag{A.34}$$

Therefore,

$$
\begin{aligned}
j_3^{'(B)}(3\omega) &= -e\phi_0^{\dagger}\hat{v}_B\phi_3 \\
&= -e\times(-\beta)\times(a_3b_0^{*}+b_3a_0^{*}) \\
&= e\beta\times(a_3b_0^{*}+b_3a_0^{*}) \\
&= \frac{-e^4E^3\beta}{24i\omega^6\hbar^3\varepsilon(\omega\hbar-\varepsilon-i\delta)(\omega\hbar-2\varepsilon-i\delta)(3\omega\hbar-2\varepsilon-i\delta)}\{I\}-\frac{\alpha e^4E^3\beta}{24i\omega^5\hbar^2\varepsilon(\omega\hbar-\varepsilon-i\delta)(3\omega\hbar-2\varepsilon-i\delta)}\{II\} \\
&\quad -\alpha\frac{e^4E^3\beta}{6i\omega^5\hbar^2\varepsilon(\omega\hbar-2\varepsilon-i\delta)(3\omega\hbar-2\varepsilon-i\delta)}\{III\}
\end{aligned}
\tag{A.35}
$$

The optical current density corresponding to velocity operator $\hat{v}_B$is:

$$
\begin{aligned}
J_3^{'(B)}(3\omega) &= \frac{1}{4\pi^2\hbar^2}\Re\int\frac{-e^4E^3\beta}{24i\omega^6\hbar^3\varepsilon(\omega\hbar-\varepsilon-i\delta)(\omega\hbar-2\varepsilon-i\delta)(3\omega\hbar-2\varepsilon-i\delta)}\{I\}-\frac{\alpha e^4E^3\beta}{24i\omega^5\hbar^2\varepsilon(\omega\hbar-\varepsilon-i\delta)(3\omega\hbar-2\varepsilon-i\delta)}\{II\} \\
&\quad -\frac{e^4E^3\alpha\beta}{6i\omega^5\hbar^2\varepsilon(\omega\hbar-2\varepsilon-i\delta)(3\omega\hbar-2\varepsilon-i\delta)}\{III\}pdpd\theta \\
&= \frac{e^4E^3\beta}{96\pi^2\omega^6\hbar^5}\int\Im\left(\frac{1}{i\varepsilon}\right)\Im\left(\frac{\{I\}pdpd\theta}{(\omega\hbar-\varepsilon-i\delta)(\omega\hbar-2\varepsilon-i\delta)(3\omega\hbar-2\varepsilon-i\delta)}\right)+\frac{\alpha\beta e^4E^3}{96\pi^2\omega^5\hbar^4}\Im\left(\frac{1}{i\varepsilon}\right)\Im\left(\frac{\{II\}pdpd\theta}{(\omega\hbar-\varepsilon-i\delta)(3\omega\hbar-2\varepsilon-i\delta)}\right) \\
&\quad +\frac{e^4E^3\alpha\beta}{24\omega^5\hbar^4}\Im\left(\frac{1}{i\varepsilon}\right)\Im\left(\frac{\{III\}pdpd\theta}{(\omega\hbar-2\varepsilon-i\delta)(3\omega\hbar-2\varepsilon-i\delta)}\right) \\
&= \frac{-e^4E^3\beta}{96\pi^2\omega^6\hbar^5}\int\frac{1}{\varepsilon}\Im\left(\frac{\{I\}pdpd\theta}{(\omega\hbar-\varepsilon-i\delta)(\omega\hbar-2\varepsilon-i\delta)(3\omega\hbar-2\varepsilon-i\delta)}\right)-\frac{\alpha\beta e^4E^3}{96\pi^2\omega^5\hbar^4}\int\frac{1}{\varepsilon}\Im\left(\frac{\{II\}pdpd\theta}{(\omega\hbar-\varepsilon-i\delta)(3\omega\hbar-2\varepsilon-i\delta)}\right) \\
&\quad -\frac{e^4E^3\alpha\beta}{24\omega^5\hbar^4}\int\frac{1}{\varepsilon}\Im\left(\frac{\{III\}pdpd\theta}{(\omega\hbar-2\varepsilon-i\delta)(3\omega\hbar-2\varepsilon-i\delta)}\right)
\end{aligned}
\tag{A.36}
$$

The first term can be simplified as followed:

$$
\begin{aligned}
& \frac{-e^4E^3\beta}{96\pi^2\omega^6\hbar^5}\int\frac{1}{\varepsilon}\Im\left(\frac{\{I\}pdpd\theta}{(\omega\hbar-\varepsilon-i\delta)(\omega\hbar-2\varepsilon-i\delta)(3\omega\hbar-2\varepsilon-i\delta)}\right)\\
= & \frac{-e^4E^3\beta}{96\pi^2\omega^6\hbar^5}\int\frac{\{I\}pdpd\theta}{\varepsilon}\Im\left(\frac{1}{(\omega\hbar-2\varepsilon)(3\omega\hbar-2\varepsilon)(\omega\hbar-\varepsilon-i\delta)}+\frac{1}{(\omega\hbar-\varepsilon)(3\omega\hbar-2\varepsilon)(\omega\hbar-2\varepsilon-i\delta)}+\frac{1}{(\omega\hbar-\varepsilon)(\omega\hbar-2\varepsilon)(3\omega\hbar-2\varepsilon-i\delta)}\right)\\
= & \frac{-e^4E^3\beta}{96\pi^2\omega^6\hbar^5}\int\frac{\{I\}pdpd\theta}{\varepsilon}\left(\frac{\pi\delta(\omega\hbar-\varepsilon)}{(\omega\hbar-2\varepsilon)(3\omega\hbar-2\varepsilon)}+\frac{\pi\delta(\omega\hbar-2\varepsilon)}{(\omega\hbar-\varepsilon)(3\omega\hbar-2\varepsilon)}+\frac{\pi\delta(3\omega\hbar-2\varepsilon)}{(\omega\hbar-\varepsilon)(\omega\hbar-2\varepsilon)}\right)\\
= & \frac{-e^4E^3\beta}{96\pi\omega^6\hbar^5}\int\frac{\{I\}pdpd\theta}{\varepsilon}\left(\frac{\varepsilon\times\delta(\theta-\theta_0)}{3\alpha\beta p^3\sqrt{1-X(p)^2}(\omega\hbar-2\varepsilon)(3\omega\hbar-2\varepsilon)}+\frac{\varepsilon\times\delta(\theta-\theta_0')}{6\alpha\beta p^3\sqrt{1-X'(p)^2}(\omega\hbar-\varepsilon)(3\omega\hbar-2\varepsilon)}+\frac{\varepsilon\times\delta(\theta-\theta_0'')}{6\alpha\beta p^3\sqrt{1-X''(p)^2}(\omega\hbar-\varepsilon)(\omega\hbar-2\varepsilon)}\right)\\
= & \frac{-e^4E^3}{288\pi\alpha\omega^6\hbar^5}\int\{I\}dpd\theta\left(\frac{\delta(\theta-\theta_0)}{p^2\sqrt{1-X(p)^2}(\omega\hbar-2\varepsilon)(3\omega\hbar-2\varepsilon)}+\frac{\delta(\theta-\theta_0')}{2p^2\sqrt{1-X'(p)^2}(\omega\hbar-\varepsilon)(3\omega\hbar-2\varepsilon)}+\frac{\delta(\theta-\theta_0'')}{2p^2\sqrt{1-X''(p)^2}(\omega\hbar-\varepsilon)(\omega\hbar-2\varepsilon)}\right)\\
= & \frac{-e^4E^3}{288\pi\alpha\omega^6\hbar^5}\int dp\left(\frac{\{I\}_{\theta=\theta_0}}{p^2\sqrt{1-X(p)^2}(\omega\hbar-2\omega\hbar)(3\omega\hbar-2\omega\hbar)}+\frac{\{I\}_{\theta=\theta_0'}}{2p^2\sqrt{1-X'(p)^2}(\omega\hbar-\omega\hbar/2)(3\omega\hbar-2\times\omega\hbar/2)}\right.\\
& \left.+\frac{\{I\}_{\theta-\theta_0''}}{2p^2\sqrt{1-X''(p)^2}(\omega\hbar-3\omega\hbar/2)(\omega\hbar-2\times3\omega\hbar/2)}\right)\\
= & \frac{-e^4E^3\hbar}{288\pi\alpha(\omega\hbar)^8}\int dp\left(\frac{\{I\}_{\theta=\theta_0}}{p^2\sqrt{1-X(p)^2}(-\omega\hbar)(\omega\hbar)}+\frac{\{I\}_{\theta=\theta_0'}}{2p^2\sqrt{1-X'(p)^2}(\omega\hbar/2)(2\omega\hbar)}+\frac{\{I\}_{\theta-\theta_0''}}{2p^2\sqrt{1-X''(p)^2}(-\omega\hbar/2)(-2\omega\hbar)}\right)\\
= & \frac{-e^4E^3\hbar}{288\pi\alpha(\omega\hbar)^6}\int dp\left(-\frac{\{I\}_{\theta=\theta_0}}{p^2\sqrt{1-X(p)^2}}+\frac{\{I\}_{\theta=\theta_0'}}{2p^2\sqrt{1-X'(p)^2}}+\frac{\{I\}_{\theta=\theta_0''}}{2p^2\sqrt{1-X''(p)^2}}\right)\\
= & \frac{-e^4E^3}{288\pi\alpha\omega^6\hbar^5}\left(-[I]_{\theta_0}+\frac{1}{2}[I]_{\theta_0'}+\frac{1}{2}[I]_{\theta_0''}\right)
\end{aligned}
\tag{A.37}
$$

where θ_0, θ_0', $X(p)$ and $X'(p)$ are defined previously in Eq. (A.20) and Eq. (A.23), respectively. θ_0'' is given by:

$$\theta_0'' \equiv \frac{1}{3}\cos^{-}1(X''(p)) \tag{A.38}$$

$$X''(p) \equiv \frac{\alpha^2 p^4 + \beta^2 p^2 - \frac{9\omega\hbar}{4}}{2\alpha\beta p^3} \tag{A.39}$$

and the integral is denoted by

$$[I]_{\theta_0^{(a)}} \equiv \int \frac{\{I\}_{\theta=\theta_0^{(a)}}}{p^2\sqrt{1-X^{(a)}(p)^2}} \tag{A.40}$$

where $a =',''$ or $'''$. The second term of $J_3^{'(B)}(3\omega)$ is given by

$$\begin{aligned}
\frac{-\alpha\beta e^4E^3}{96\pi^2\omega^5\hbar^4}\int\frac{1}{i\varepsilon}\Im\left(\frac{\{II\}pdpd\theta}{(\omega\hbar-\varepsilon-i\delta)(3\omega\hbar-2\varepsilon-i\delta)}\right) &= \frac{-\alpha\beta e^4E^3}{96\pi^2\omega^5\hbar^4}\int\frac{\{II\}pdpd\theta}{\varepsilon}\Im\left(\frac{1}{(3\omega\hbar-2\varepsilon)(\omega\hbar-\varepsilon-i\delta)}+\frac{1}{(\omega\hbar-\varepsilon)(3\omega\hbar-2\varepsilon-i\delta)}\right)\\
&= \frac{-\alpha\beta e^4E^3}{96\pi^2\omega^5\hbar^4}\int\frac{\pi\times\{II\}pdpd\theta}{\varepsilon}\left(\frac{\delta(\omega\hbar-\varepsilon)}{3\omega\hbar-2\varepsilon}+\frac{\delta(3\omega\hbar-2\varepsilon)}{\omega\hbar-\varepsilon}\right)\\
&= \frac{-e^4E^3}{288\pi\omega^5\hbar^4}\int\{II\}dpd\theta\left(\frac{\delta(\theta-\theta_0)}{p^2\sqrt{1-X(p)^2}(3\omega\hbar-2\varepsilon)}+\frac{\delta(\theta-\theta_0'')}{2p^2\sqrt{1-X''(p)^2}(\omega\hbar-\varepsilon)}\right)\\
&= \frac{-e^4E^3}{288\pi\omega^5\hbar^4}\int\{II\}dpd\theta\left(\frac{\delta(\theta-\theta_0)}{p^2\sqrt{1-X(p)^2}(3\omega\hbar-2\varepsilon)}+\frac{\delta(\theta-\theta_0'')}{2p^2\sqrt{1-X''(p)^2}(\omega\hbar-\varepsilon)}\right)\\
&= \frac{-e^4E^3\hbar}{288\pi(\omega\hbar)^6}\int dp\left(\frac{\{II\}_{\theta=\theta_0}}{p^2\sqrt{1-X(p)^2}}-\frac{\{II\}_{\theta=\theta_0''}}{p^2\sqrt{1-X''(p)^2}}\right)\\
&= \frac{-e^4E^3\hbar}{288\pi(\omega\hbar)^6}\left([II]_{\theta_0}-[II]_{\theta_0''}\right) \qquad \text{(A.41)}
\end{aligned}$$

The third term of $J_3^{'(B)}(3\omega)$ is given by

$$\begin{aligned}
\frac{-e^4E^3\alpha\beta}{24\pi^2\omega^5\hbar^4}\int\frac{1}{\varepsilon}\Im\left(\frac{\{III\}pdpd\theta}{(\omega\hbar-2\varepsilon-i\delta)(3\omega\hbar-2\varepsilon-i\delta)}\right) &= \frac{-e^4E^3\alpha\beta}{24\pi^2\omega^5\hbar^4}\int\frac{\{III\}pdpd\theta}{\varepsilon}\Im\left(\frac{1}{(3\omega\hbar-2\varepsilon)(\omega\hbar-2\varepsilon-i\delta)}+\frac{1}{(\omega\hbar-2\varepsilon)(3\omega\hbar-2\varepsilon-i\delta)}\right)\\
&= \frac{-e^4E^3\alpha\beta}{24\pi\omega^5\hbar^4}\int\frac{\{III\}pdpd\theta}{\varepsilon}\left(\frac{\delta(\omega\hbar-2\varepsilon)}{3\omega\hbar-2\varepsilon}+\frac{\delta(3\omega\hbar-2\varepsilon)}{\omega\hbar-2\varepsilon}\right)\\
&= \frac{-e^4E^3}{144\pi\omega^5\hbar^4}\int\{III\}dpd\theta\left(\frac{\delta(\theta-\theta_0')}{p^2\sqrt{1-X'(p)^2}(3\omega\hbar-2\varepsilon)}+\frac{\delta(\theta-\theta_0'')}{p^2\sqrt{1-X''(p)^2}(\omega\hbar-2\varepsilon)}\right)\\
&= \frac{-e^4E^3\hbar}{288\pi(\omega\hbar)^6}\int dpd\left(\frac{\{III\}_{\theta=\theta_0'}}{p^2\sqrt{1-X'(p)^2}}-\frac{\{III\}_{\theta=\theta_0''}}{p^2\sqrt{1-X''(p)^2}}\right)\\
&= \frac{e^4E^3\hbar}{288\pi(\omega\hbar)^6}\left([III]_{\theta_0'}-[III]_{\theta_0''}\right) \qquad \text{(A.42)}
\end{aligned}$$

We can then write the optical conductivity corresponding to Eq. (A.36) compactly as:

$$\sigma_3^{(B)}(3\omega)=\frac{-e^4E^2}{72\pi\alpha(\omega\hbar^6)}\left(-[I]_{\theta_0}+\frac{1}{2}[I]_{\theta_0'}+\frac{1}{2}[I]_{\theta_0''}\right)-\frac{e^4E^3\hbar}{72\pi(\omega\hbar)^6}\left([II]_{\theta_0}-[II]_{\theta_0''}\right)-\frac{e^4E^3\hbar}{72\pi(\omega\hbar)^6}\left([III]_{\theta_0'}-[III]_{\theta_0''}\right) \qquad \text{(A.43)}$$

and following the same procedures, we obtain optical conductivity corresponding to $\hat{v}_A$ as:

$$\sigma_3^{(A)}(3\omega)=\frac{e^4E^3\hbar}{36\pi\beta(\omega\hbar^6)}\left(-[I]_{\theta_0}^{(A)}+\frac{1}{2}[I]_{\theta_0'}^{(A)}+\frac{1}{2}[I]_{\theta_0''}^{(A)}\right)+\frac{\alpha e^4E^3\hbar}{36\pi\beta(\omega\hbar)^6}\left([II]_{\theta_0}^{(A)}-[II]_{\theta_0''}^{(A)}\right)+\frac{\alpha e^4E^3\hbar}{36\pi\beta(\omega\hbar)^6}\left([III]_{\theta_0'}^{(A)}-[III]_{\theta_0''}^{(A)}\right) \qquad \text{(A.44)}$$

Finally, the full triple-frequency third-order nonlinear optical conductivity is given by

$$\sigma_3(3\omega) = \sigma_3^{(A)}(3\omega) + \sigma_3^{(B)}(3\omega) \tag{A.45}$$